UNIVERSITÀ DEGLI STUDI DI MILANO

DOTTORATO DI RICERCA IN SCIENZE DELLA TERRA
"Sistema Terra: Processi e modellazione"
Ciclo XXXV

DIPARTIMENTO DI SCIENZE DELLA TERRA

MULTISCALE GEOCHEMICAL STUDY OF THE CORNO ALTO COMPLEX (ADAMELLO BATHOLITH)

Geo 08 – Geochimica e Vulcanologia

Tesi di dottorato di
ANGELICA MOSCONI

Tutor
Prof. Massimo Tiepolo

Coordinatore del dottorato
Chiar.ma Prof.ssa Maria Iole Spalla

Anno Accademico
2021/2022

Abstract

Granitoid batholiths are important end products of the Earth's long-term compositional differentiation, representing either the addition of juvenile material to the crust or the reworking of older crustal components. The nature and composition of crustal granitoids significantly changed at the Archean-Proterozoic boundary highlighting major changes in the mechanisms of continental crust formation/differentiation throughout the Earth's history. In particular, the transition from the typical Archean TTG rocks to the post-Archean calc-alkaline granitoids is marked, in all cratons, by the occurrence of distinctive rocks called sanukitoids. These latter have been linked to subduction-related partial melting of enriched mantle and hence signal the onset of the modern plate-tectonic regime. In this context, modern analogues of the Archean granitoids provide valuable clues for investigating continental crust formation/differentiation and its secular evolution.

This study focuses on the Corno Alto complex, the oldest intrusion of the Adamello batholith and also the oldest known intrusive complex of the whole Periadriatic magmatism. The Corno Alto intrusion is crucial to shed light on the tectono-magmatic conditions active at the onset of alpine magmatism; conditions that are not yet fully understood.

In the field, three distinct types of granitoid rocks have been recognized, ranging in composition from tonalite to granodiorite and without encompassing the trondhjemitic terms described in the literature. Whole-rock chemistry reveals peculiar features with respect to the other units of the Adamello batholith, and to typical I-type and S-type granitoid rocks. The Corno Alto rocks exhibit the highest SiO_2 contents, K_2O+Na_2O up to 7.2%, a strong enrichment in Ba and to a minor extent in Sr (Ba + Sr ≈ 1100-1900 ppm). Other geochemical features include a moderately-to-strong enrichment in LREE over HREE ($La_N/Yb_N > 20$) and Y ($Sr/Y > 40$).

U-Pb geochronology on zircon shows an east-west trend of decreasing ages in the intrusive complex, with three main recurring age peaks, at c. 44 Ma, c. 42 Ma, and c. 39 Ma. The different zircon domains have significantly distinct Hf isotopes (up to 18 ε_{Hf} units of variation) with some values trending towards the isotopic composition of the depleted mantle (DM). The evidence of multiple components in the petrogenesis of the Corno Alto is also supported by the occurrence of multiple plagioclase populations as suggested by their crystals zoning and the

intense chemical disequilibria for major and trace elements, as well as for Sr isotopes (determined in situ by LA-ICP-MS).

The new geochronological data presented in this study indicate an incremental assembly of the Corno Alto complex by multiple and possibly discrete magma injections in a time span of about ~5 Myr. These results refine the current knowledge of the Corno Alto complex emplacement as a single event at 43 Ma. Noticeably, the observed age trend parallel that observed on a larger scale by Ji et al (2019) being perpendicular to the direction of the Giudicarie line, which is located right above the European slab edge (Sun et al., 2019; Zhao et al. 2016). The new data suggest that the NW migration of the magmatism observed at the orogen scale as a consequence of the Eocene-Oligocene slab steepening is also evident at the scale of Corno Alto complex.

Major-trace element mineral chemistry, Hf isotope on zircon and Sr isotope on plagioclase suggest that the Corno Alto is the product of a multi-stage and multi-component process involving a high Ba component with high Sr and La/Yb ratios and a juvenile component. The overall geochemical signature of the Corno Alto rocks resembles that of a peculiar group of Phanerozoic rocks known as high Ba-Sr granites which are considered as modern analogues of the Archean sanukitoids. The relatively high thermal gradient required to generate such peculiar melts, typical of the Archean, are likely ensured during the Eocene by the thermal perturbation induced by rising asthenospheric material along the slab tear in response to slab edge effects.

Index

Chapter I
General Introduction

Since its formation, the Earth has undergone a complex evolution consisting of both closed system differentiation and additions of extra-terrestrial material (Rudnick and Gao, 2005). Our knowledge of the differentiation mechanisms active during the "youth" of our planet has still many gaps, such as the actual chondritic composition of the planet or how the elements were added, how they were distributed during differentiation, and finally how their deep cycle evolved to the origin of life. Among the mechanisms of planetary differentiation, the origin of the Archean continental crust is still much debated (Moyen, 2011).

Many questions are still open, for example, it is not yet clear if the crust extraction from the mantle was a continuous or an episodic process (Laurent et al., 2014). In any case, the rate of continental extraction and the mechanisms of continental crust differentiation changed through the Earth's history, as evidenced by a major change in the nature of the granitoids types.

One of the key components of the early continental crust is an association of sodic granitoids rocks of tonalitic-trondhjemitic-granodioritic composition called TTG (Jahn et al., 1981; Drummond and Defant, 1990; Martin, 1994), characterized by low K_2O/Na_2O and highly fractionated REE patterns (Moyen, 2011). Noticeably, TTGs are missing in the modern continental crust and, therefore, they appear to be essentially related to the early part of Earth's history.

It is now widely recognized that the sporadic occurrence in post-Archean times of rocks compositionally analogous to the early continental crust and, in turn, compositionally distinct to modern granitoids, may help developing the discussion of the secular evolution of crust composition and the processes of its formation.

In this framework, this study aimed to define the petrogenetic processes at the origin of modern analogues of the Archean granitoids to extrapolate the processes responsible for the formation of the early continental crust. In order to do this, the Corno Alto complex in the Adamello batholith was chosen as the case study for its peculiar composition. Indeed, the Corno Alto complex was described in the literature as an association of tonalite-trondhjemite-granodiorite rocks and thus considered a potential equivalent to the early igneous products at the origin of the continental crust.

The Corno Alto rocks also reveal peculiar features compared to the rest of the Adamello batholith and in turn to typical I-type and S-type granites. Being also the oldest intrusion not only of the whole batholith (Ji et al., 2019; Schaltegger et al., 2019) but also of the whole Periadriatic magmatism, the Corno Alto complex is a key geological record to investigate the petrogenetic processes at the origin of the early melts in the alpine orogeny and their bearing on the general architecture of the Alpine evolution. The approach to the study has been multi-scale and involved different geochemical analytical techniques. Particularly, two main approaches have been applied:

* Fieldwork, associated with the petrographic study and geochemical analyses on whole-rock samples (major and trace element compositions) has led to the recognition of the different rock types occurring in the Corno Alto complex and their detailed geochemical characterization.
* In situ trace element and isotopic analyses of zircons (trace elements and U-Pb by LA ICP-MS, and Hf isotopes by LA-MC-ICP-MS) and plagioclase feldspars (trace elements by LA ICP-MS and Sr isotopes by LA-MC-ICP-MS) have allowed the geochronological characterization of the Corno Alto complex and the recognition of chemical disequilibria at the micro-scale.

The structure of the thesis is as follows:

* Chapter 1 is a general introduction illustrating the aim of the study.
* Chapter 2 provides an overview of the genesis of the continental crust, as it was deemed necessary to summarize the main concepts relating to the transition from Archaean to present-day crust in order to better comprehend the proposed analogies in the interpretation.
* Chapter 3 serves as a review of the current state of knowledge regarding Periadriatic magmatism, and in particular of the Adamello batholith and the Corno Alto case study.
* Chapter 4 includes the field and petrographic study, mineral major element analyses and whole-rock and zircon geochemistry of the Corno Alto rocks. The results and petrological implications have been discussed in the frame of periadriatic magmatism and constituted the object of a paper submitted to Lithos magazine.
* Chapter 5 represents a preliminary study of the Corno Alto plagioclase felsdpars. The applied approach made it possible to identify a multi-stage and multi-component formation mechanism consistent with the interpretations discussed in Chapter 4.
* Chapter 6 summarizes the main common geochemical features and differences between the Corno Alto rocks and the Archean TTG and Sanukitoids.

* Chapter 7 presents a comprehensive summary of the most important results, highlighting the contributions of this research. It also provides insights into the possible future implications and directions for further research.

Chapter 2
Secular evolution of the continental crust

2.1 Introduction

Our planet is made up of two distinct types of crust: the oceanic and the continental crust (Rudnick & Gao, 2004). The oceanic crust is thin (~7 km on average) and composed of relatively dense rock types such as basalt which are recycled back into the mantle by subduction within 200 Ma. Differently, the continental crust is composed of buoyant quartzofeldspatic materials that it is difficult to destroy by subduction (Kemp and Hawkesworth, 2003). Thus, among the extensive geological record stored in the continental crust, there are the oldest rocks and minerals yet observed on Earth (e.g. the 4.0 Ga Acasta gneiss and 4.4 Ga detrital zircons from the Slave Craton of the Northwest Territories in Canada; Bowring and Williams, 1999; Wilde et al., 2001). The continental crust is therefore a record of how Earth's conditions have changed, and how mechanisms of crust generation have evolved through geological times (Kemp and Hawkesworth, 2003).

2.2 The Archean TTGs

Much of the Earth's continental crust was produced during the Archean Eon (4.0 - 2.5 billion years ago) and it is currently exposed in ancient cratons (Johnson et al., 2019). These Archean terranes mostly consist of orthogneisses complexes, called "grey gneiss complexes" (Moyen, 2011). The key component (but not the most abundant; Moyen, 2011) of these latter, is represented by the association of deformed and metamorphosed sodic granitoids termed the "TTG series", since they are composed by tonalites, trondhjemites and granodiorites.

TTG are sodic granitoids (K_2O/Na_2O <1), characterized by significantly higher La/Yb ratios, higher Sr concentrations and no Eu anomalies. In contrast, post-Archean granitoids show a more potassic nature (K_2O/Na_2O>1), a marked decrease in La/Yb, in Sr concentrations and emergence of negative Eu anomalies (Laurent et al., 2020).

The absence of TTG in the modern Earth and their exclusive occurrence during the Archean, underlines a secular variation of felsic magmatism on Earth (Moyen, 2011).

It is now generally accepted that this first generation of continental crust was formed by partial melting and/or crystallization of hydrous, low-potassium basaltic rocks (Moyen and Martin, 2012). However, no general consensus has been reached on the geodynamic regime of formation of Archean TTG magmas, when the existence of plate tectonics remains unproven (Laurent et al., 2020). Different hypothesis were proposed, both following actualistic and non-uniformitarian views.

According to some authors, TTGs formed in subduction zones as a consequence of the partial melting of the subducted oceanic lithosphere (Foley et al., 2002; Rapp et al., 2003; Martin et al., 2005). Others sustain non-uniformitarian models, at least in the early Archean, with the TTG formation in the lower levels of thick (<30 km) plateau-like mafic crust after multistage reworking of primitive high-MgO primary crust (Smithies, 2000; Johnson et al., 2019).

Although some evidence suggests localized episodes of subduction in the early Archean (Jenner et al., 2009; O'Neil et al., 2011; Turner et al., 2014), it is more plausible that most TTG magmas were formed through melting in the lower levels of a thick, deformable, and relatively continuous mafic crust (such as the deformable stagnant lid or plutonic squishy lid regime), at least prior to the Mesoarchean (Johnson et al., 2019; Gardiner et al., 2017; Johnson et al., 2014, 2017; Rozel et al., 2017; Sizova et al., 2015; Smithies et al., 2003, 2007; Van Kranendonk et al., 2015a). It is important to note that the existence of different geodynamic environments on Earth at any given time is expected, considering that upper mantle temperatures may have varied by 120°C or more around the globe during the Archean, as they do today (Johnson et al., 2019; Herzberg et al., 2007).

Moyen (2011) subdivided TTG rocks according to the potential P-T-conditions of their formation based on La_N/Yb_N and Sr/Y ratios and the Al_2O_3 contents at 70 wt.% SiO_2. In this way, TTG's were classified as high-pressure (≥1.5 GPa), medium-pressure (1.0-1.5 GPa) and low-pressure (≤1.0 GPa) rocks, depending on depth of their melt extraction. While low-pressure and medium-pressure TTG source regions are consistent with the primitive Archean mafic crust (20-40 Km thick; Herzberg et al., 2010), high-pressure TTGs would require mafic rocks burial to mantle depths, at temperature conditions compatible with a "hot subduction" (Laurent et al., 2020).

However, thermo-mechanical models have proven the implausible occurrence of subduction at early Archean ambient mantle temperatures, which is estimated to be >200 K hotter than today (Laurent et al., 2020; Sizova et al., 2015). Thus, melting of delaminated mafic crust has been proposed as pivotal mechanism for high-pressure TTGs, with the issue that TTGs require a fertile, hydrated mafic protolith whereas delamination is fostered by refractory and anhydrous lower crust (Laurent et al., 2020). Noticeably, as already stated by Moyen (2011),

models proposed for Archean geodynamics based on assumption of a unique site of crustal growth should be disused, whereas intermediate or mixed models should be encouraged. Recent studies (Smithies et al., 2019; Laurent et al., 2020) subverted previous views by suggesting the absence of pressure melting at ≥ 1.5 GPa in the Archean and ascribed the high-pressure signature to felspar accumulation or hornblende fractionation. However, the authors emphasise that the process involved in their model is not exclusive to a particular geodynamic setting but could occur both in convergent and extensional settings (Laurent et al., 2020).

2.3 The Archean-Proterozoic transition

The Archean-Proterozoic transition (~2500 Ma) is marked by the emplacement of a new type of igneous complexes, termed "sanukitoids" after Shirey and Hanson (1984). Sanukitoids are thought to record the evolution of crustal growth processes, in that both their compositional and chronological character are intermediate between typical Archean TTG and modern arc granitoids (Martin et al., 2005).

The sanukitoid series are composite magmatic complexes (Laurent et al., 2014) which include a wide range of (ultra)mafic to felsic rocks, the latter being generally dominant in terms of volume. The major and trace elements geochemistry of these rocks was initially constrained by Stern et al., (1989). Their definition however took into consideration only LILE- and LREE-rich diorites with high Mg#, and only a minor part of all sanukitoids described worldwide matched the proposed criteria. A new and exhaustive definition was then proposed from Heilimo et al., (2010) who introduced the so-called "sanukitoid suite", comprehensive of sanukitoids s.s. and their differentiated products with SiO_2 >60% wt.% (granodiorites and granites). According to Laurent et al. (2014), the sanukitoid series can be compositionally constrained as follow: they are calc-alkaline to alkali-calcic, metalouminous ($0.7 \leq A/CNK \leq 1.0$) rocks with SiO_2 content extending from 45 wt.% to 70 wt.%; K_2O is variable ($1.5 \leq K_2O \leq 5.0$ wt.%), leading to a wide range of K_2O/Na_2O ratios, generally ≥0.5. The CaO and ferromagnesian oxides are typically high ($5 \leq FeOt + MgO + MnO + TiO_2 \leq 25$ wt.%). Sanukitoids s.l. show a wide range of La_N/Yb_N ratios (10-75, but most often >25), variable Eu anomaly ($0.5 \leq Eu_N/Eu^* \leq 1.0$) and are notably characterized by negative anomalies in Nb-Ta. Another key geochemical feature of sanukitoid rocks is the enrichment in Ba (generally >1000 ppm) and Sr (generally >400 ppm), which results in high Ba/Rb and Sr/Y ratios, and a relatively high content in transition elements such as V (>50 ppm), Ni (15–200 ppm) and Cr (20–500 ppm), thus preserving both "mantle" and "crustal" signature.

Petrogenetic models on the origin of sanukitoid rocks have positioned their source region in the supra-subduction mantle wedge (Fowler & Rollinson, 2012), thus suggesting major changes in the geodynamic setting of melt production at the Archean-Proterozoic transition.

One of the first models for the petrogenesis of sanukitoids was proposed by Martin et al. (2009), based on the assumption that Archean TTG formed in a subduction environment, where melting of subducted oceanic crust occurred. According to these authors, during the Late Archean the Earth's heat production started to decline with a consequent decrease in slab-melting efficiency.

Following their model, in the Early Archean, the slab-melts/mantle-peridotite ratios were high with the rising of TTG melts in the crust ('adakite model'). Conversely, at the Archean-Proterozoic boundary, these ratios started to decrease, with the slab-melts totally consumed in the reaction with mantle wedge. Sanukitoids could thus result from a single event where mantle contamination and melting are concomitant, or from a two-step process where the metasomatized mantle is subsequently molten (Martin et al., 2009).

While in the model of Martin et al (2009), the agent of the mantle-wedge enrichment was a slab-derived adakitic melt, Laurent et al. (2011) proposed melting of subducted terrigenous sediments. Following this latter model, the lower geothermal gradients at the Archean-Proterozoic boundary favoured sediment rather than basalt melting, evidencing a progressively more important role played by erosion and sedimentation process and recycling of detrital material into the mantle (Laurent et al., 2011). Moreover, sanukitoids represent direct evidence of involvement of a mantle-wedge, and thus of modern high-angle subduction (Fowler and Rollinson, 2012).

2.4 Modern Analogues to the Archean granitoids

Subduction-driven plate tectonics is a gradual mechanism which is thought to have started at ca. 3.0 Ga and evolved to a modern style by ca. 2.5 Ga (Archean-Proterozoic boundary; Condie et al., 2016). Since the onset of plate-tectonics, magma generation in subduction zones is considered the main mechanism for the growth of new continental crust (Hawkesworth et al., 2020).

Thermal models of the last decades (e.g. Syracuse et al., 2010) better constrained thermal conditions of subduction environments, revealing that direct melting of subducted oceanic crust is only possible under exceptional circumstances for very young and hot slabs. In this sense, direct slab-melting is considered between the possible mechanisms at the origin of the TTG suites, due to the steeper geothermal gradients in the Archean (Rapp et al., 2003).

In modern subduction environments, the burial of cold material from the Earth's surface reduce temperature of the surrounding mantle (Rustioni et al., 2021). Melting point depression is likely reached by the addition of water into the mantle wedge rather than by elevated temperatures, consistently with the generally elevated water contents in arc magmas (Metrich and Wallace, 2008).

Subducted crustal rocks undergo intermediated- to ultrahigh-pressure metamorphism, leading to the liberation of metamorphic fluids (i.e. aqueous fluid and hydrous silicate melt) that ascend into the mantle wedge, above the subduction zone, and induce partial melting (Tatsumi and Eggins, 1995; Zheng, 2012; Hermann et al., 2013). H_2O and incompatible elements with relatively high fluid mobility like K, Ba, Rb, Sr, Pb, U and to a lesser extent Ce are released from the subducting slab and incorporated into the mantle wedge. Other elements rather immobile in the fluid phase, like Y, Zr and Nb are preferentially subducted to the deeper mantle (Tatsumi and Eggins, 1995; Zheng et al., 2011; Hermann et al., 2013). Fluid-mediated mass transport in subducted crust is at the origin of arc magmatism in post-Archean times and deeply affected the long-term differentiation of the Earth. Basically, the source of juvenile continental crust thus changed from metabasalt to fluid-metasomatized mantle peridotite (Laurent et al., 2020; Martin et al., 2005). This resulted in the secular variation of the magmatic product related to subduction environments, marking the decline of both TTG and sanukitoids and leaving the scene to the Phanerozoic granitoid rocks (Fig. 2.1).

In comparison with the Archean TTG, modern arc granitoids are commonly richer in K_2O (granodiorites to granites) and evolve through K-enrichment during differentiation. Moreover, post-Archean granitoids have both higher HREE contents, and negative Eu, Nb-Ta, Sr and Ti anomalies (Moyen and Martin, 2012). However, occasionally, petrological and compositional equivalents of archean granitoids, and in particular of Sanukitoids, are widespread in Phanerozoic orogenic belts (Fan et al., 2004; Fowler et al., 2008; Jiang et al., 2006; Yuan et al., 2010), and in particular, from the late Cretaceous and Tertiary (Fowler et al., 2008; Tarney and Jones, 1994; Ye et al., 2008; Figure 2.2).

These modern analogous are the high Ba-Sr granitoids, firstly recognized by Tarney and Jones (1994) and defined on the basis of their trace element character, especially the high Ba (>500 ppm) and Sr (>300 ppm) concentrations. Other distinctive trace element signatures are high LREE, low Nb, Ta and heavy HREE (Fowler et al., 2008). These characteristics set them apart from typical modern granitoids, and therefore require fundamentally different petrogenesis (Fowler et al., 2001). Many possible petrogenetic processes were advanced to explain the exotic

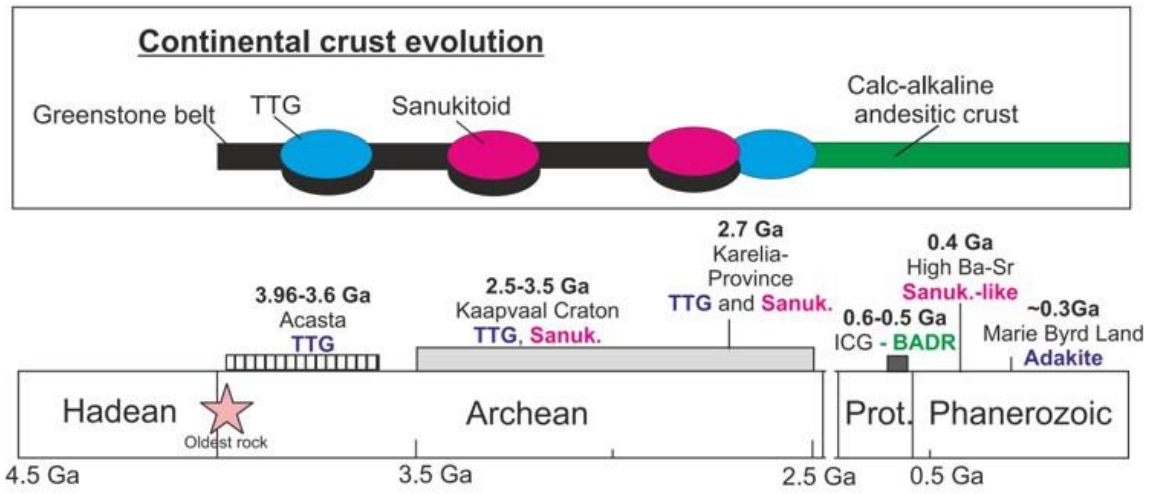

Figure 2.1 After Bruand et al., (2020). Cartoon of continental crust evolution, from TTG (blue) and sanukitoid (pink) in the Archean towards typical arc magma (green) in Proterozoic and Phanerozoic.

signature of the high Ba-Sr magmas. Among these, subduction of ocean plateaux, underplating by high Ba-Sr mafic magmas and lithospheric enrichment by carbonatitic melts were proposed (Tarney and Jones, 1994). Some High Ba-Sr plutons are briefly described in Table 2.1.

Fowler and Rollinson (2012) compared major element, trace element and isotopic compositions of Caledonian High Ba-Sr granitoids from the Northern Highlands of Scotland (Fowler et al., 2008) with those of the Archean sanukitoids from the Panozero pluton in the Baltic (Fennoscandian) schield (Lobach-Zhuchenko et al., 2005; 2008). For both the rock suites, the authors suggested a similar derivation from an enriched subcontinental lithospheric mantle, involving melting of subducted sediment as the cause of LILE transfer into the overlying mantle wedge. Several studies investigated the role of aqueous fluids or melts as agents of LILE transfer at pressure-temperature conditions pertinent to deeply subducting slabs (Fowler and Rollinson, 2012). Among these, Hermann and Rubatto (2009) suggested a key role of accessory minerals (e.g. rutile, allanite, monazite, zircon and apatite) being critical host for Rb, Sr, Ba, light REEs, Th and U, and concluded that only hydrous melts efficiently released such elements at subarc depths. Moreover, the analysis of volatiles and trace elements in melt inclusions in olivines from Kamchatka arc by Portnyagin et al. (2007) revealed that only melts or supercritical fluids from sediments could carry thousands of parts per million of Ba and Sr.

The high Ba-Sr granitoid may thus help to recognize the occasional recurrences of thermal regimes similar to those of the Archean or similar tectonomagmatic circumstances that led to analogous magmatic products.

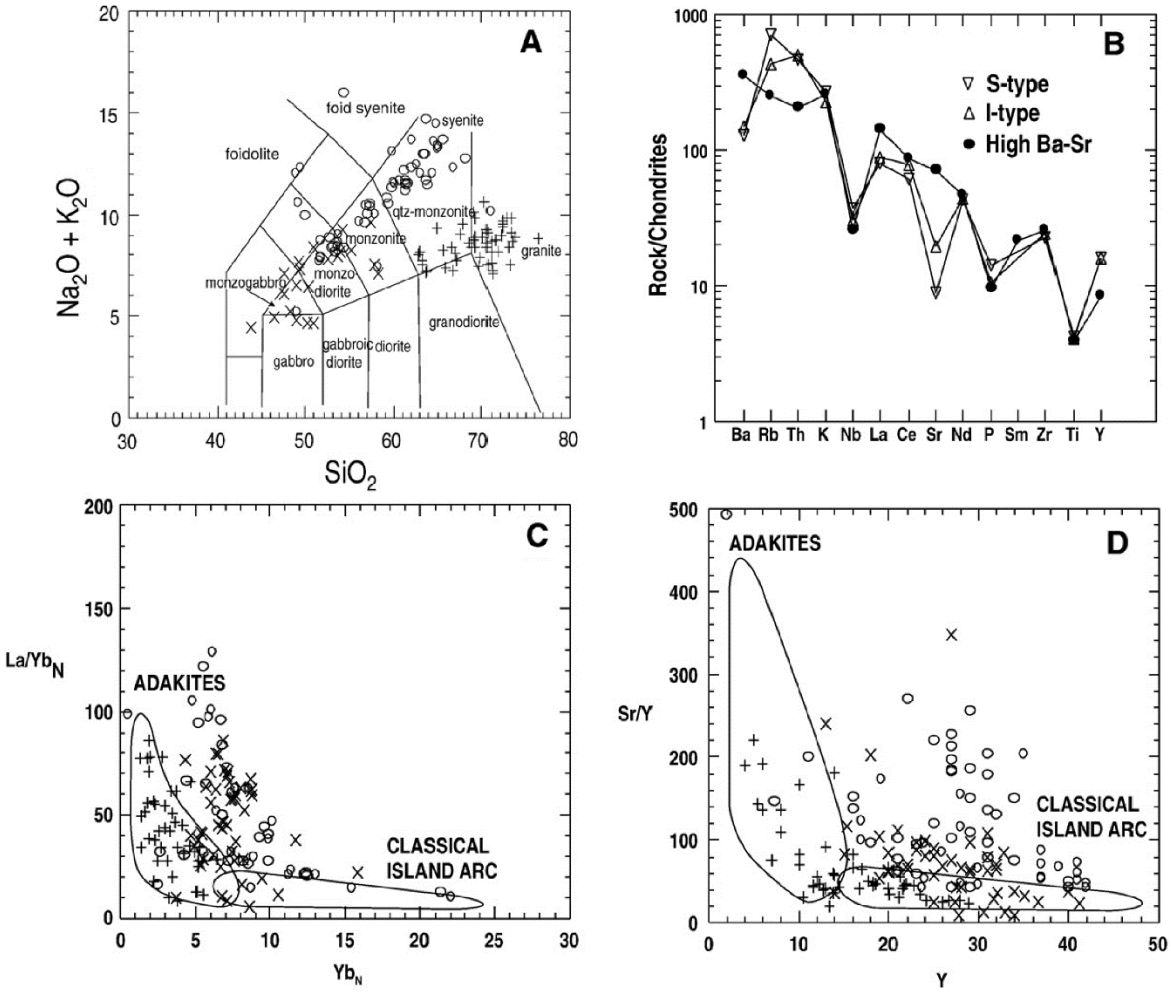

Figure 2.2 Modified after Fowler et al., (2008). A) Total alkalis vs. silica classification amongst the high Ba-Sr granitoid suites of the Caledonian high Ba-Sr plutons. B) Comparative multi-element chondrite-normalised plots illustrating the essential differences between high Ba-Sr granitoids and I/ S-types. C-D) Comparison between the high Ba-Sr granitoids, the adakitic rocks and classical island arc.

Pluton	Location	Age	Authors	Description	Interpretation
Rogart and Strontian plutons (Late Caledonian orogeny)	Northern Highlands (Scotland)	Paleozoic (420-425 Ma)	Fowler et al., (2001; 2008); Tarney and Jones (1994)	Alkaline syenites and calc-alkaline granites. High Ba (up to 2890 ppm) and Sr (up to 2807 ppm).	Crystal fractionation from the associated shoshonitic magmas derived from melting of an enriched lithospheric mantle by pleagic sediments (Fowler et al., 2001). Tarney and Jones (1994) proposed mixing and migling of mafic and felsic magmas generated from enriched mantle and lower crust and lithospheric enrichment by carbonatite melts.
Karibasheng and Kuzigan plutons	Western Tibetan Plateau (China)	Miocene (12–10 Ma)	Jiand et al., (2012)	Shoshonitic granites and syenites with high Ba (2200–9100 ppm) and Sr (840–3100 ppm, most > 1100 ppm)	Partial melting of the veined lithospheric mantle that had been hybridized by continental slab-derived melts. The continental slab break-off was most likely the pivotal mechanism.
Teixeira Batholith (Alto Pajeú domain)	Borborema Province (Brazil)	Late-Neoproterozoic (590 Ma)	Lima et al., (2021)	metaluminous, oxidized I-type granites with shoshonitic to high-K calc-alkaline affinities. High Ba (1825–7370 ppm), Sr (1110–2530 ppm)	magma generation by partial melting of Paleoproterozoic mafic/intermediate lower crust, leaving a plagioclase-free and garnet and/or amphibole-bearing residue.
Haemi area (Gyeonggi Massif)	South Korea	Mesozoic (233 Ma)	Choi et al., (2009)	Granites with a high-K calc-alkaline affinity and containts intermediate enclaves have a shoshonitic affinity High Ba (1541-1610 ppm) and Sr (530-598 ppm)	Post-collisional lithospheric delamination model. crustal The component in their genesis and probably also a contribution from subduction (pre-collision event)-related magmatism
Buya appinite-granite (Kunlun Orogen)	Tibetan plateau	Paleozoic (430 Ma)	Ye et al., (2008)	Alkaline feldspar granites with coeval appinite enclaves. High Ba (1036-1433 ppm) and Sr (655-1100 ppm)	Partial melting of a thickened mafic lower crust with minor involvement of enriched mantle-derived appinite magma.

Table 2.1 Short summary of the main features of the High Ba-Sr plutons worldwide.

Chapter 3
Geological background

3.1 Brief outline of the Alpine orogen

The Alpine orogen formed during Mesozoic and Cenozoic times as a result of the oblique subduction of the Alpine Tethys under the Adriatic microplate, and consequent continental collision between the European and Adriatic paleomargins (e.g. Stamplfi et al., 1998, 2002; Schmid et al., 2004; Handy et al., 2010). The opening of the southern Atlantic Ocean in the Early Cretaceous has been considered the cause of the relative motions of Adria, Africa and stable Eurasia (Lustrino et al., 2011).

From the Middle Jurassic (~170 Ma) until Cretaceous (~120 Ma), the southern Ligurian-Piedmontese and the northern Valais oceanic basins formed (Agard and Handy, 2021). These paleo-oceans were separated by a peninsula of thinned continental crust called Brianconnais micro-continent (Davies and von Blanckenburg, 1995; Schmid et al., 2004). The Ligurian-Piedmontese Basin consisted of oceanic crust (Sanfilippo & Tribuzio 2011, 2013) overlain by Lower Cretaceous sediments with a substantial terrigenous component (Bracciali et al., 2007), whereas the Valais Basin was more similar to the transitional domain between typical oceanic and continental crust (OCT; ocean-continent transition) in present-day magma-poor rifted margins.

The convergence between the Adriatic microplate (an African promontory) and Europe initiated at ~85-100 Ma (Rosenbaum and Lister, 2005; Handy et al., 2010; Zanchetta et al., 2012), starting with the subduction of oceanic crust below the Adriatic continent (Fig. 3.1). At this stage, the separation of thrust sheets from the southern basement and the thrusting as nappes ("Austroalpine") over booth oceanic basins and peninsulars ("Penninic") occurred (Davies and von Blanckenburg, 1995). During this time, there is no magmatic record of subduction initiation and closure of the Piedmont-Liguria ocean (McCarthy et al., 2018). The oceanic basins were closed during the Eocene, when Adria moved north to northwestward (Davies and von Blanckenburg, 1995). In particular, the latest known stage of Ligurian-Piedmontese lithosphere subduction is dated at ~45 Ma by eclogite-facies metamorphic rocks (Rubatto & Hermann, 2003). For the Valais rocks, the HP-LT metamorphic event is constrained at ~46-39 Ma and

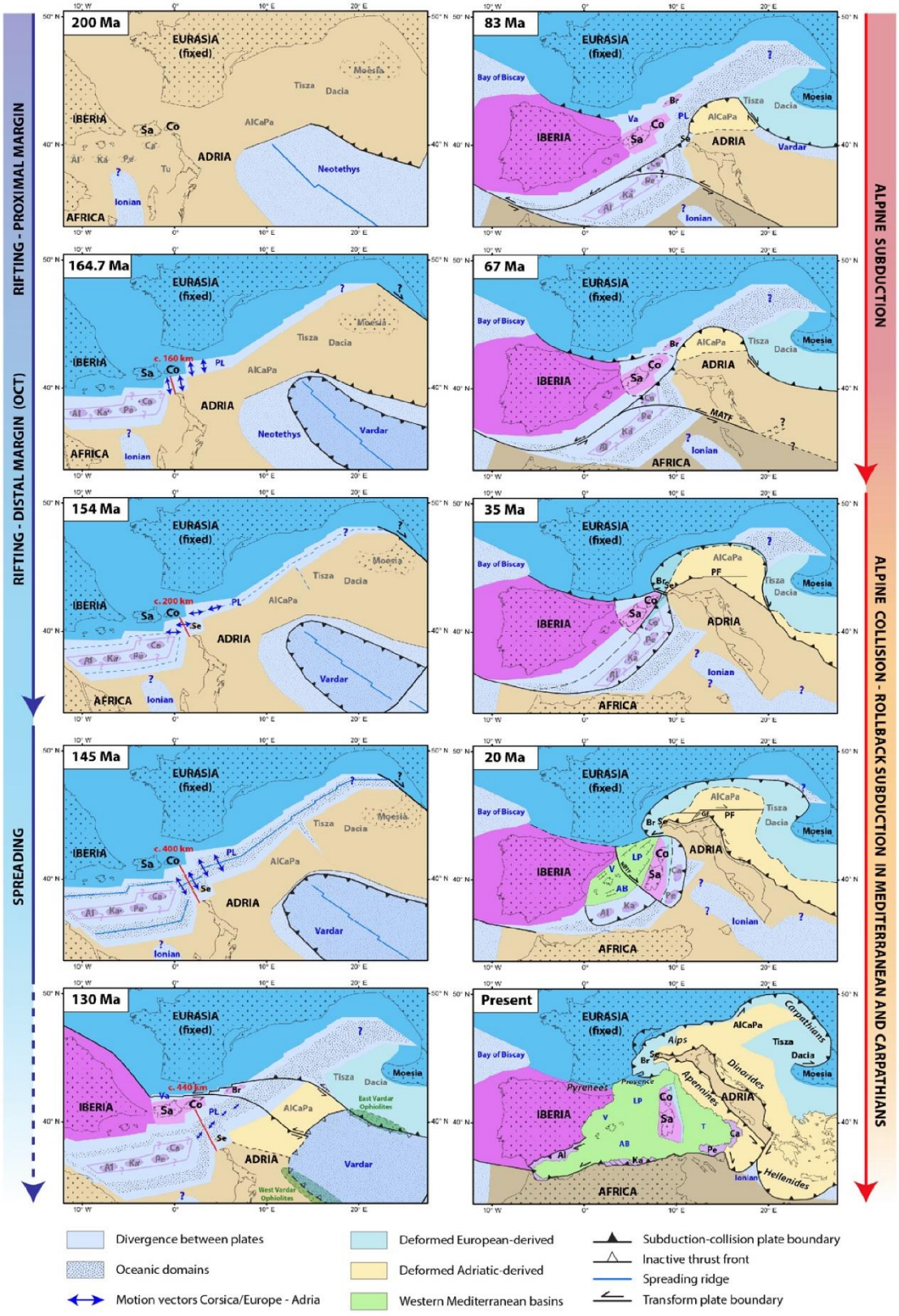

Figure 3.1 After Le Breton et al., 2020. Modified tectonic maps of the Alpine-Mediterranean area from 200 to 130 Ma and from 83 to 0 Ma, relative to Eurasia fixed.

~35-30 Ma in the Central and Western Alps (Ratschbacher et al. 2004; Glodny et al. 2005; Liati et al. 2005; Liati & Froitzheim 2006; Wiederkehr et al. 2009; Beltrando et al. 2010).

Despite the long-lived subduction (40-50 Ma; Bergomi et al., 2015), subduction-related magmatism is restricted to the period prior to the collision of Europe and Adria (Agard and Handy, 2021) from ~43 Ma to ~34 Ma, and followed by continental arc magmatism until ~30-29 Ma (Müntener et al., 2021).

After the Oligocene events, convergence continued up to the present day, and formed the deep root now observed below the Alps (Müller, 1989). The mechanisms triggering the Tertiary magmatism are still matter of debates and will be discussed in the following sections.

3.1.1 The Periadriatic Magmatism

The Middle Eocene-Late Oligocene orogenic magmatism in the Alps consists of plutons, dykes and volcanics that are distributed along the Periadriatic Fault System (PFS), and are therefore termed Periadriatic (von Blanckenburg & Davies, 1995; Bergomi et al., 2015). The Periadriatic Fault System, and in particular, the Insubric Fault, separates two paleogeographic domains (Austroalpine units and Southern Alps) both derived from the northern margin of the Africa-Adria plate (Handy et al., 2010; Bergomi et al., 2015).

The structural study of both plutons and host rocks revealed that magma ascent occurred along the main fault system during transpressive displacements (Rosenberg et al., 1995). The linear distribution of Middle Eocene-Late Oligocene igneous rocks is a striking feature, pointing to regional-scale control on magma emplacement (Lustrino et al., 2011). According to some authors (e.g. Pamic et al., 2002), these plutons are part of a wider magmatic province that continues eastward and include the Dinarides and Hellenides.

A peculiar feature of the Periadriatic magmatism is the surprisingly small volume of exposed plutonic rocks and the exceedingly rare occurrence of volcanism (Müntener et al., 2021). Indeed, despite the widespread occurrence of dikes, rare volcanic products are localized around the Insubric Line (Callegari et al., 2004) and beneath the Po Plain (Mattioli et al., 2002). Concomitant to the orogenesis of the Alpine belt, intraplate magmatism also occurred intermittently in the Cenozoic (Veneto Volcanic Province; e.g. Brombin et al., 2021), though its relationship with the subduction processes is still debated.

Based on radioisotopic ages, the orogenic magmatic activity of the Alps range from ~43 Ma to ~24 Ma (Ji et al., 2019), with the magmatic "climax" in the Early Oligocene, during the interval 34-28 Ma (Rosenberg, 2004; Lustrino et al., 2011). The main Cenozoic igneous rocks are represented in Figure 3.2 (Lustrino et al., 2011). The Adamello batholith (~43–32 Ma; Ji et

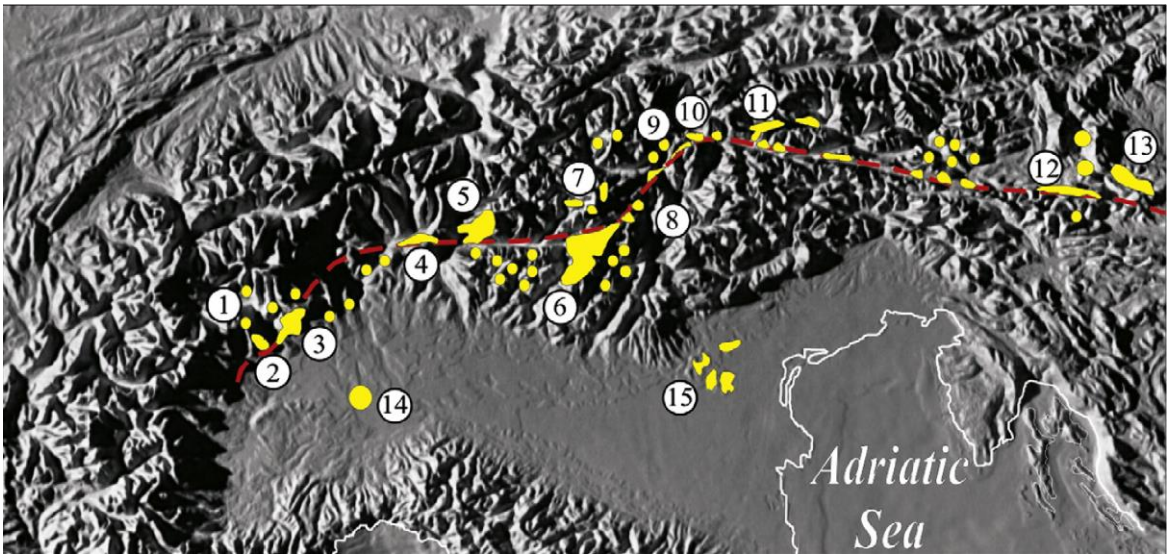

Figure 3.2 - Digital elevation model of topography and bathymetry in the Alpine region by Lustrino et al. (2011) ahowing the main Cenozoic igneous rock outcrops and buried bodies. 1=Lamprophyric/lamproitic and calcalkaline dykes (~30 Ma); 2=Traversella (~32–29 Ma); 3=Biella (~31 Ma); 4=Novate (~26–24 Ma); 5=Bergell (~33–26 Ma); 6=Adamello (~42–27 Ma); 7=Gran Zebru, Mare and Grunsee; 8=Rumo and Samoclevo; 9=Merano; 10=Rensen (~29 Ma); 11=Rieserferner (~32 Ma); 12=Karawanken; 13=Pohorje (~19 Ma); 14=Tertiary Mortara Volcano (~30 Ma; buried under ~5000 m thick sediments of the Po Plain); 15=Veneto Volcanic Province with within-plate geochemical characteristics (~60–25 Ma).

al., 2019; Schaltegger et al., 2019) and the Bergell (also known as Bregaglia; ~32-24 Ma; Oberli et al., 2004; Ji et al., 2019) are the two major intrusions. In order of decreasing size, the other most prominent intrusive bodies are: the Pohoroje (~19-16 Ma; Fodor et al., 2008); the Rieserferner (or Vedrette di Ries; ~32 Ma; Romer and Siegesmund, 2003), and the Biella (or Valle del Cervo; ~33-31 Ma; Romer et al., 1996; Ji et al., 2019). Smaller intrusions comprise the Traversella, Karawanken, Rendes, Altenberg and Zinsnok, other than many tonalitic lamellae scattered along the Pearadriatic fault (Lustrino et al., 2011).

The Periadriatic intrusive suites are lithologically and petrographically quite heterogeneous, mostly including calc-alkaline I-type granitoids with 'TTG' (Tonalite-Trondhjemite-Granodiorite) affinity (Lustrino et al., 2011), but also encompassing minor syenites, gabbros and wherlites (Ulmer et al., 1983). Moreover, mafic enclaves and basic synplutonic dykes, showing calc-alkaline to shoshonitic affinity, occur in most plutons. Ultrapotassic dikes (i.e. lamproites) also occur, but they are confined to the Western Alps (Dal Piaz et al., 1979; Conticelli et al., 2009).

The range of $^{87}Sr/^{88}Sr_{(i)}$ and $^{143}Nd/^{144}Nd(i)$ isotopic ratios of most of the Periadriatic intrusive suites show a typical mixing array between crustal and mantle values (Fig. 3.3; von Blanckenburg & Davies, 1995). The granitoid rocks composing the largest part of these plutons

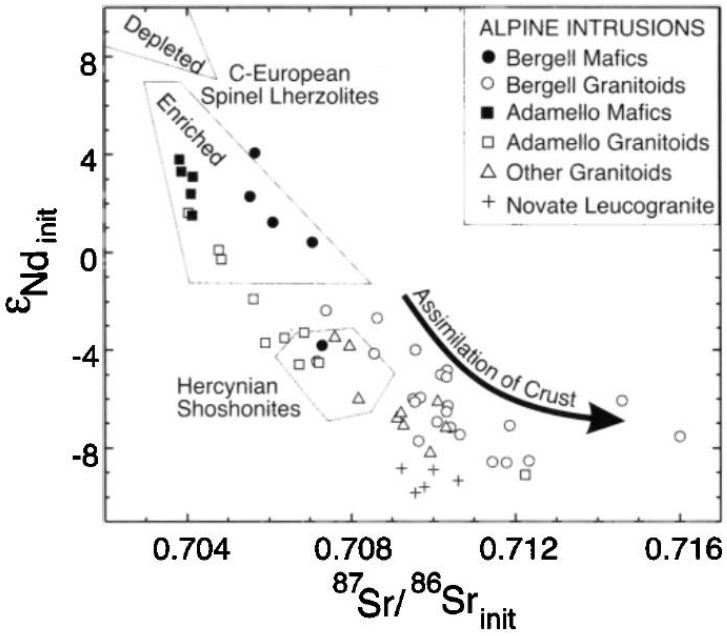

Figure 3.3- Initial εNd versus initial 87Sr/86Sr for Periadriatic intrusions and dykes. After von Blanckenburg & Davies (1995).

result from mixing of basaltic partial melts with partially melted mafic lower crust, followed by fractional crystallization and assimilation of crust (AFC; Lustrino et al., 2011).

Exclusively crustal sources are invoked for rare leucogranitic plutons emplaced within the Periadriatic Fault mylonites in the Central Alps (e.g. Novate granite), whose S-type character is interpreted to derive by fluid-fluxed melting during high-grade metamorphism (von Blanckenburg & Davies, 1995; Lustrino et al., 2011).

In order to explain the onset of magmatism and the initial exhumation of high-pressure rocks during Middle-Eocene in the Alps, syn-collisional slab breakoff was firstly hypnotized by von Blanckenbourg and Davies (1995). Slab-breakoff is defined as "the buoyancy-driven detachment of subducted oceanic lithosphere from the light continental lithosphere that follows it during continental collision" (Fig. 3.4; Davies and von Blanckenbourg, 1995; von Blanckenbourg and Davies, 1995). The low density of the continental crust generates its buoyancy and tensional forces in the relatively high density oceanic lithosphere which result in a near-horizontal rupture in the syn-collisional (post-subduction) down-going slab (Lustrino et al., 2011). Slab-breakoff also envisages for slab tearing along the transition between subducting continental and oceanic crust (von Blanckenbourg and Davies, 1995).

This model has been invoked to explain a large variety of phenomena, including the linear distribution of the Periadriatic intrusives, the brief and nearly coeval emplacement of most plutons, and their apparent mantle-related magmatic sources (Lustrino et al., 2011). It thus has been widely accepted as the most reliable theoretical model, overpassing other proposed

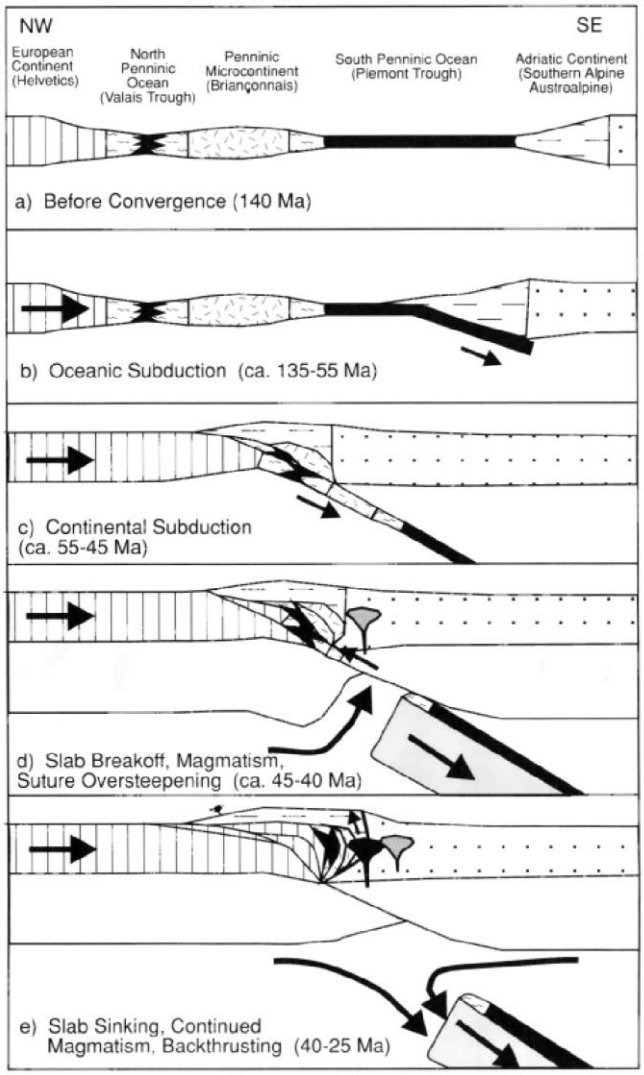

Figure 3.4 - Cartoon illustrating the tectonic evolution of the Alps following the slab-breakoff model. After von Blanckenburg & Davies (1995)

mechanisms such as delamination (Bird, 1979) or convective removal of the thickened thermal boundary layer (Houseman et al., 1981).

Recent geophysical and geochemical data have undermined well-known models such as slab-breakoff process (von Blanchenburg & Davies, 1995), invoking the existence of a continuous slab and a decisive role of slab steepening for magma generation (e.g. Zhao et al., 2016; Ji et al., 2019). Zhao et al. (2016) presented new high-resolution tomography images of the Alpine region in order to better constrain the poorly known structure of the Alpine and Appenninic slabs and their complex transition along strike. By revealing the lateral continuity of the European slab from the Western Alps to the Central Alps, and the downdip continuity beneath the Central Alps, their results ruled out the hypothesis of slab break-off to explain Cenozoic Alpine magmatism.

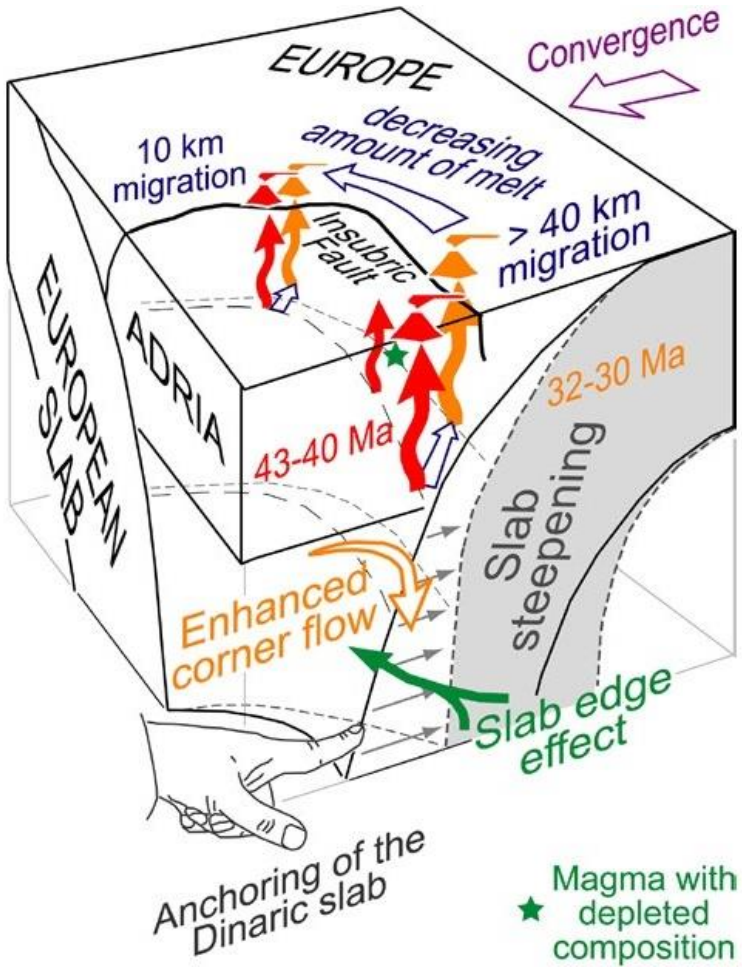

Figure 3.5 3-D model by Ji et al. (2019) showing the proposed relationships between slab steepening and Periadriatic magmatism in the absence of slab breakoff. Slab steepening enhances the corner flow, more asthenospheric material is involved in source partial melting thus triggering magmatism. This process is more effective in the Central Alps (right side of the model) because of (i) the free boundary represented by the slab edge, (ii) the anchoring of the Dinaric slab that may have pushed back the European slab, and (iii) a minor amount of buoyant continental crust subducted at the trench. Magmas with depleted compositions (green star) are generated in the vicinity of the torn edge of the European slab, due to the greater contributions of juvenile components during source melting (slab edge effect in the cartoon). After Ji et al., (2019).

On the basis of the geophysical data presented by Zhao et al., (2016), Ji et al. (2019) conducted a detailed geochemical study consisting of U-Pb ages and Hf isotopic composition of zircons from the main Periadriatic intrusive bodies of the Central and Western Alps (from Traversella to Adamello). These authors identify a regular NW-ward progression of decreasing U-Pb ages in the direction perpendicular to the strike of the European slab consistent with a progressive slab steeping during Eocene-Oligocene. Particularly, high $\varepsilon Hf_{(t)}$ values in the oldest plutons of the Adamello batholith (Corno Alto and Re di Castello units) testify a great contribution of juvenile components during the early stages of source melting, thus suggesting the role of an enhanced corner flow with more asthenospheric material improved by slab steepening (Fig. 3.5).

3.2 The Adamello batholith

The Adamello batholith is the largest and oldest Tertiary Periadriatic intrusion in the Alps (Schaltegger et al, 2019). It is located in the Southern Alps (Northern Italy; Fig. 3.6) covering an area of ~670 km^2 with up to 3 km of vertical relief (Schaltegger et al., 2009; Callegari and Brack, 2002). The Adamello batholith was emplaced along the Periadriatic fault system during Eocene and Oligocene, following the collision between the paleo-European and paleo-African continental plates (e.g., Tiepolo et al., 2011 and reference therein). It is pinched between the dextral Tonale Line to the North (Werling, 1991) and the Giudicarie Line, to the southeast, with sinistral transpressive displacement (Viola et al., 2001; Pennacchioni et al., 2006; Schaltegger et al., 2019).

The calc-alkaline magmas that assembled the Adamello batholith were intruded into the Variscan metamorphic basement that varies between greenschist to amphibolite facies and unmetamorphosed Permian-Triassic cover series (Del Moro et al., 1983b; Schaltegger et al., 2019). The contacts with the wall rocks are sharp and well preserved all along the entire perimeter of the batholith, except for the north-eastern part, in correspondence of the Giudicarie Line (Note illustrative della Carta Geologica D'Italia, foglio 041). The intrusion generated a contact aureole of about 2 km of width, often characterized by syn-intrusive deformations and accompanied by local collapse structures in the wall rock (Brack et al., 1983; Callegari & Brack 2002).

The Adamello igneous intrusive suite is made up of discrete petrographically and isotopically distinctive plutons (Ulmer et al., 1983) of calc-alkaline affinity ranging in composition from quartz-diorite to granodiorite (Dupuy et al., 1982). Mafic rocks are locally associated with the coeval evolved lithologies, both as satellite bodies at the pluton margins and as syn-plutonic intrusions (Blundy & Schimizu, 1991). It has been divided into units by Callegari & Brack (2002) based on their differences in the mineralogical composition, the texture of the tonalitic rocks and depending on their location within the batholith (Bianchi et al., 1970).

Recently, according to new geochronological data, Schaltegger et al. (2019) subdivided the Adamello batholith into 7 units slightly deviating from the originally 4 units proposed by Callegari & Brack (2002): the Re di Castello North (i) and South (ii) units; the Central Adamello (iii) and the Western Adamello (iv) units in the central part of the massif; the Corno Alto (v) unit, located at the eastern border and previously considered as part of the Re di Castello unit, and the Avio (vi) and Presanella (vii) units in the northern sector (Fig. 3.6).

The Re di Castello super-unit has the most peculiar composition, with gabbro-tonalite-granodiorite as the dominant rock suites (Callegari & Dal Piaz 1973; Brack, 1983; Ulmer et al.,

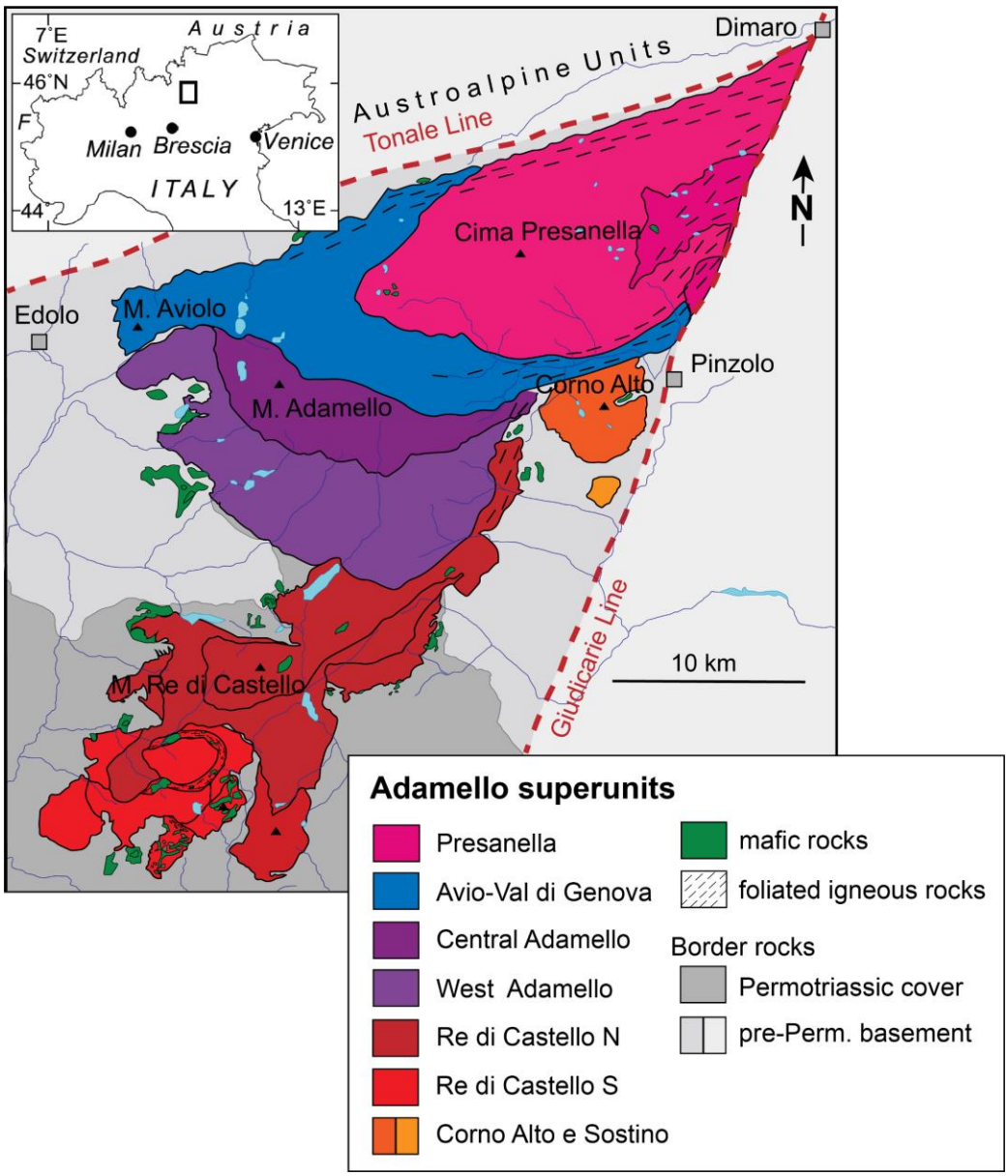

Figure 3.6 - Geological map of the Adamello batholith in N Italy. Modified after Schaltegger et al., (2009).

1983), locally associated with mafic bodies and ultramafic cumulates at the border of the unit, and best exposed in the Re di Castello South unit, especially in Val Fredda and Cornone di Blumone areas (Tiepolo et al., 2011). The Re di Castello South unit yielded older radiometric ages than the northern unit, ranging from 42.6 ± 0.03 Ma to 40.4 ± 0.2 Ma (Schaltegger et al., 2019; Broderick et al., 2015; Schoene et al., 2012) thus providing evidence for c.2-3 Ma of magmatic activity. Moreover, evidence for a magmatic activity as starting at 51.0 ± 1.1 Ma was found in the hornblendites of Passo di Val Fredda (Tiepolo et al., 2011). The Re di Castello North unit is slightly younger, ranging from 39.7 ± 0.4 Ma to 39.1 Ma ± 0.3 (Schaltegger et al., 2019).

The Western and Central Adamello units consist of the Western Adamello tonalite and the amphibole-poor Central Adamello leucotonalite, emplaced between 38.2 ± 0.2 Ma and 36.9 ± 0.2 Ma (Schaltegger et al., 2019; Ji et al., 2019).

North of the Gallinera Line crops out the Avio unit, between the Central Adamello and the Presanella units. It is characterized by uniform medium-grain tonalites, containing small fine-grain mafic patches, and peripheral gabbros and quartzgabbros. The Avio rocks are progressively foliated towards the northern contact. Available U-Pb literature ages on zircons for the Avio unit suggest an intrusion age between 36.2 ± 0.2 Ma and 34.4 ± 0.3 Ma (Schaltegger et al., 2019). In the northernmost part of the batholith, the Presanella unit was emplaced between 34.5 ± 0.5 Ma and 33.1 ± 0.6 Ma (Schaltegger et al., 2019) and therefore it represents the most recent pluton of the batholith. It mainly consists of medium-grained tonalite, with biotite and both anhedral and euhedral amphibole showing a preferred orientation, locally crosscut by muscovite-bearing aplitic dykes (Schaltegger et al., 2019). Foliated lithotypes outcrop both in the Presanella super-unit and in the Avio super-unit (Note illustrative della Carta Geologica D'Italia, foglio 041) along the northern margin, near the Tonale and Giudicarie tectonic lines. Here the batholith was affected by an intense ductile-fragile deformation, concentrated in bands up to 4 km wide (Dal Piaz, 1953; Montresor & Rigatti, 1995).

In the eastern part of the batholith, close to the southern Giudicarie Line (Mayer et al., 2003) and in contact with the Avio unit crops out the Corno Alto unit, (Fig. 3.6). The Corno Alto is a rounded shape pluton intruded into the low-grade Variscan basement (Rendena Schists) that has been described as consisting of granodiorite to trondhjemite rocks (Callegari & Dal Piaz, 1973; Schaltegger et al., 2019). Plagioclase is the dominant mineral, while less abundant are quartz and K-feldspar with muscovite and biotite being primary minerals (Mayer et al., 2003). The Corno Alto intrusion has been considered for a long time a northward extension of the Re di Castello pluton because of the similar age, petrological and geochemical features (e.g. Callegari, 1985). Specifically, the similar low anorthite (An) content of plagioclase, the significantly higher Ba and Sr contents in the whole rocks compared to those of the other units, and the similar initial $^{87}Sr/^{86}Sr$ ratio (0.704-0.706) supported a genetic relationship between these plutons (Mayer et al., 2003; Del Moro et al., 1985a). However, recent geochronological U-Pb data on zircons (e.g. Ji et al., 2019; Schaltegger et al., 2019) identified the Corno Alto intrusion as the oldest magmatic unit with an average age of 43.47 ± 0.16 Ma. It thus represents the only exception to the ~10 Myr south to north-east temporal emplacement sequence and it is thought to be the center of nucleation of the batholith (Del Moro et al., 1983a; 1983b; Villa 1983; Hansmann & Oberli, 1991; Kagami et al., 1991; Mayer et al., 2003).

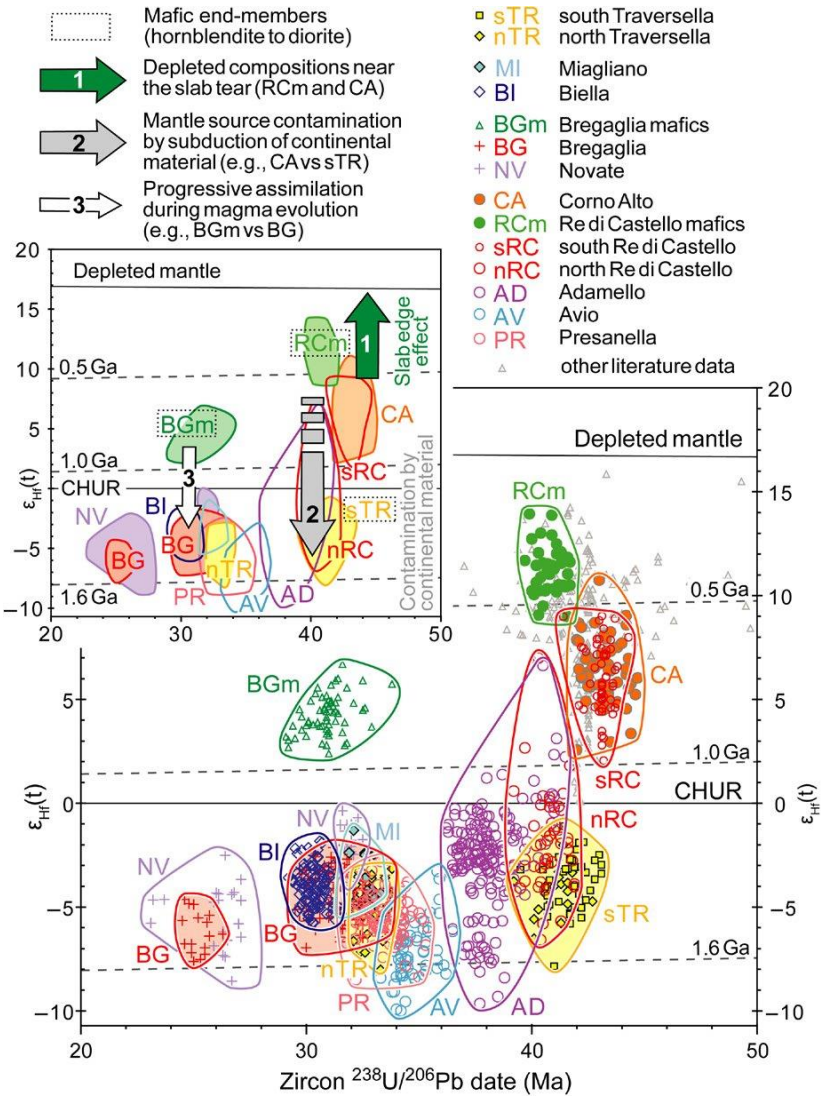

Figure 3.7 Modified after Ji et al., (2019). In situ U-Pb dates and Hf isotopes of zircons from the main Periadriatic intrusions of the Central and Western Alps (from Ji et al., 2019). Literature data (grey symbols) are from Tiepolo et al. (2014), Schoene et al., (2012) and Broderick et al., (2015).

Based on whole-rock stable (Cortecci et al., 1979) and radiogenic lines of evidence (Del Moro et al., 1983a; Kagami et al., 1991), the Adamello intrusive suite has been interpreted as having evolved by fractional crystallization from a picrobasaltic parental magma (Ulmer et al., 1983; Kagami et al., 1991), which experienced an increasing degree of crustal contamination during the sequential emplacement of the batholith. This is confirmed by the recent in situ Hf isotopes analyses in zircons from the different units of the Adamello batholith (fig. 3.7; Ji et al., 2019; Schaltegger et al., 2019; Broderick et al., 2015). Indeed, large variation in Hf isotopes are observed in the North Re di Castello, Adamello, Avio, and Presanella units where negative εHf(t) values are dominant. Instead, positive Hf isotopic values are found in samples from Corno Alto ($\varepsilon Hf_{(t)}$ ranges from +2.6 to +10.8) and south Re di Castello, with particularly high values ($\varepsilon Hf_{(t)}$ > 10) displayed by the more mafic samples from the latter (Ji et al., 2019).

Confirming the isotopic evidence, Relvini et al. (2022) used thermodynamic modelling to indicate that the Corno Alto felsic rocks were formed by mixing between anatectic melts generated in the lower crust and melts produced by fractional crystallization of mantle-derived magmas (e.g. Ulmer et al., 1983), arguing against an origin of the studied rocks in a closed system.

3.3 The case study: the Corno Alto complex

3.3.1 Introduction

The Corno Alto complex is located in Val Rendena (fig. 3.8), in the eastern border of the Adamello batholith. With its rounded shape, it covers an area of about 20 Km^2 and reaches 2427 m of altitude with its major peak (Cima Costaccia). South to the Corno Alto unit, a minor intrusion (1 Km^2) called Sostino body crops out.

Since the first studies on the Adamello batholith, a co-genetic relation between these two igneous bodies was suggested based on geological observations. Trener (1912) first recognized the composite nature of the Adamello suite and identified the 'granitic to granodioritic' masses of the Corno Alto and Sostino as the oldest intrusions. This idea was later discarded by Bianchi & Dal Piaz (1948; 1950; 1973) who interpreted the whole magmatic rock sequence of the Adamello batholith as the product of igneous differentiation, and thus considered the widespread tonalitic rocks as older than the Corno Alto granodiorites. Trener's view was later reconsidered on the basis of numerous radiometric data on muscovite and biotites (Ferrara, 1962; Del Moro et al., 1985), and finally confirmed by recent U-Pb dates on zircons (Schaltegger et al., 2019; Ji et al., 2019). For this reason, the term 'Corno Alto complex' as comprehensive of both Corno Alto and Sostino bodies have been adopted in this study.

3.3.2 Lithological variability of the Corno Alto rocks

The Corno Alto complex is described in the literature as a fairly homogeneous magmatic body, mainly consisting of partially cataclastic and altered granodiorite to trondhjemite rocks (Callegari & Dal Piaz, 1973; Schaltegger et al., 2019).

The dominant lithotype in the Corno Alto area is interpreted as a trondhjemite (e.g. Callegari & Brack, 2002; Zattin et al., 1995; Schaltegger et al., 2019; Ji et al., 2019; Relvini et al., 2021): a coarse-grained hetero-granular leucocratic granitoid rock. Locally, this rock shows different grain-size, assuming a slightly porphyritic character ('plagioporphyric'; Callegari & Brack, 2002). It is composed in order of abundance by plagioclase, quartz, K-feldspar, biotite

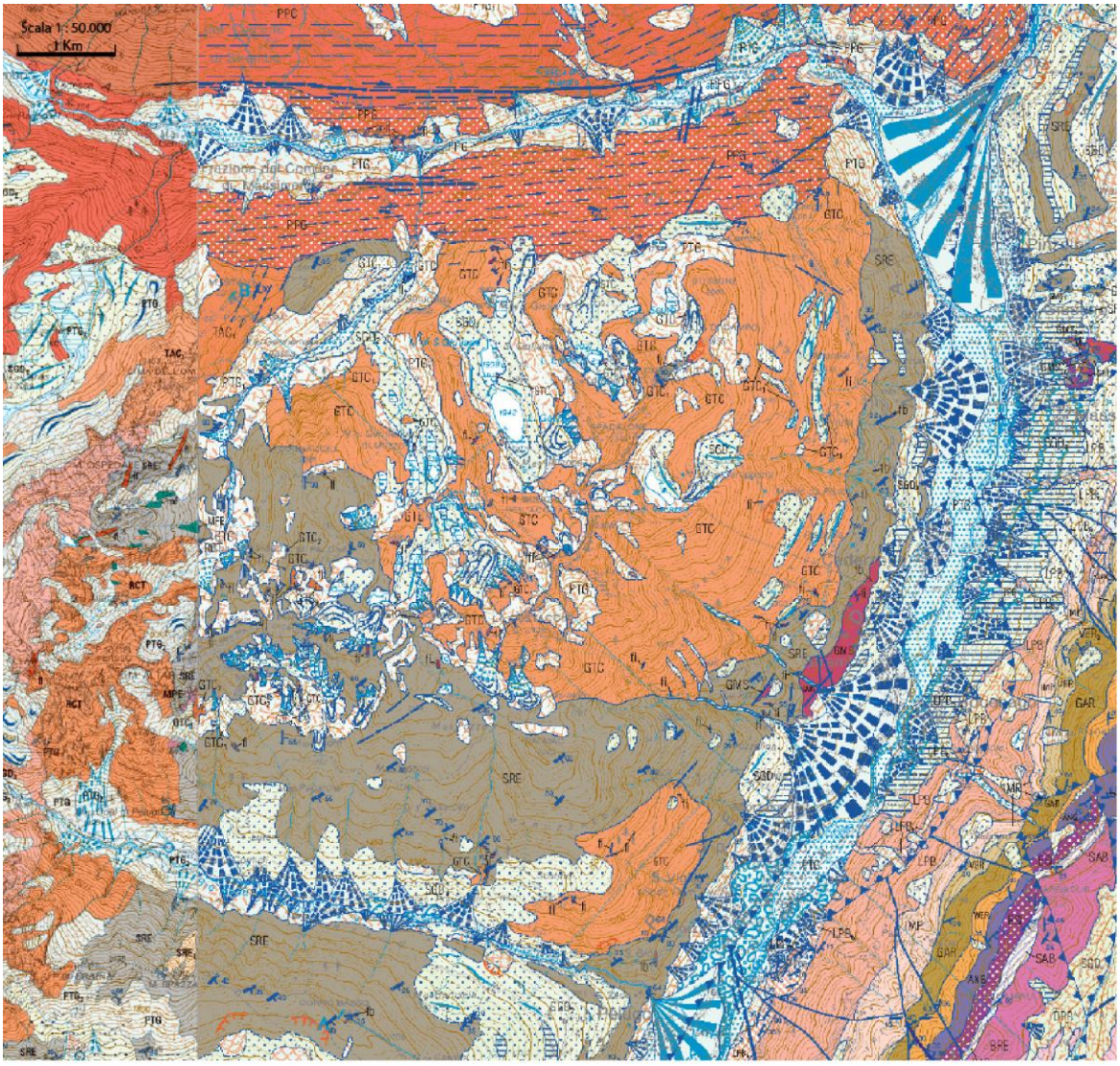

Figure 3.8 - Modified after Carta Geologica d'Italia - Provincia Autonoma di Trento, Foglio 058 and 059 (Dati elaborati dal Servizio geologico della Provincia autonoma di Trento).

(the only mafic mineral phase), and by variable amount of primary white-mica (muscovite). When K-feldspar is more abundant and small fragments of hornblende the transition from trondhjemite to muscovite-bearing biotite granodiorite occurs (Callegari & Brack, 2002). The intense vegetation limits the rock exposure in the Corno Alto area and thus igneous contacts between the different lithotypes are difficult to observe.

The massive structure of the rock in the internal part of the unit becomes increasingly foliated (cataclastic to mylonitic) towards the eastern border of the intrusion, in correspondence

of the Giudicarie Line. Especially in this sector of the intrusion, towards the contact with the basement (Rendena schists), dismembered fragments of dioritic rocks often displaying a plagioporphyric texture occur.

Sporadical dioritic bodies of the order of few meter in size are also reported in the northern sector of the unit. In particular, diorite rocks outcrop along the northwest margin in Val Seniciaga Bassa and in the high valley (Val Seniciaga Alta) where they seem to be intruded by the Re di Castello and Adamello tonalites in correspondence of Mt. Ospedale (Zattin et al., 1995). According to the literature, these rocks are fine- to medium-grained and are composed by brown to green hornblende, zoned plagioclase sometimes with calcic cores and Mg-rich biotites.

The rock-type of the Sostino apophysis is described as a medium-grained massive hornblende-bearing biotite granodiorite, locally showing a plagioporphyric texture (Callegari & Brack, 2002).

3.3.3 U-Pb age of the Corno Alto rocks

The Corno Alto complex represents the oldest intrusion related to the Adamello batholith (Schaltegger et al., 2019; Ji et al., 2019). Schaltegger et al. (2019) dated two samples from the central-eastern part of the unit by LA-ICP-MS. One sample returned a mean age of 43.4 ± 0.2 Ma (MSWD= 0.75; n=10), after rejection of five older analysis between 44 and 45 Ma. The second sample returned a mean age of 43.1 ± 0.2 Ma (MSWD=1.6; n=8), obtained after rejection of older and younger dates. Ji et al., (2019) obtained similar results on three other samples from the central-northern part of the unit: respectively 43.2 ± 0.4 Ma (MSWD= 3.8; n=21); 43.4 ± 0.4 Ma (MSWD=2.6; n=20); and 43.2 ± 0.3 Ma (MSWD=1.6; n=21).

In general, all these dates are in good agreement with the SIMS age of 42.2 ± 1.1 given by Mayer et al., (2003).

Chapter 4
Geochemistry and geochronology of the Corno Alto complex

This chapter constituted the object of a paper submitted to Lithos magazine.

4.1 Introduction

The nature and composition of granitoids significantly changed throughout the Earth's history highlighting major changes in the mechanisms of continental crust formation and differentiation (Laurent et al., 2014). The early continental crust is typically dominated by the tonalite-trondhjemite-granodiorite association, known as TTG (Hawkesworth et al., 2020), whose origin is ascribed to the partial melting of mafic lithologies either as subducting hydrated basalts (Foley et al., 2002; Martin, 1999) or in a overthickened eclogitic crust (Condie, 2005; Rapp et al., 2003).

Many Archean cratons show the occurrence of younger intrusive intermediate-felsic rocks with different composition relative to TTG. In fact, these rocks, which are known as archean sanukitoids (Shirey and Hanson, 1984), are enriched in LILE (e.g. Sr, Ba and LREE) and exhibit a moderately high concentration in compatible elements (e.g. Mg, Ni, and Cr). Sanukitoids are interpreted to mark the change in the site of partial melting from the subducting slab to the mantle wedge (Fowler and Rollinson, 2012) as a consequence of a modified tectono-thermal regime. The progressive cooling of the Earth definitely marked the decline of both TTG and sanukitoids leaving the scene to Phanerozoic granitoid rocks. However, occasionally, compositional equivalents of sanukitoids, known as "high Ba-Sr" granites, are recognized and widespread in late Cretaceous and late Cenozoic orogenic belts (Fowler et al., 2008). These rocks are extremely important because they may help recognizing not only occasional recurrences of thermal regimes similar to those in the Archean but also similar tectono-magmatic events. Identification of modern analogues of Archean-Proterozoic granitoids can also help constrain early continental crust formation and differentiation processes and their variations through Earth's evolution.

The Corno Alto unit, the oldest intrusion in the tertiary Adamello batholith (Schaltegger et al., 2019) share a resemblance to TTG associations (Lustrino et al., 2011). In particular, trondhjemites are considered to be the main lithology of the pluton (Macera et al., 1983).

Being the oldest intrusion formed during the Alpine orogenesis (Ji et al., 2019), the Corno Alto pluton can be crucial to shed light into the tectono-magmatic conditions active at the onset of the alpine magmatism; conditions that are not yet fully understood. Different models were proposed to account for magma generation during the Alpine Orogen such as post-collision lithospheric extension (Laubscher, 2010), slab-breakoff process (Blanckenburg and Davies, 1995) or steepening of a continuous slab (e.g. Ji et al., 2019; Zhao et al., 2016; Bergomi et al., 2015). In this frame, Ji et al. (2019) also suggested that at the junction between the Alpine and Dinaric subductions slab tear may have contributed to the genesis of adakite-like melts such as those reported in the Re di Castello Unit (Tiepolo and Tribuzio, 2005).

This study, focused on the Corno Alto complex, aims to investigate the petrogenetic processes generating the early melts in the Alpine orogeny and their bearing on the general architecture of the Alpine evolution. We present a new comprehensive dataset combining whole-rock and in situ zircon geochemistry and geochronology (U-Pb dates, trace element composition and Hf isotopes) on different lithotypes of the Corno Alto complex. Geochemical data revealed a high Ba-Sr character of the complex, peculiar compared to the other Adamello units, which is discussed in light of recent geodynamic constraints for the Alpine region.

4.2 Geological setting

The Adamello batholith is the largest and oldest composite intrusion in the Alpine belt emplaced along the Periadriatic fault system during Eocene and Oligocene, following the collision between the paleo-European and paleo-African continental plates (e.g., Callegari and Brack, 2002; fig. 4.1a).

The Adamello batholith is made up of discrete petrographically and isotopically distinctive plutons (Ulmer et al., 1983) of calc-alkaline affinity ranging in composition from quartz-diorite to granodiorite (Dupuy et al., 1982). Mafic rocks are locally associated with coeval felsic lithologies, both as satellite bodies at the pluton margins and as syn-plutonic intrusions (Blundy and Shimizu, 1991). Based on whole-rock stable (Cortecci et al., 1979) and radiogenic data (e.g., Kagami et al., 1991), the Adamello batholith is interpreted as having evolved by fractional crystallization from a picrobasaltic parental magma (Ulmer et al., 1983; Kagami et al., 1991), which experienced an increasing degree of crustal contamination during the sequential emplacement of the batholith. This model has been recently confirmed by in situ Hf isotopes analyses in zircons from the different units of the batholith (Ji et al., 2019; Schaltegger et al., 2019).

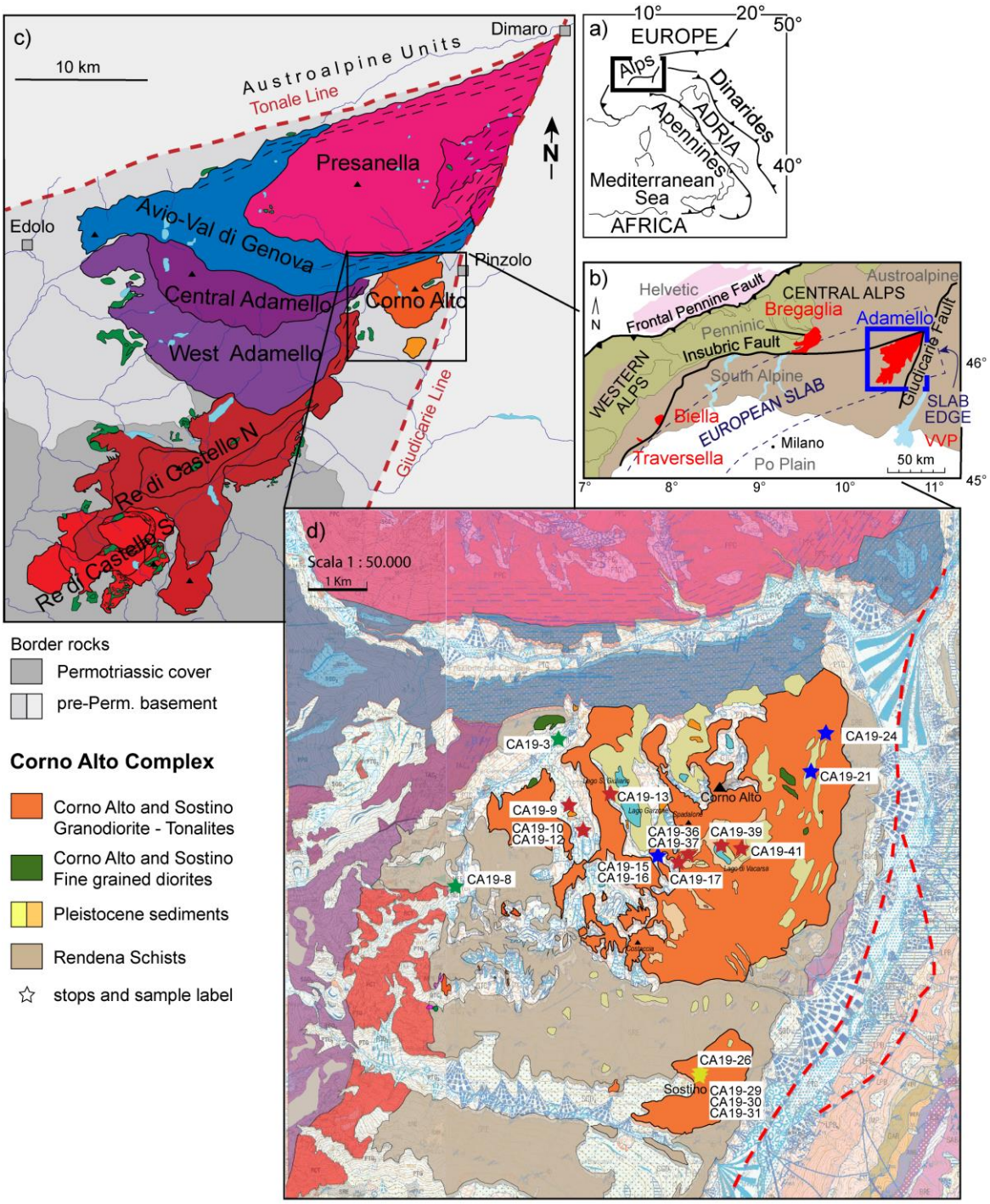

Figure 4.1 a-b) Modified after Ji et al., (2019); c) Modified after Schaltegger et al. (2009); d) Modified after Carta geologica Provincia autonoma di Trento – Dati elaborati dal Servizio Geologico della provincia Autonoma di Trento (Sez. N. 59050-59010-59090).

The Corno Alto intrusive complex crops out in the eastern part of the batholith, close to the South Giudicarie Fault and include the Sostino apophysis to the southeast (Fig. 4.1).

The complex is granodioritic to trondhjemitic in composition (Schaltegger et al., 2019) and intruded into the low-grade Variscan basement (Rendena Schists). Plagioclase is the dominant mineral, while less abundant are quartz and K-feldspar with muscovite and biotite being primary

minerals (Mayer et al., 2003). The recent geochronological U-Pb data on zircons (e.g. Ji et al., 2019; Schaltegger et al., 2019) identified the Corno Alto intrusion as the oldest magmatic unit with an average age of 43.47 ± 0.16 Ma. According to Relvini et al. (2022), the Corno Alto felsic rocks were formed by mixing between anatectic melts, generated in the lower crust, and melts produced by fractional crystallization of mantle-derived magmas. A complete and detailed geochemical characterisation of the different lithologies forming the Corno Alto intrusive complex is still missing, hampering a better understanding of the relationships between its olde age and peculiar geochemical signature.

4.3 Methods

Whole rock major and trace element analyses were carried out at the Central Analytical Facility (CAF) of the Stellenbosch University, South Africa. Major element compositions were determined by X-ray fluorescence on fused discs with a PANalytical Axios Wavelenght Dispersive spectrometer equipped with a Rh tube at 3kW operating power. The standards used in the calibration procedures for major element analyses were BE-N and BHVO-1 (basalts), JB-1 (depleted-basalt), and JG-1 (granodiorite). Accuracy is better than 1% for major elements present at a concentration of greater than 1 wt% (Table A.4 in Appendix A).

Bulk trace element concentrations were determined on the same materials by LA-ICP-MS using an Agilent 8800 ICP-MS coupled with a 193 nm M50 excimer laser normalizing to NIST SRM 612 glass (Jochum et al., 2011). Data reported in this study represent the average of four ablation spots. Certified BCR and BHVO basaltic glass (Jochum et al., 2005), BHVO and BCR powder (Jochum et al., 2016) were used as reference material. Data reduction was carried out using Iolite v. 3.71 software. Analytical accuracy is typically better than 12% (Table A.5).

Major element compositions of rock-forming minerals (plagioclase, epidote, biotite and white-mica) were measured at the Department of Earth Sciences "A. Desio" (ESD), University of Milano (Italy) by electron microprobe JEOL Superprobe 8200. The analyses were performed with a WDS system at 15.0 kV, 5nA for the electron beam and 1 μm beam size. Natural minerals were used as standards for the different elements (the numbers refer to the international standards): Mg on olivine 153, Fe on fayalite 143, Na on omphacite 154, Ti on ilmenite, Mn on rodonite, K on K-feldspar 113, Al and Ca on anorthite 137, Cr on metallic/pure Cr and Si on wollastonite.

Samples selected for zircon separation were crushed and sieved to a grain size of ca. 250 μm. Zircon crystal separation process included hydrodynamic, magnetic (Frantz), and dense-liquid separation using diiodomethane. Zircon grains were mounted in epoxy resin, polished,

and then characterized for internal structure and inclusions using a JEOL JSM-IT 500 scanning electron microscope (SEM) equipped with a DEBEN CENTAURUS CL detector at the ESD.

Zircon trace element composition and U-Pb dating were carried out by Laser-Ablation Inductively Coupled Plasma Mass Spectrometry (LA-ICP-MS) at the ESD using a Thermo Fisher Scientific iCAP RQ ICP-MS coupled to a 193nm Excimer Laser Ablation System (Analyte Excite by Teledyne Cetac Technologies). Conditions for trace element determinations in zircon were: spot diameter of 25 μm, repetition rate of 10 Hz and a fluence of 2 J/cm^2. Helium was used as carrier gas with flow rates of 0.500 l/min in the sample cell, and 0.200 l/min in the cup. The SiO_2 concentration in zircon was fixed at the stoichiometric value of 32.78% wt.% and used as internal standard. Glass reference materials NIST-SRM 612 (Jochum et al., 2011) and BCR-2G (Jochum et al., 2005b) were used respectively as external standard and as quality control. On the glass references the spot diameter was set at 40 μm, repetition rate at 10 Hz and fluence at 6 J/cm^2 (NISTSRM612) and 3 J/cm^2 (BCR-2G).

The same LA-ICP-MS instrumentation was used for U-Pb in zircon geochronology. The analyses were carried out with a laser spot of 25 μm, the laser fluence set at 3 J/cm^2, and the repetition rate at 7 Hz. Helium flow rate within the ablation cell and cup were the same than that used for the trace element determination. The reference materials 91500 zircon (Wiedenbeck et al., 2004) and Plešovice zircon (Sláma et al., 2008) were used as external standard and quality control, respectively. Data reduction was carried out with the Glitter software (Griffin et al., 2008) whereas concordia age calculations was performed with IsoplotR (Vermeesch, 2018).

On the same zircon domains of U-Pb dating, in-situ Hf isotope analyses were performed using the same laser ablation system connected with a Thermo Fisher Scientific MC-ICP-MS Neptune XT at ESD. The initial $^{176}Hf/^{177}Hf$ ratio and initial εHf was calculated for each spot analysis according to the corresponding U/Pb date. During the course of this study, a laser repetitition rate of 6 Hz was used and the beam diameter was 50 μm. Laser beam energy density was set at 3.5 J/cm^2. Errors are reported as 2 standard error (2s). The detailed analytical procedures were similar to those described by Fisher et al. (2014) and is given in Appendix A. The determined $^{175}Hf/^{177}Hf$ ratios of 0.282675 ± 0.000047 (2s; n=58) for Temora-2 and of 0.282486 ± 0.000044 (2s; n=60) for Plesovice standards are in good agreement with the reported values (Sláma et al., 2008; Woodhead and Hergt, 2005).

4.4 Sampling and petrography

We carried out a detailed sampling of the Corno Alto complex, including the Sostino apophysis (Fig. 4.1d and 4.2, Table A.1) and four main lithologies were identified. These are: i) two-mica granodiorite (TMG; Fig. 4.3a), cropping out in the central and western part of the unit; ii) porphyritic tonalite (PTN; Fig. 4.3b), cropping out mainly in the central part of the pluton, which are subordinate and without visible contact with the granodiorites; iii) equigranular tonalite (ETN; Fig. 4.3c-d), sporadically cropping out in the north-eastern part of the unit; iv) epidote-bearing granodiorite (EBG), in the Sostino apophysis, south to the Corno Alto (fig. 4.1d). Northwest to the Corno Alto pluton, a km scale diorite body is reported and one sample was collected (MDR; Fig. 4.3e). One tonalite (OTN; Fig. 4.3f) from the Mt. Ospedale area was also collected for comparison. Clear contacts between the different lithologies are not evident in the field due to the extensive vegetation characterising the area.

Nineteen samples representative of the above mentioned lithologies were selected including: 9 two-mica granodiorites, 4 tonalites, 4 epidote-bearing granodiorites, 1 diorite and 1 hornblende-bearing tonalite from the Mt. Ospedale area. Detailed samples' location with GPS coordinates are reported in Appendix (Table A.1).

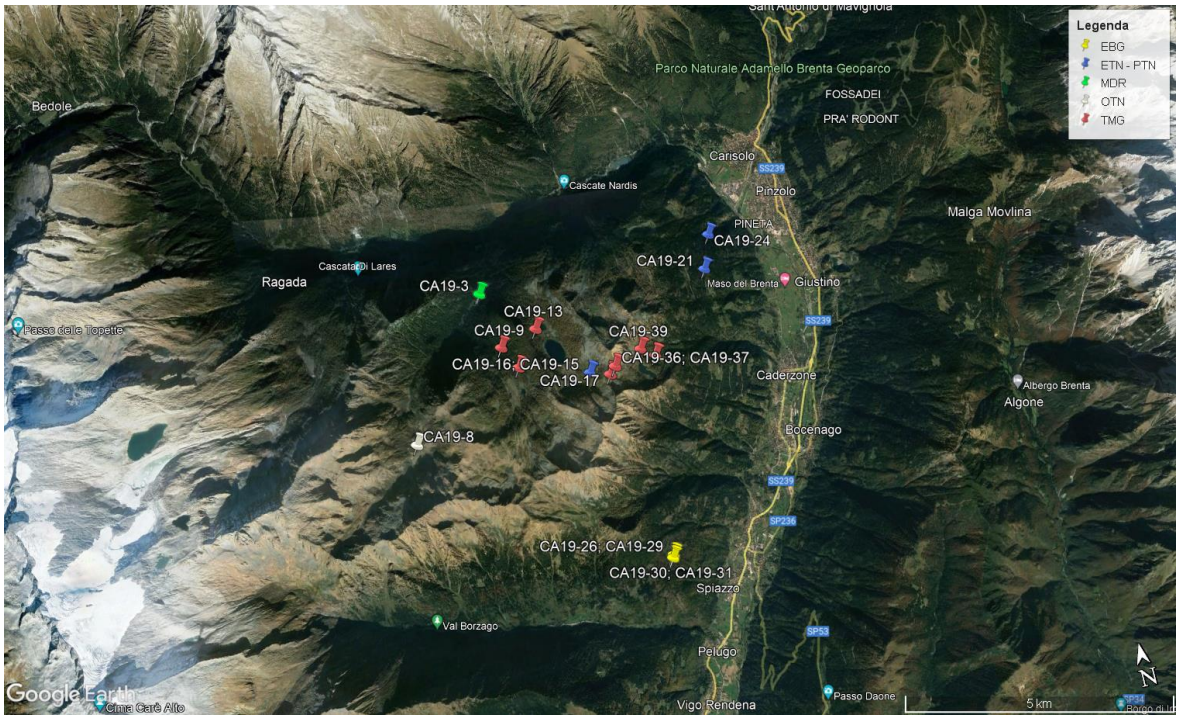

Figure 4.2 Satellite view of the Corno Alto complex with sample locations.

Figure 4.3 Field photograph. a) Typical aspect of the two-mica granodiorite (TMG); c) Porphyric tonalite (PTN); c) Rare equigranular tonalite (ETN) outcrop; d) Equigranular tonalite (ETN) detail; e) Diorite (MDR); f) Mt. Ospedale tonalite (OTN).

4.4.1 Two-mica granodiorites (TMG)

Two-mica granodiorites are fine- to medium-grained and contain 35-45% plagioclase, 25-35% quartz, 10-15% biotite, 5-10% K-feldspar and 5% white mica. Accessory minerals are magnetite, titanite, apatite, and zircon.

Plagioclase is subhedral to euhedral and occurs as: (i) individual crystals up to 1 cm in size, commonly displaying evidence of resorption (fig. 4.4a); (ii) centimetric monomineralic *glomerocrysts* (Bennett et al., 2019; Hogan, 1993) consisting of several subhedral to anhedral plagioclase crystals (fig. 4.4b). Rarely, small crystals (< 400 μm) of epidote, often showing allanite inner domains, were found enclosed in some plagioclase cores (fig. 4.4c).

Biotite has euhedral to subhedral habitus and rarely exceeds 1 mm in size. It occurs mainly as interstitial grains between plagioclase, K-feldspar, and quartz but it may occur also as inclusions inside plagioclase and white mica (fig. 4.4d).

Primary white mica is generally millimetric in size, subhedral and with equilibrium contacts with plagioclase and biotite (fig. 4.4d). Alkali-feldspars occur both as anhedral perthitic microcline crystals and as small interstitial grains. Quartz occurs either as tiny interstitial crystals in a fine assemblage along some grain boundaries or as large grains (up to 4 mm) forming nodules that give a pseudo-porphyric texture to the rocks.

4.4.2 Tonalites (ETN and PTN)

Based on rock-texture, two types of tonalites were found: (i) equigranular (ETN) and (ii) porphyric (PTN) tonalite. The ETN are generally medium-grained with crystal reaching up to 4 mm in size while in the PTN plagioclase crystals may exceed one centimetre in length. Both types consist of plagioclase (50-60%), quartz (25-35%), biotite (10-15%), and minor interstitial K-feldspar and igneous epidote. Accessory phases are magnetite, allanite, titanite, and zircon.
In ETN, plagioclase is subhedral to euhedral and occurs either as small, partially resorbed crystals or as bigger crystals forming *glomerocrysts* (fig 4.4e). Differently, in PTN plagioclase occurs also as euhedral centimetric-size grains (Fig. 4.2f) characterized by oscillatory zoning and by an external rim enriched of tiny quartz inclusions (Fig. 4.4g). In both types, biotite is euhedral to subhedral (Fig. 4.4h) and occasionally occurs as inclusion hosted within the rim of plagioclase large crystals. Quartz and K-feldspar are anhedral and interstitial. Weakly pleochroic epidote (< 500 μm in dimensions) with euhedral to subhedral shapes, occurs as minor phase (< 1 vol.%).

The sharp contacts with biotite, the euhedral habit when included into biotite and its occurrence as overgrowth on euhedral allanite grains are evidence for its igneous origin (Fig. 4.4h,i,j).

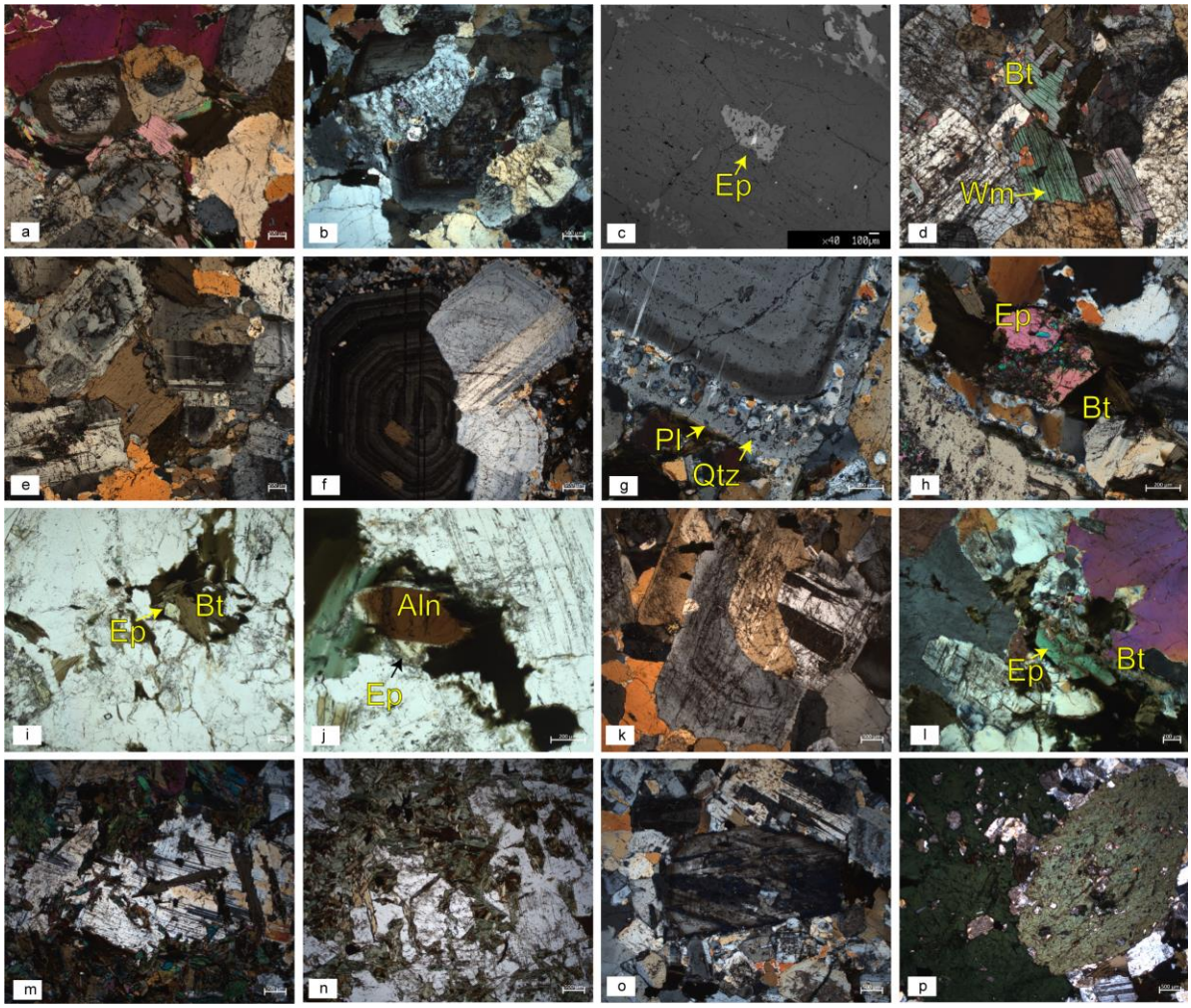

Figure 4.4 a) Two plagioclase crystals of type 1 with linear contacts with white mica in sample CA19-17; b) Plagioclase glomerocryst in sample CA19-10; c) Epidote crystal enclosed in plagioclase in sample CA19-13; d) Lamellar primary white mica with sharp contacts against plagioclase and biotite and inclusions of biotite crystals in sample CA19-36; e) nearly equigranular tonalite (ETN; sample CA19-21); f) big oscillatory zoned plagioclase in sample CA19-16 g) Tiny quartz crystals enclosed in the rim of plagioclase phenocrysts in PTN sample CA19-16; h) Epidote crystal with linear rims against biotite in sample CA19-21; i) Epidote euhedral inclusion in biotite in sample CA19-21; (j) Epidote overgrowth on euhedral allanite grains in sample CA19-15; k) Plagioclase glomerocrysts in sample CA19-26 and CA19-31; l) Euhedral epidote grains in sample CA19-30 and CA19-29; m) Resorbed plagioclase crystal with biotite and amphibole inclusions; n) Acicular amphibole ad biotite crystals in fine-grained aggregates in sample CA19-3; o) Plagioclase crystals with complex zoning and polysynthetic twinning in a groundmass of plagioclase tiny crystals in sample CA19-8; p) Coarse amphibole crystals with abundant inclusions in sample CA19-8.

4.4.3 Epidote-bearing granodiorites (EBG)

A fine- to medium-grained epidote-bearing granodiorite is the main lithology in the Sostino apophysis. Major phases are plagioclase (35-40%), quartz (25-35%), biotite (10-15%), K-feldspar (10%) and epidote (5%). Apatite, titanite, zircon, magnetite, and allanite are common accessory minerals with relatively large dimensions (up to 1mm).

Rocks are texturally very similar to the two mica granodiorites of the Corno Alto, mainly for the occurrence of rounded quartz nodules and for the widespread occurrence of plagioclase glomerocrysts (fig. 4.4k). The Sostino granodiorites however show a higher amount of interstitial microcline, the occurrence of abundant igneous epidote as a major mafic phase (fig. 4.2l), and the absence of primary white mica.

4.4.4 Diorites (MDR)

Dioritic rocks (CA19-3) are medium to fine grained and mainly consist of hornblende (45 vol%), plagioclase (40 vol.%), biotite (10 vol.%), and quartz (5 vol.%). Accessory minerals are zircon, apatite, and oxides.

Hornblende occurs in fine-grained aggregates of acicular crystals often in association with biotite crystals (Fig. 4.4n). Plagioclase (0.5-2.5 mm in size) has subhedral habit and often shows resorption rims (Fig. 4.4m). Biotite has subhedral to euhedral habit and occur both in association with hornblende and as inclusion in plagioclase crystals. Quartz shows anhedral habit.

4.4.5 Mt. Ospedale tonalites (OTN)

Tonalitic rocks from the Mt. Ospedale (sample CA19-8) are medium- to coarse-grained with porphyric texture. They consist of euhedral to subhedral amphibole (up to 1 cm across), biotite (<7 mm), and plagioclase (up to 3 mm) dispersed in a finer grained matrix of quartz, biotite, plagioclase and microcline. Mineral proportions are: plagioclase (45 vol.%), quartz (20 vol.%), biotite (17 vol.%), amphibole (13 vol.%), microcline (5 vol.%). Accessory minerals are apatites, zircons, titanites and oxides. The euhedral coarse plagioclase grains have complex zoning and polysynthetic twinning (Fig. 4.4o). Those in the groundmass are tiny, subhedral with local resorption in correspondence of the crystal's core. The groundmass plagioclase is commonly associated with anhedral quartz grains and tiny subhedral microcline crystals. Biotite often shows inclusions of plagioclase, apatite, and oxides. Amphibole euhedral coarse crystals are green in colour (Fig. 4.4p) and show inclusions of partially chloritized biotite, apatite, oxide and plagioclase.

4.5 Whole-rock geochemistry

Whole-rock major and trace element compositions of the Corno Alto rock suite are reported in Tables A.2 and A.3.

The Corno Alto and Sostino granitoids are calcic, with only a few samples that straddle the boundary with the calc-alkaline field (Fig. 4.5a). The granitoids are both metaluminous and peraluminous (0.98 ≤A/CNK≥ 1.20; Fig. 4.5b), silica-rich and (65.3 ≤SiO_2≤ 71.5 wt.%, Fig. 4.5a) characterized by relatively low K_2O/Na_2O ratios (ranging from 0.35 to 0.80). According to the normative feldspar classification diagram for the granitoids (An-Ab-Or, Barler, 1979), the rocks of Corno Alto and Sostino rocks plot on the granodiorite and tonalite fields (Fig. 4.5c) although they follow a trondhjemitic trend in the ternary K-Na-Ca plot (Fig. 4.5d; e.g.,Macera et al., 1983). Remarkably, although these rocks have been commonly referred to as "trondhjemites" in the literature (Macera et al., 1983; Relvini et al., 2022), none of the studied samples plot in the trondhjemite field. Diorite and the Mt. Ospedale tonalite are metaluminous (A/CNK≤ 1.0) and less evolved (49.4 ≤ SiO_2 ≤ 62.9 wt.%) but with similar K_2O/Na_2O ratios.

Major element compositions (normalized to 100 wt.% anhydrous) were plotted in Harker diagrams using SiO_2 content on the x-axis (Fig. 4.6-7). The TMG rocks have the highest SiO_2 content close to 70.0 wt% and Mg# (molar ratio Mg/(Mg+Fe)) ≈ 0.40. These samples also display the lowest CaO (2.39- 3.25 wt%), $Fe_2O_{3(tot)}$ (1.89-2.41 wt.%), MgO (0.62-0.84 wt.%), and TiO_2 (≈ 0.22 wt.%) contents. K_2O is quite variable, ranging from 1.58 to 3.14 wt.%. These rocks represent the most peraluminous rocks with A/CNK ≥ 1.10 (Fig. 4.5b). Compared to the TMG, the EBG rocks have slightly lower SiO_2 contents (≈ 69 wt.%), similar Na_2O, K_2O and $Fe_2O_{3(tot)}$, but slightly higher CaO (up to 3.51 wt.%), TiO_2 (≈ 0.32 wt.%) and MgO (0.89-1.05 wt.%) contents. They are also characterized by a slightly metaluminous character (0.98 ≤ A/CNK ≥ 1.03; Fig. 4.5b). Both ETN and PTN rocks are less evolved in compositions, with SiO_2 ≈ 66 wt.%, and higher CaO (4.13-4.46 wt.%), Al_2O_3 (up to 17.9 wt.%), $Fe_2O_{3(tot)}$ (up to 3.93 wt.%), MgO (1.37-1.66 wt.%), and TiO_2 (≈ 0.40 wt.%) than the granodiorites. K_2O abundances are comparable to those of the less potassic TMG, while Na_2O and MnO are in the range of all the other rocks. Mg# is ≈ 0.45, similarly to the EBG rocks. The dioritic rocks (MDR) have lower SiO_2 (49.3 wt.%) and higher Fe_2O_3 (9.38 wt.%), CaO (9.11 wt.%), TiO_2 (1.32 wt.%) and MgO (9.72 wt.%) at comparable Al_2O_3, K_2O and Na_2O with the more evolved lithotypes of the CA unit. The Mt. Ospedale tonalite is lower in SiO_2 (62.6 wt.%) and Na_2O contents (3.01 wt.%) compared to the CA tonalites. Whereas higher TiO_2 (0.62 wt.%), Fe_2O_3 (5.37 wt.%), CaO (5.52 wt.%), and MgO contents (2.22 wt.%) are observed.

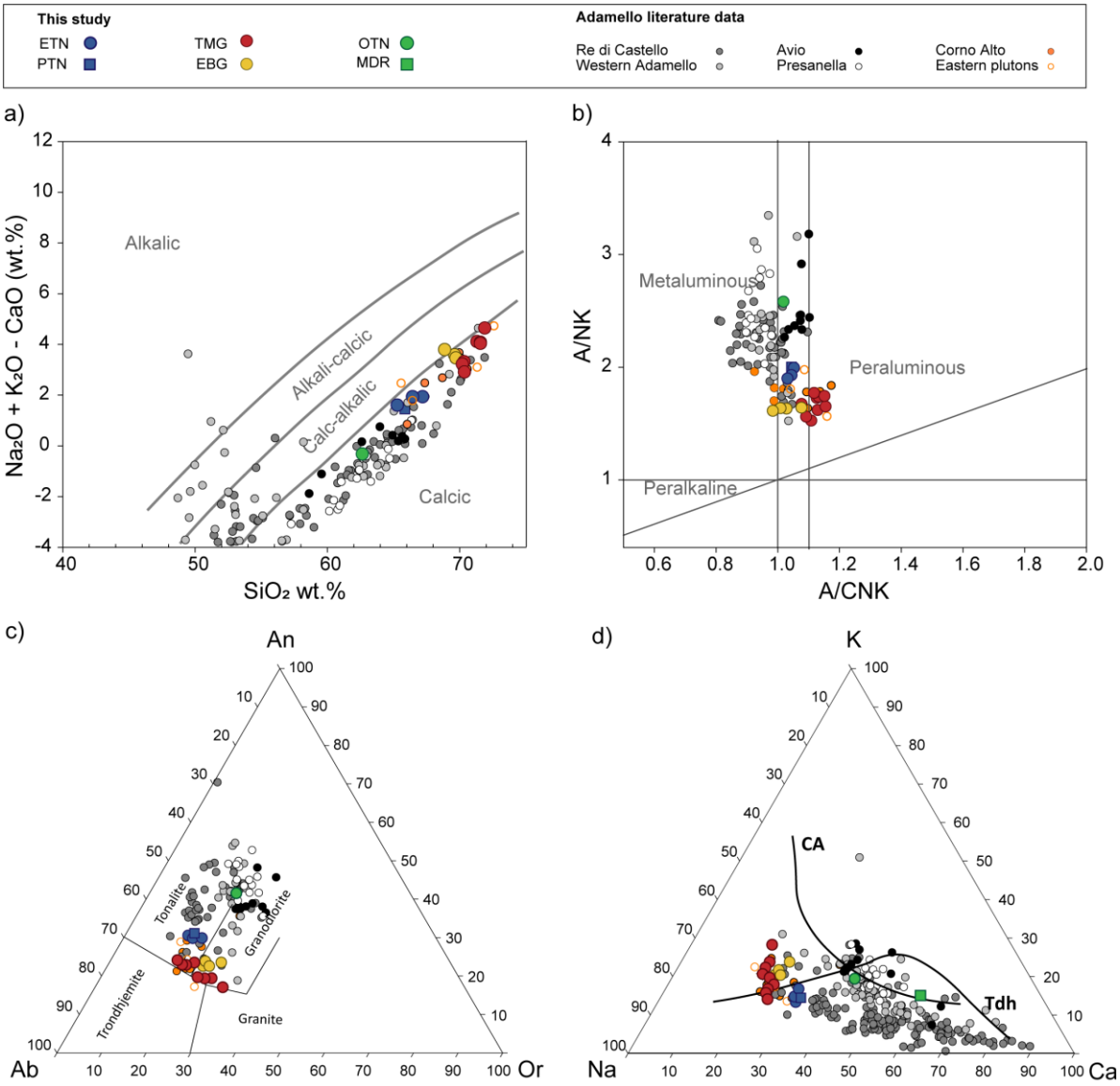

Figure 4.5 a) A/CNK (A/CNK = Al / (2 Ca + Na + K) expressed as molar proportion atoms) vs A/NK (A/NK = Al /(Na + K) expressed as molar proportion atoms) b) MALI index ([Na_2O + K_2O] - CaO) vs. SiO_2 diagram; c) Normative An-Ab-Or diagram (after Barker, 1979) for Corno Alto plutonic rocks. d) Ternary K-Na-Ca plot. The classification curves are from Barker & Arth (1976). Literature data are SiO_2-rich Adamello rocks with SiO_2 > 56 wt.% (data from: Dupuy et al., 1982; Macera et al., 1983; Kagami et al., 1991; Blundy & Sparks, 1992; Ji et al., 2019; Relvini et al., 2022).

The chondrite normalized REE patterns of the studied rocks are all characterized by strong enrichment in LREEs (up to 500 times chondrites) over HREEs (< 10 times chondrites). The $(La/Yb)_N$ ratio range from 14.2 to 30.7 in both TMG and EBG whereas is up to 61.2 in both types of tonalitic rocks (ETN and PTN). Eu anomaly is not pronounced ($Eu/Eu^* \approx 0.80$-1.04). Diorites and the Mt. Ospedale tonalite (MDR and OTN) show less fractionated REE patterns ($[La/Yb]_N$: 13.1-14.2) and a more pronounced negative Eu anomaly ($Eu/Eu^* \approx 0.76$-0.93).

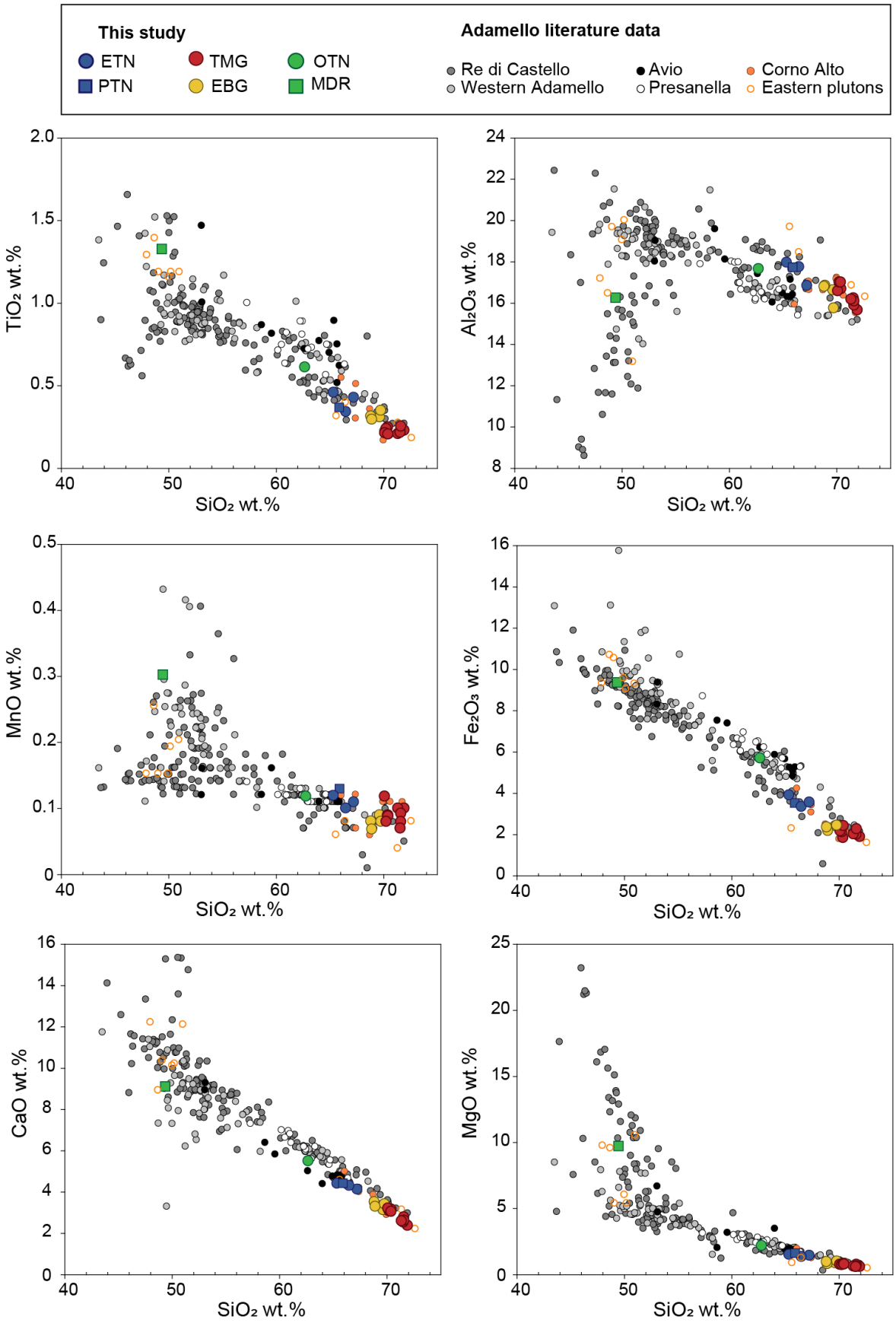

Figure 4.6 Major-element geochemistry of the Corno Alto and Sostino rocks compared with literature data (grey dots: Adamello literature data from Dupuy et al., (1982); Macera et al., (1983), Kagami et al., (1991), Blundy & Sparks, (1992), Ji et al., (2019), Relvini et al., (2022).

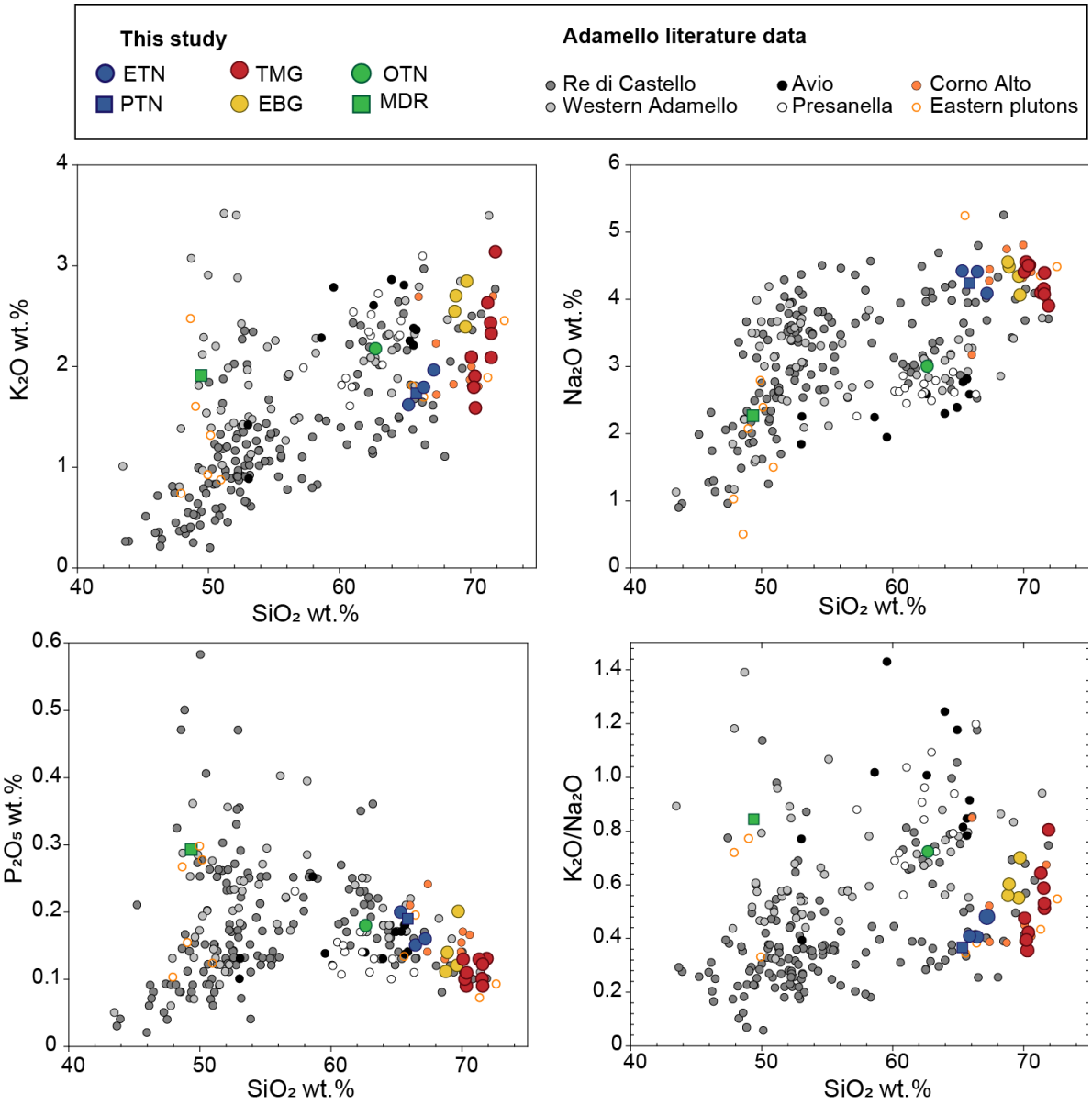

Figure 4.7 (Part 2) Major-element geochemistry of the Corno Alto and Sostino rocks compared with literature data (grey dots: Adamello literature data from Dupuy et al., (1982); Macera et al., (1983), Kagami et al., (1991), Blundy & Sparks, (1992), Ji et al., (2019), Relvini et al., (2022).

The primitive mantle normalized trace element pattern (Fig. 4.8a) is characterized by negative Nb, Ta, P, and Ti anomalies relative to the neighbouring elements and by enrichments in K, Pb, U, Th and LILEs (especially Sr and Ba; Fig. 4.5b).

The highest Sr contents (884 ppm) pertain to the PTN tonalitic rocks whereas the epidote-bearing granodiorites (EBG) and the two-mica granodiorites (TMG) are characterized by slightly lower contents (404-551 ppm) but still higher than those characterizing the diorites (MDR), the Mt. Ospedale tonalites (OTN) and most of other granitoid rocks in the Adamello batholith.

The epidote-bearing granodiorites (EBG) are very Ba-rich (1069-1614 ppm) and exhibit a higher Pb, Th and U concentrations compared to the other rock types.

Overall, the magmatic rocks in the Corno Alto-Sostino pluton have higher Ba than granitoids from other part of the Adamello batholith (Fig. 4.8b). The concentration in high-field strength elements (HFSE) is similar in the different rock types with the exception of the diorites (MDR) and Mt.Ospedale tonalites (OTN).

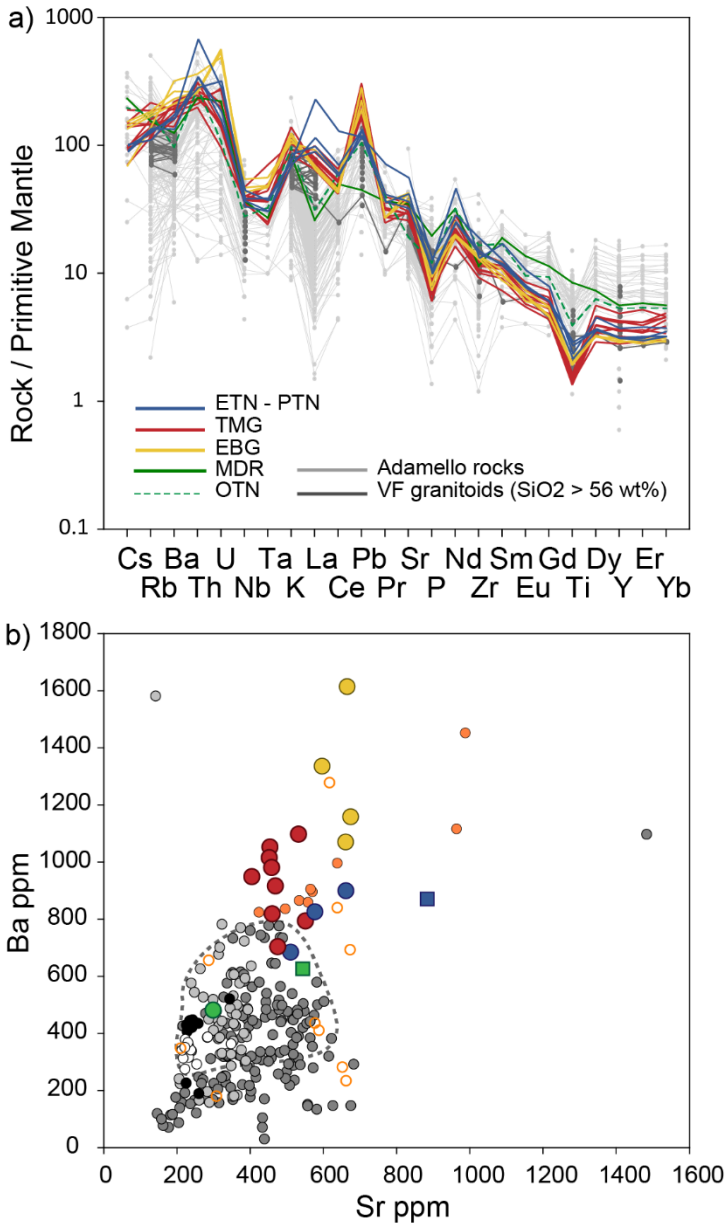

Figure 4.8 Trace element composition of the Corno Alto rocks compared to the other other Adamello rocks (the dashed patterns define the SiO_2-rich Adamello rocks with SiO_2 > 56 wt.%); symbols are the same of Fig. 4.4. a) Multi-element patterns of average composition for each group normalized to Primitive Mantle (McDonough and Sun, 1995); b) Ba (ppm) vs. Sr (ppm) diagram for the Corno Alto rocks (coloured dots) and the other Adamello rocks (grey dots). Literature data from Dupuy et al., (1982), Macera et al., (1983), Kagami et al., (1991), Blundy & Sparks, (1992), Ji et al., (2019), Relvini et al., 2022.

4.6. Mineral Chemistry

Representative compositions of the analysed minerals are given in Appendix A (Tables A.6, A.7, A.8, A.9, A.19).

4.6.1 Plagioclase

The total range of plagioclase composition in the Corno Alto unit is An_{92-12}, with the majority of analysis ranging between An_{30} and An_{40} and minor differences between the different lithotypes (Fig. 4.9; Table A.6). The EBG rocks display the most albitic compositions with less variation in An contents from the core (An_{35-37}) to the rim (An_{13-22}). Plagioclase crystals from the TMG glomerocrysts display andesine composition at the core (An_{30-50}) and mostly oligoclase composition at the rims (An_{14-35}). TMG rocks contain sporadic plagioclase cores with high-An contents (up to An_{87}). These crystals are normally zoned and are characterized by an abrupt decrease in An (An_{rim12}) at their external margin featuring. ETN rocks display the narrowest range of An contents (An_{30-69}). Plagioclase crystals in the PTN display discrete compositional variations: An_{45-65} at the cores and An_{25-40} at the rims. Moreover, in these rocks few plagioclase crystals with extremely Ca-rich cores (up to An_{92}) followed by more albitic composition at the rim (An_{23}) were found. Plagioclase from diorites show a narrow compositional variability (An_{42-56}). Plagioclase crystals from OTN rocks have compositions varying from An_{41} to An_{73}.

4.6.2 Biotite

Biotite (Table A.3b) from TMG rocks have Fe# [$Fe^{2+}/(Fe^{2+} + Mg^{2+})$] ranging from 0.46 to 0.51 and TiO_2 contents are between 1.85 and 2.68 wt.%.

In ETN and PTN rocks, biotite has variable Fe# in the range 0.33-0.95 and TiO_2 spanning from 2.03 to 2.76 wt.%. In EBG rocks, biotite crystals have major element composition analogous with that of the crystals in the TMG rocks (Fe#: 0.46-0.49; TiO_2 ranging from 2.38 to 3.46 wt.%). MDR biotites exhibit Fe# ranging from 0.38 and 0.45 and TiO_2 from 2.13 to 2.49 wt.%. In OTN rocks, biotite shows Fe# of 0.50-0.51 and TiO_2 contents in the range 2.13-2.49 wt.%.

4.6.3 Epidote

Epidote shows narrow compositional variations in the different rock types (Table A.10). Pistacite contents (Ps = molar [$Fe^{3+}/(Fe^{3+} + Al)$] x100) vary between 21.1 and 30.3 %, with most of the compositions with pistacite content > 26%, for both interstitial epidote and epidote inclusions in plagioclase. TiO_2 contents are below 0.2 wt.% for all the grains. The euhedral habit,

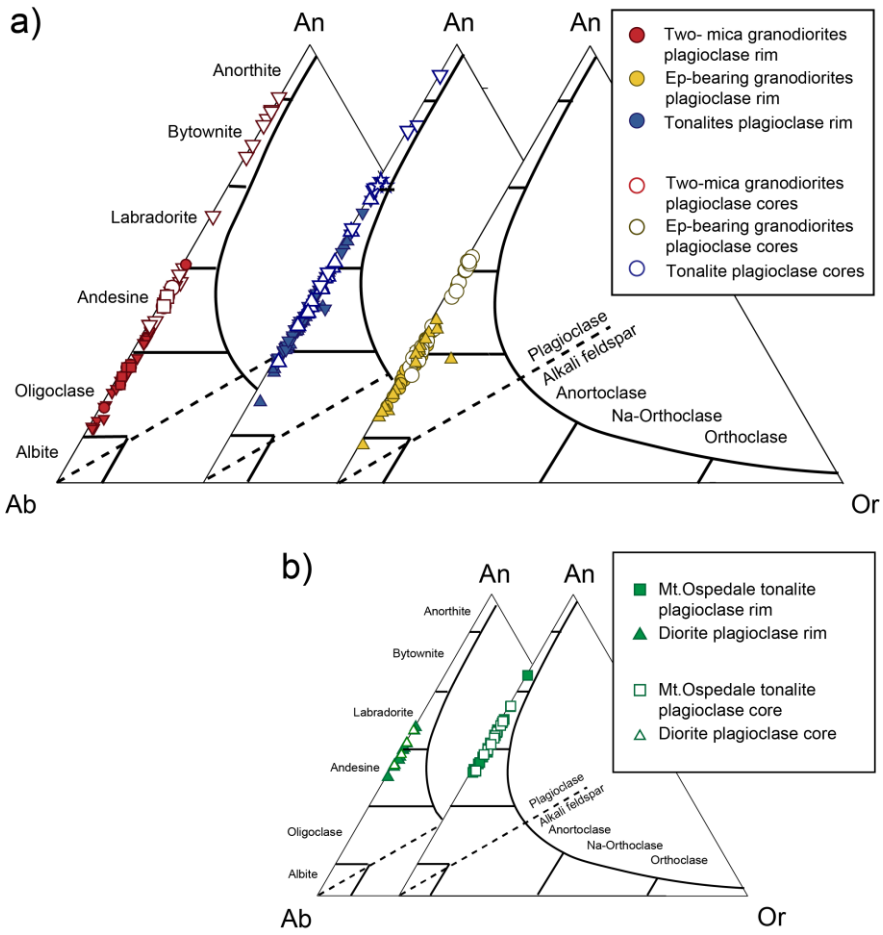

Figure 4.9 Anorthite-Albite-Orthoclase classification diagram for feldspars.

the allanite-rich cores, the Ps content varying between 24 and 35 mol% and the low TiO_2 contents (<0.2) are evidence for an igneous origin of epidote (Lima et al., 2021; Schmidt and Poli, 2004; Zen and Hammarstrom, 1984).

4.6.4 White mica

White mica occurs exclusively in the TMG (Table A.8). Si contents are slightly higher than typical muscovites from peraluminous granitoids (3.09 - 3.18 a.p.f.u., based on 11 oxygen) and point to low-Si phengites compositions.

3.6.5 Amphibole

Amphibole in MDR and OTN is hornblende in composition (Table A.9). The Mg# [Mg/(Mg+Fe^{tot}), in apfu)] of amphibole in MDR is slightly higher (0.57-0.61) than in OTN (0.47-0.52). TiO_2 is in the range 0.65-1.20 wt.% in MDR amphiboles whereas it does not exceed 0.9 wt.% in those from OTN. Alkali content (Na+K) range from 0.45 to 0.55 in OTN, while in MDR values vary from 0.32 to 0.47.

4.7 U-Pb zircon geochronology

At least two samples for each of the main lithologies of the Corno Alto complex, one samples of diorite, and one sample for the Mt. Ospedale tonalite were selected for U-Pb zircon geochronology, trace element and in-situ Hf isotope determinations. U-Pb ages are reported in Table A.11 and U-Pb Concordia diagrams are presented in the Appendix A (Fig. A.1-2). Analyses yielding >2% discordancy were not considered.

Based on CL textures three different domains, variably combined, can be identified in zircons from the different lithologies (Fig. 4.10). A-type domain are characterized by oscillatory zoning with medium- to low-luminescence. B-type domain are unzoned to weakly zoned, characterized by medium- to high-luminescence, often displaying a dissolution surface at their boundary. Finally, C-type domain are rounded and exhibit bright-CL. In figure 4.11, the U-Pb weighted mean of magmatic zircon grains for all the analysed samples are presented.

4.7.1 Two-mica granodiorites (TMG)

Zircons from the two-mica granodiorites are prismatic to stubby, ranging in size from 75 μm to 400 μm. The length/width ratio is typically 2.5:1 to 4:1 and only a few grains are fractured. Most of zircon grains have centres showing C-type and B-type domains and are mantled by domains with A-type texture. Only a subset of grains show only A-type domains.

In sample CA19-10, thirty-one analyses has been carried out. Of these, nine discordant analyses were discarded. Six analyses on inherited crystals (C-type textures) yielded dates ranging from 449 ± 9 Ma to 980 ± 20 Ma. The remaining twenty-four analyses on both cores and rims do not allow calculating a single mean concordia age. On a probability density plot the analyses reveal the occurrence of at least two populations with distinct U-Pb ages. Most of the analyses pertaining to both B-type and A-type domains define a main peak with a mean concordia age at 39.1 ± 0.3 Ma (MSWD for c+e: 1; Fig. 4.11). Data carried out on A-type domains rimming C-type cores yield an older peak with a mean concordia age at 43.4 ± 0.4 Ma (MSWD for c+e = 2.8).

Fourteen analyses have been performed on zircon grains of sample CA19-13. Of these, two analyses yield discordant ages. Twelve analyses yield concordant dates that allowed to calculate a mean concordia age at 43.6 ± 0.4 Ma (n=12, MSWD for c+e = 1.4).

In sample CA19-37, twenty-five analyses has been carried out. Of these, four analyses gave discordant dates whereas six analyses returned U-Pb ages ranging from 471 ± 12 Ma to 2461 ± 71 Ma. The remaining fifteen analyses suggest the occurrence of two zircon populations with distinct U-Pb ages: most of the analyses yield a mean concordant age of 41.7 ± 0.4 Ma (n=11;

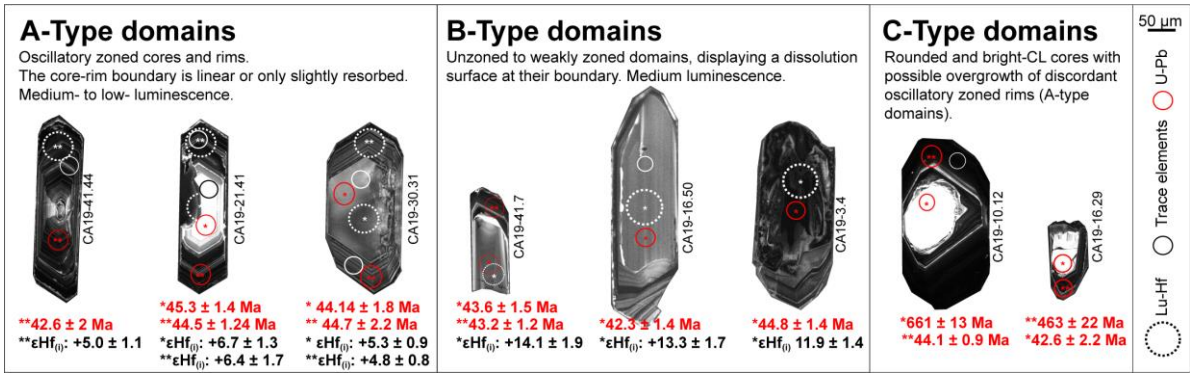

Figure 4.10 Cathodoluminescence images of representative zircon grains from the Corno Alto unit divided by domains. Zircons with multiple domains also occur (e.g. crystal CA19-41.7 has a B-type texture at the core and A-type at the rims). U–Pb and εHf errors are reported as 2s

MSWD for c+e = 0.43), whereas few analyses gave an older mean concordant age at 44.4 ±0.7 Ma (n= 4; MSWD for c+e = 0.25).

Fifty-four analyses have been carried out on sample CA19-41. Eleven analyses returned discordant ages whereas fourteen analyses carried out on C-type domains gave old and highly variable ages, from 151 ± 7 Ma to 1068 ± 30 Ma. Most of the analyses yield a mean concordia age at 43.7 ± 0.3 Ma (n=21; MSWD for c+e = 1.3). A subset of eight analyses yielded younger mean concordia age at 41.4 ± 0.5 Ma (n=8; MSWD for c+e = 0.7).

4.7.2 Tonalites (ETN and PTN)

Zircons from tonalite rocks are mostly prismatic, rarely with stubby habitus. They range in dimensions from ~100 µm to more than 300 µm with a typical length/width ratio of 2.5:1.

In sample CA19-16, (PTN) most of the zircon display A-type domains in correspondence of both core and rim. Few zircon centers display B-type and C-type textures surrounded by A-type textures. Sixty-four analyses were carried out on the zircon grains from PTN rock CA19-16. Of these, seven analyses were discordant. Five analyses on C-type domains returned dates spanning from 186 ± 4 Ma to 867 ± 19 Ma. Fifty analyses on both cores and rims revealed the occurrence of two populations with distinct U-Pb ages. Most of the analyses yield a mean concordant age at 41.9 ± 0.2 Ma (n= 37; MSWD for c+e = 0.79); another subset of fifteen analyses returned older concordant dates and a mean concordia age at 44.2 ± 0.3 Ma (n=14; MSWD for c+e = 0.75).

Most of zircon crystals in sample CA19-21 (ETN) have A-type textures and only one core with C-type texture was found. Thirty-eight spot analyses in zircon grains from CA19-21 were performed. Of these, fifteen analyses are discordant. Twenty-three analyses yield a mean concordia age at 44.7 ± 0.3 Ma (n=23; MSWD for c+e = 0.7). One analysis performed on a C-type domain returned an age of 433 Ma ± 11 Ma.

4.7.3 Epidote-bearing granodiorites (EBG)

Most zircons from epidote- bearing granodiorites are prismatic, with elongated shape, sharp facets, and pointed tips. Zircon crystals are mainly colourless and transparent, with lengths ranging from 50 to 300 μm and length/width ratio of 2.5:1.

In sample CA19-26, zircon grains have either A-type and C-type cores. Forty-one analyses were carried out and of these, three analyses were discordant and ten analyses on C-type domains gave dates from 333 ± 18 Ma to 2174 ± 64 Ma. Twenty-eight analyses were concordant and yielded a mean concordia age at 44.0 ± 0.3 Ma (n=28; MSWD for c+e = 0.43).

In sample CA19-30, all grains display cores and rims with A-type texture while no B- or C-type domains were found. Twenty-seven analyses were carried out and twenty-two analyses of both cores and rims yield concordant dates and returned a mean concordia age at = 44.3 ± 0.3 Ma (n=22, MSWD for c+e = 0.52).

4.7.4 Diorite (MDR)

Zircon grains from the diorite (CA19-3) are mostly fractured with fragments reaching 300 μm in size. Zircon CL textures are peculiar and cannot be classified into A- B- or C-type domains. Zircons are characterised by patchy textures with faint zoning and irregular longitudinal streak as well as occasional spongy textures at the core. Seventeen analyses were performed on zircon grains from sample CA19-3. Of these, one returned discordant date. Fifteen analyses yield a mean concordant age at 39.7 ± 0.4 Ma (MSWD for c+e = 0.56). One analyses on a zircon core gave a date at 44.8 ± 1.4 Ma.

4.7.5 Mt. Ospedale tonalite (OTN)

Zircons from the Mt. Ospedale tonalite (CA19-8) are prismatic to stubby, ranging in dimension from to 300 μm, with length/width ratio of 2.5:1 to 4:1.

Most of zircon grains are characterised by cores and rims with A-type texture. Twenty-two analyses were carried out and two analyses on C-type domains returned dates at 736 ± 36 Ma and 941 ± 54 Ma. The remaining twenty analyses on both cores and rims yielded a mean concordant age at 36.8 ± 0.4 Ma (n= 20; MSWD for c+e = 1.2). This age suggests that the Mt. Ospedale tonalite pertain to the Adamello unit rather than to the older Corno Alto or Re di Castello unit.

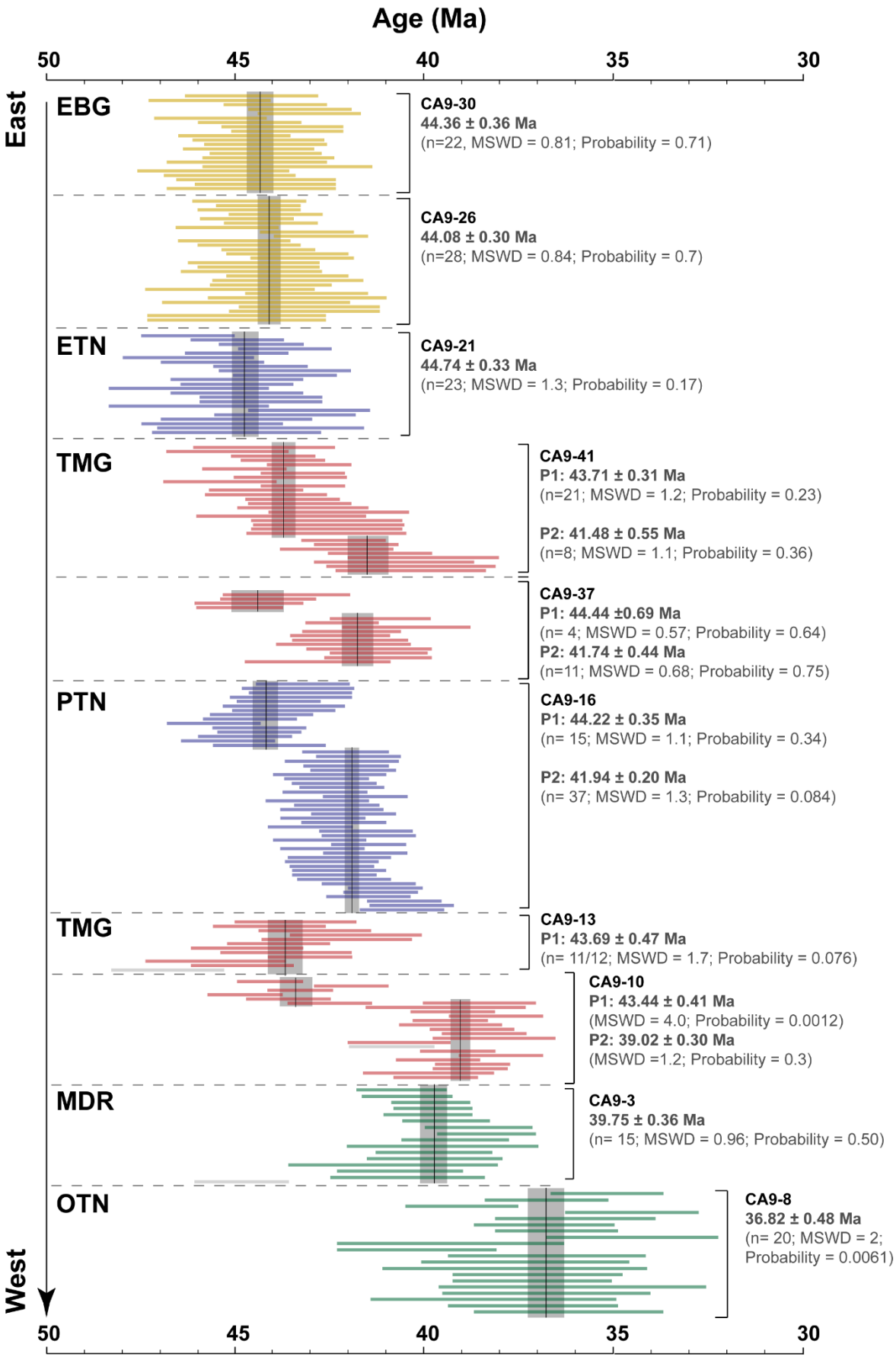

Figure 4.11 Compilation of weighted average ages of zircon from the Corno Alto complex by laser-ablation ICP-MS. Error are reported as 2se.

4.8. Zircon geochemistry

4.8.1 Trace element compositions

Zircon trace element composition (Table A.12) was determined for some of the previously dated domains. Being the composition of zircon grains in the different samples similar, trace element contents are presented as a function of the domain type and only for the magmatic domains A- and B-type (Fig. 4.12). A-type domains show similar chondrite-normalized (McDonough and Sun, 1995) REE patterns, characterized by HREE enrichment [$(Lu/Gd)_N$ > 26-100], positive Ce anomaly, and negative Eu anomaly (Eu/Eu* down to ~ 0.4).

These domains also have relatively high Nb, Ta (up to 86 ppm and 18 ppm, respectively) and U contents (~ 750-5550 ppm) while their Th/U ratio is low (< 0.5). B-type domains have REE patterns characterized by higher ΣLREE contents, a less pronounced HREE enrichment [$(Lu/Gd)_N$ ~ 9-40], positive Ce anomaly, and absent or slightly negative Eu anomaly (Eu/Eu* ~ 0.7). The concentrations in Nb and Ta are very low (up to a maximum of 10 ppm and 2.2 ppm, respectively), and Th/U values range between 0.80 to 1.72.

4.8.2 Hf isotopic compositions

In-situ Hf isotope composition of magmatic zircons was carried out on selected previously dated domains (Fig. 4.13; Table A.13).

Zircon grains from the TMG show considerable variation in $\varepsilon Hf_{(i)}$ (-3.2 to +14.1) with a multimodal distribution of data characterized by the occurrence of at least three dominant clusters at around +3, +8, and +13. Interestingly, the higher $\varepsilon Hf_{(i)}$ values pertain to the B-type textural zircon domains.

Zircon from the tonalitic rocks also have a large scatter in the $\varepsilon Hf_{(i)}$ isotopic composition, ranging between +2.5 and +13.0, with most of the values at ca. +6. The highest $\varepsilon Hf_{(i)}$ values are usually associated with B-type textural domains at the core of the grains (e.g., sample CA19-16, PTN). Noticeably, in sample CA19-21 (ETN), no $\varepsilon Hf_{(t)}$ values higher than +7 have been found.

The zircons from the EBGs show a more restricted variation in the $\varepsilon Hf_{(i)}$ isotopic compositions with most of values giving a nearly unimodal distribution at about +5. Few data gave lower and higher values (down to -2.5 and up to +9.1).

Most of the zircons from the MDR have $\varepsilon Hf_{(t)}$ values close to +6, with a few exceptions showing slightly negative value ($\varepsilon Hf_{(i)}$ down to -0.7). Noticeably, the old zircon core at 44 Ma shows $\varepsilon Hf_{(t)}$ at +12.0 ± 1.5 (2s). Negative $\varepsilon Hf_{(t)}$ values ranging from -3.2 to -9.6 are reported in the OTN sample.

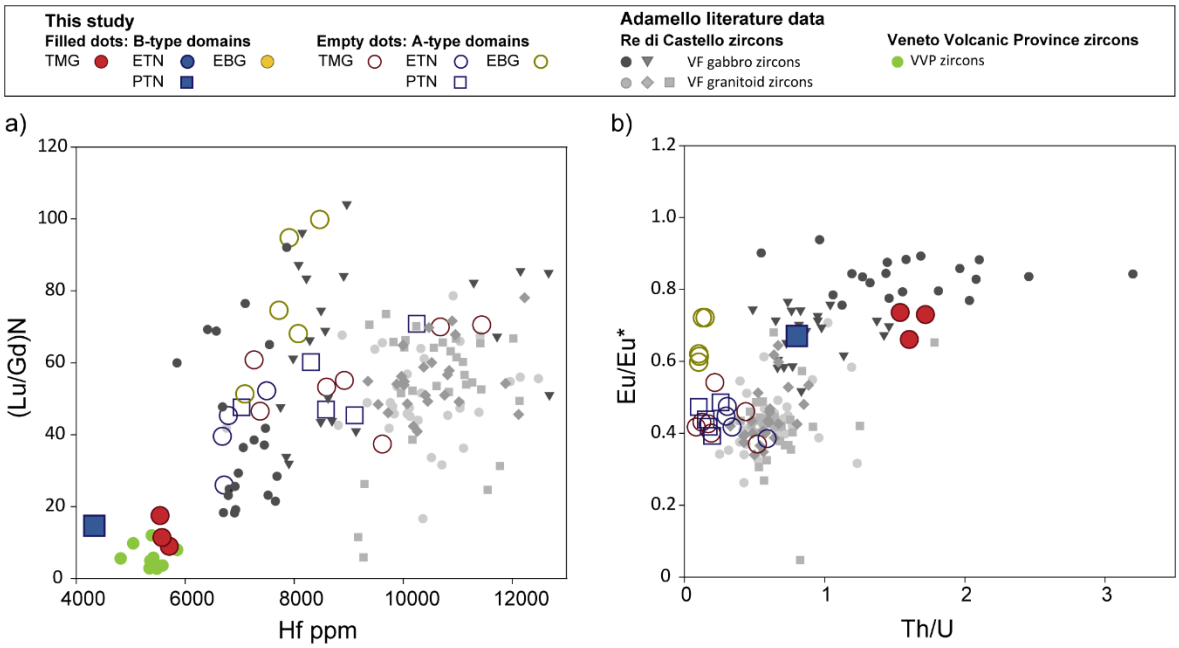

Figure 4.12 Hf (ppm) vs. $(Lu/Gd)_N$ and Th/U vs. Eu/Eu* diagrams from the Corno Alto zircons compared to Val Fredda (grey dots; Broderick et al. 2015) and the Veneto Volcanic Province (VVP) zircon crystals (green dots; from Visonà et al. 2007). Errors are within symbol.

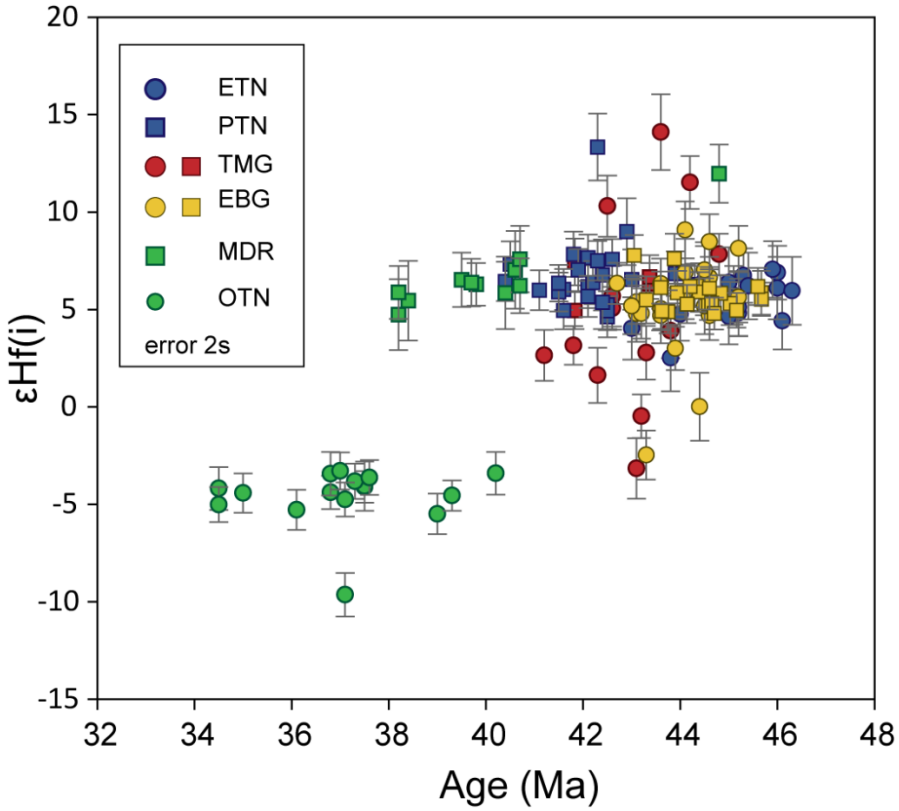

Figure 4.13 Single zircon dates and Hf isotopes compositions from the Corno Alto and Mt. Ospedale rocks.

4.9 Discussion

4.9.1 Is the Corno Alto complex peculiar in the Adamello batholith framework?

The Corno Alto and Sostino granitoids have been described as an association of granodiorite to trondhjemite rocks (Bianchi et al., 1970; Callegari & Dal Piaz, 1973; Macera et al., 1983; Relvini et al., 2022; Schaltegger et al., 2019), with distinct mineralogical and chemical characteristic from the rest of the Adamello Batholith.

Here, we showed that none of the granitoids in the Corno Alto and Sostino unit is a trondhjemite according to the Ab-An-Or normative diagram of Barker (1979). Moreover, considering all the available data in the literature on the Corno Alto and Sostino rocks, only a very restricted number of samples effectively fall in the compositional trondhjemite field with the vast majority being instead granodiorites and tonalites (Fig. 4.5c). The Corno Alto rocks have however some peculiar petrographic and geochemical features relative to the other units of the batholith even if compared with rocks of similar age (e.g., south Re di Castello).

Petrographically, we observe the igneous epidote is almost ubiquitous replacing other major mafic phase such as amphibole and/or pyroxene. The most extreme example of this feature is represented by the oldest EBG rocks from Sostino. The occurrence of epidote as inclusions into both plagioclase and biotite suggest that epidote started crystallization at relatively high pressure before plagioclase and thus likely in the lower crust (> 0.8 GPa; Schmidt & Poli 2004). Then the magma followed a path of isobaric cooling crossing the plagioclase-in and biotite-in reactions (< 700°C) before emplacement at shallow levels in the crust (ca. 3.5-4 kbar, P proposed for the Corno Alto pluton based on apatite fission track; e.g. Martin et al., 1998; Relvini et al., 2022) outside the stability field of amphibole. The dissolution of epidote in granitic magmas is a relatively fast process (Brandon et al., 1996; Sial et al., 2008) and its occurrence in low pressure rocks such as those of the Corno Alto thus implies a fast melt ascent. This is also consistent with the occurrence of centimetric oscillatory-zoned plagioclase phenocrysts displaying albite-rich pecilitic rims with tiny quartz inclusions, interpreted as evidence of an initial slow crystallization followed by fast-cooling and intrusion into cooler regions of the lithosphere during the final stage of the crystallization.

The Corno Alto granitoids also have a distinctive chemical composition. These rocks represent the most differentiated products of the Adamello batholith (SiO_2 up to 72 wt.%) and show the most peraluminous compositions ($0.98 \leq A/CNK \leq 1.2$; Fig. 4.5b). Moreover, at any given SiO_2 content, the Corno Alto rocks have slightly higher Na_2O than most of the Adamello granitoids. Exception is made only for some SiO_2-rich rocks from the Val Fredda Complex (Re

di Castello unit) and W-Adamello (Blundy and Sparks, 1992; Dupuy et al., 1982; Macera et al., 1983; Ulmer et al., 1983). The trace element composition of the Corno Alto rocks reveals also peculiar features that include a strong Ba (Fig. 4.8), and to a minor extent Sr enrichment (Sr/Y > 40) and light-REE enrichment over HREE ($La_N/Yb_N > 20$) and Y, at any given SiO_2 content.

4.9.2 Timing of the assembly of the Corno Alto complex

The new geochronological data presented in this work refine the current knowledge on the age of the Corno Alto complex (Ji et al., 2019; Schaltegger et al., 2019) suggesting an assembly by multiple and possibly discrete magma injections in time span of ~5 Ma (Fig. 4.11).

U-Pb concordant data shows the occurrence in the Corno Alto complex of three main recurring age peaks, at c. 44 Ma, c. 42 Ma, and c. 39 Ma (Fig. 4.14). The easternmost sector of the Corno Alto unit (fig. 4.14a) exhibits the oldest ages with dates that are exclusively around ca. 44 Ma. These dates are equivalent to those reported by Schaltegger et al. (2019) and Ji et al. (2019) for the Corno Alto complex and likely represents the oldest igneous event in the Adamello batholith. The rocks dominating the central sector of the unit (fig. 4.14c) show a relatively large age dispersion with a major peak at 42 Ma and a poorly defined inflection at 44 Ma. Noticeably, in the PTN sample the 42 Ma peak is statistically different from that at 44 Ma, which mostly results from the analysis of zircon cores (Fig 4.14.c2). In this sample, no age distinction was observed between the different zircon types recognised under cathodoluminescence. The 42 Ma peak is thus interpreted as a second distinct and younger magmatic pulse, which likely assembled the central sector of the Corno Alto complex. Here, the 44 Ma domains are interpreted as antecrysts (e.g., Miller et al., 2007) – *i.e.* zircon grains crystallized from earlier magmatic pulses and mechanically incorporated into the intruding magma during emplacement. The youngest age cluster at 39 Ma, which is also distinct from the event at 42 Ma, characterises the lithologies at the western border of the complex (fig. 4.14e). The occurrence of antecryst zircons at 44 Ma suggests that also this younger event recycled previous intrusions. The widespread occurrence of several inherited zircon grains of Proterozoic to Paleozoic age suggests extensive interaction of the magma with a host basement constituted by metasedimentary rocks in agreement with Boriani & Giobbi-Origoni (1982).

The three magmatic pulses that assembled the Corno Alto complex are not distributed randomly but identify an EW-ward trend of decreasing ages (Fig. 4.11). The progressive W-ward rejuvenation of the Corno Alto rocks could also be interpreted as induced by partial resetting of the U-Pb zircon system in response to the emplacement of the younger western Adamello units (e.g. Re di Castello North and Adamello). However, the multiple zircon populations (also within a single hand sample) characterizing the central sector of the unit argue against such an

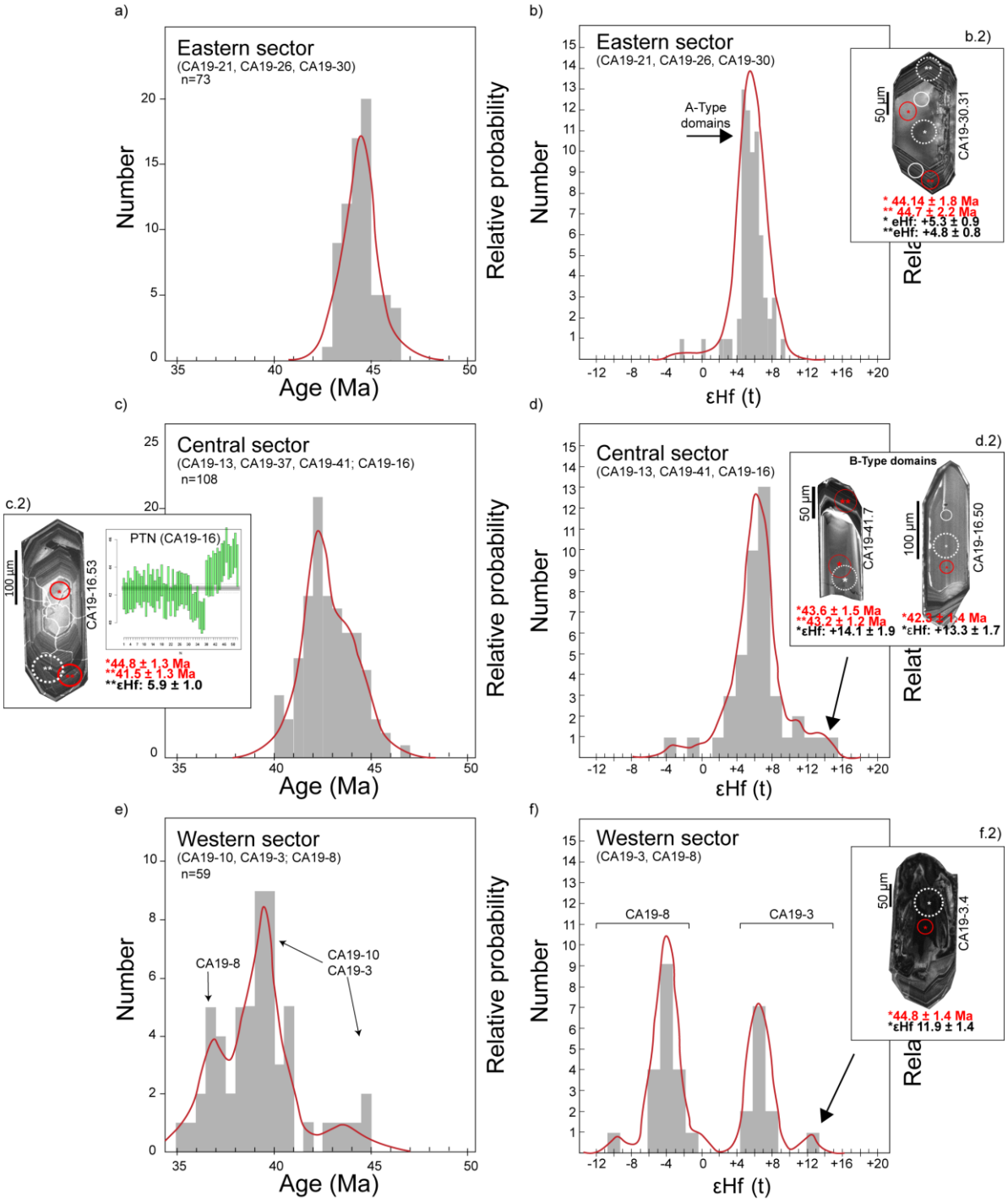

Figure 4.14 On left in image, geochronological results (U-Pb concordant data) for the Corno Alto rocks from the eastern (a), central (c) and western (e) parts of the Complex. On the right (b, d, f), distribution of εHf(t) values in zircon grains from the same rocks. Errors for Hf are reported as 2s.

interpretation of the U-Pb zircon dates. The EW-ward trend of decreasing ages is roughly perpendicular to the direction of the Giudicarie line, which is located right above the European slab edge (Sun et al., 2019; Zhao et al. 2016) possibly formed by tearing after interaction between the European and Dinaric slabs (Ji al., 2019; Malusà et al., 2021). In the Corno Alto complex,

we can thus identify a progressive migration of igneous activity away from the slab tear through time.

At the regional scale, it is noteworthy that the earliest magmatic events recorded in the Corno Alto rocks (at c. 44 Ma) also occur as xenocrystic zircon cores in the mafic rocks of the South Re di Castello unit (Tiepolo et al., 2011). This finding suggests that the onset of subduction-related igneous activity at 44 Ma in the Southern Alps was not restricted to the Corno Alto complex (D'Adda et al., 2011). It likely affected a wider crustal area, currently extending south-west towards the Val Fredda complex, paralleling the Giudicarie Fault and, thus, the trace of the European slab tear inferred on a geophysical ground (Malusà et al., 2021).

In support of this conclusion is also the stringent analogy in trace element composition and Hf isotopes of the B-type domains of the Corno Alto zircons with those of the Mt. Mattoni gabbro and Blumone hornblende-rich quartz diorite zircons (Broderick et al., 2015; Schoene et al., 2012) which strongly suggests a common origin. On the other hand, the A-type domains identified in the Corno Alto zircons also match the composition of the differentiated rocks of the Val Fredda complex suggesting a common evolution with time of the entire crustal sector (Fig. 4.12). In this regard, the U-Pb ages of the Corno Alto and Val Fredda complexes fit the ages characterizing the youngest magmatic episodes of the intraplate Veneto Volcanic Province (VVP) in the Lessini Mts. and Val d'Adige, at ~51 Ma, ~45 Ma and ~42 Ma (Brombin et al., 2019; Visonà et al., 2007), which are also located along the inferred trace of the European slab tear.

4.9.3 Geochemically distinct sources at the origin of the Corno Alto complex

The granitoid rocks from Corno Alto complex show the coexistence of at least two geochemically distinct components: i) a high Ba component characterised by high Sr and La/Yb ratios; ii) a juvenile component whose affinity is recorded by zircon cores having depleted mantle εHf(t) signature as well as by the occurrence of high Ca plagioclase cores.

The high Ba-La/Yb component

The SiO_2 > 60 wt% of the Corno Alto rocks, their Sr/Y > 40, and $(La/Yb)_N$ > 10 (Fig. 4.15a, b) roughly recall the geochemical signatures of a particular group of arc related melts known as adakites (Defand and Drummond, 1990). In particular, the Corno Alto rocks have major and trace element compositional features (i.e., mg# ≈ 0.5, Na_2O > 3.5%, K_2O/Na_2O ratios ≈ 0.4, Y <18, Yb <1.8 ppm and Sr >400 ppm) that fulfil the criteria used by Martin et al., (2005) to define high-SiO_2 adakites (HSA). However, the extremely high Ba and, to a minor extent, Sr

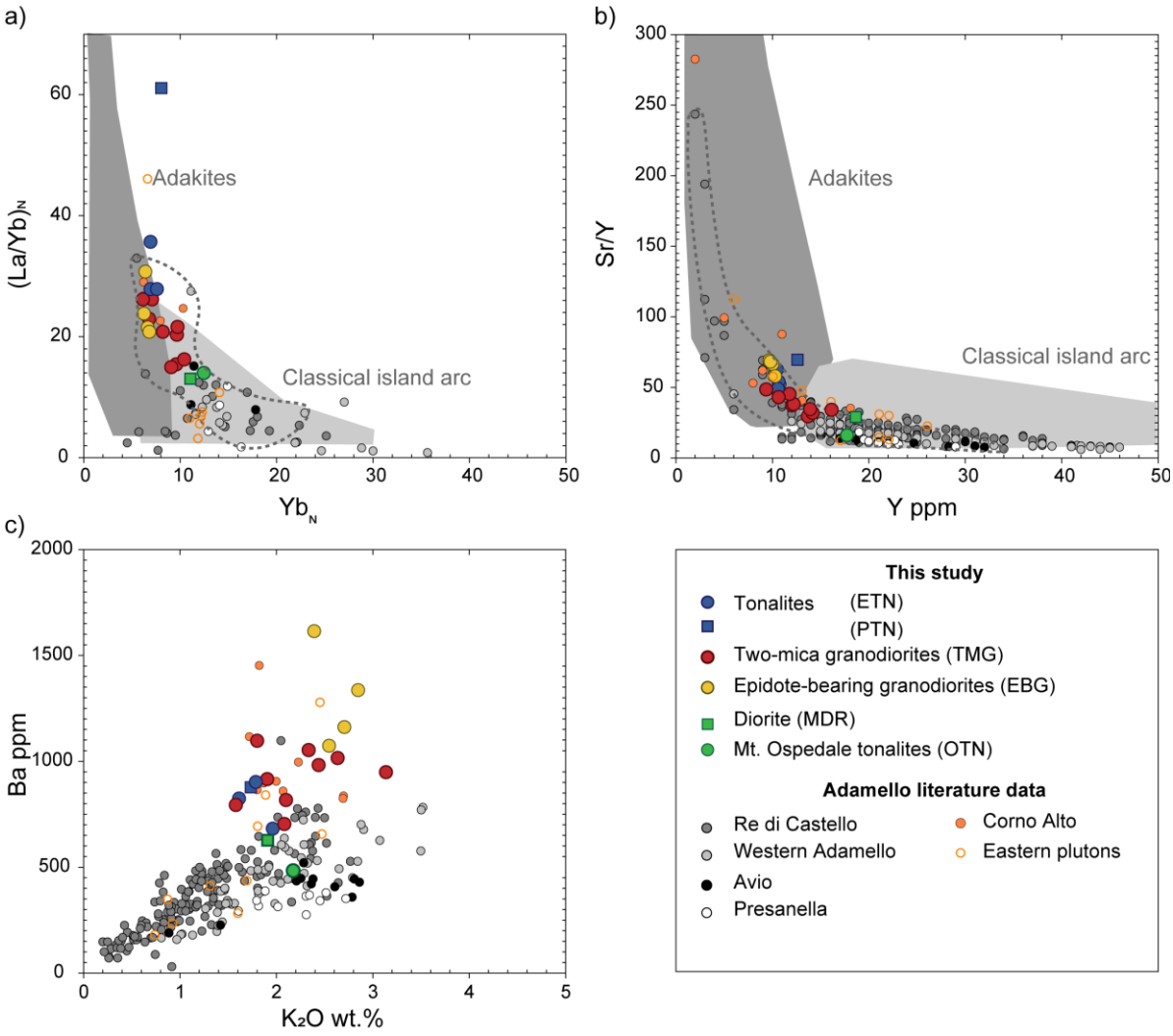

Figure 4.15 Chondrite normalized (McDonough and Sun, 1995) $(La/Yb)_N$ vs. Yb_N (a) and Sr/Y vs. Y (ppm) (b) diagrams for the Corno Alto granitoids compared with classical island arc (light grey, Martin, 1999) and adakite fields (dark grey, Defant and Drummond, 1990); c) Ba (ppm) vs K_2O (wt.%) diagram showing the Ba-K decoupling for the Corno Alto rocks compared to literature data from the Adamello (Dupuy et al., (1982), Macera et al., (1983); Kagami et al., (1991), Blundy & Sparks, (1992); Ji et al., (2019); Relvini et al., 2022).

contents (≈1900 and 1100 ppm, respectively) shown by the Corno Alto suite is not properly consistent with adakites but more closely resemble the geochemical signature of a particular group of Phanerozoic rocks called 'high Ba-Sr granites' (Fowler and Rollinson, 2012).

A key aspect in the interpretation of the high Ba (-Sr) signature of the Corno Alto rocks is relative to the discussion of the mechanism responsible for the decoupling between Ba and K. In fact, Corno Alto rocks have higher Ba concentrations at any given K content with respect to all the other Adamello rocks (Fig. 4.15c). Fractional crystallisation of plagioclase and/or biotite, which are the main rock-forming minerals in the studied rocks, does not account for the Ba-K decoupling indicating that an external source for Ba (and Sr) enrichment is thus required. Relvini et al. (2022) suggested an input from anatectic melts from metapelites in the lower crust, but

also in this case, the main hosts for Sr and Ba in the middle-lower crust are plagioclase and biotite, respectively.

During partial melting the effect of biotite destabilization lead to the enrichment in the melt of both K and Ba instead of causing their decoupling. We also exclude that shallow level crustal contamination is responsible for the high Sr, Ba and La/Yb ratios of the Corno Alto rocks. The low-grade Variscan basement (Rendena Schists) hosting the Corno Alto intrusion does not show high Ba contents (Bigazzi et al., 1986) and is also not characterised by high La/Yb ratios. The Ba (and Sr) enrichment relative to K is likely a primary feature of the parental melt inherited from the source.

Partial melting of a metasomatized phlogopite-bearing mantle wedge (e.g., Finero phlogopite-peridotite; Zanetti et al., (1999) would generate Ba and K-rich melts. The K and Ba decoupling is accomplished only by involving minerals strongly discriminating elements by charge, i.e., capable of preferentially accept large 2+ cations (e.g., Ba^{2+} and Sr^{2+}) rather than 1+ cations (e.g. K^{+}) such as carbonates or sulphates. Pelagic sediments were reported to be possibly extremely rich in Ba and Sr and also LREE-enriched (e.g., Fowler et al., 2008; Plank and Langmuir, 1998). Barium and Sr in pelagic sediments are notably linked to biological productivity (i.e., barite precipitation) and biogenic phases (i.e., Sr in biogenic carbonates). Strontium is particularly abundant in Cenozoic carbonate oozes (up to 1500-2000 ppm) while it is relatively low in average shales (150-200 ppm). High Ba concentrations characterize proximal hydrothermal sediments where barite is commonly present, and in sediments related to high biological productivity which contain barite in association with organic matter and siliceous plankton (Plank, 2014).

In Fig. 4.16a the Ba-Sr composition of the Corno Alto rocks is plotted together with bulk estimates for several key drilled sections of present-day near deep-trenches from all around the world (Columbia, Kermadec, Katchatka, Aleutians, Sandwich, Ryuku, Marianas), composed of different proportions of the diverse sedimentary constituents (Plank, 2014). The Corno Alto rocks follow a trend pointing to the composition of the entirely carbonatic Columbia subducting trench, while they are highly different from the pelitic- and terrigenous-dominated subducting trenches (e.g., Aleutians, Kermadec, Sandwich). The Corno Alto rocks plot together with the Kermadec subducting sediment trench, which is composed of a high proportion of carbonatic material and whose proportion of the sedimentary constituents closely resemble that of the Penninic units of the Tauern Window in the Eastern Alps (Fig. 4.16b-1 and 4.16b-2; e.g. Kurz et al., 1998). All the above pieces of evidence strongly suggest that the Ba enrichment shown by the Corno Alto rocks is related to the involvement of a carbonate-rich component in the source, as expected for the sediments deposited on top of the Neo-Tethyan oceanic crust.

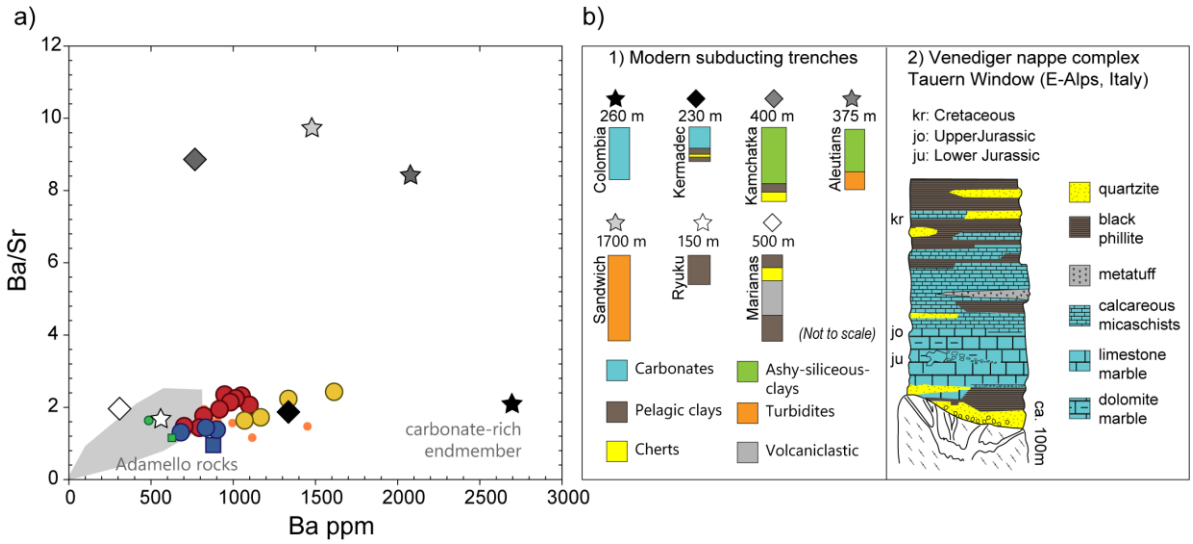

Figure 4.16 Ba/Sr ratio versus Ba ppm for the Corno Alto rocks and bulk estimates for some complete sections near deep-trenches from all around the world (data from Plank et al., 2014). Grey field reports the variability of other Adamello rocks; b-1) Summary lithology subducting at each considered trench modified from Plank et al. (2014); b-2) Representative stratigraphic section for the Tauern Window (modified after Kurz et al., 1998). Symbols are the same of Figure 4.15.

Experimental studies indicate that Ba (and Sr) are highly soluble in the fluid phase (e.g., Kessel et al., 2005) compared to REE that are more prone to be retained in the solid residue of the slab. However, it has been documented that the presence of Cl in the system enhance the mobility of several trace elements, including REE (Rustioni et al., 2021). In this frame, Cl-bearing aqueous fluids following dehydration of carbonate-rich slab-top sediments could operate the transfer from the slab to the mantle wedge. In the absence of halogens, REE transfer requires the involvement of silicate hydrous melts or supercritical fluids (Kessel et al., 2005; Fowler and Rollinson, 2012; Hermann et al., 2013; Hermann and Rubatto, 2009).

The juvenile component

Evidence for the occurrence of a more juvenile component into the petrogenesis of the Corno Alto rocks comes from trace element and in-situ-Hf isotopes. Zircon in the 44 Ma Sostino and ETN rocks are characterized by A-type textures and $\varepsilon Hf_{(t)}$ values close to +6 (±0.5 2SE).

Zircon grains in all the other lithologies reveal multiple domains with both A-type and B-type (Fig. 4.6). $\varepsilon Hf_{(t)}$ values in A-Type domains are identical to those observed in the older rocks. B-type domains instead possess highly positive $\varepsilon Hf_{(t)}$ values (up to +14), low incompatible elements concentrations (e.g., U, Nb, Ta) and a weak Eu anomaly, all features suggesting crystallisation from a juvenile melt whose $\varepsilon Hf_{(t)}$ is close to that of DM (Vervoort and Kemp, 2016).

Noticeably, B-type domains are always at the core of the crystals and show resorption boundaries. Some B-type domains yield dates clearly older than the rim (e.g., MDR sample), in other cases the difference in age is below the analytical capability of the applied technique. In any case, the resorption boundary characterising B-type domains is evidence for their xenocrystic origin (Fig. 4.10). We thus suggest that at 44 Ma mantle-derived melts with a $\varepsilon Hf_{(t)}$ signature close to MORB, crystallised at depth and were lately (42-39 Ma) cannibalised by the younger igneous pulses. This is also in agreement with our finding of corroded An_{90} domains at the core of more albitic plagioclase crystals. Noticeably this process was already reported in the evolved rocks of the Re di Castello unit (Blundy and Shimizu, 1991).

A-type domains, with high incompatible elements concentrations and deep negative Eu anomaly, likely crystallized from the same parental melt but after melt differentiation by fractional crystallization and assimilation of the shallow crust (e.g., Relvini et al., 2022) which is likely characterised by lower $\varepsilon Hf_{(t)}$.

4.9.4 Constraints on melt generation and geodynamic implications

The Corno Alto complex is the oldest intrusive igneous complex of the entire Alpine Orogen (Ji et al., 2019). Representing the onset of the Alpine Orogen igneous activity, the Corno Alto complex has particular importance in the interpretation of the geodynamic evolution of the Alps.

Many models were proposed to account for the long-lasting absence of magmatic activity during the Alpine Tethys subduction, whose beginning is approximately set at ~100–95 Ma (e.g., Dewey et al., 1989; Malusà et al. 2015; Agard, 2021, and reference therein). Most of these models agree on the absence of sufficient fluids to promote partial melting in the mantle wedge (Agard, 2021). This is consistent with the reconstructed cold path of Alpine subduction, very close to the so-called forbidden zone, as recorded by exhumed (U)HP rocks (Malusà et al. 2015). This evidence is reinforced by exhumed alpine high-P and ultrahigh-P metasedimentary rocks still retaining most of their volatile fraction (Busigny et al., 2003; Bebout et al., 2013; Garofalo, 2012). The onset of magmatism at 44 Ma, was likely triggered by the thermal perturbation induced by rising asthenospheric material along the slab tear located beneath the area encompassing the Adamello batholith, the Veneto Volcanic Province and the Giudicarie Fault, and was subsequently sustained by a corner flow of asthenospheric material during progressive slab steepening (Ji et al., 2019). Remarkably, Brombin et al., (2021) invoked a mechanism of asthenospheric poloidal flow to account for the middle Eocene magmatism in the Veneto Volcanic Province (VVP; NE Italy).

In this study, we showed that the parental melts of the Corno Alto complex record the presence of a component derived from the subducted carbonates, which is not occurring in all the younger units of the batholith. This evidence is essential in the interpretation of the evolution of the Alpine subduction because it implies a change with time in the sources activated for magma production. The loss of the carbonate input after 41 Ma may be accounted for by a change in the composition of the subducted material or, alternatively in the mechanism responsible for the element transfer from the slab to the mantle wedge.

The Alpine Tethys seafloor consisted of a complex assemblage of variably refertilized exhumed mantle rocks, irregularly distributed mafic magmatic rocks and pelagic sediments, together with ocean-continent transition lithosphere (OCT) domains and extensional allochthons (Malusà et al. 2018; Agard 2021). The slab compositional heterogeneities could therefore account for a sporadic carbonate input into the mantle wedge. However, the carbonate input does not recur in the younger units of the Adamello batholith as would be expected during the subduction of a compositionally heterogenous slab. Alternatively, being melt production very close to the onset of continental collision in the Central Alps after complete consumption of the Tethyan oceanic basin (e.g., Agard, 2021). Palinspastic reconstructions of the Alpine region consistently show that the inception of continental subduction migrated progressively from the Western to the Central Alps (Ford et al., 2006; Malusà et al., 2015), with the OCT lithosphere reaching the trench at ca 50-45 Ma (Malusà et al., 2018; Ji et al. 2019). Therefore, the formation of the Corno Alto marks may have taken place at the transition from oceanic subduction to the beginning of OCT subduction. In this scenario, the OCT subduction may lead to an increase in the terrigenous components in the subducting material, with this increase that should be clearly visible in the chemistry of the produced melts. A similar model was proposed by Tiepolo et al., (2014) that ascribed the difference in the chemistry between the amphibole-rich mafic rocks of the Adamello (Mt. Mattoni) and Bergell intrusions to differences in the composition of the subducting lithosphere. In particular, the enrichment in elements with high crustal affinity and the lower $\varepsilon Hf_{(t)}$ signature characterising the Bergell primary melts was related to the subduction of a thinned continental lithosphere. In the Adamello batholith the recognition of a terrigenous input in the source is difficult to assess mostly due to the superimposed effect of shallow level crustal contamination. Despite this limitation, we reckon that the similar Th/Nb ratio exhibited by these rocks of the Corno Alto system and younger Adamello units of similar composition suggests that no significant changes in the terrigenous input have occurred (Plank, 2005).

The carbonate input characterizing the Corno Alto rocks is likely a consequence of a mechanism of element transfer from the slab to the mantle wedge, active only at the onset of

the magmatism at 44 Ma. The thermal perturbation in response to the rise asthenospheric material was particularly important near the torn edge of the European slab where roughly the Corno Alto is located (Ji et al., 2019). Recent experiments revealed that under hydrous conditions temperatures in the range 850 – 900 °C at 4.2 – 6 GPa (pertaining to warm subduction thermal conditions; Syracuse et al., 2010), may enhance partial melting of the carbonate fraction (Schettino and Poli, 2020). We thus propose that the high thermal conditions, in response to the asthenosphere upwelling, locally induced partial melting of the carbonate fraction of the sediment cover of the slab. Low-degree melting of carbonated sediments of slab origin were documented to be responsible of the strong enrichment in LREE of the mantle under the north China Craton (Chen et al., 2017). Carbonate melting thus can account also for the relatively high La/Yb ratios characterizing the Corno Alto melts (Fig. 4.17). Interestingly, Zaccaria et al. (2021) found in the melt inclusions into zircon megacrysts of the middle Eocene VVP enrichments in BaO - SrO and evidence for S, and CO_2-rich fluids that were correlated to a source metasomatized by carbonatitic-kimberlitic liquids. The stringent analogy with the geochemical peculiarities found in the Corno Alto complex suggests a genetic link between the two complexes that is worth of detailed future investigations.

The high thermal conditions suitable for carbonate melting lasted approximately 5 Ma and were possibly at the origin of melts with adakitic signature reported in the Re di Castello unit (e.g., Tiepolo and Tribuzio, 2005). With the progressive lowering of the thermal conditions, slab dehydration become the dominant mechanism of element transfer from the slab to the mantle wedge. Being carbonate Hf-free, carbonate melting does not affect the $\varepsilon Hf_{(t)}$ signature of the mantle derived melts. We thus interpret the depleted $\varepsilon Hf_{(t)}$ signature found in the Corno Alto and approaching that of MORB (Vervoort et al., 2011), as reflecting the DM nature of the mantle source. Likely all the lower $\varepsilon Hf_{(t)}$ values found in zircon of the evolved Corno Alto lithologies reflect at various extent shallow level crustal contamination. Noticeably, depleted $\varepsilon Hf_{(t)}$ signatures also characterise zircons from the slightly younger products (39-41 Ma) of the southern Adamello (Ji et al., 2019; Schaltegger et al., 2019; Tiepolo et al., 2011), implying that no significant changes in the mantle source region have occurred. A larger scale mantle source homogeneity is also testified by the occurrence of a DM signature in the igneous products of the VVP (Beccaluva et al., 2007; Bianchini et al., 2008) and interpreted as the mantle signature prior the subduction-related metasomatism (Brombin et al., 2019). This is further evidence for common inputs of deep asthenospheric mantle material in the source regions of the oldest Adamello products and the VVP (Fig. 4.17).

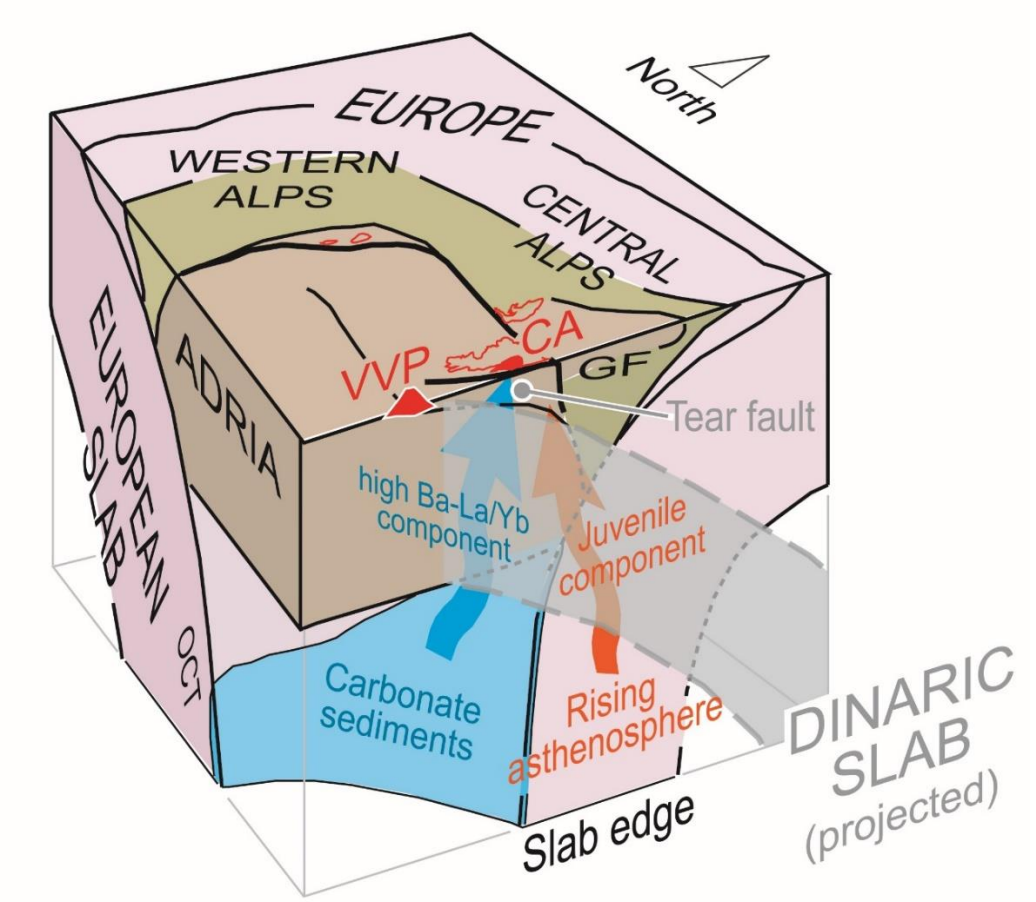

Figure 4.17 Modified from Ji et al., (2019). 3-D model showing the proposed relationships between slab steepening and Corno Alto magmatism (CA) in the absence of slab breakoff. The model highlight the influx of the high Ba-La/Yb component deriving from subducted carbonate sediments. Projection of the Veneto Volcanic Province (VVP) is also shown (see text for details).

4.10 Conclusions

A pervasive geochemical study of the Corno Alto complex has been carried out. Three distinct types of granitoid rocks have been recognized. The composition of the rocks is granodioritic to tonalitic rather than trondhjemitic.

Their whole-rock chemistry is very peculiar, showing the coexistence of at least two geochemically distinct components: i) a high Ba component characterised by high Sr and La/Yb ratios, likely derived from melting of carbonated sediments of slab origin; and ii) a juvenile component, interpreted as the mantle signature survived from the subduction-related metasomatism.

Moreover, the assembly occurred by multiple magma injections in a relatively large time span of about ~5 Myr evidencing a EW-ward migration of the igneous activity perpendicular to the strike of the subducted slab, interpreted as a consequence of the progressive steepening of the subducted slab.

Chapter 5
Constraints on the assembly of the Corno Alto complex based on plagioclase geochemistry

5.1 Introduction

The Corno Alto complex represents the oldest and most differentiated product related to the Adamello batholith (see Chapter 4). Its crucial role in understanding the petrological processes occurring during the early stages of Alpine magmatism is clear and dealt with in Chapter 4.

Despite its key role, the Corno Alto complex represents one of the least studied areas of the Adamello batholith. The extreme gradualness of the lithological transitions and the pervasive vegetation prevented the realization of a geological map with a detail greater than 1: 50.000. Moreover, the lack of mafic rocks in the Corno Alto complex made it a less attractive case study than others, for example, the Re di Castello unit, in which the entire succession of ultramafic-gabbroic to tonalitic-trondhjemitic rocks crops out (Ulmer et al., 1983). Indeed, the less evolved igneous products are more representative of the magma prior to differentiation, and thus more useful to constrain mantle sources and geodynamic processes at the origin of their activation. Granitoids are on the contrary the results of more complex igneous evolution and are less informative on mantle sources.

Minerals regularly used for petrological modelling are those capable of hosting many petrologically useful trace elements and those allowing pressure, temperature and oxygen fugacity calculations. Amphibole, which is ubiquitously present in the rest of the Adamello batholith and that was extensively used for petrological modelling (e.g., Tiepolo et al., 2001; 2011; Skopelitis, 2014; PhD Thesis) is, however, missing in the Corno Alto rocks. The shortage of mineral phases composing the Corno Alto rocks imposed a shift on other phases, such as plagioclase which is the dominant component in these rocks and shows a bewildering range of forms and patterns.

Indeed, zoned plagioclase crystals are petrographically endemic in all granitoid types and exhibit signs of relic cores, resorption, and recrystallization, indicating the existence of multiple populations and pointing to conditions of intense chemical disequilibrium.

Moreover, the peculiar Sr- and Ba-enrichment documented in these rocks (as described in Chapter 4) could be better understood by investigating the minerals that host both these elements, such as plagioclase.

Plagioclase feldspar is the most common mineral in the continental crust. Its ubiquity in igneous rocks is due to the extended temperature and compositional stability field during igneous differentiation (Ginibre et al., 2002). Plagioclase feldspars can serve as a recorder of chemical and physical changes occurring in the magma chamber during its formation (Blundy and Wood, 1991; Davidson & Tepley, 1997), and thus, help to identify processes such as magma evolution, replenishment, mixing and crystal cycling. This information is precisely provided by zoning textures, namely the expression of compositional variability within a single crystal (Streck, 2008).

The major element composition of plagioclase is influenced by multiple factors: temperature, pressure, the composition of the melt and the water content of the system (Ginibre et al., 2002). Hereafter is a short summary:

* at constant H_2O content and P, the An content decreases as melt differentiation progresses and the T drops;
* at constant T and water-saturated conditions, the effect of higher pressure is an increase in plagioclase stability tending to more sodic compositions;
* if the melt is water-undersaturated, a decrease of P will cause the dissolution of plagioclase, resulting also in a more calcic composition (Nelson and Montana, 1992);
* in water-saturated conditions, a decrease in pressure will cause degassing and decompression-induced crystallization of sodic plagioclase (Blundy and Cashman, 2005).

In the last decades, technological improvements have provided the opportunity to analyze isotopic compositions at the grain and sub-grain scale (Davidson et al., 2007), allowing the integration petrographic observations, geochemical compositions and isotopic tracing. Indeed, it is now widely demonstrated that mineral phases in volcanic rocks are generally not in isotopic equilibrium with their host groundmass (Davidson et al., 2007), and primary isotopic heterogeneity at the grain- and sub-grain scale is commonplace.

Two assumptions are fundamental in understanding why integrating in-situ isotope analysis is one of the definitive ways to explore crystal origins:

* a crystal growing from a magma has the same isotopic composition as the host magma (Davidson et al., 2007; Davidson et al., 1998);

* changes in the isotopic composition of the magma will be recorded by the isotopic composition of the crystal layers that subsequently grow (Davidson et al., 2007; Davidson et al., 1998).

Moreover, the isotopic ratio is not affected by short-term fluctuation of the intensive parameters such as P, T, and H_2O, and therefore it is more sensitive to variations induced by a single changing parameter. As a result, the isotopic profiles from the core to the rim of these minerals provide a record of the magma's evolution from crystal nucleation to emplacement (Figure 5.1; Davidson et al., 2007).

Combining isotopic micro-sampling with petrographic and geochemical approaches is crucial to fully understanding magma evolution. The analysis of trace element profile across crystals growth zones allows us to link isotopic changes to events like recharge and mixing (testified by dissolution horizons and inclusion zones) and to determine the timescale of these processes (Davidson et al., 2007; Turner and Costa, 2007).

In Figure 5.1 (from Davidson et al., 2007) a schematic illustration explaining how isotope variations in single crystals might reflect magmatic evolution processes is reported. In the first case (A), a contaminated crustal magma, with a peculiar radiogenic Sr signature, is modified by multiple pulses of a more primitive magma, with a less radiogenic Sr signature. Here, each recharge event causes partial dissolution and subsequent regrowth of crystals from a new, progressively more primitive hybrid composition.

In scenario B, the composition of the magma is changing as more primitive, less radiogenic, recharge liquid is mixed in. The crystal similarly displays continuous zoning, reflecting growth during the mixing process (compared to the more abrupt disequilibrium and re-equilibration growth scenario in scenario A). Scenario C represents the opposite situation of B, where a magma progressively changes its composition by mixing with a more radiogenic crustal contaminant. The crystal is continuously zoned as in B but in the opposite sense. Scenario D represents crystal transfer among distinct magma storage systems with different isotopic compositions. In this case, the association of zoning and dissolution (as in scenario A) is contingent on the degree of thermal and compositional (including water) disequilibrium among the magmas. In scenario E, crystals are transferred among different sites of a single isotopically zoned magma. Scenario F represents the formation of crystals at a boundary layer with changes in the amount of contaminants (and likely composition) through time. This situation is likely possible at a small scale in any of the previous magma systems and produces an early-formed crystal with a core composition similar to that of the contaminant, and a smaller later-formed

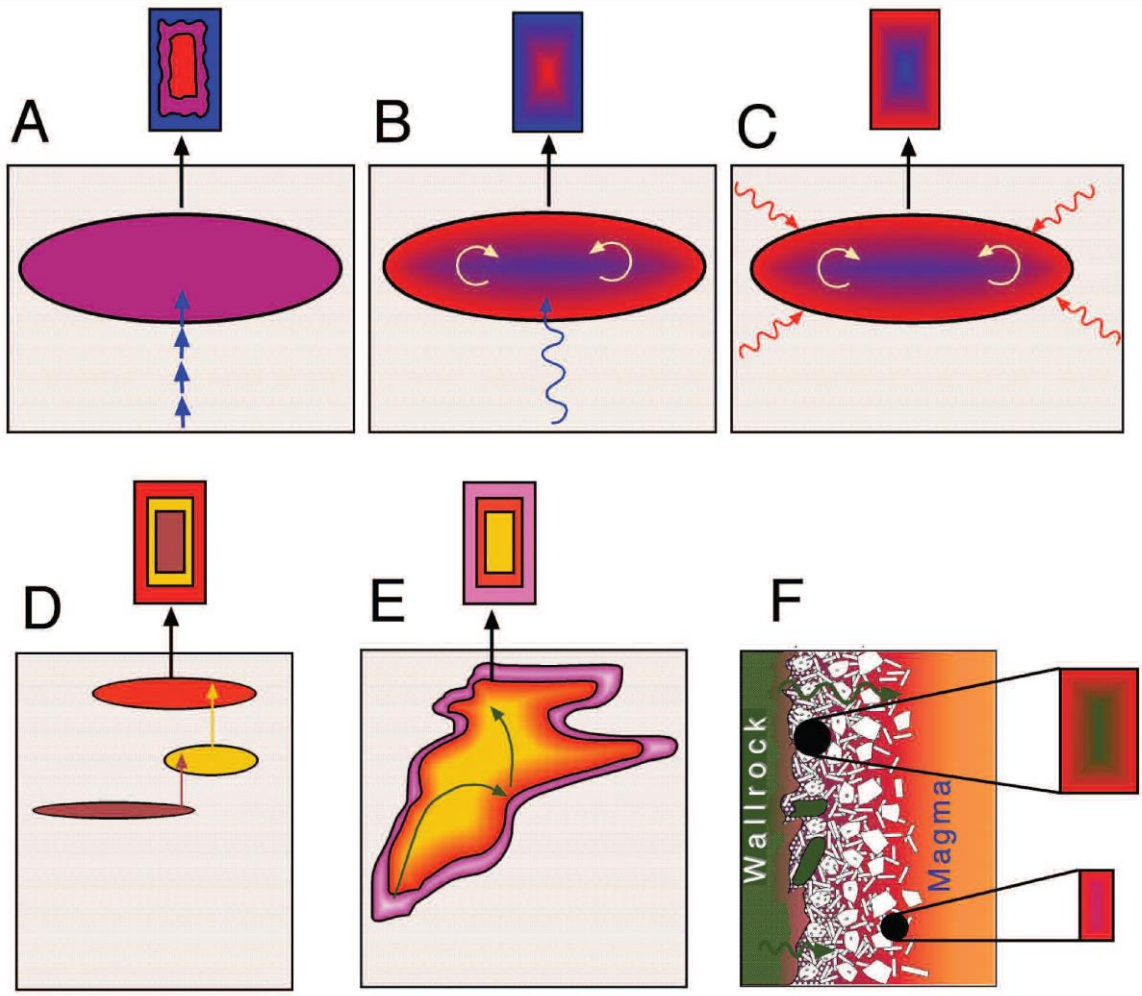

Figure 5.1 After Davidson et al., (2007). A schematic illustration showing how variations in isotopes within individual crystals might reflect magmatic evolution processes. Colour variations symbolize isotopic compositional variations, with the compositional variations in schematic crystals corresponding to the colours in the underlying cartoon representation of magma systems.

crystal that preserves a less extended evolutionary history due to its greater isolation from the wall-rock contaminant.

Short review of plagioclase zoning patterns and micro-structures

Given the huge variety of possible textures for plagioclase, there is also much confusion about the appropriate terminology that has to be used. For this reason, a brief description of the possible zoning patterns and micro-textures is essential. Plagioclases generally show one of the zoning patterns described in detail by Streck (2008) and resumed in the following lines and Figure 5.2. These are simply textural distinctions even if they vaguely match with a compositional classification (Blundy and Shimizu, 1991).

* Normal zoning and reverse zoning (Fig. 5.2 a-b) Normal zoning consists of compositional changes in the crystal from core to rim. This variation reflects the

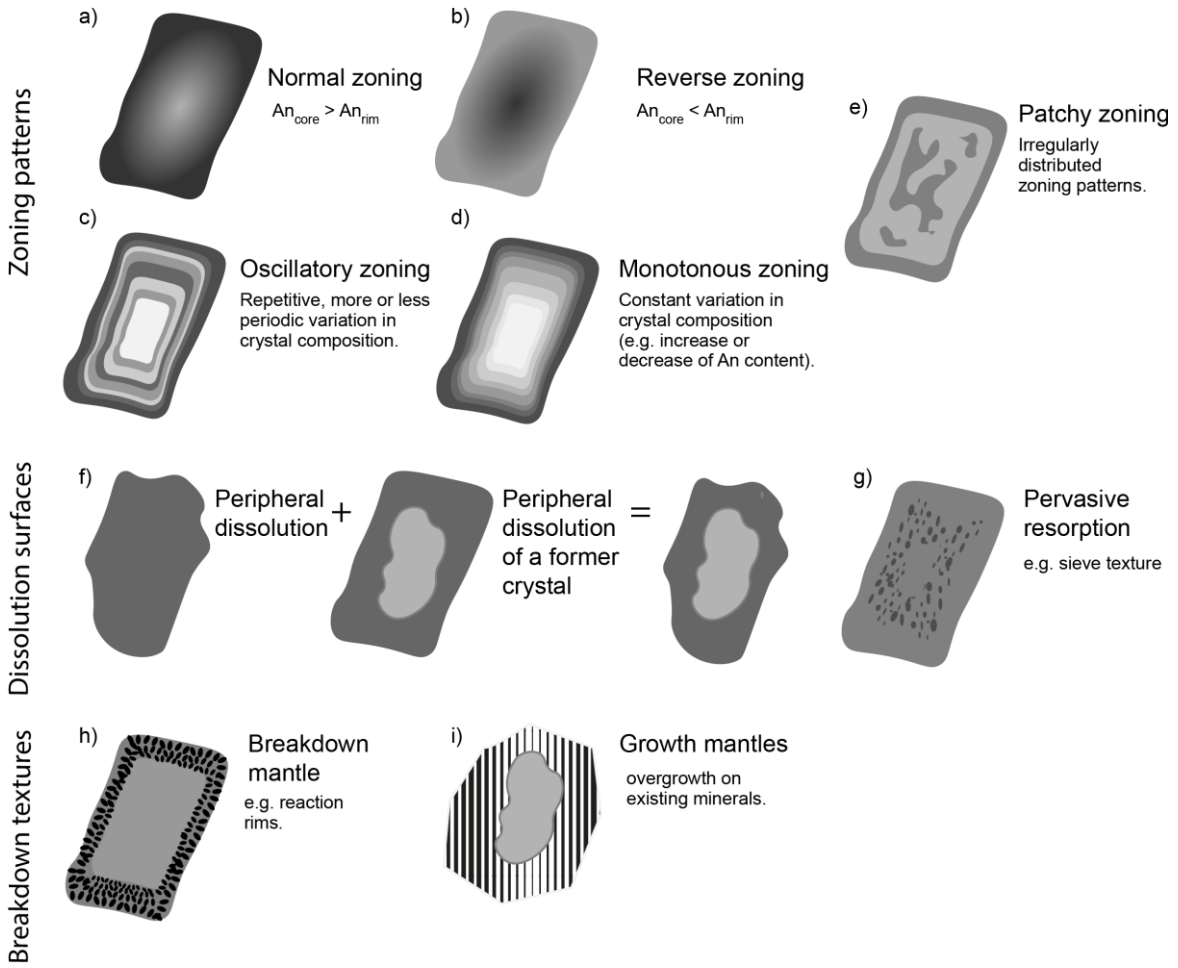

Figure 5.2 Sketches of plagioclase textures typically found in igneous rocks.

progressively evolving composition of the melt as it follows a liquid line of descent during cooling, resulting in a monotonic decrease in An from core to rim. Thereby, normal zoning is related to magma evolution by crystallization and may not be related to additional differentiation processes (Ginibre et al., 2002). Reverse zoning, on the other hand, indicates the increasing An content towards the rim of a crystal, indicating growth from a more calcic melt. This may be due to the addition of a more mafic melt or increased temperature or pressure under water-saturated conditions. Correlating changes in An content with minor or trace elements (Ruprecht and Wörner, 2007) or isotopic composition (Tepley et al., 2000) may help in differentiating between options.

* *Oscillatory zoning* and *monotonous zoning* (Fig. 5.2 c-d). Oscillatory zoning indicates repetitive, more or less periodic variation in crystal composition. This results in concentric growth zones from a few tens of microns in width (Ginibre et al., 2002). On the contrary, monotonous zoning indicates a constant increase or decrease of An content. The occurrence of oscillatory rather than monotonous zoning may be directly

related to the growth conditions. Based on the observation of experimentally produced plagioclase, the development of oscillatory zoning is favoured by slow growth rates of 10^{-11} to 10^{-13} m/s (Shore and Fowler, 1996). Monotonous zoning may appear instead from faster growth rates. Moreover, monotonous zoning can be related to latent heat release during crystal growth (Blundy et al., 2006), convective process in a magma chamber (Tepley III et al., 1999), crystallization and fluctuation in X_{H2O} causing an increase in overpressure or decompression driven crystallization during ascent (Smith et al., 2009; Humprhreys et al., 2006).

* *Patchy zoning* and *concentric zoning* (Fig. 5.2 e). Patchy zoning indicates irregularly distributed zoning patterns (Vance, 1962). This term is used in opposition to concentric zoning and it is difficult to associate with "normal" or "reverse" zoning. Such zoning has been the focus of much debate, being sometimes interpreted as a growth feature. According to Ginibre et al. (2002), patchy zones are more likely the results of resorption-regrowth events where the earlier grown inner zone remains as irregular patches and is overgrown by calcic plagioclase that forms during the dissolution.

In addition, some crystal textures may overlay zonations. These are primarily:

* *Dissolution surface* and *pervasive resorption* (Fig. 5.2 f-g). Resorption processes result in the removal of previously crystallized material. This can occur as peripheral dissolution forming strongly rounded or embayed crystals or only subtle rounding of edges. Alternatively, pervasive resorption may result in a porous, cellular mineral structure with varying appearances (e.g. sieve texture, dusty texture and so on; Streck, 2008).

* *Breakdown mantle (reaction rim)* and *growth mantle* (Fig. 5.2 g-h). Breakdown textures occur when an existing mineral becomes unstable and starts to recrystallize into a new set of minerals, rather than dissolving (Rutherford and Hill, 1993). These textures can either be limited to the rim areas of crystals, producing reaction rims or affect the entire crystals, resulting in pseudomorphs. In contrast, overgrowths on existing minerals are called growth mantles and may occur when nucleation on pre-existing minerals is more energetically favourable than nucleating new crystals.

Single plagioclase crystals often exhibit a multi-stage growth and resorption history, leading to a complex array of textures and compositions.

Previous studies on plagioclase crystals of the Adamello batholith

Blundy and Schimizu (1991) studied the trace element zoning in plagioclase feldspars from different rock types, ranging from hornblende-gabbros to diorites, tonalites and granodiorites, within the Val Fredda Complex. The analyzed plagioclases displayed a wide range of zoning textures (Fig. 5.3), accompanied by significant variations in both anorthite content and trace elements, particularly Sr and Ba, regardless of the host-rock composition.

In particular, individual plagioclase crystals preserving calcic-cores (An >80 mol%) overgrown by sodic rims were found ubiquitously also in the high-SiO_2 rocks. The authors attributed the major and trace element zonation mainly to a compositional variation in the coexisting melt, rather than changes in pressure or temperature alone. They identified a two-stage crystallization history consistent with (i) the early crystallization of the calcic plagioclase in a common magma chamber at 6-10 kbar and followed by (ii) re-entrain of the cumulus crystals into more evolved magmas crystallising at the emplacement level (1-5 kbar). The recycling of deeper dense calcic cores within the derivative felsic magma occurred on a relatively short time scale suggesting vigorous convection as the pivotal mechanism.

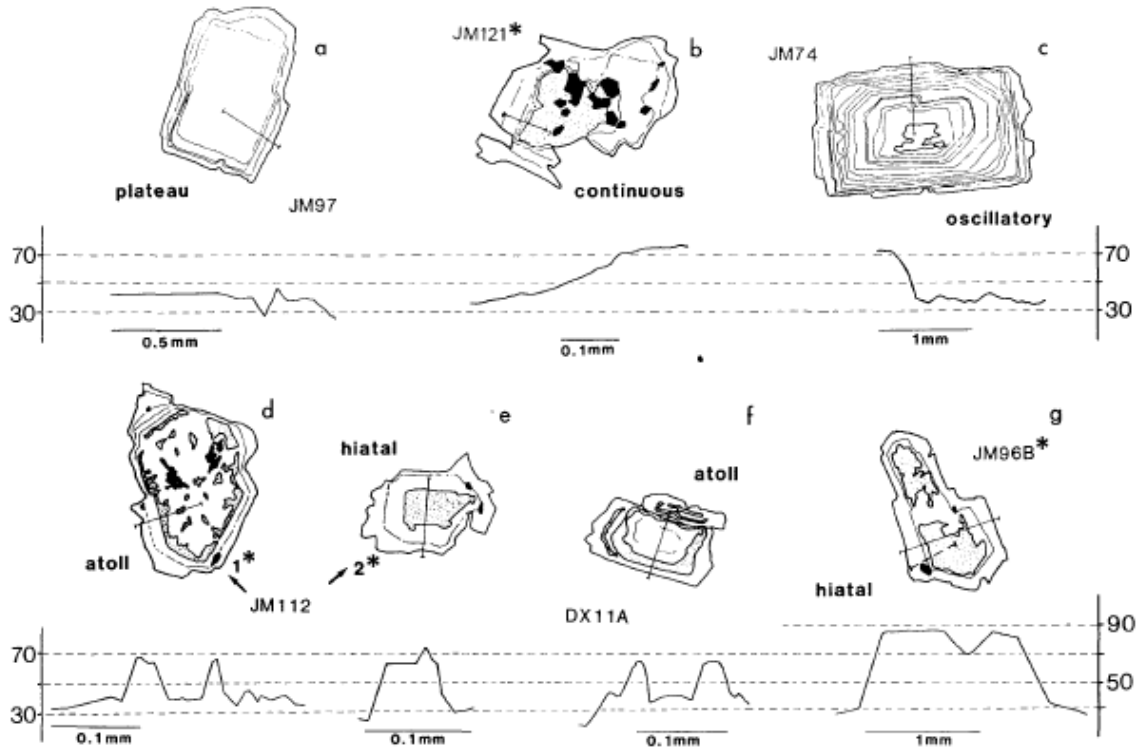

Figure 5.3 Modified from Bludy and Schimizu (1991). Sketches representing the textural types and Anorthite zoning patterns of the Val Fredda plagioclase.

Objectives of this study

The Corno Alto granodiorites and tonalites contain complexly zoned plagioclases similar to those observed in the Re di Castello rocks by Blundy and Schimizu (1991).

To determine the origin of zoned plagioclases, and in particular, for tracing contributions of possible distinct sources, the Sr isotopic composition across plagioclase traverses has been analyzed using LA-MC-ICP-MS. Major and trace element zoning patterns were also determined.

Moreover, plagioclase crystals from the Cornone di Blumone olivine-gabbros (Re di Castello unit, southern Adamello) were analyzed as representative of possible primary melt. These are characterized by unzoned plagioclases showing high-An content, in accordance with the early crystallization of plagioclase relative to amphibole (Tiepolo et al., 2002). This latter is a unique feature that does not occur in the other Adamello mafic rocks (e.g. Val Fredda rocks analyzed by Blundy and Schimizu, 1991) and which is indicative of the extremely primitive nature of the Cornone di Blumone rocks. The approach of this study provides a unique opportunity to discriminate between closed- and open-system behaviour, which possibly involved crustal contamination, magma recharge and recycling of older cumulates.

5.2 Methods

5.2.1 Major and trace element composition of plagioclase

Plagioclase feldspars in thin sections were analyzed with an JEOL 8200 Super Probe at the University of Milan with the following analytical conditions: 15 kV acceleration voltage, counting times of 30 s on the peaks and 10 s on the backgrounds, 5 nA beam current and a defocused beam of 1 μm.

Trace element compositions were analyzed with LA ICP-MS at the University of Milan using an Analyte excite 193 nm ArF excimer laser coupled to iCAR-RQ. For each analyses point was used major element concentrations from EPMA as internal standards (Ca for feldspars). To reduce the data was used the GLITTER software (Griffin, W. L. 2008), with NIST 612 50 ppm as internal standard and theBCR-2g as quality controller. The laser beam was 2.5 J/cm^2. The spot size used was 65 μm. The relative accuracy for feldspars is less than 15% except for some elements such as Y, Zr.

5.2.2 Sr isotope determination by laser ablation MC-ICP-MS

In-situ Sr isotopes in plagioclase were determined via laser ablation (LA) multi collector (MC)-ICP-MS at the laboratory of Geochemistry, Geochronology, and Isotope Geology of the Earth Science Department of the University of Milano. The instrument couples a 193nm excimer laser

ablation microprobe, equipped with a double volume Helix cell (Analyte Excite from Teledyne Photo Machines), with a MC-ICP-MS Neptune *XR* (ThermoFisher) equipped with 9 Faraday Cup collectors with 10^{11} Ω amplifier resistors, high sensitivity X-and Jet-cones and Jet-pump interface.

The plagioclase $^{87}Sr/^{86}Sr$ ratio measured via *in-situ* LA-MC-ICP-MS typically differs from the true ratio due to a number of fractionation effects: i) the ^{87}Rb interference on mass ^{87}Sr that cannot be resolved with the mass resolving power (MRP) of the instrument; ii) the instrumental mass discrimination related to physical effects in the ICP torch and in the ionic path into the mass spectrometer; iii) the mass discrimination induced during laser sampling; iv) the interference of double charged Er and Yb ions on mass 87 and 86 and v) the interference of Kr on mass 84 and 86.

Interferences due to Kr on mass 82 and 83 were found to be negligible and thus not considered during data reduction. To correct for the ^{87}Rb interference on mass ^{87}Sr we used a peak-stripping approach. The signal of ^{87}Rb was calculated from the signal of ^{85}Rb, and then subtracted from the ^{87}(Rb + Sr) signal. The mass discrimination effect on the $^{87}Sr/^{86}Sr$ (the so-called β_{Sr}) was corrected with an exponential law approach starting from the measured $^{88}Sr/^{86}Sr$ ratio. To correct for the $^{85}Rb/^{87}Rb$ mass discrimination (the so-called β_{Rb}) we assumed that Rb and Sr have a similar behavior and derived the correction factor from the $^{88}Sr/^{86}Sr$ ratio, then corrected using an exponential law approach. Given the low abundance of Er and Yb in the measured plagioclases (at ppb level), the potential interferences from double charged ions were considered negligible. According to Zang et al. (2017), for HREE concentrations lower than 4 $\mu g/g^{-1}$ and (^{167}Er + ^{173}Yb)/^{86}Sr ratios lower than 0.025 the shift on the $^{87}Sr/^{86}Sr$ ratio is around 50 ppm.

Sample	$^{87}Sr/^{86}Sr$
SO5/1	0.703751 ± 15
SOX/1	0.704063 ± 16

Table 5.1 ID-TIMS data for the two *in-house* reference plagioclase

Sample SO5/1 was used for bracketing the unknown samples whereas sample SOX/1 was adopted as quality control. The analytical run consisted of four analyses of the reference plagioclase SO5/1 bracketing a maximum of 20 analyses of the unknowns. The calculated d-bias correction factor is the difference between the mean Rb-corrected $^{87}Sr/^{86}Sr$ measured ratio and the reference value. During our analytical runs, the d-bias values remained constant, thus no time dependence recalculation of the correction factors was required.

Ablation was carried out with a spot size of 85 μm and with the parameters reported in table 5.2. The signal of masses ^{82}Kr, ^{83}Kr, ^{84}Sr, ^{85}Rb, ^{86}Sr, $^{87}(Sr + Rb)$ and ^{88}Sr were acquired with the cup configuration reported in the Table 5.3. The mass spectrometer was tuned first with a standard 20 ppb solution of Sr (NBS 987) and then ablating the BCR-2G reference basaltic glass to maximize the signal intensity while monitoring the formation of double charged ions and oxide formation. Typical MC-ICP-MS conditions are reported in table 5.2. Each analysis consisted of acquisition of 30 seconds of background signal and 60 seconds of ablation signal.

MC-ICP-MS parameters	
ICP RF power	1200 W
Makeup gas	12 l/min
Auxiliary gas	0.9 l/min
Sample gas	1.2 l/min
Laser Ablation Microprobe parameters	
Laser wavelength	193 nm
Laser frequency	10 Hz
Laser Fluence	3 J/Cm^2
Cup gas flow	0.18-0.24 L/min
Cell gas flow	0.51 L/min

Table 5.2

L4	L3	L2	L1	C	H1	H2
^{82}Kr	^{83}Kr	^{84}Sr	^{85}Rb	^{86}Sr	^{87}Sr	^{88}Sr

Table 5.3

5.3 The Corno Alto plagioclase feldspars

A total of 4 thin sections (representative of each rock type) were observed under a polarizing microscope with special emphasis on micro-texture in plagioclase. Plagioclase crystal cargo of the Corno Alto rocks shows a wide range of morphologies, irrespectively from the rock type.

Most of the crystals show rounding of edges or embayed margins, evidence of external resorption (Fig. 5.4a). The largest crystals have a diameter of 1 cm. Individual crystals may also show internal domains characterized by rounded boundaries caused by former resorption events. These relict plagioclase crystals may also show cracks and fractures. In the PTN sample,

large individual plagioclase with prominent oscillatory zoning exhibit an external rim enriched with tiny quartz inclusions (Fig. 5.4b).

Subhedral to anhedral plagioclase crystals, joined along resorbed margins, compose monomineralic aggregates called g*lomerocrysts* (Bennett et al., 2019; Hogan, 1993; Renjith et al., 2014; Fig. 4c). Plagioclase crystals composing *glomerocrysts* often show more than one zoning type: e.g. polysynthetic twinning and oscillatory zoning. In places, compositional zoning may be truncated along the margins of the embayment. The interstices resulting from the misfit between adjacent plagioclase crystals are infilled by late crystallizing phases (e.g alkali-feldspar). Plagioclase fragments composing *glomerocrysts* are often altered in secondary minerals.

A total of thirteen crystals have been selected and described. Some plagioclase crystals composing *glomerocrysts* have been deconstructed and considered individually for analysis where feasible. The prerequisites for the selection were being unaltered and large enough to accommodate laser spot transects. Three plagioclase crystals from the two-mica granodiorites (TMG), two crystals from the equigranular tonalites (ETN), five crystals from the porphyric tonalites (PTN) and three crystals from the epidote-bearing granodiorites (EBG) were selected for the analysis. Four plagioclase crystals from a Cornone di Blumone gabbro (Re di Castello unit) were also analysed for comparison (Fig. 5.4d). The selected crystals were fully characterized for chemical composition and internal distribution. Back-scattered electron images (BSE) and compositional maps were carried out by EMPA whereas trace elements (Sr, Ba, LREEs and Pb) and Sr isotopes characterization were carried out by LA-ICP-MS and LA-MC-ICP-MS, respectively.

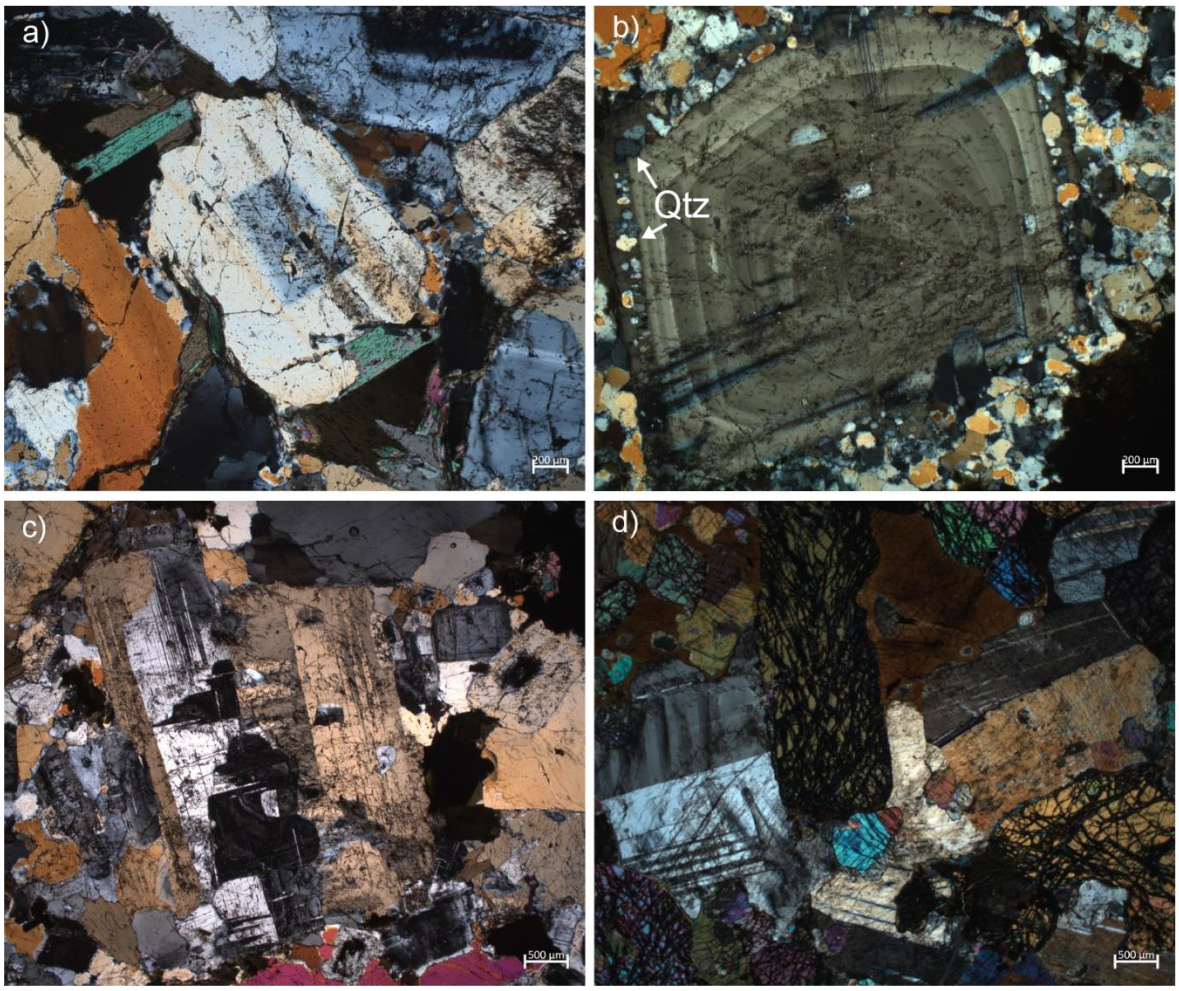

Figure 5.4 Representative plagioclase crystals in the Corno Alto and Blumone rocks. a) Single plagioclase crystal showing external resorption in a TMG rock; b) plagioclase glomerocryst in EBG rock; c) oscillatory zoned plagioclase with the external rim enriched with tiny quartz inclusions in PTN rocks; d) Unzoned subhedral plagioclase crystals in the Cornone di Blumone rocks.

5.3.1 Major and trace element compositions

Analysed crystals show a large range of An contents, ranging from almost albitic to bythownitic compositions. (Figure 5.5).

The two-mica granodiorites display the largest variations in An composition: overall, the An contents vary from An_{35-84} in correspondence of the cores and An_{14-46} at the rims. The Sr content ranges from 430 to 2500 ppm and shows a positive correlation with An (Fig. 5.6); Ba varies from 76 to 590 ppm and Pb content is between 9 and 60 ppm, both showing a negative correlation with An. $(La/Sm)_N$ ranges from 7 to 37 and Eu/Eu* from 3 to 12.

Plagioclase crystals from the equigranular tonalites (ETN) do not display significant An variations from core to rim. Sr displays a slight positive correlation with An, ranging from 960 to 1400 ppm. Ba and Pb are both negatively correlated with An and vary from 110 to 290 ppm and 20 to 60, respectively. Overall, $(La/Sm)_N$ ranges from 6 to 63 and Eu/Eu* from 6 to 14.

Porphyric tonalites (PTN) show a large variation in An composition, with the cores varying from An_{85} to An_{41} and the rim ranging from An_{65} to An_{23}. Sr content varies from 860 ppm and 4120 and shows a positive correlation with An. Ba and Pb vary respectively from 86 ppm to 400 and from 8 to 63 ppm, without showing a clear negative correlation with An. LREEs are variably enriched over MREE with $(La/Sm)_N$ ranging from 7 to 90, whereas Eu/Eu* varies from 3 to 20, both without clear distinctions from core to rim.

Plagioclases from the epidote-bearing granodiorites (EBG) are all normally zoned, with labradorite to andesine cores (An = 35-49) and oligoclase rims (An = 17-28). Sr shows a positive correlation with An and varies from 460 to 2440 ppm. Ba is highly variable (100-745 ppm) and is positively correlated with An (up to An values of 35 mol.%) and negatively correlated with An for compositions higher than An_{35}. Pb is negatively correlated with An and ranges from 10 to 70 ppm. $(La/Sm)_N$ range from 5 to 50 whereas Eu/Eu* is in the range 5-20.

Plagioclase crystals from the Cornone di Blumone gabbros have a homogeneous major and trace element composition. The An content is relatively high (~87) and Sr contents are up to 2570 ppm. All crystals have low Ba (80 ppm) and Pb (< 3 ppm) contents.

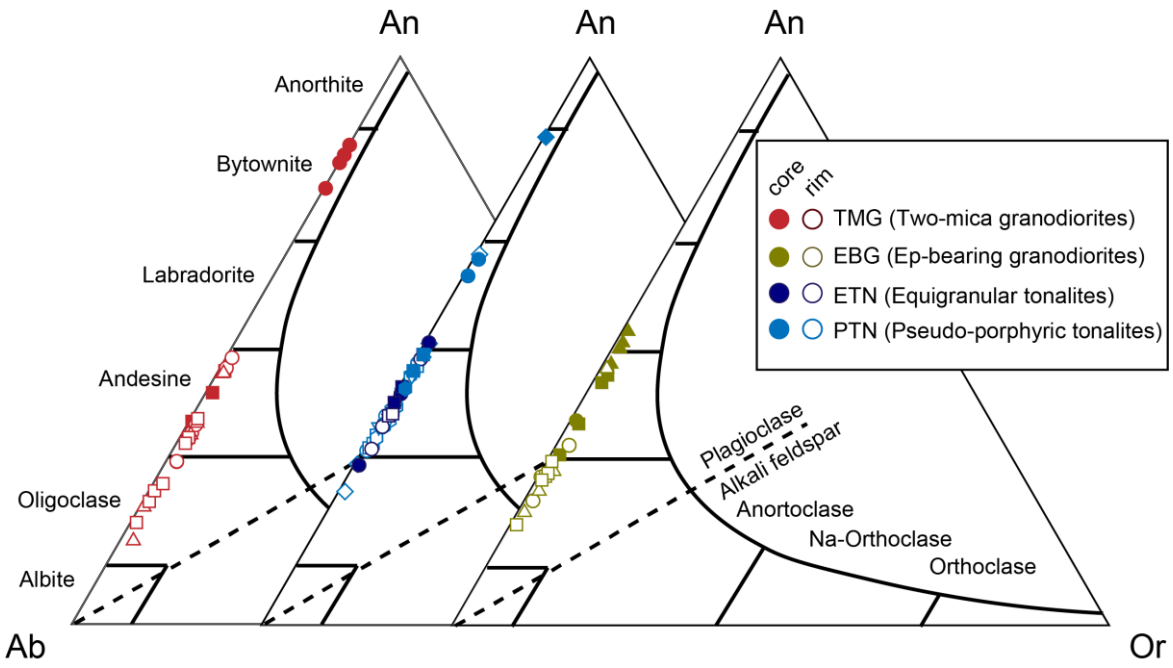

Figure 5.5 Anorthite-Albite-Orthoclase classification diagram for feldspars.

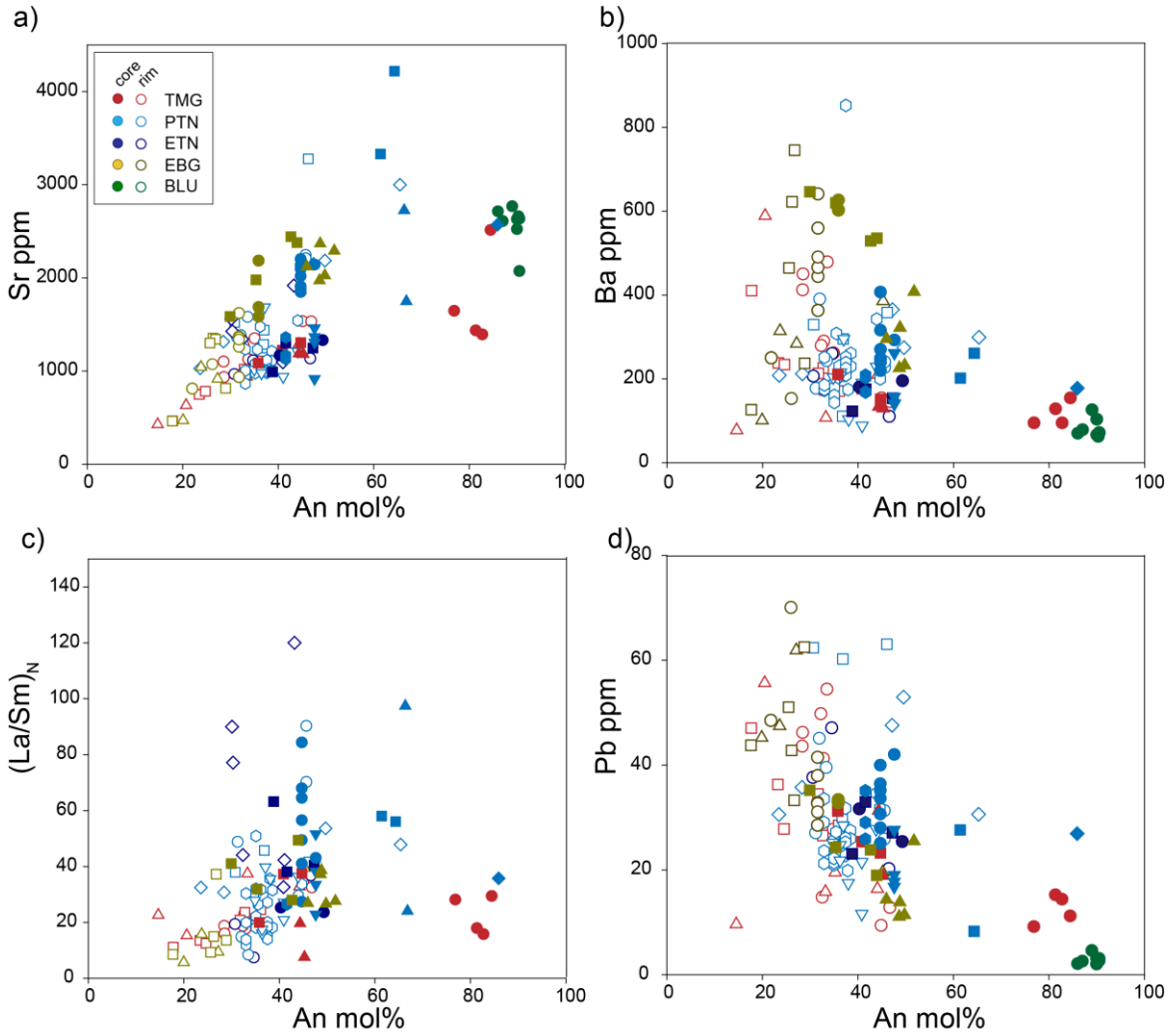

Figure 5.6 Binary diagrams of An content versus trace element compositions of the analyzed plagioclase crystals.

5.3.2 Sr isotopic variations

Six plagioclase crystals from four rock samples were chosen for Sr isotope analyses: crystal #1 from TMG; crystals #14, #29, #30, and #31 for PTN and crystal #20 for EBG. This selection was driven by the availability of space to accommodate the laser spot (80 μm), the textural variability and the lack of surface alteration and inclusions. A minimum of 4 to a maximum of 26 laser spots were carried out on the same crystal.

In-situ analyses of plagioclase in the four samples yield a range of the $^{87}Sr/^{86}Sr$ ratio of 0.7047-0.7065. Noticeably, the overall variability observed in the analysed crystals (0.0018) is significantly higher than the mean analytical uncertainty (± 0.00011).

Crystal #1 from TMG rocks shows an isotopic variability (0.7047-0.7061) encompassing almost the entire range observed in the plagioclase crystals of the whole Corno Alto complex (Fig.4.7a). Crystals showing the smallest intra-crystal range are #29 ($^{87}Sr/^{86}Sr$ = 0.7061-0.7064, #30 (0.7062-0.7065; difference = 0.0003) and #31 (0.7064-7065) from PTN. A small intra-sample variability is also shown by crystal #20 from EBG ($^{87}Sr/^{86}Sr$ = 0.7052-0.7060).

Plagioclase crystals from the Cornone di Blumone area (#41, #42, #43 and #44) have within error Sr radiogenic signature with a mean value of 0.7038 ±0.00009 (2se).

In general, the more calcic plagioclases are typically less radiogenic compared to the more sodic compositions (Figure. 5.7b). However, significantly different $^{87}Sr/^{86}Sr$ ratios may pertain to the same An content. This is especially evident in PTN samples. A rough negative correlation between Sr concentration and Sr radiogenic component is evident if the PTN samples are neglected (Fig. 5.7c). Ba shows a rough positive correlation with $^{87}Sr/^{86}Sr$ in plagioclase crystals from TMG and PTN rocks whereas a negative correlation is observed for plagioclase crystals of EBG rocks (Fig. 7.4d). $^{87}Sr/^{86}Sr$ ratios show a positive correlation with both the Pb contents and the La_N/Sm_N ratio in plagioclase which become more scattered with the increase in the radiogenic component (Fig. 5.7e-f).

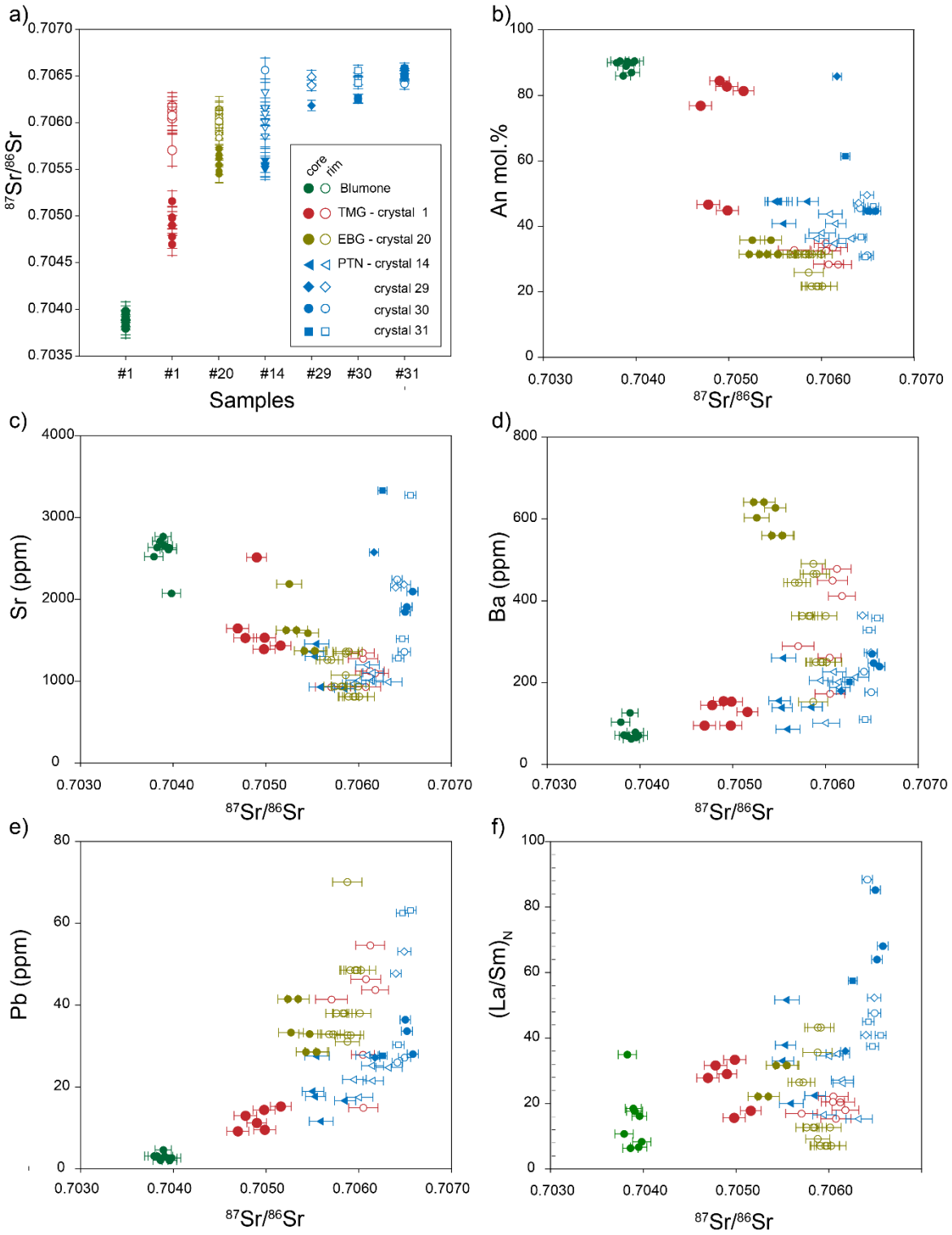

Figure 5.7 Relationship between elemental and isotopic Sr composition of the Corno Alto plagioclases.

5.4 Micro-chemical profiles across plagioclase crystals

5.4.1 TMG micro-chemical profiles

Crystal #1 has a diameter of ~5 mm and displays peripheral dissolution resulting in strongly embayed margins (Fig. 5.8). The core is cracked, with a resorption surface at the core-rim boundary and is extremely Ca-rich (up to An_{84}). The outer domain has a normal zonation with almost albitic composition (An_{14}) at the outermost margin. The Sr zoning pattern follows a similar trend: the highest contents are at the core (up to 2500 ppm) and the lowest at the rim (down to 928 ppm). Conversely, from core to rim, there is an overall increase of Ba (from 94 to 450 ppm) and Pb (9-55 ppm) with a sudden decrease in the outermost rim (down to 280 and 40 ppm, respectively). Crystal #1 also shows the highest intra-crystal isotopic heterogeneity, with a total $^{87}Sr/^{86}Sr$ variability between 0.7047 ± 0.0001 (2se) and 0.7061 ± 0.0001 (2se). The Sr isotopic profile is characterized by distinct domains across the crystal: the core has an average $^{87}Sr/^{86}Sr$ value of 0.7049 ± 0.00011 (2se) whereas the rims have significantly more radiogenic compositions with an average $^{87}Sr/^{86}Sr$ of 0.7060 ± 0.00015 (2se).

Crystal #3 has a diameter < 1.5 mm and shows only subtle rounding of edges. The internal part is fractured (Fig. 5.9). The crystal is normally zoned, with andesine core (An_{45}) and oligoclase rim (An_{14}). From core to rim, an overall decrease in Sr (from 1200 to 420 ppm) and an almost constant Ba content (~200 ppm) is observed. Similarly, Pb in both crystals does not show great fluctuation, averaging at 30 ppm.

Crystal #4 (diameter < 2mm) shows subtle external resorption (Fig. 5.9). It shows almost identical An, Sr, Ba and Pb compositions of crystal #3. The crystal is normally zoned with core up to An_{44} and rim down to An_{17}. Sr concentrations decrease from core to rim (1300-460 ppm), whereas Ba shows subtle reverse zoning (150-400 ppm). Pb zoning pattern shows constant values averaging at 30 ppm.

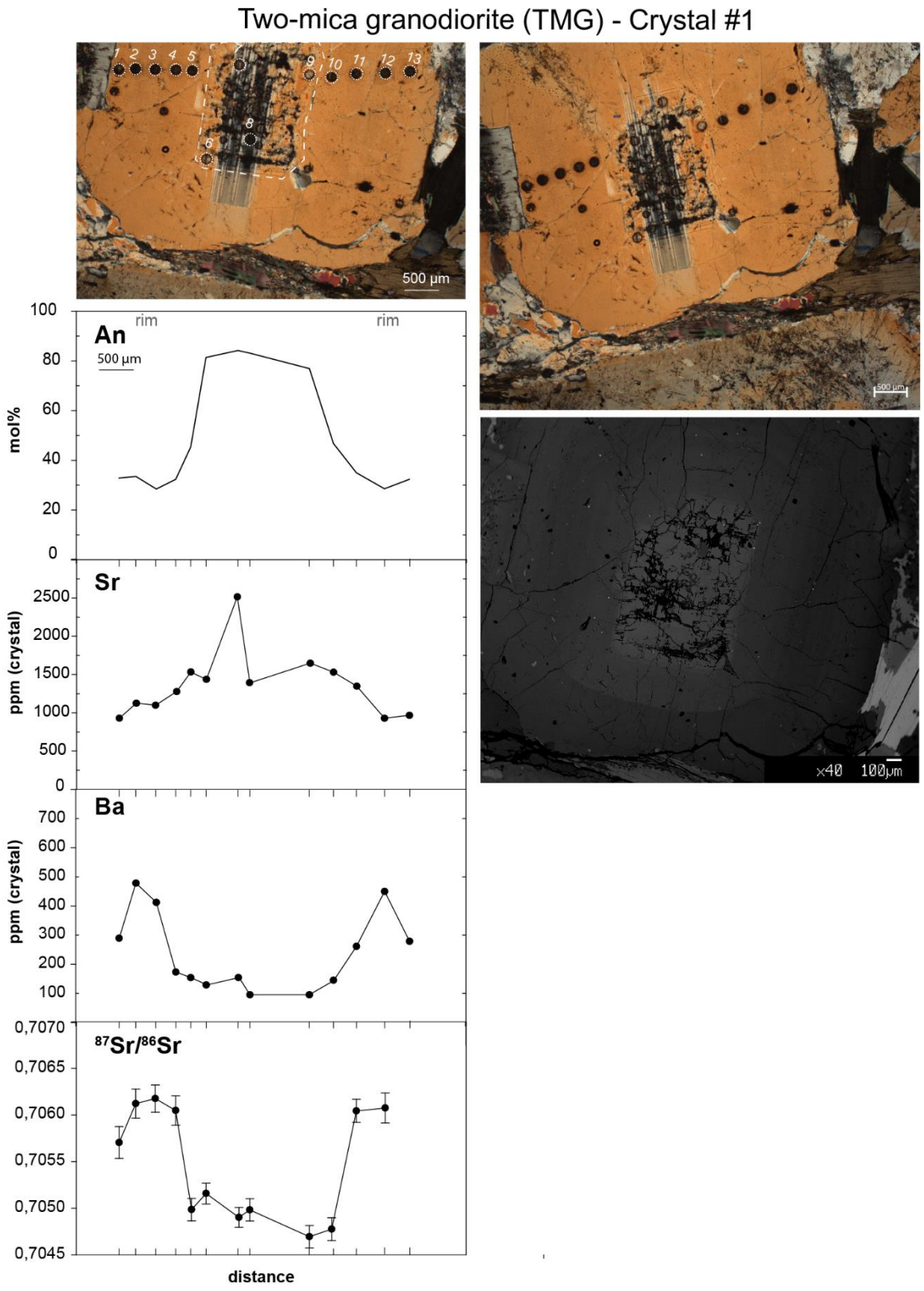

Figure 5.8 Traverse analyses from rim to core to rim of crystal #1 (TMG).

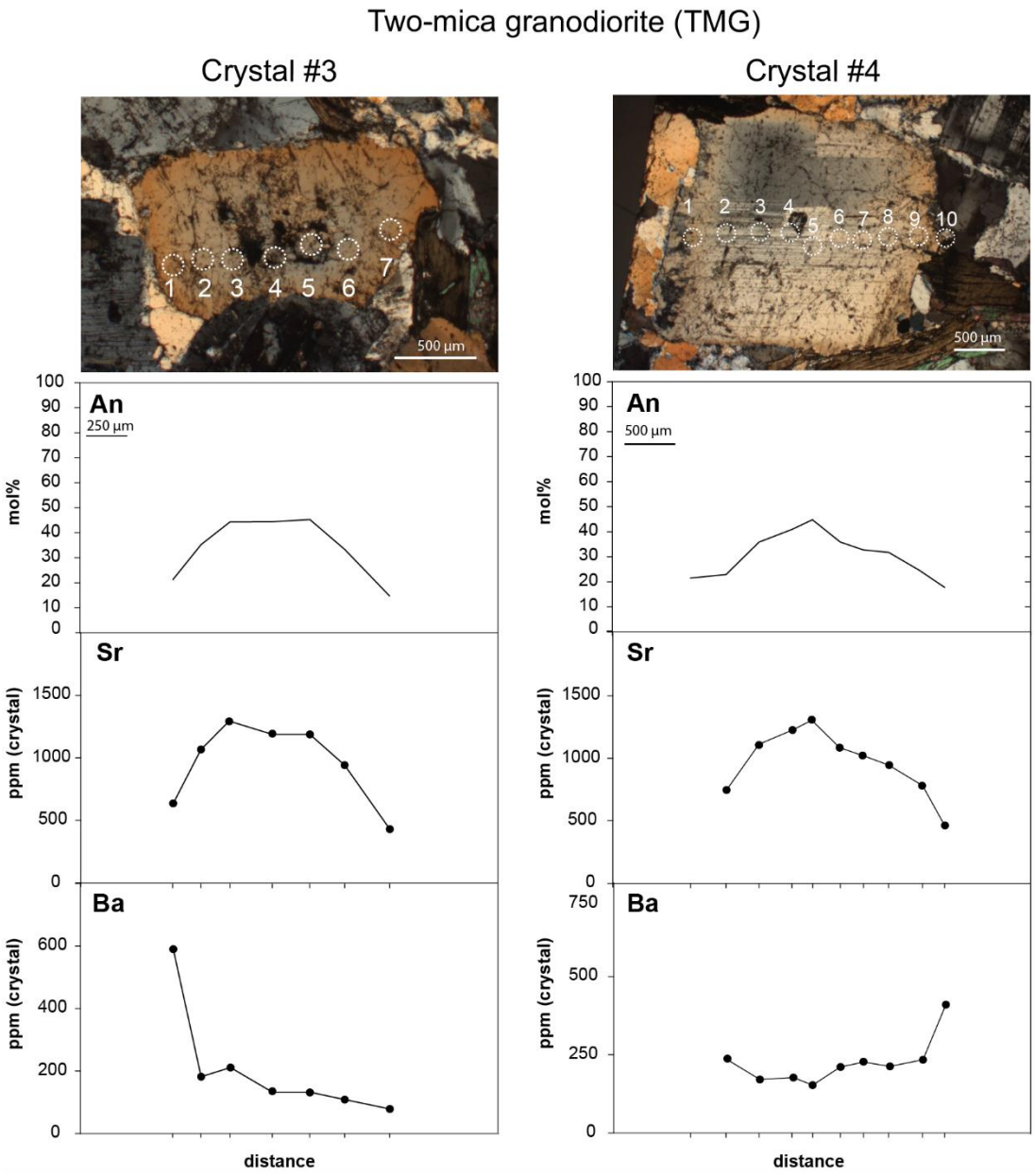

Figure 5.9 Traverse analyses from rim to core to rim of crystals #3 and #4 (TMG).

5.4.2 ETN micro-chemical profiles

Crystal #7 has a maximum diameter of 1 mm (Fig. 5.10). It shows partial peripheral resorption and fracturing in the inner zone. The An profile shows normal zoning, with core up to An_{49} and rim down to An_{36}. Sr shows a slight decrease from the core (1330 ppm) to the rim (960 ppm). Ba and Pb do not follow the same trend, displaying the lowest concentrations at the core (110 ppm and 20 ppm, respectively) and the highest at the rim (260 ppm and 47 ppm).

Crystal #8 has a diameter size < 1 mm (Fig. 5.10). The crystal is partially resorbed. Sieve texture and fracturing occur mainly in the inner zone. It shows slight normal zonation, with cores up to An_{47} in composition and rim down to An_{36}. Sr, Ba and Pb concentrations are slightly

lower at the core (990 ppm, 122 ppm and 23 ppm, respectively) than at the rim (1400 ppm, 294 ppm and 60 ppm).

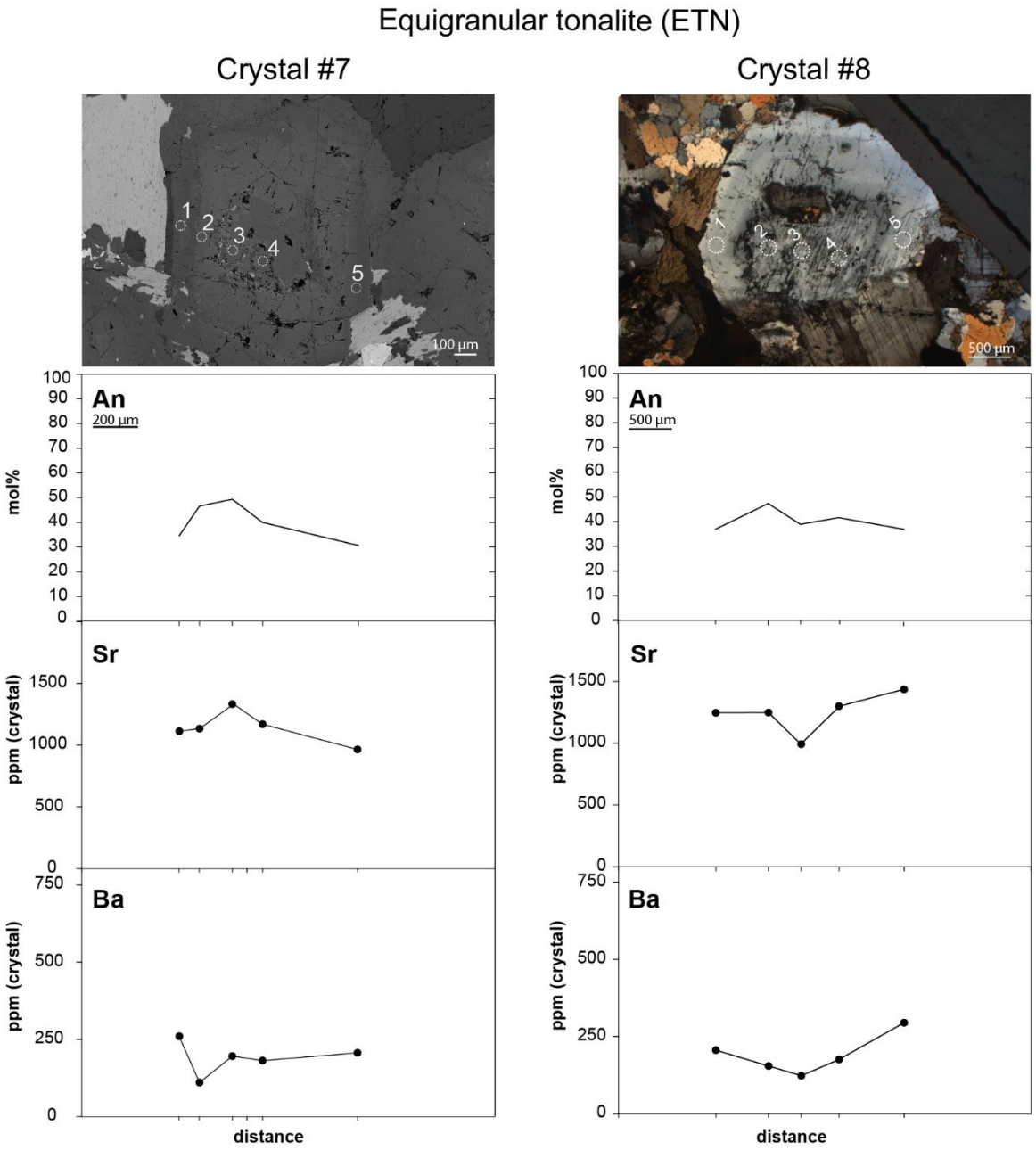

Figure 5.10 Traverse analyses from rim to core to rim of crystals #7 and #8 (ETN).

5.4.3 PTN micro-chemical profiles

Crystal #13 has a maximum diameter of ~0.6 cm (Fig. 5.11). It is characterized by an external band containing tiny quartz inclusions. The external band was not large enough to be analyzed for trace elements. Biotite inclusions also occur in the crystal. Crystal #13 has a core-mantle-rim oscillatory zoning pattern with An contents in the range of 44-32 mol%. The Sr zoning pattern parallel that of An, with a relatively high concentration at the core (up to 1360 ppm) followed by an oscillatory trend (with concentrations down to 860 ppm) and a final peak up to

1850 ppm towards the rim, before the sodic band. The Ba zoning pattern is likewise characterized by relatively high values at the core (up to 210 ppm), a weak oscillatory trend at the mantle and a subsequent increase at the rim (up to 340 ppm). Pb concentrations parallel the trend of Ba and range between 20 and 35 ppm.

Crystal #14 has a diameter of ~0.6 cm and shows prominent oscillatory zoning (visible in the compositional map in Fig. 5.11). It is characterized by a more calcic band followed by a sodic band rich in tiny quartz inclusions (Fig 5.4b). The sodic band has too many inclusions and was too small to accommodate the laser spots. The compositional map of Ca reveals inclusions of smaller, rounded, resorbed plagioclase crystals. It shows an andesine core (An_{47}), a decrease of the An component in the mantle of the crystal (down to An_{34}) and an increase in correspondence of the rim (An_{43}). Analogously, Sr, Ba and Pb show almost identical zoning patterns, with a high concentration at the core (respectively, 1450 ppm, 260 ppm and 27 ppm), a sudden decrease in the domain mantling the core (down to 910 ppm, 86 ppm and 12 ppm) and a final increase toward the rim (up to 1670 ppm for Sr, 290 ppm for Ba, and 27 for Pb). In crystal #14, the Sr isotopic composition at the core is 0.7055 ±0.0001 (2se) and at the rim 0.7065 ±0.0001 (2se). The core-to-rim transition is quite continuous and is devoid of abrupt variations.

Crystal #29 has a diameter of almost 1 mm. It is characterized by a Ca-rich core (light-grey in BSE image in Fig. 5.12) with tabular habit. The core does not show evidence of resorption surfaces against the mantle, although it locally shows alteration. External resorption and quartz inclusions occur. It shows a normal zonation of An with a bytownitic core (or atoll, with An ~ 85) and a oligoclase rim (An ~ 23). Sr concentrations parallel the An distribution, with the highest values at the core (up to ~3000 ppm) and the lowest at the rim (~1200 ppm). Ba and Pb do not follow the same trend, displaying the lowest concentrations at the core (down to ~180 ppm and ~25 ppm, respectively) followed by a sudden increase (up to ~360 ppm and ~50 ppm) and a final decrease at the rim (down to ~200 ppm for Sr and ~30 ppm for Pb). The Sr isotopic profile shows limited variability, with a $^{87}Sr/^{86}Sr$ composition of 0.7061 ± 0.0001 (2se) at the core and 0.7064 ± 0.0001 (2se) at the rim.

Crystal #30 has a diameter of approximately 0.5 mm and a tabular Ca-rich core (Fig. 5.13). Quartz inclusions occur in the external part. Crystal #30 shows normal An zonation with labradoritic core (An ~ 61-64) and the rim andesine (An ~ 30-46) in composition. It shows a very high Sr concentration at the core (up to 4210 ppm) and a decrease toward the rim (down to 1500 ppm). Ba and Pb show an inverse trend with respect to Sr and An (with Ba ranging from 110 ppm at the core and 360 ppm at the rim and Pb from 8 ppm to 60 ppm). The Sr

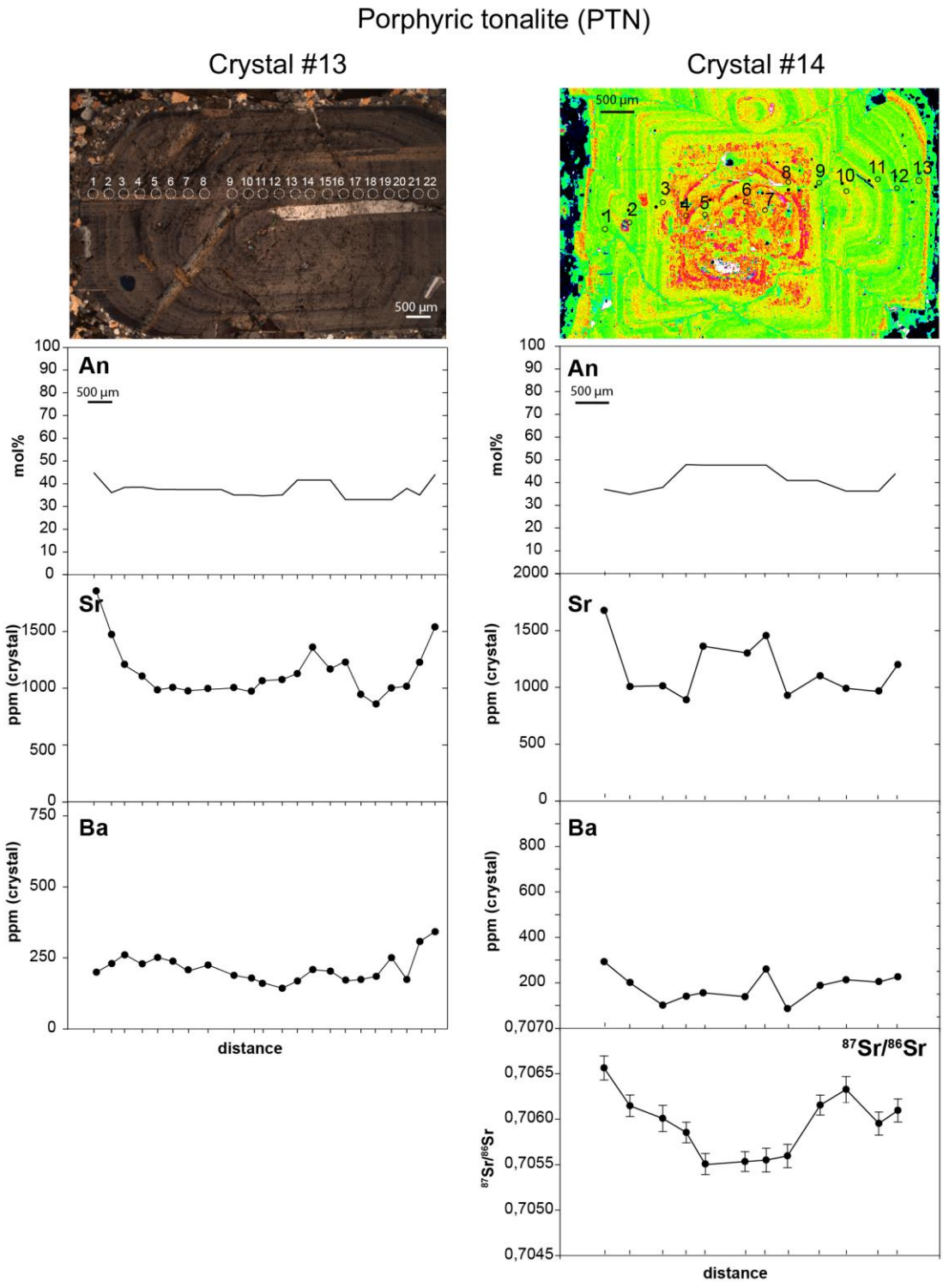

Figure 5.11 Traverse analyses from rim to core to rim of crystals #13 and #14 (PTN).

isotopic composition is nearly constant all along the profile: the core has a $^{87}Sr/^{86}Sr$ ratio of 0.7062 ± 0.0000 (2se) and 0.7065 ± 0.0001 (2se) at the rim.

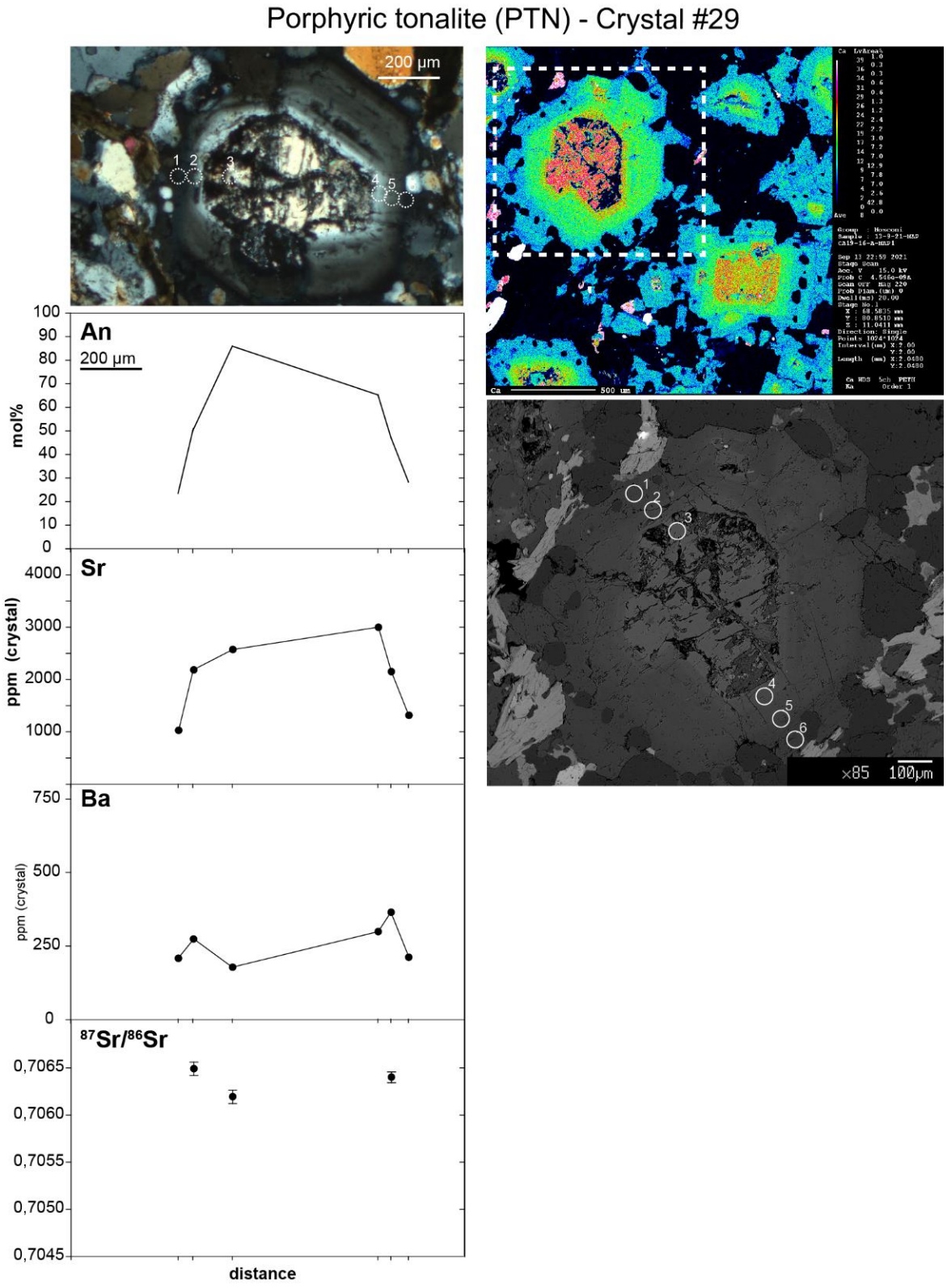

Figure 5.12 Traverse analyses from rim to core to rim of crystal #29 (PTN).

Crystal #31 (max diameter of 2 mm) has a large core showing sieve-texture and several mineral and melt inclusions (Fig. 5.14). Partially resorbed rims and rounded quartz inclusion occur in the external part of the crystal. A smooth normal An zonation is shown by crystal #31, where

both core and rim are andesine (An 31-47) in composition. Crystal #31 shows a plateau-like trend for Sr, with the highest concentration at the core (2200 ppm) and an abrupt decrease at the rim (1350 ppm). Ba and Pb follow an oscillatory trend varying from 400 to 175 ppm and 45 to 25 ppm, respectively. The Sr isotopic profile shows constant compositions of 0.7065 ± 0.0001 (2se).

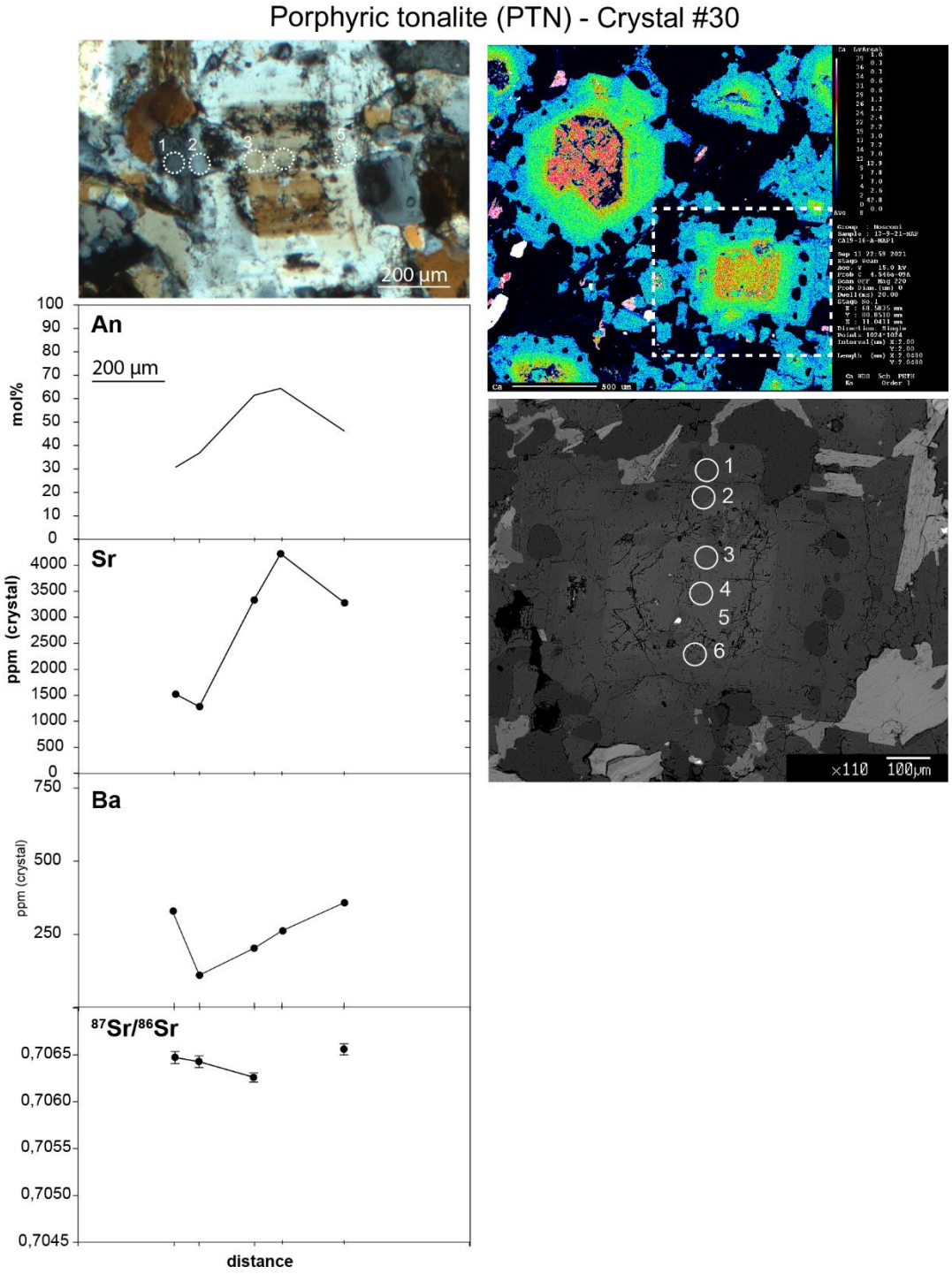

Figure 5.13 Traverse analyses from rim to core to rim of crystal #31 (PTN).

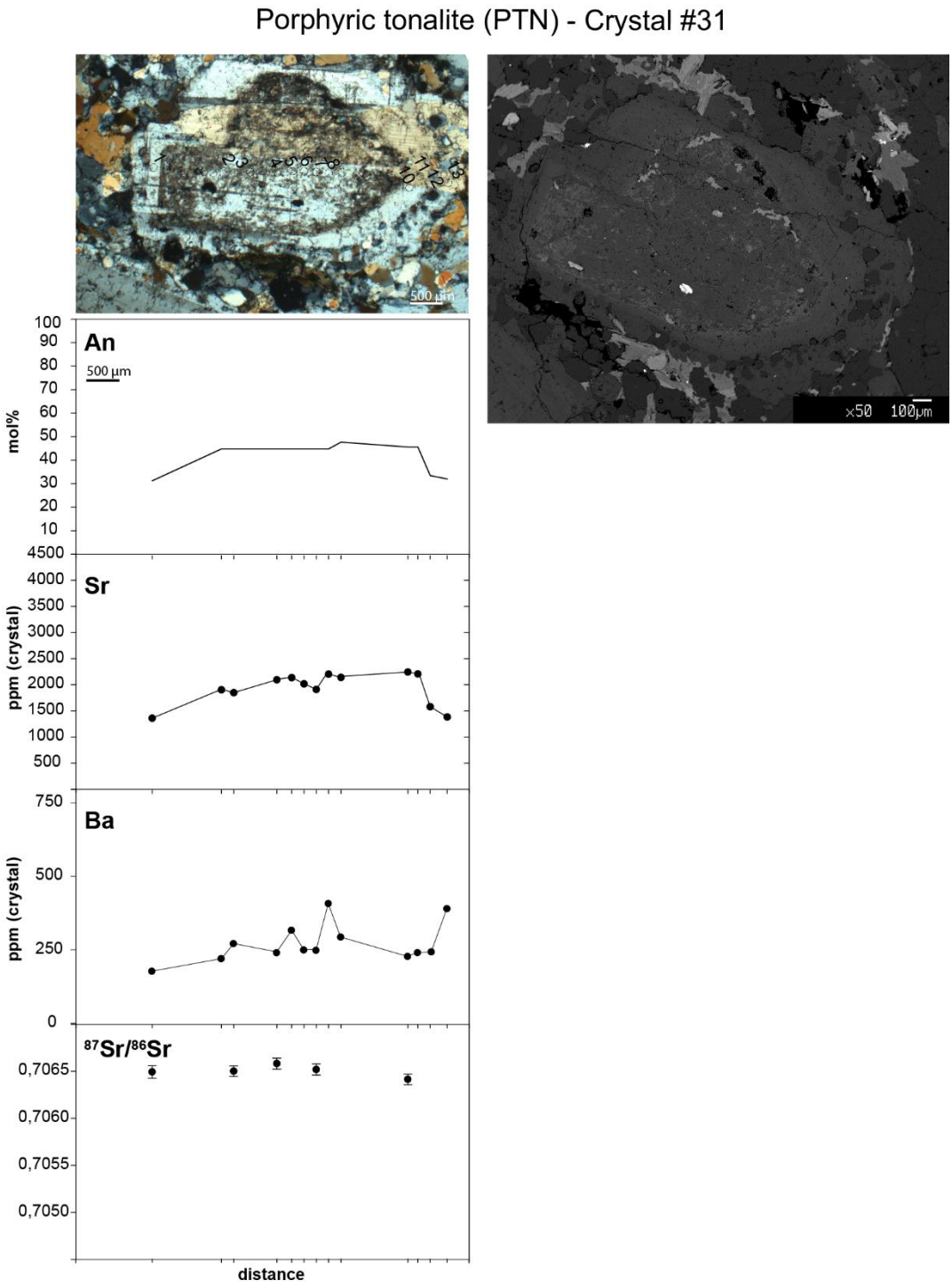

Figure 5.14 Traverse analyses from rim to core to rim of crystal #31 (PTN).

5.4.4 EBG micro-chemical profiles

Crystal #17 has a diameter of <1.5 mm and show internal and external resorption (Fig. 5.15). The core is fractured and shows an intense sieve texture. It shows normal An zonation with andesine core (up to An_{49}) and oligoclase rim (down to An_{19}). Sr concentrations show the highest values at the core (up to 2370 ppm) and the lowest at the rim (470 ppm). Ba mimics the above variation with up to 410 ppm and down to 100 ppm at the rim. Pb zoning pattern follows a monotonous increase from the core (10 ppm) to the rim (60 ppm).

Plagioclase #18 has a maximum diameter <1 mm and subtle rounding of edges (Fig. 5.16) The core is partially fractured. It shows An normal zoning with andesine core (up to An_{43}) and oligoclase rim (down to An_{17}). The trace element zoning patterns of crystal #18 are almost identical to those of crystal #17. Sr zoning pattern show decreasing concentrations from the core (2440 ppm) to the rim (458 ppm). Similarly, Ba concentrations decrease from the core (up to 744 ppm) to the rim (down to 125 ppm). Pb zoning pattern shows a monotonous increase from the core (20 ppm) to the rim (60 ppm).

Plagioclase crystal #20 has a diameter of ~3mm and is partially compenetrated with another crystal that will not be considered (Fig. 5.16). Rounded edges indicate external resorption. The Ca compositional maps show the occurrence of subtle oscillatory zoning mainly in the internal part where two or more resorbed cores are included and embedded.

Crystal #20 shows a smooth normal An zonation, with the core andesine in composition (An_{35}) and oligoclase rim (An_{21}). Trace element profiles across the crystal show a monotonous decrease of Sr and Ba from core to rim, with an overall variation in the range of 2180-800 ppm for Sr and 640-150 ppm for Ba. Pb zoning pattern shows an oscillatory trend varying from 28 to 70 ppm. In the central zone of the crystal, the $^{87}Sr/^{86}Sr$ ratios vary between 0.7052 ± 0.0001 (2se) and 0.7055 ± 0.0001 (2se). The Sr isotope ratios gradually become more radiogenic towards the rim, with an average value of 0.7059 ± 0.0001 (2se).

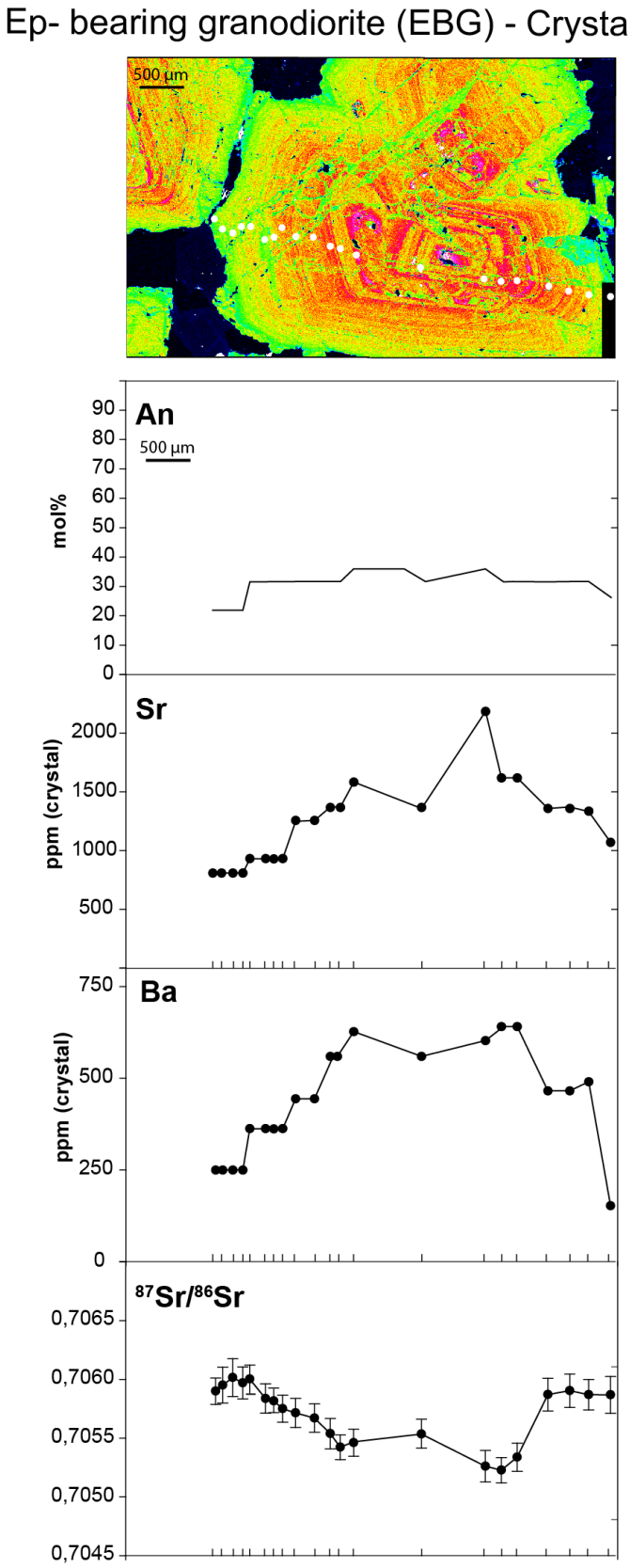

Figure 5.15 Traverse analyses from rim to core to rim of crystal #20 (EBG).

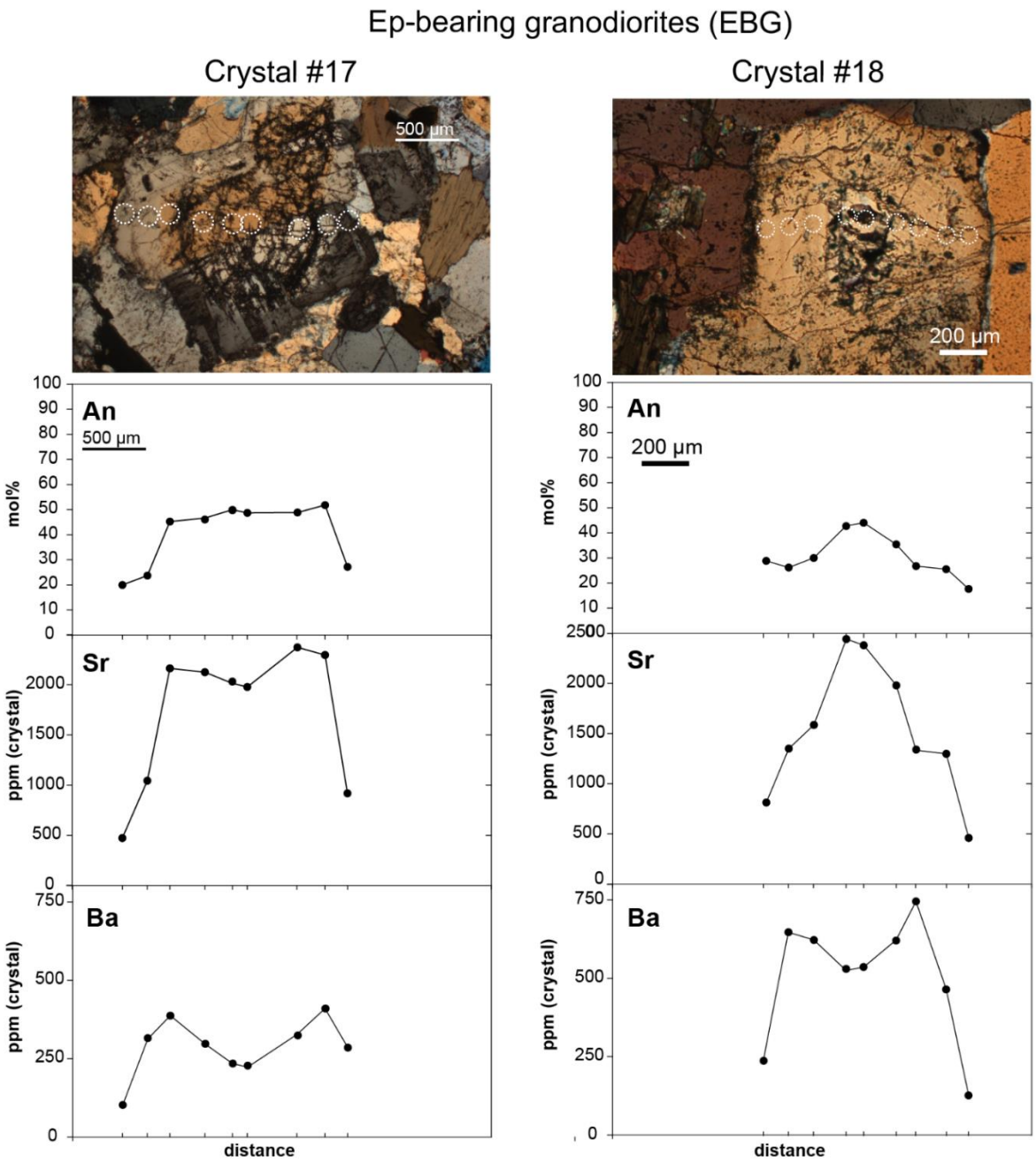

Figure 5.16 Traverse analyses from rim to core to rim of crystals #17 and #18 (EBG).

5.5 Discussion

Previous studies based on plagioclase major and trace element zonation and aimed to constrain magma differentiation processes were carried out in either volcanic or plutonic systems (Ginibre et al., 2007), also including the southern Adamello (Val Fredda Complex; Blundy and Shimizu, 1991). Here, the occurrence of high-Ca plagioclase cores in both primitive and granitoid rocks was crucial in understanding the evolution of magma. Through a combined study of plagioclase zonation and composition (major and trace elements), Blundy and Shimizu (1991) demonstrated that individual plagioclase crystals have been exposed to an extreme range of liquid compositions. They identified a two-stage crystallization history, consistent with the early crystallisation of calcic plagioclases that were lately recycled by a compositionally different magma through vigorous convection. However, the sole use of trace element profiling did not allow to distinguish between open-system and closed-system evolution. Here, the combination of plagioclase zonation with composition both in major, trace element and the isotopic signature has allowed a significant step further in the interpretation of rock petrogenesis from plagioclase.

Plagioclase crystal cargo from the Corno Alto complex exhibits a wide array of zoning patterns and textural types (such as large phenocrysts and glomerocrysts) as well as the occurrence of resorption surfaces suggesting a complex petrological history characterised by multiple episodes of chemical disequilibrium. The scenario is similar to that described by Blundy and Shimizu (1991); although the relatively high SiO_2 of the studied rocks, plagioclase shows a broad compositional spectrum with the An content extending from albite to bytownite. A similar large variation is observed for the Sr isotopic signature (Figure 5.7) and noticeably this variation is evident not only in the same rock (intra-sample) but also in the single mineral grain (intra-grain). The reader would consider that the range of intra-grain and intra-sample Sr isotope variability found in this study cover the entire range reported by Relvini et al. (2022) considering the bulk rock isotope signature of samples with significantly different degree of differentiation (from diorite to granodiorite). Sr isotopic variability in the Corno Alto plagioclase crystals is much higher in the cores than in the rims, which form a relatively restricted compositional cluster (Fig. 5.7). The highly variable isotopic signatures (from 0.7055 to 0.7065) of plagioclase cores in the PTN sample are clear evidence of intra-sample heterogeneity. Instead, the abrupt variation in $^{87}Sr/^{86}Sr$ ratios from core to rim of crystal #1 from the TMG sample is clear evidence of intra-grain heterogeneity. Both the large intra-sample and intra-grain heterogeneity strongly suggests the involvement of melts at different degree of differentiation and thus are evidence of a melt evolution in an open-system.

Overall, based on the intra-sample and intra-grain isotopic variation, four isotopically distinct components can be recognized in the Corno Alto: component (1) with $^{87}Sr/^{86}Sr$ ratio of ~0.7050; component (2) with $^{87}Sr/^{86}Sr$ of ~0.7055; component (3) with $^{87}Sr/^{86}Sr$ of ~0.7060, and component (4) with $^{87}Sr/^{86}Sr$ ~0.7065. Noticeably, all these components are statistically discriminated by the associated errors.

Based on the trace element composition of plagioclase cores and their Sr isotopic signature a magmatic differentiation trend driven by an AFC process cannot be outlined. This holds also if the Sr isotopic composition of the Cornone di Blumone plagioclase crystals is considered, which are the less differentiated terms available (Fig 5.7). Textural and chemical evidence suggests that the interaction of distinct and geochemically different components has occurred.

A clear example of this is found in crystal #1 (TMG) where the abrupt variation in the Sr isotopic signature between the core (component-1) and the rim (component-3) clearly suggests the sudden interaction of two geochemically distinct systems. Likely, a magma with the Sr isotopic signature of component-3 trapped the crystal core with the isotopic signature of component-1, as testified by the occurrence of a resorption surface at the core-rim boundary. In other words, (the observed stepped profile suggests that) the Sr isotopic depleted core, corresponding to component-1, did not spend its entire crystallization history in the magma in which it is finally hosted but likely was grown in a different place at different times in the magma system, and can be thus referred to as *antecryst* (Davidson et al., 2007). The distinct origin of component-1 and component-3 is also supported by their different An content and trace elements composition.

In particular, component-1 corresponds to high An and Sr contents and a significantly less Ba- and Pb-rich character than component-3.

The smooth increase in the radiogenic Sr component observed in crystal #20 (EBG rock) implies that a magma with the Sr isotopic signature of component-2 gradually changed its composition towards that of component-3. The smooth Sr isotopic profile is associated with gradually varying elemental composition, suggesting growth in magma-changing composition rather than punctuated events (Davidson et al., 2007). Component-2 is characterized by high Ba (and Sr) concentrations. Instead, component-3 records the highest Pb concentrations and the lowest Ba and Sr of the Corno Alto complex. The normal Ba profile is anomalous compared to the inverse trend recorded by the plagioclase crystals of the other rocks. The Ba-rich nature of component-2 may result from the early crystallization of plagioclase in the EBG rocks with respect to other K-rich phases, such as biotite and K-feldspar.

Remarkably, the PTN crystal cargo includes both plagioclase crystals displaying a gradual shift from component-2 to -3 (#14) similar to EBG plagioclases, and plagioclases with the

signature of component-4 (e.g. #29, #30 and #31). Noteworthy is that PTN crystals all display the composition of component-4 localised at the outer rim thus suggesting that component 4 pertains to the latest stages of crystallization. Component-4 is characterized by the most radiogenic signature coupled with high An content (up to An_{85}) and particularly high Sr and LREE concentrations. In light of its exotic radiogenic and elemental compositions, component-4 likely corresponds to a recharge event from a different source.

5.6 The Corno Alto assembly

The integrated in situ study of U-Pb ages and Hf isotopes on zircons and trace element and isotopic characterisation of plagioclase crystals from the different rock types of the Corno Alto has allowed the identification of at least three distinct igneous stages that contributed to the assembly of the igneous complex.

Stage 1; > 44 Ma

The first stage is older than 44 Ma and has a Sr isotopic signature of 0.7050 (component-1). This stage is testified by the plagioclase antecrysts in the two-mica granodiorite of the Corno Alto complex (TMG). The age of emplacement is undefined. Zircon grains in the TMG rocks likely date the igneous event that recycled the antecrysts. These latter should be thus older than 44 Ma. A possible source for the antecryst could be the pre-alpine host basement after extensive interaction with the parental magma of TMG rocks. Indeed, as extensively treated in Chapter 3, several inherited zircon crystals in the TMG rocks (although there is no direct evidence in the same sample) record Proterozoic to Paleozoic ages, thus suggesting extensive crustal assimilation. However, the polymetamorphic basement (Rendena Schists) is unlikely the source for the observed antecrysts. The relatively high abundance of inherited zircons in TMG rocks and the relatively low antecryst $^{87}Sr/^{86}Sr$ signature (~0.7050 ± 0.0001) suggest the assimilation of relatively unradiogenic material, contrasting with the high Sr isotopic signature (>0.7350; Bigazzi et al., 1986) of the polymetamorphic basement. Moreover, plagioclase antecrysts are coarse-grained and undeformed, contrasting with the features of plagioclase crystals from the Rendena Schists. Texturally antecrysts are more similar to plagioclase from the Permian granitoid intrusive complex of Mt. Sabion (Rottura et al., 1997) that could represent a possible candidate for being assimilated. However, the bulk-rock $^{87}Sr/^{86}Sr$ ratios of the Permian intrusion ($^{87}Sr/^{86}Sr > 0.7080$; Rottura et al., 1997) do not reconcile with the Sr isotopic values in the antecryst of the TMG rocks. Furthermore, the plagioclase crystals of the two complexes significantly differ in the An content.

Alternatively, plagioclase antecrysts could be survivors of older mafic intrusions after extensive interaction with the parental melts of the TMG rocks. Plagioclase antecrysts found in the TMG rocks have high An content (up to 85) suggesting the crystallisation from a relatively primitive melt. Mafic rocks possessing An-rich plagioclase were reported only in the Cornone di Blumone intrusion and in a few mafic rocks of the Val Fredda complex in the southern Re di Castello Unit (Blundy and Shimizu, 1991; Tiepolo et al., 2002). Noticeably, antecrysts found in the TMG rocks show intermediate elemental and isotopic composition between the most differentiated plagioclase crystals from the Corno Alto (see next sections) and those of the Cornone di Blumone/Val Fredda complex (Fig. 5.7). An origin from a common source cannot be ruled out, but with slightly different degrees of differentiation. Specifically, the Re di Castello mafic rocks are less affected by crustal contamination.

The co-genetic relation between Corno Alto antecrysts and mafic rocks from Re di Castello is also in accord with the occurrence in the TMG rocks of relict zircon crystals with a depleted Hf isotopic signature, similar to that of the Cornone di Blumone zircons (Schoene et al., 2012). However, it should be noted that zircons in the Cornone di Blumone rocks yield remarkably younger ages (42 Ma; Schoene et al., 2012) than the TMG rock. Therefore, the parental magma of component-1 is likely a mafic melt similar to that of the Cornone di Blumone, but it certainly does not pertain to the same igneous event.

I verified through an assimilation and fractional crystallisation model if a source similar to that of the primary melt of the Cornone di Blumone can be at the origin of the component-1. First, a binary mixing model was used. The Rendena Schists ($^{87}Sr/^{86}Sr$ of 0.7390 and 68 ppm Sr; Bigazzi et al., 1986) and the primary melt calculated in equilibrium with plagioclases of the Cornone di Blumone ($^{87}Sr/^{86}Sr$ 0.7037 and 1800 ppm) were assumed as end members. The melt in equilibrium with plagioclase was calculated following Blundy and Wood (1991). The model shows that the most primitive compositions of the component -1 is achieved with proportions of about 20 % of the Rendena Schists.

Stage 2; 44 Ma

The second stage corresponds to the main and older igneous activity (44.0 ± 0.3 Ma; EBG sample) strictly related to the assembly of the Corno alto complex. The Sr isotopic signature is 0.7055 (component-2) for the less evolved products and 0.7060 (component-3) for the more differentiated EBG rocks.

The gradual enrichment in radiogenic Sr (and elemental Pb) suggests a continuous process of enrichment in the radiogenic component and likely, a melt differentiation driven by an AFC process. Considering the Rendena Schists as the contaminant ($^{87}Sr/^{86}Sr$ ratio of ~0.7390;

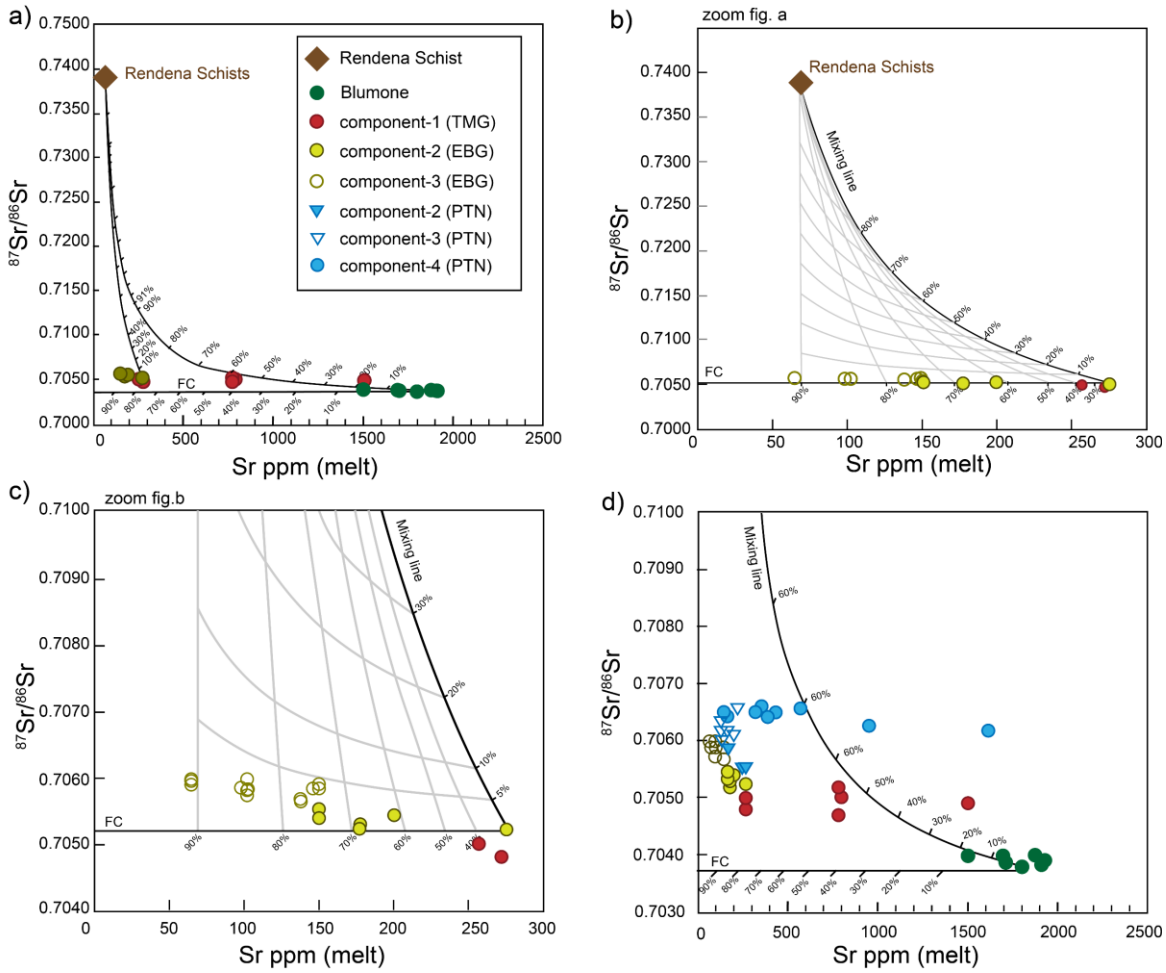

Figure 5.17 Mixing and fractional crystallization model for the Corno Alt plagioclases.Melt in equilibrium with plagioclase crystals are calculated following Blundy and Wood (1991). A temperature of 1000°C has been applied in the formula following Blundy and Shimizu (1991). Kd of the rock phases are from Blundy and Shimizu (1991). a) Mixing model between the Rendena Schists and the melt calculated in equilibrium with the Cornone di Blumone plagioclases; b) Zoom of (a) where fractional crystallization is also shown; c) zoom of (b): d) zoom of composition of melts in equilibrium with component-4.

Relvini et al., 2022; Bigazzi et al., 1986; Del Moro et al., 1983), the observed shift in $^{87}Sr/^{86}Sr$ ratio and elemental Sr from component-2 to component-3 is accounted with less than 5% of assimilated material and between 60 and 90 % of fractional crystallisation (see fig. 5.17 for details of the modelling). This component represents the oldest dated igneous activity documented in the Corno Alto Complex (see Chapter 4), thus the origin of component-2 is worth deeper discussion.Under the hypothesis that the crypto component-1 is alpine-related, component-2 may represent the expression of its differentiation. However, the strong difference in elemental composition, especially the Ba-rich nature of component-2, cannot result from the assimilation of the Ba-poor host-basement (Rendena Schists). The high Ba concentration in component-2 is likely a primary feature of the parental melt (as discussed in section 4.9.3), and thus suggests a source distinct from that at the origin of component-1. As discussed in Chapter 4 for bulk-

rock compositions, the Ba enrichment could be related to the involvement of a carbonate-rich component in the source.

Stage 3 – 42 Ma

The third stage corresponds to a late-stage crystallisation of a melt with 0.7065 Sr isotopic signature (component-4) associated with a rapid migration of the melt towards shallower levels. This stage is evident in the PTN rocks where two distinct age peaks at 44 Ma and 42 Ma were found. Textural and chemical features suggest that plagioclases crystallised from component-4 are the youngest (thus pertaining to the event at 42 Ma). The occurrence of An-rich plagioclase crystals among those of component-4 suggests that they may represent a magma recharge by mafic inputs. The high Sr isotopic signature would imply the assimilation of highly radiogenic material such as the Rendena Schists. Crystals displaying both component-2 and -3 are instead inherited from stage 2 (44 Ma). A series of structures developing during a rapid decompression, such as the presence of multiple quartz inclusions at the rims of crystals, as well as the cracked appearance of crystals (Blundy and Shimizu, 1991; Mason, 1985) suggest that the process of magma recharge by mafic inputs likely induced a rapid ascent of the melt to shallower levels. In this case, it cannot be ruled out that a proto-eruptive magmatic system was forming in the Corno Alto complex (fig. 5.18).

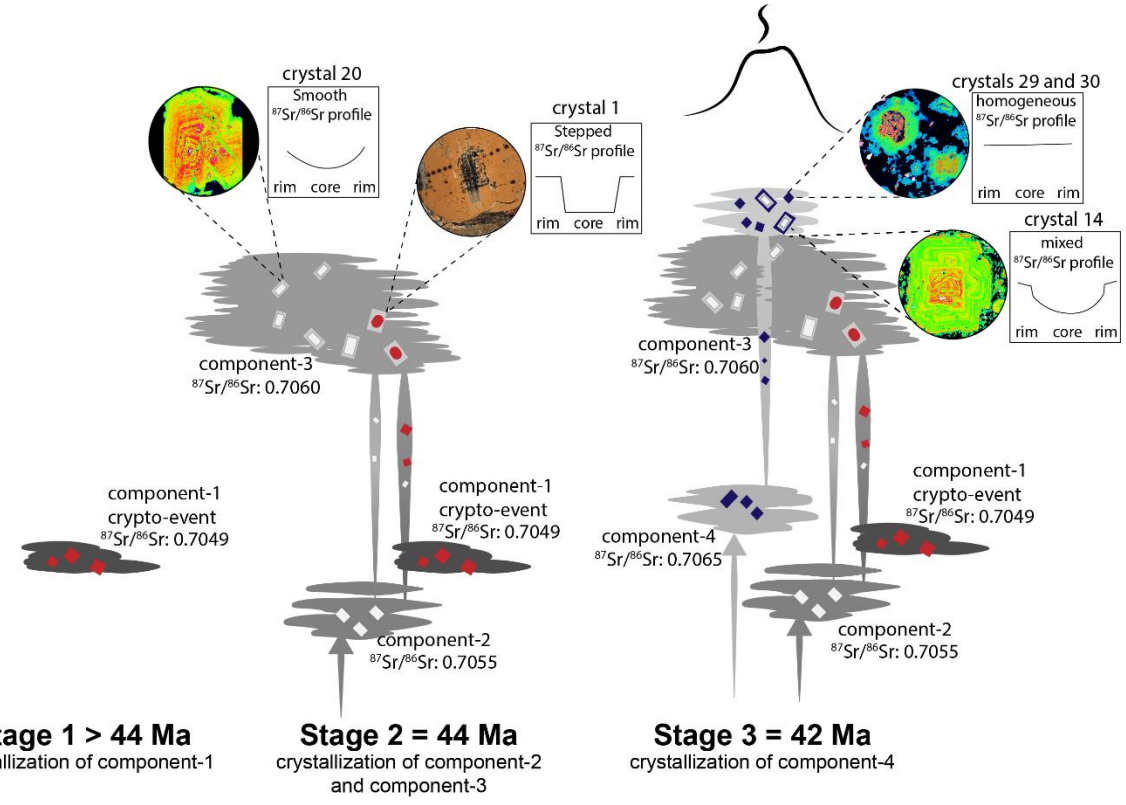

Figure 5.18 Sketch of the assembly of the Corno Alto complex.

Chapter 6
Comparison with the Archean granitoid record

The objective of this PhD project was to compare the Corno Alto complex with the Archean TTG suites due to their apparent petrographic similarities. However, as we have seen in previous sections, trondhjemites are almost absent, even though it was previously considered a TTG suite in the literature. Notwithstanding, the Corno Alto rocks share some notable chemical similarities with the Archean TTGs and other late Archean rocks.

In figure 6.1, the Corno Alto rocks have been plotted together with the database of Archean gneissic and plutonic rocks assembled and published by Moyen (2011). The latter were divided into four groups (three TTG, and one potassic) primarily based on their HREE and Sr concentrations (Moyen, 2011). These chemical features were interpreted as reflecting the distinct melting depths, corresponding to different mineral assemblages (i.e. more or less garnet and plagioclase-rich; Moyen, 2011). The four groups are: (i) high-pressure TTG; (ii) medium-pressure TTG; (iii) low-pressure TTG; (iv) potassic granites. Later studies (Rollinson 2021; Johnson et al., 2019) argued against this subdivision, demonstrating that the distinction could be an artefact of crystal fractionation (see Chapter 2). However, it is beyond the scope of this study to validate or not this subdivision.

The Corno Alto granitoids are characterized by high sodic contents and low K_2O/Na_2O ratios, resulting in a trondhjemitic trend (Fig. 4.5d; e.g., Macera et al., 1983) and as shown in Fig. 6.1 they match the composition of the TTG rocks. In particular, the relatively high Na_2O (>4 wt.%), Al_2O_3 (>16 wt.%) and #Mg (> 39) and low MgO (<1.8 wt.%) suggest similarities with the medium- and low-pressure TTG. Nonetheless, similarities in trace element compositions are also observed with the medium-high pressure TTG. Of relevance are the high Sr (> 400 ppm at $SiO_2 \approx 70$ wt.%) and La contents (>10 ppm), and the low Yb and Y (<2 and <20 ppm, respectively) of the Corno Alto rocks. These values result in relatively high Sr/Y and La_N/Yb_N that match the compositions of all the TTG groups (Fig. 6.1). Differently, the other Adamello granitoids fall in the low-pressure TTG field or even within no field at all (grey dots in figure 6.1) for both major and trace element compositions.

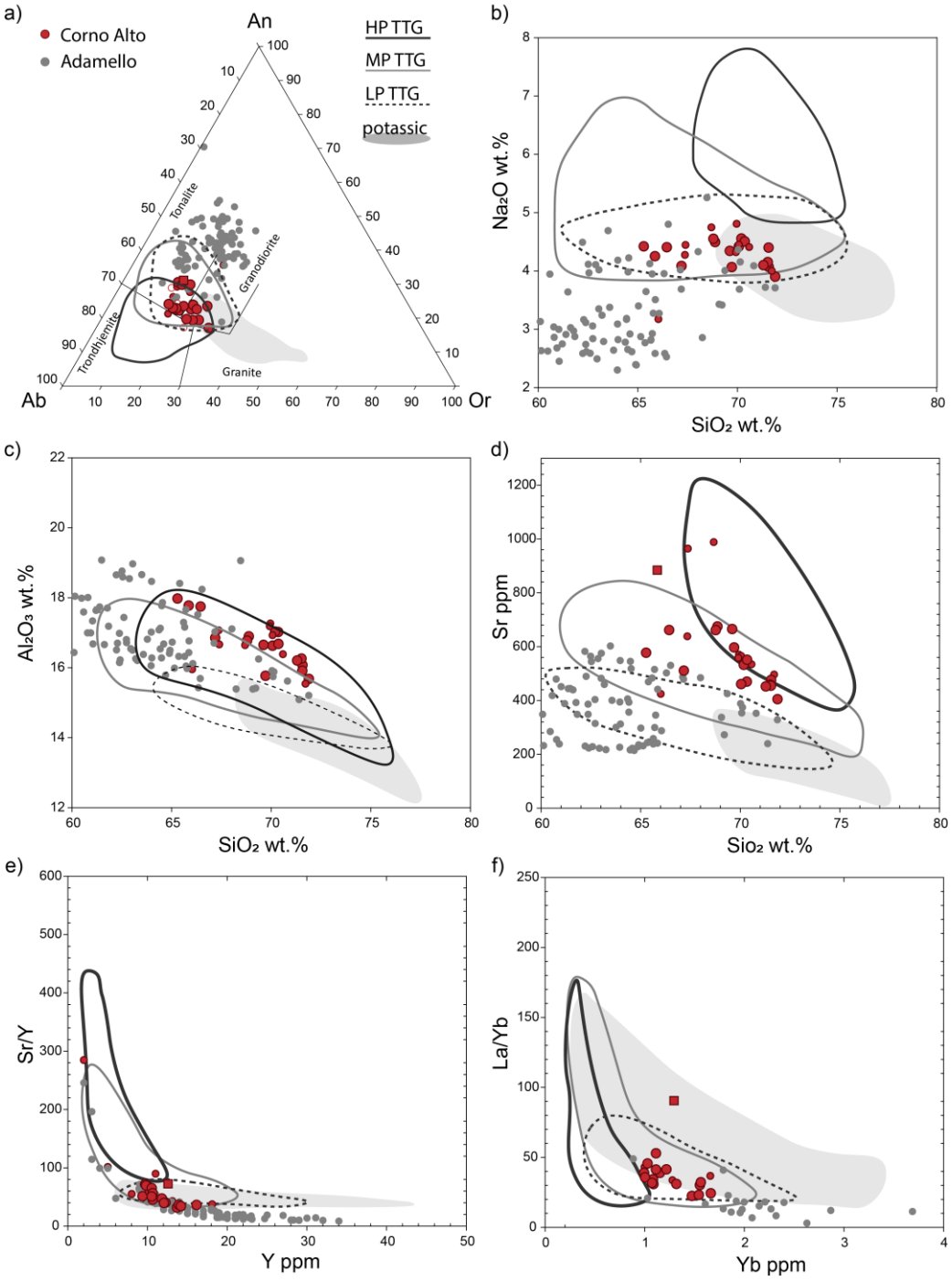

Figure 6.1 Major and trace elements comparison with the Archean TTG. The compilation includes a total of 1700 analyses with SiO_2 > 60 wt.% from Martin and Moyen (2002); Anhaeusser and Robb (1983); Garde (1997); Steenfelt et al. (2005); Bédard (2006); Champion and Smithies (2007); Benn and Moyen (2008), as well as unpublished data from the previously cited authors.

The most apparent differences between the Corno Alto rocks and the TTGs are the Eu negative anomaly and the enrichment in Ba of the former. The Eu negative anomaly testifies, contrarily to the Archean gneissic and plutonic rocks, the involvement in the Corno Alto petrogenesis of a component residual after plagioclase crystallisation and thus that they are not the product of a single-stage melting process. This was also evident from the mineral-scale chemical

disequilibria in plagioclase and zircon (see Chapters 4 and 5). The first important conclusion is thus that the TTG-like compositions observed in the Corno Alto complex can be replicated by open system processes involving multiple components. This evidence supports all the recent studies suggesting that TTG Archean magmatism was likely more complex than a simple, single-stage fluid absent melting process (Huang et al., 2022; Roman & Arndt, 2020; Smithies et al., 2021; Arnd, 2013; Kendrick et al., 2022).

The higher Ba concentrations of the Corno Alto rocks relatve to the TTGs and, in particular, the high Ba/K ratios are a key point. High Ba contents are not properly typical of the TTGs, which only begin to record high Ba concentrations (>1000 ppm) after 3.7 Ga (Huang et al., 2022) but rather characterise a particular group of rocks that appear during the Archean-Proterozoic transition called Sanukitoids. Among these sanukitoids, rocks with high Ba and low K, similar to those of the Corno Alto are found (Fig. 6.2).

Sanukitoids *s.l.* have transitional geochemical compositions between Archean TTG (high LREE and low HREE contents) and Phanerozoic arc series (i.e. BADR, characterized by calc-alkaline differentiation trends; Laurent et al., 2011). Most studies on sanukitoids, supported by experimental evidence, revealed that their transitional characteristics are the result of hybridization between peridotite and felsic, TTG-like melts during petrogenesis (Laurent et al., 2011; Rapp et al., 2010; Heilimo et al., 2010; Martin et al., 2005, 2009; Shirey and Hanson, 1984; Smithies and Champion, 1999, 2000; Stern, 1989). Although the geodynamic settings where sanukitoids are generated remain a topic of discussion, subduction zones are widely considered the most likely locations for the interactions between a felsic melt and peridotite (Laurent et al., 2011). According to Martin et al., (2009), the temperatures during the late Archean are still high enough for melting the hydrous basalt in the subducting slab. This process would generate a TTG-like melt that ascending through the mantle wedge would metasomatize the mantle peridotite generating orthopyroxene and amphibole or phlogopite (Martin et al., 2009). The subsequent low-degree melting of this metasomatized mantle would give rise to mafic sanukitoid magmas that subsequently differentiate. Other studies (Halla, 2005; Kamber et al., 2002; Stern and Hanson 1991) argue that sanukitoids can be generated by metasomatism of the mantle wedge by fluids generated by slab dehydration. However, this hypothesis does not explain the high HFSE contents that cannot be significantly dissolved in fluids due to their high $Kd^{melt/fluid}$ (e.g. Laurent et al., 2011; Audétat and Keppler, 2005).

According to Laurent et al. (2011), in the sanukitoids petrogenesis, no melting of metabasalt is required but the involvement of a siliceous-melt derived from terrigenous sediments holding for the high Ba contents and the high K/Na and HFSE, especially Nb. Thermal regimes are thus 50-100 °C lower than those allowing hydrous basalts partial melting

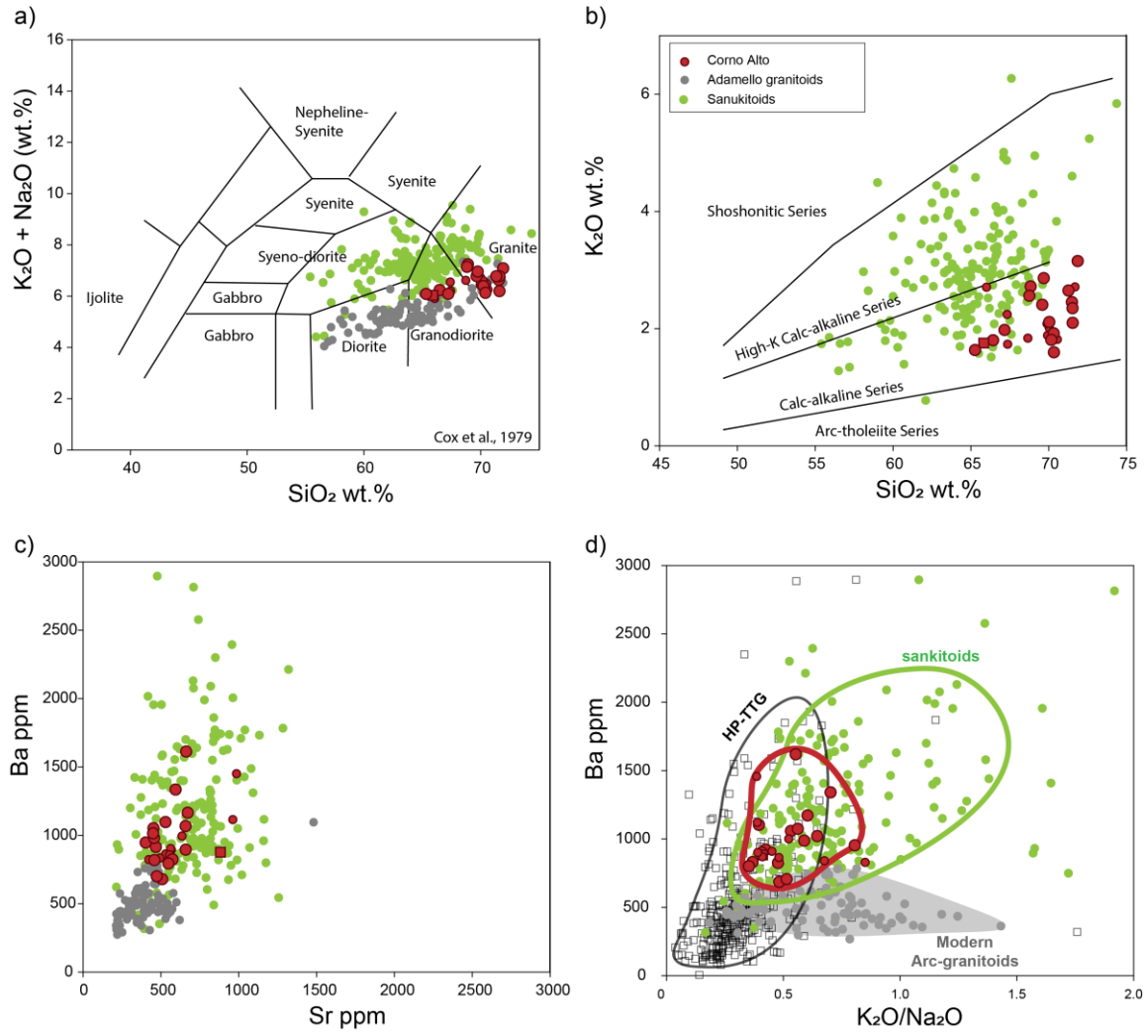

Figure 6.2 Major and trace elements comparison with the Sanukitoids (SiO_2 > 55 wt.%). Data are from Heilimo et al. (2010) and Laurent et al. (2011).

at slab pressures (2.5-4 GPa; Laurent et al., 2011; Hermann and Green, 2001; Johnson and Plank, 2000).

The petrogenetic processes inferred for the Corno Alto rocks suggest an alternative model for the petrogensis of the high Ba/K sanukitoids. As previously described in detail (see Chapter 4) the petrogenesis of the Corno Alto rocks has been traced back to a carbonate input in the source which transfers to the melt its distinctive high Ba/K ratio by hydrous-melts or supercritical fluids. The key factors for this process are thus a carbonatic source of the metasomatic agent and the availability of thermal conditions high enough for the carbonate partial melting.

During Early Archean, although thermal conditions were sufficient for carbonate melting, carbonate inputs in subducting systems was almost negligible due to the paucity of carbonate marine organism (Veizer & McKenzie, 2003; Ernst, 2009; Fig. 6.3). Carbonate platforms began to appear during the late Archean but have become increasingly widespread since the

Proterozoic and Phanerozoic when subduction thermal conditions do not reach the temperatures necessary for carbonate melting (Laurent et al., 2011). It follows that the full accomplishment of the conditions required for the genesis of the high Ba/K sanukitoids is mostly found at the Archean-Proterozoic transition.

In conclusion, the anomalous thermal conditions (in the range of 850 – 900 °C at 4.2 – 6 GPa) pertaining to the Alpine subduction at 44 Ma apparently parallel those at the Archean-Proterozoic transition. The Corno Alto suite, as well as other Ba-Sr granites (Fowler and Rollinson, 2012) could thus represent a kind of modern analogues of the high Ba/K sanukitoids.

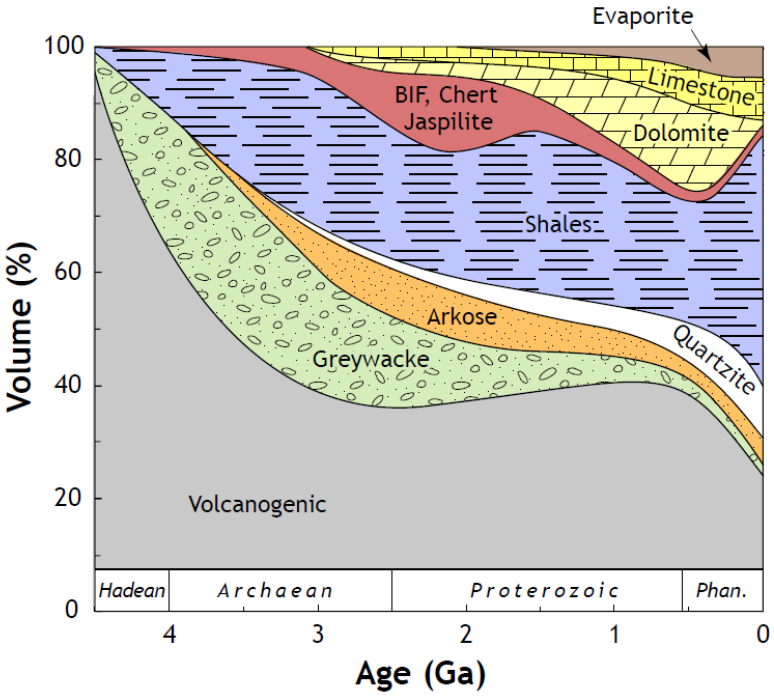

Figure 6.3 Modified after Laurent (Phd thesis), Veizer & McKenzie (2003) and Ernst (2009). Evolution of the proportions of various sedimentary lithologies as a function of time.

Chapter 7
Summary and conclusions

Granitoid batholiths are important end products of the Earth's long-term compositional differentiation, representing either the addition of juvenile material to the crust or the reworking of older crustal components (Moyen et al., 2021).

This thesis has explored the potential of studying the isotopic disequilibria at the microscale in minerals from granitoid rocks to evaluate possible contributions of distinct sources, including isotopically primitive mantle melts or older crustal materials.

The focus of the study was the Corno Alto complex, the oldest intrusive body of the Adamello batholith and of the whole Periadriatic magmatism. In this framework, this project aimed to investigate the petrogenetic processes generating the early melts in the alpine orogeny and their bearing on the general architecture of the Alpine evolution.

The field survey of the Corno Alto complex allowed the recognition of three distinct types of granitoid rocks ranging in composition from tonalite to granodiorite without encompassing the trondhjemitic terms described in the literature.

U-Pb data of zircons revealed an incremental assembly of the Corno Alto complex by multiple and possibly discrete magma injections in a time span of ~5 Ma. In particular, three recurring age peaks, at c. 44 Ma, c. 42 Ma, and c. 39 Ma, distributed along an EW-ward trend of decreasing ages, have been identified. The geochronological data presented in this work refine the current knowledge on the age of the Corno Alto complex and identify a progressive migration of igneous activity away from the slab tear through time.

The combined use of the whole-rock chemistry and Hf isotopic data on zircons revealed peculiar features compared to the other Adamello rocks, and in turn to typical I-type and S-type granites. In particular, the studied rocks showed the coexistence of at least two geochemically distinct components: i) a high Ba component characterised by high Sr and La/Yb ratios, likely derived from melting of carbonated sediments of slab origin; and ii) a juvenile component, interpreted as the mantle signature survived from the subduction-related metasomatism.

The above evidence provided important clues for the evolution of the Alpine subduction. In particular, the high thermal conditions required for inducing partial melting of the carbonate fraction of the sediment cover of the slab likely derived from the rise of asthenospheric material near the torn edge of the European slab where roughly the Corno Alto is located.

Moreover, the detailed geochemical characterization of the Corno Alto rocks revealed a compositional analogy with the Phanerozoic high Ba-Sr granites, considered modern analogous of the Archean sanukitoids. The proposed model contextualizes the petrogenesis of the high Ba-Sr magmatism in the Alpine geodynamic setting but may also help settle critical issues about the Archean sanukitoids, recognizing not only occasional recurrences of thermal regimes similar to those in the Archean but also similar tectono-magmatic events.

Parallel to this, the pervasive occurrence of zoned plagioclase crystals showing evidence of intense chemical disequilibria, such as relic cores, resorption, and recrystallization textures, aroused the interest to conduct a systematic geochemical study on plagioclase. In situ trace elements and Sr isotope analysis proved to be particularly advantageous to identify mineral-scale heterogeneity and characterize representative populations of plagioclase crystals.

In particular, four isotopically distinct components have been recognized in the Corno Alto plagioclase feldspars. The integration of U-Pb ages and Hf isotopes on zircons to the study of plagioclase crystals helped to identify at least three distinct igneous stages that contributed to the assembly of the igneous complex. The first stage corresponds to the crystallization at depth of isotopically depleted cryptic materials, then cannibalized by further magma injections crystallizing during the second stage occurring at 44 Ma. The origin of the cryptic material is attributed to the crystallization of a mafic melt similar in composition to that of the 42 Ma old Cornone di Blumone complex (southern Adamello), but certainly not pertaining to the same igneous event. The second stage at 44 Ma involved the crystallization of a Ba-rich melt, likely suffering an increasing degree of assimilation of the Rendena Schist basement. The primary geochemical features of the melt crystallizing during the second stage are compatible with the carbonate-rich component in the source identified by whole-rock studies. The third stage corresponds to a process of magma recharge by mafic inputs occurring at 42 Ma and associated with a rapid migration of the melt towards shallower levels.

By employing various analytical and methodological approaches, a thorough model was developed to elucidate the petrogenetic evolution of the Corno Alto complex, which was found to be the outcome of a multi-stage and multi-component process.

The results of this thesis underscore the significance of investigating the isotopic diversity at the micro-scale in order to uncover open-system processes occurring during magmatic differentiation.

The same micro-scale approach, especially the application of in situ Sr isotope measurements on plagioclase, could be applied to similar magmatic intrusive suites, such as the other intrusive units of the Adamello batholith or similar high Ba-Sr granites suites.

Bibliography

Agard, P., 2021. Subduction of oceanic lithosphere in the Alps: Selective and archetypal from (slow-spreading) oceans. Earth-Science Rev. 214, 103517. https://doi.org/10.1016/j.earscirev.2021.103517

Agard, P., Handy, M.R., 2021. Ocean subduction dynamics in the Alps. Elem. An Int. Mag. Mineral. Geochemistry, Petrol. 17, 9–16.

Anhaeusser, C.R., Robb, L.J., 1983. Chemical analyses of granitoid rocks from the Barberton Mountain Land. Geological Society of South Africa Special Publication 9, 189–219.

Audétat, A., Keppler, H., 2005. Solubility of rutile in subduction zone fluids, as determined by experiments in the hydrothermal diamond anvil cell. Earth Planet. Sci. Lett. 232, 393–402.

Barker, F., 1979. Chapter 1 - Trondhjemite: Definition, Environment and Hypotheses of Origin, in: BARKER, F.B.T.-D. in P. (Ed.), Trondhjemites, Dacites, and Related Rocks. Elsevier, pp. 1–12. https://doi.org/https://doi.org/10.1016/B978-0-444-41765-7.50006-X

Bebout, G.E., Agard, P., Kobayashi, K., Moriguti, T., Nakamura, E., 2013. Devolatilization history and trace element mobility in deeply subducted sedimentary rocks: Evidence from Western Alps HP/UHP suites. Chem. Geol. 342, 1–20. https://doi.org/10.1016/j.chemgeo.2013.01.009

Beccaluva, L., Bianchini, G., Bonadiman, C., Coltorti, M., Milani, L., Salvini, L., Siena, F., Tassinari, R., 2007. Intraplate lithospheric and sublithospheric components in the Adriatic domain: Nephelinite to tholeiite magma generation in the Paleogene Veneto volcanic province, southern Alps. Spec. Pap. Geol. Soc. Am. 418, 131–152. https://doi.org/10.1130/2007.2418(07).

Bédard, J., 2006. A catalytic delamination-driven model for coupled genesis of Archaean crust and sub-continental lithospheric mantle. Geochimica Cosmochimica Acta 70, 1188–1214.

Beltrando, M., Compagnoni, R., Lombardo, B., 2010. (Ultra-) High-pressure metamorphism and orogenesis: an Alpine perspective. Gondwana Res. 18, 147–166.

Benn, K., Moyen, J.-F., 2008. Geodynamic origin and tectonomagmatic evolution of the Late Archean Abitibi-Opatica terrane, Superior Province: Magmatic modification of a plateau-type crust and plume-subduction interaction. In: Condie, K.C., Pease, V. (Eds.), When did plate tectonics begin on Earth? Special Paper. Geological Society of America, Boulder, pp. 173–198.

Bennett, E.N., Lissenberg, C.J., Cashman, K. V., 2019. The significance of plagioclase textures in mid-ocean ridge basalt (Gakkel Ridge, Arctic Ocean). Contrib. to Mineral. Petrol. 174, 1–22. https://doi.org/10.1007/s00410-019-1587-1

Bergomi, M.A., Zanchetta, S., Tunesi, A., 2015. The Tertiary dike magmatism in the Southern Alps: geochronological data and geodynamic significance. Int. J. Earth Sci. 104, 449–473. https://doi.org/10.1007/s00531-014-1087-5

Bianchi, A., Dal Piaz, G., 1950. Il problema dell'età del Corno Alto nel massiccio dell'Adamello. Società Cooperativa Tipografica.

Bianchini, G., Beccaluva, L., Siena, F., 2008. Post-collisional and intraplate Cenozoic volcanism in the rifted Apennines/Adriatic domain. Lithos 101, 125–140. https://doi.org/10.1016/j.lithos.2007.07.011

Bigazzi, G., Del Moro, A., Macera, P., 1986. A quantitative approach to trace element and Sr isotope evolution in the Adamello batholith (northern Italy). Contrib. to Mineral. Petrol. 94, 46–53. https://doi.org/10.1007/BF00371225

Blanckenburg, F. Von, Davies, J.H., 1995. I i : olo : ot 14, 120–131.

Blundy, J., Cashman, K., 2005. Rapid decompression-driven crystallization recorded by melt inclusions from Mount St. Helens volcano. Geology 33, 793–796. https://doi.org/10.1130/G21668.1

Blundy, J., Cashman, K., Humphreys, M., 2006. Magma heating by decompression-driven crystallization beneath andesite volcanoes. Nature 443, 76–80. https://doi.org/10.1038/nature05100

Blundy, J.D., Shimizu, N., 1991. Trace element evidence for plagioclase recycling in calc-alkaline magmas. Earth Planet. Sci. Lett. 102, 178–197. https://doi.org/10.1016/0012-821X(91)90007-5

Blundy, J.D., Sparks, R.S.J., 1992. Petrogenesis of mafic inclusions in granitoids of the adamello massif, Italy. J. Petrol. 33, 1039–1104. https://doi.org/10.1093/petrology/33.5.1039

Blundy, J.D., Wood, B.J., 1991. Crystal-chemical controls on the partitioning of Sr and Ba between plagioclase feldspar, silicate melts, and hydrothermal solutions. Geochim. Cosmochim. Acta 55, 193–209. https://doi.org/10.1016/0016-7037(91)90411-W

Bowring, S.A., Williams, I.S., 1999. Priscoan (4.00–4.03 Ga) orthogneisses from northwestern Canada. Contrib. to Mineral. Petrol. 134, 3–16.

Bracciali, L., Marroni, M., Luca, P., Sergio, R., 2007. Geochemistry and petrography of Western Tethys Cretaceous sedimentary covers (Corsica and Northern Apennines): from source areas to configuration of margins.

Brandon, A.D., Creaser, R.A., Chacko, T., 1996. Constraints on Rates of Granitic Magma Transport from Epidote Dissolution Kinetics. Science (80-.). 271, 1845–1848. https://doi.org/10.1126/science.271.5257.1845

Broderick, C., Wotzlaw, J.-F., Frick, D., Gerdes, A., Ulianov, A., Günther, D., Schaltegger, U., 2015. Linking the thermal evolution and emplacement history of an upper-crustal pluton to its lower-crustal roots using zircon geochronology and geochemistry (southern Adamello batholith, N. Italy). Contrib. to Mineral. Petrol. 170. https://doi.org/10.1007/s00410-015-1184-x

Brombin, V., Bonadiman, C., Jourdan, F., Roghi, G., Coltorti, M., Webb, L.E., Callegaro, S., Bellieni, G., De Vecchi, G., Sedea, R., Marzoli, A., 2019. Intraplate magmatism at a convergent plate boundary: The case of the Cenozoic northern Adria magmatism. Earth-Science Rev. 192, 355–378. https://doi.org/10.1016/j.earscirev.2019.03.016

Brombin, V., Pettitt, E.A., Fahnestock, M.F., Casalini, M., Webb, L.E., Bryce, J.G., Bianchini, G., 2021. New geochemical and geochronological data on the Cenozoic Veneto Volcanic Province: Geodynamic inferences. Lithos 406–407, 106507. https://doi.org/10.1016/j.lithos.2021.106507

Busigny, V., Cartigny, P., Philippot, P., Ader, M., Javoy, M., 2003. Massive recycling of nitrogen and other fluid-mobile elements (K, Rb, Cs, H) in a cold slab environment: Evidence from HP to UHP oceanic metasediments of the Schistes Lustrés nappe (western Alps, Europe). Earth Planet. Sci. Lett. 215, 27–42. https://doi.org/10.1016/S0012-821X(03)00453-9

Callegari, E., Brack, P., 2002. Geological map of the Tertiary Adamello Batholitih (Northern Italy). Mem. di Sci. Geol. Padova 54, 19–49.

Callegari, E., Cigolini, C., Medeot, O., D'Antonio, M., 2004. Petrogenesis of calc-alkaline and shoshonitic post-collisional Oligocene volcanics of the Cover Series of the Sesia Zone, Western Italian Alps. Geodin. Acta 17, 1–29.

Callegari, E., Dal Piaz, G., (Italia), C. nazionale delle ricerche, 1973. Field relationships between the main igneous masses of the Adamello intrusive massif (Northern Italy). Società cooperativa tipografica.

Champion, D.C., Smithies, R.H., 2007. Geochemistry of Paleoarchean granites of the East Pilbara Terrane, Pilbara Craton, Western Australia: implications for early Archean crustal growth. In: Van Kranendonk, M.J., Smithies, R.H., Bennett, V. (Eds.), Earth's Oldest Rocks. Developments in Precambrian Geology. Elsevier, pp. 369–410.

Chen, C., Liu, Y., Foley, S.F., Ducea, M.N., Geng, X., Zhang, W., Xu, R., Hu, Z., Zhou, L., Wang, Z., 2017. Carbonated sediment recycling and its contribution to lithospheric

refertilization under the northern North China Craton. Chem. Geol. 466, 641–653. https://doi.org/10.1016/j.chemgeo.2017.07.016

Condie, K.C., 2005. TTGs and adakites: Are they both slab melts? Lithos 80, 33–44. https://doi.org/10.1016/j.lithos.2003.11.001

Condie, K.C., Aster, R.C., Van Hunen, J., 2016. A great thermal divergence in the mantle beginning 2.5 Ga: Geochemical constraints from greenstone basalts and komatiites. Geosci. Front. 7, 543–553. https://doi.org/10.1016/j.gsf.2016.01.006

Conticelli, S., Guarnieri, L., Farinelli, A., Mattei, M., Avanzinelli, R., Bianchini, G., Boari, E., Tommasini, S., Tiepolo, M., Prelević, D., 2009. Trace elements and Sr–Nd–Pb isotopes of K-rich, shoshonitic, and calc-alkaline magmatism of the Western Mediterranean Region: genesis of ultrapotassic to calc-alkaline magmatic associations in a post-collisional geodynamic setting. Lithos 107, 68–92.

Cortecci, G., Del Moro, A., Leone, G., Pardini, G.C., 1979. Correlation between strontium and oxygen isotopic compositions of rocks from the Adamello massif (Northern Italy). Contrib. to Mineral. Petrol. 68, 421–427. https://doi.org/10.1007/BF01164526

D'Adda, P., Zanchi, A., Bergomi, M., Berra, F., Malusà, M.G., Tunesi, A., Zanchetta, S., 2011. Polyphase thrusting and dyke emplacement in the central Southern Alps (Northern Italy). Int. J. Earth Sci. 100, 1095–1113. https://doi.org/10.1007/s00531-010-0586-2

Davidson, J.P., Morgan, D.J., Charlier, B.L.A., Harlou, R., Hora, J.M., 2007. Microsampling and isotopic analysis of igneous rocks: Implications for the study of magmatic systems. Annu. Rev. Earth Planet. Sci. 35, 273–311. https://doi.org/10.1146/annurev.earth.35.031306.140211

Davidson, J.P., Tepley, F.J., 1997. Recharge in Volcanic Systems: Evidence from Isotope Profiles of Phenocrysts. Science (80-.). 275, 826–829. https://doi.org/10.1126/science.275.5301.826

Defant, M.J., Drummond, M.S., 1990. Derivation of some modern arc magmas by melting of young subducted lithosphere. Nature 347, 662–665. https://doi.org/10.1038/347662a0

Del Moro, A., Ferrara, G., Tonarini, S., Callegari, E., 1983a. Rb-Sr systematics on rocks from the Adamello batholith (Southern Alps). Mem. della Soc. Geol. Ital. 26, 261–284.

Del Moro, A., Pardini, G.C., Quercioli, C., Villa, I.M., Callegari, E., 1983b. Rb/Sr and K/Ar chronology of Adamello granitoids, southern Alps. Mem. della Soc. Geol. Ital. 26, 285–299.

Drummond, M.S., Defant, M.J., 1990. models in various tectonic settings . A specific subtype of various proposed. J. Geophys. Res. 95, 21,503-21,521.

Dupuy, C., Dostal, J., Fratta, M., 1982. Geochemistry of the Adamello Massif (Northern Italy). Contrib. to Mineral. Petrol. 80, 41–48. https://doi.org/10.1007/BF00376733

Epstein, G.S., Bebout, G.E., Angiboust, S., Agard, P., 2020. Scales of fluid-rock interaction and carbon mobility in the deeply underplated and HP-Metamorphosed Schistes Lustrés, Western Alps. Lithos 354–355, 105229. https://doi.org/10.1016/j.lithos.2019.105229

Ernst, W.G., 2009. Archean plate tectonics, rise of Proterozoic supercontinentality and onset of regional, episodic stagnant-lid behavior. Gondwana Res. 15, 243–253.

Ferrara, G., Hirt, B., Jäger, E., Niggli, E., 1962. Rb-Sr and U-Pb age determinations on the pegmatite of I Mondei (Penninic Camughera-Moncucco-Complex, Italian Alps and some gneisses from the neighborhood). Eclogae Geol. Helv. 55.

Fisher, C.M., Vervoort, J.D., Dufrane, S.A., 2014. Accurate Hf isotope determinations of complex zircons using the "laser ablation split stream" method. Geochemistry, Geophys. Geosystems 15, 121–139. https://doi.org/10.1002/2013GC004962

Fodor, L.I., Gerdes, A., Dunkl, I., Koroknai, B., Pécskay, Z., Trajanova, M., Horváth, P., Vrabec, M., Jelen, B., Balogh, K., 2008. Miocene emplacement and rapid cooling of the Pohorje pluton at the Alpine-Pannonian-Dinaridic junction, Slovenia. Swiss J. Geosci. 101, 255–271.

Foley, S., Tiepolo, M., Vannucci, R., 2002. Growth of early continental crust controlled by melting of amphibolite in subduction zones. Nature 417, 837–840. https://doi.org/10.1038/nature00799

Fowler, M., Rollinson, H., 2012. Phanerozoic sanukitoids from Caledonian Scotland: Implications for Archean subduction. Geology 40, 1079–1082. https://doi.org/10.1130/G33371.1

Fowler, M.B., Henney, P.J., Darbyshire, D.P.F., Greenwood, P.B., 2001. Petrogenesis of high Ba-Sr granites: The Rogart pluton, Sutherland. J. Geol. Soc. London. 158, 521–534. https://doi.org/10.1144/jgs.158.3.521

Fowler, M.B., Kocks, H., Darbyshire, D.P.F., Greenwood, P.B., 2008. Petrogenesis of high Ba-Sr plutons from the Northern Highlands Terrane of the British Caledonian Province. Lithos 105, 129–148. https://doi.org/10.1016/j.lithos.2008.03.003

Garde, A.A., 1997. Accretion and evolution of an Archaean high-grade grey gneiss -amphibolite complex: the Fiskefjord area. Southern West Greenland, GEUS, Copenhagen.

Garofalo, P.S., 2012. The composition of Alpine marine sediments (Bündnerschiefer Formation, W Alps) and the mobility of their chemical components during orogenic metamorphism. Lithos 128–131, 55–72. https://doi.org/10.1016/j.lithos.2011.10.009

Ginibre, C., Kronz, A., Wörner, G., 2002. High-resolution quantitative imaging of plagioclase composition using accumulated backscattered electron images: New constraints on oscillatory zoning. Contrib. to Mineral. Petrol. 142, 436–448.

https://doi.org/10.1007/s004100100298

Ginibre, C., Wörner, G., 2007. Variable parent magmas and recharge regimes of the Parinacota magma system (N. Chile) revealed by Fe, Mg and Sr zoning in plagioclase. Lithos 98, 118–140. https://doi.org/10.1016/j.lithos.2007.03.004

Glodny, J., Ring, U., Kühn, A., Gleissner, P., Franz, G., 2005. Crystallization and very rapid exhumation of the youngest Alpine eclogites (Tauern Window, Eastern Alps) from Rb/Sr mineral assemblage analysis. Contrib. to Mineral. Petrol. 149, 699–712.

Green, D.H., Ringwood, A.E., 1967. The genesis of basaltic magmas. Contrib. to Mineral. Petrol. 15, 103–190. https://doi.org/10.1007/BF00372052

Halla, J., 2005. Late Archean high-Mg granitoids (sanukitoids) in the southern Karelian domain, eastern Finland: Pb and Nd isotopic constraints on crust− mantle interactions. Lithos 79, 161–178.

Handy, M.R., M. Schmid, S., Bousquet, R., Kissling, E., Bernoulli, D., 2010. Reconciling plate-tectonic reconstructions of Alpine Tethys with the geological-geophysical record of spreading and subduction in the Alps. Earth-Science Rev. 102, 121–158. https://doi.org/10.1016/j.earscirev.2010.06.002

Hansmann, W., Oberli, F., 1991. Zircon inheritance in an igneous rock suite from the southern Adamello batholith (Italian Alps) - Implications for petrogenesis. Contrib. to Mineral. Petrol. 107, 501–518. https://doi.org/10.1007/BF00310684

Hawkesworth, C.J., Cawood, P.A., Dhuime, B., 2020. The Evolution of the Continental Crust and the Onset of Plate Tectonics. Front. Earth Sci. 8, 1–23. https://doi.org/10.3389/feart.2020.00326

Heilimo, E., Halla, J., Hölttä, P., 2010. Discrimination and origin of the sanukitoid series: Geochemical constraints from the Neoarchean western Karelian Province (Finland). Lithos 115, 27–39. https://doi.org/10.1016/j.lithos.2009.11.001

Hermann, J., Green, D.H., 2001. Experimental constraints on high pressure melting in subducted crust. Earth Planet. Sci. Lett. 188, 149–168.

Hermann, J., Rubatto, D., 2009. Accessory phase control on the trace element signature of sediment melts in subduction zones. Chem. Geol. 265, 512–526. https://doi.org/10.1016/j.chemgeo.2009.05.018

Hermann, J., Zheng, Y.F., Rubatto, D., 2013. Deep fluids in subducted continental crust. Elements 9, 281–287. https://doi.org/10.2113/gselements.9.4.281

Herzberg, C., Condie, K., Korenaga, J., 2010. Thermal history of the Earth and its petrological expression. Earth Planet. Sci. Lett. 292, 79–88. https://doi.org/10.1016/J.EPSL.2010.01.022

Hogan, J.P., 1993. Monomineralic glomerocrysts: textural evidence for mineral resorption during crystallization of igneous rocks. J. Geol. 101, 531–540. https://doi.org/10.1086/648245

Huang, G., Mitchell, R. N., Palin, R. M., Spencer, C. J., & Guo, J., 2022. Barium content of Archaean continental crust reveals the onset of subduction was not global. Nature Communications, 13(1), 6553.

Humphreys, M.C.S., Blundy, J.D., Sparks, R.S.J., 2006. Magma Evolution and Open-System Processes at Shiveluch Volcano: Insights from Phenocryst Zoning. J. Petrol. 47, 2303–2334. https://doi.org/10.1093/petrology/egl045

Huw Davies, J., von Blanckenburg, F., 1995. Slab breakoff: A model of lithosphere detachment and its test in the magmatism and deformation of collisional orogens. Earth Planet. Sci. Lett. 129, 85–102. https://doi.org/10.1016/0012-821X(94)00237-S

Jahn, B.-M., Glikson, A.Y., Peucat, J.J., Hickman, A.H., 1981. REE geochemistry and isotopic data of Archean silicic volcanics and granitoids from the Pilbara Block, Western Australia: implications for the early crustal evolution. Geochim. Cosmochim. Acta 45, 1633–1652.

Ji, W.Q., Malusà, M.G., Tiepolo, M., Langone, A., Zhao, L., Wu, F.Y., 2019. Synchronous Periadriatic magmatism in the Western and Central Alps in the absence of slab breakoff. Terra Nov. https://doi.org/10.1111/ter.12377

Jiang, Y.H., Jiang, S.Y., Ling, H.F., Dai, B.Z., 2006. Low-degree melting of a metasomatized lithospheric mantle for the origin of Cenozoic Yulong monzogranite-porphyry, east Tibet: Geochemical and Sr-Nd-Pb-Hf isotopic constraints. Earth Planet. Sci. Lett. 241, 617–633. https://doi.org/10.1016/j.epsl.2005.11.023

Jochum, K.P., Weis, U., Schwager, B., Stoll, B., Wilson, S.A., Haug, G.H., Andreae, M.O., Enzweiler, J., 2016. Reference Values Following ISO Guidelines for Frequently Requested Rock Reference Materials. Geostand. Geoanalytical Res. 40, 333–350. https://doi.org/10.1111/j.1751-908X.2015.00392.x

Jochum, K.P., Willbold, M., Raczek, I., Stoll, B., Herwig, K., 2005. Chemical characterisation of the USGS reference glasses GSA-1G, GSC-1G, GSD-1G, GSE-1G, BCR-2G, BHVO-2G and BIR-1G using EPMA, ID-TIMS, ID-ICP-MS and LA-ICP-MS. Geostand. Geoanalytical Res. 29, 285–302. https://doi.org/10.1111/j.1751-908x.2005.tb00901.x

Johnson, M.C., Plank, T., 2000. Dehydration and melting experiments constrain the fate of subducted sediments. Geochemistry, Geophys. Geosystems 1.

Johnson, T.E., Kirkland, C.L., Gardiner, N.J., Brown, M., Smithies, R.H., Santosh, M., 2019. Secular change in TTG compositions: Implications for the evolution of Archaean geodynamics. Earth Planet. Sci. Lett. 505, 65–75.

Kagami, H., Ulmer, P., Hansmann, W., Dietrich, V., & Steiger, R. H., 1991. Nd-Sr isotopic and geochemical characteristics of the southern Adamello (northern Italy) intrusives: Implications for crustal versus mantle origin. Journal of Geophysical Research: Solid Earth, 96(B9), 14331-14346

Kamber, B.S., Ewart, A., Collerson, K.D., Bruce, M.C., McDonald, G.D., 2002. Fluid-mobile trace element constraints on the role of slab melting and implications for Archaean crustal growth models. Contrib. to Mineral. Petrol. 144, 38–56.

Kemp, A.I.S., Hawkesworth, C.J., 2003. Granitic Perspectives on the Generation and Secular Evolution of the Continental Crust. Treatise on Geochemistry 3–9, 350–410. https://doi.org/10.1016/B0-08-043751-6/03027-9.

Kendrick, J., Duguet, M., Yakymchuk, C., 2022. Diversification of Archean tonalite-trondhjemite-granodiorite suites in a mushy middle crust. Geology 50, 76–80.

Kessel, R., Schmidt, M.W., Ulmer, P., Pettke, T., 2005. Trace element signature of subduction-zone fluids, melts and supercritical liquids at 120-180 km depth. Nature 437, 724–727. https://doi.org/10.1038/nature03971

Laubscher, H., 2010. Jura, Alps and the boundary of the Adria subplate. Tectonophysics 483, 223–239. https://doi.org/10.1016/j.tecto.2009.10.011.

Laurent, O., Martin, H., Doucelance, R., Moyen, J.F., Paquette, J.L., 2011. Geochemistry and petrogenesis of high-K "sanukitoids" from the Bulai pluton, Central Limpopo Belt, South Africa: Implications for geodynamic changes at the Archaean-Proterozoic boundary. Lithos 123, 73–91.

Laurent, O., Björnsen, J., Wotzlaw, J.F., Bretscher, S., Pimenta Silva, M., Moyen, J.F., Ulmer, P., Bachmann, O., 2020. Earth's earliest granitoids are crystal-rich magma reservoirs tapped by silicic eruptions. Nat. Geosci. 13, 163–169.https://doi.org/10.1038/s41561-019-0520-6

Laurent, O., Martin, H., Moyen, J.F., Doucelance, R., 2014. The diversity and evolution of late-Archean granitoids: Evidence for the onset of "modern-style" plate tectonics between 3.0 and 2.5 Ga. Lithos 205, 208–235. https://doi.org/10.1016/j.lithos.2014.06.012

Lemoine, M., 2003. Schistes lustrés from Corsica to Hungary : back to the original sediments and tentative dating of partly azoic metasediments. Bull. la Société Géologique Fr. 174, 197–209. https://doi.org/10.2113/174.3.197

Liati, A., Froitzheim, N., 2006. Assessing the Valais ocean, Western Alps: U-Pb SHRIMP zircon geochronology of eclogite in the Balma unit, on top of the Monte Rosa nappe. Eur. J. Mineral. 18, 299–308.

Liati, A., Froitzheim, N., Fanning, C.M., 2005. Jurassic ophiolites within the Valais domain of the Western and Central Alps: geochronological evidence for re-rifting of oceanic crust. Contrib. to Mineral. Petrol. 149, 446–461.

Lima, B.T.A., Ferreira, V.P., Ardila, D.H., Neves, C.H.F.S., Sial, A.N., 2021. Crystallization conditions of the Carmo stock, NE Brazil: Implications for magmatic epidote-bearing granitoids petrogenesis. J. South Am. Earth Sci. 110, 103427. https://doi.org/10.1016/j.jsames.2021.103427

Lobach-Zhuchenko, S.B., Rollinson, H., Chekulaev, V.P., Savatenkov, V.M., Kovalenko, A. V, Martin, H., Guseva, N.S., Arestova, N.A., 2008. Petrology of a Late Archaean, Highly Potassic, Sanukitoid Pluton from the Baltic Shield: Insights into Late Archaean Mantle Metasomatism. J. Petrol. 49, 393–420. https://doi.org/10.1093/petrology/egm084

Lobach-Zhuchenko, S.B., Rollinson, H.R., Chekulaev, V.P., Arestova, N.A., Kovalenko, A. V, Ivanikov, V. V, Guseva, N.S., Sergeev, S.A., Matukov, D.I., Jarvis, K.E., 2005. The Archaean sanukitoid series of the Baltic Shield: geological setting, geochemical characteristics and implications for their origin. Lithos 79, 107–128. https://doi.org/https://doi.org/10.1016/j.lithos.2004.04.052

Lustrino, M., Duggen, S., Rosenberg, C.L., 2011. The Central-Western Mediterranean: Anomalous igneous activity in an anomalous collisional tectonic setting. Earth-Science Rev. 104, 1–40. https://doi.org/10.1016/j.earscirev.2010.08.002

Macera, P., G., F., A., P., E., C., 1983. A geochemical study on the acid and basic rocks of the Adamello batholith. Mem. Soc. Geol. It. 26, 223–259.

Macera, P., Gasperini, D., Ranalli, G., Mahatsente, R., 2008. Slab detachment and mantle plume upwelling in subduction zones: An example from the Italian South-Eastern Alps. J. Geodyn. 45, 32–48. https://doi.org/10.1016/j.jog.2007.03.004

Martin, H., 1999. Adakitic magmas: Modern analogues of Archaean granitoids. Lithos 46, 411–429. https://doi.org/10.1016/S0024-4937(98)00076-0

Martin, H., 1994. The Archean grey gneisses and the genesis of continental crust, in: Developments in Precambrian Geology. Elsevier, pp. 205–259.

Martin, H., Moyen, J.F., 2002. Secular changes in tonalite-trondhjemite-granodiorite composition as markers of the progressive cooling of Earth. Geology 30, 319–322.

Martin, H., Moyen, J.F., Rapp, R., 2009. The sanukitoid series: Magmatism at the Archaean-Proterozoic transition. Earth Environ. Sci. Trans. R. Soc. Edinburgh 100, 15–33. https://doi.org/10.1017/S1755691009016120

Martin, H., Smithies, R.H., Rapp, R., Moyen, J.F., Champion, D., 2005. An overview of adakite, tonalite-trondhjemiten-granodiorite (TTG), and sanukitoid: Relationships and some implications for crustal evolution. Lithos 79, 1–24. https://doi.org/10.1016/j.lithos.2004.04.048

Martin, S., Bigazzi, G., Zattin, M., Viola, G., Balestrieri, M.L., 1998. Neogene kinematics of the Giudicarie fault (Central-Eastern Alps, Italy): new apatite fission-track data. Terra Nov. 10, 217–221. https://doi.org/https://doi.org/10.1046/j.1365-3121.1998.00119.x

Mattioli, M., Di Battistini, G., Zanzucchi, G., 2002. Geochemical features of the Tertiary buried Mortara volcanic body (Northern Apennines, Italy). Boll. Soc. Geol. It. 1, 239–249.

Mayer, A., Cortiana, G., Dal Piaz, G., Deloule, E., Pieri, R., Jobstraibizer, P., 2003. U-Pb single zircon ages of the Adamello batholith, Southern Alps. Mem. di Sci. Geol. 55, 151–167.

McCarthy, A., Chelle-Michou, C., Müntener, O., Arculus, R., Blundy, J., 2018. Subduction initiation without magmatism: The case of the missing Alpine magmatic arc. Geology 46, 1059–1062.

McDonough, W.F., Sun, S. s., 1995. The composition of the Earth. Chem. Geol. 120, 223–253. https://doi.org/10.1016/0009-2541(94)00140-4

Métrich, N., Wallace, P.J., 2008. Volatile Abundances in Basaltic Magmas and Their Degassing Paths Tracked by Melt Inclusions. Rev. Mineral. Geochemistry 69, 363–402. https://doi.org/10.2138/rmg.2008.69.10

Miller, J.S., Matzel, J.E.P., Miller, C.F., Burgess, S.D., Miller, R.B., 2007. Zircon growth and recycling during the assembly of large, composite arc plutons. J. Volcanol. Geotherm. Res. 167, 282–299. https://doi.org/10.1016/j.jvolgeores.2007.04.019

Montresor, L., Rigatti, G., 1995. Le tonaliti foliate nel settore Nord-Orientale del Plutone della Presanella-Nota preliminare. Atti Tic. Sc. Terra (Serie Spec. 3, 41–44.

Moyen, J.F., 2011. The composite Archaean grey gneisses: Petrological significance, and evidence for a non-unique tectonic setting for Archaean crustal growth. Lithos 123, 21–36. https://doi.org/10.1016/j.lithos.2010.09.015

Moyen, J.F., Janoušek, V., Laurent, O., Bachmann, O., Jacob, J.B., Farina, F., Fiannacca, P., Villaros, A., 2021. Crustal melting vs. fractionation of basaltic magmas: Part 1, granites and paradigms. Lithos 402–403. https://doi.org/10.1016/j.lithos.2021.106291

Moyen, J.F., Martin, H., 2012. Forty years of TTG research. Lithos 148, 312–336. https://doi.org/10.1016/j.lithos.2012.06.010

Müntener, O., Ulmer, P., Blundy, J.D., 2021. Superhydrous arc magmas in the alpine context. Elements 17, 35–40. https://doi.org/10.2138/GSELEMENTS.17.1.35

Nelson, S.T., Montana, A., 1992. Sieve-textured plagioclase in volcanic rocks produced by rapid decompression. Am. Mineral. 77, 1242–1249.

Pamić, J., Tomljenović, B., Balen, D., 2002. Geodynamic and petrogenetic evolution of Alpine ophiolites from the central and NW Dinarides: an overview. Lithos 65, 113–142.

Pennacchioni, G., Di Toro, G., Brack, P., Menegon, L., Villa, I.M., 2006. Brittle–ductile–brittle deformation during cooling of tonalite (Adamello, Southern Italian Alps). Tectonophysics 427, 171–197.

Plank, T., 2013. The Chemical Composition of Subducting Sediments, 2nd ed, Treatise on Geochemistry: Second Edition. Elsevier Ltd. https://doi.org/10.1016/B978-0-08-095975-7.00319-3

Plank, T., 2005. Constraints from Thorium/Lanthanum on sediment recycling at subduction zones and the evolution of the continents. J. Petrol. 46, 921–944. https://doi.org/10.1093/petrology/egi005

Plank, T., Langmuir, C.H., 1998. The chemical composition of subducting sediment and its consequences for the crust and mantle. Chem. Geol. 145, 325–394. https://doi.org/10.1016/S0009-2541(97)00150-2

Portnyagin, M., Hoernle, K., Plechov, P., Mironov, N., Khubunaya, S., 2007. Constraints on mantle melting and composition and nature of slab components in volcanic arcs from volatiles (H2O, S, Cl, F) and trace elements in melt inclusions from the Kamchatka Arc. Earth Planet. Sci. Lett. 255, 53–69. https://doi.org/https://doi.org/10.1016/j.epsl.2006.12.005

Press, C., 2010. Zoning in Igneous Plagioclase : Patchy Zoning Author (s): Joseph A . Vance Source : The Journal of Geology , Vol . 73 , No . 4 (Jul ., 1965), pp . 636-651 Published by : The University of Chicago Press Stable URL : http://www.jstor.org/stable/30069386 73, 636–651.

Rapp, R.P., Shimizu, N., Norman, M.D., 2003. Growth of early continental crust by partial melting of eclogite. Nature 425, 605–609. https://doi.org/10.1038/nature02031

Rapp, R.P., Norman, M.D., Laporte, D., Yaxley, G.M., Martin, H., Foley, S.F., 2010. Continent formation in the Archean and chemical evolution of the cratonic lithosphere: melt–rock reaction experiments at 3–4 GPa and petrogenesis of Archean Mg-diorites (sanukitoids). J. Petrol. 51, 1237–1266.

Ratschbacher, L., Dingeldey, C., Miller, C., Hacker, B.R., McWilliams, M.O., 2004. Formation, subduction, and exhumation of Penninic oceanic crust in the Eastern Alps: time constraints from 40Ar/39Ar geochronology. Tectonophysics 394, 155–170.

Relvini, A., Martin, S., Carvalho, B.B., Prosser, G., Toffolo, L., Macera, P., Bartoli, O., 2022. Genesis of the Eastern Adamello Plutons (Northern Italy): Inferences for the Alpine Geodynamics. Geosci. 12. https://doi.org/10.3390/geosciences12010013

Renjith, M.L., 2014. Micro-textures in plagioclase from 1994-1995 eruption, Barren Island Volcano: Evidence of dynamic magma plumbing system in the Andaman subduction zone. Geosci. Front. 5, 113–126. https://doi.org/10.1016/j.gsf.2013.03.006

Rollinson, H., 2021. Do all Archaean TTG rock compositions represent former melts? Precambrian Res. 367, 106448.

Roman, A., & Arndt, N. (2020). Differentiated Archean oceanic crust: Its thermal structure, mechanical stability and a test of the sagduction hypothesis. Geochimica et Cosmochimica Acta, 278, 65-77.

Romer, R.L., Siegesmund, S., 2003. Why allanite may swindle about its true age. Contrib. to Mineral. Petrol. 146, 297–307.

Rosenbaum, G., Lister, G.S., 2005. The Western Alps from the Jurassic to Oligocene: spatio-temporal constraints and evolutionary reconstructions. Earth-Science Rev. 69, 281–306.

Rosenberg, C.L., 2004. Shear zones and magma ascent: A model based on a review of the Tertiary magmatism in the Alps. Tectonics 23. https://doi.org/10.1029/2003TC001526

Rosenberg, C.L., Berger, A., Schmid, S.M., 1995. Observations from the floor of a granitoid pluton: Inferences on the driving force of final emplacement. Geology 23, 443–446.

Rottura, A., Moro, A. Del, Caggianelli, A., Bargossi, G.M., Gasparotto, G., 1997. Petrogenesis of the Monte Croce granitoids in the context of Permian magmatism in the Southern Alps, Italy. Eur. J. Mineral. 9, 1293–1310. https://doi.org/10.1127/ejm/9/6/1293

Rubatto, D., Hermann, J., 2003. Zircon formation during fluid circulation in eclogites (Monviso, Western Alps): implications for Zr and Hf budget in subduction zones. Geochim. Cosmochim. Acta 67, 2173–2187.

Rudnick, R.L., Gao, S., 2003. Rudnick_Gao_Treatise. Treatise on geochemistry 3, 1–64.

Ruprecht, P., Wörner, G., 2007. Variable regimes in magma systems documented in plagioclase zoning patterns: El Misti stratovolcano and Andahua monogenetic cones. J. Volcanol. Geotherm.Res.165,142–162. https://doi.org/https://doi.org/10.1016/j.jvolgeores.2007.06.002

Rustioni, G., Audetat, A., Keppler, H., 2021. The composition of subduction zone fluids and the origin of the trace element enrichment in arc magmas. Contrib. to Mineral. Petrol. 176, 1–19. https://doi.org/10.1007/s00410-021-01810-8

Rutherford, M.J., Hill, P.M., 1993. Magma ascent rates from amphibole breakdown: An experimental study applied to the 1980–1986 Mount St. Helens eruptions. J. Geophys. Res. Solid Earth 98, 19667–19685. https://doi.org/10.1029/93JB01613

Sanfilippo, A., Tribuzio, R., 2013. Building of the deepest crust at a fossil slow-spreading centre (Pineto gabbroic sequence, Alpine Jurassic ophiolites). Contrib. to Mineral. Petrol. 165, 705–721.

Sanfilippo, A., Tribuzio, R., 2011. Melt transport and deformation history in a nonvolcanic ophiolitic section, northern Apennines, Italy: implications for crustal accretion at slow spreading settings. Geochemistry, Geophys. Geosystems 12.

Schaltegger, U., Brack, P., Ovtcharova, M., Peytcheva, I., Schoene, B., Stracke, A., Marocchi, M., Bargossi, G.M., 2009. Zircon and titanite recording 1.5 million years of magma accretion, crystallization and initial cooling in a composite pluton (southern Adamello batholith, northern Italy). Earth Planet. Sci. Lett. 286, 208–218. https://doi.org/10.1016/j.epsl.2009.06.028

Schaltegger, U., Nowak, A., Ulianov, A., Fisher, C.M., Gerdes, A., Spikings, R., Whitehouse, M.J., Bindeman, I., Hanchar, J.M., Duff, J., Vervoort, J.D., Sheldrake, T., Caricchi, L., Brack, P., Müntener, O., 2019. Zircon Petrochronology and 40Ar/39Ar Thermochronology of the Adamello Intrusive Suite, N. Italy: Monitoring the Growth and Decay of an Incrementally Assembled Magmatic System. J. Petrol. 60, 701–722. https://doi.org/10.1093/petrology/egz010

Schettino, E., Poli, S., 2020. Hydrous Carbonatitic Liquids Drive CO2 Recycling From Subducted Marls and Limestones. Geophys. Monogr. Ser. 249, 209–221. https://doi.org/10.1002/9781119508229.ch18

Schmid, S.M., Fügenschuh, B., Kissling, E., Schuster, R., 2004. Tectonic map and overall architecture of the Alpine orogen. Eclogae Geol. Helv. 97, 93–117. https://doi.org/10.1007/s00015-004-1113-x

Schmidt, M.W., Poli, S., 2004. Magmatic epidote. Rev. Mineral. Geochemistry 56, 399–430. https://doi.org/10.2138/gsrmg.56.1.399

Schoene, B., Schaltegger, U., Brack, P., Latkoczy, C., Stracke, A., Günther, D., 2012. Rates of magma differentiation and emplacement in a ballooning pluton recorded by U-Pb TIMS-TEA, Adamello batholith, Italy. Earth Planet. Sci. Lett. 355–356, 162–173. https://doi.org/10.1016/j.epsl.2012.08.019

Shirey, S.B., Hanson, G.N., 1984. Mantle-derived Archaean monozodiorites and trachyandesites. Nature 310, 222–224. https://doi.org/10.1038/310222a0

Shore, M., Fowler, A.D., 1996. Oscillatory zoning in minerals; a common phenomenon. Can. Mineral. 34, 1111–1126.

Sial, A.N., Vasconcelos, P.M., Ferreira, V.P., Pessoa, R.R., Brasilino, R.G., Morais Neto, J.M., 2008. Geochronological and mineralogical constraints on depth of emplacement and ascencion rates of epidote-bearing magmas from northeastern Brazil. Lithos 105, 225–238. https://doi.org/10.1016/j.lithos.2008.04.002

Sizova, E., Gerya, T., Stüwe, K., Brown, M., 2015. Generation of felsic crust in the Archean: A geodynamic modeling perspective. Precambrian Res. 271, 198–224. https://doi.org/10.1016/j.precamres.2015.10.005

Skopelitis, A., 2014. Formation of a Tonalitic Batholith Through Sequential Accretion of Magma Batches : A Study of Chemical Composition , Age and Emplacement Mechanisms of the Adamello Batholith , N . Italy 328.

Sláma, J., Košler, J., Condon, D.J., Crowley, J.L., Gerdes, A., Hanchar, J.M., Horstwood, M.S.A., Morris, G.A., Nasdala, L., Norberg, N., Schaltegger, U., Schoene, B., Tubrett, M.N., Whitehouse, M.J., 2008. Plešovice zircon - A new natural reference material for U-Pb and Hf isotopic microanalysis. Chem. Geol. 249, 1–35. https://doi.org/10.1016/j.chemgeo.2007.11.005

Smith, V.C., Blundy, J.D., Arce, J.L., 2009. A Temporal Record of Magma Accumulation and Evolution beneath Nevado de Toluca, Mexico, Preserved in Plagioclase Phenocrysts. J. Petrol. 50, 405–426. https://doi.org/10.1093/petrology/egp005

Smithies, R.H., Champion, D.C., 2000. The Archaean high-Mg diorite suite: links to tonalite–trondhjemite–granodiorite magmatism and implications for early Archaean crustal growth. J. Petrol. 41, 1653–1671.

Smithies, R.H., Champion, D.C., 1999. Late Archaean felsic alkaline igneous rocks in the Eastern Goldfields, Yilgarn Craton, Western Australia: a result of lower crustal delamination? J. Geol. Soc. London. 156, 561–576.

Smithies, R.H., 2000. The Archaean tonalite-trondhjemite-granodiorite (TTG) series is not an analogue of Cenozoic adakite. Earth Planet. Sci. Lett. 182, 115–125. https://doi.org/10.1016/S0012-821X(00)00236-3

Smithies, R.H., Lu, Y., Johnson, T.E., Kirkland, C.L., Cassidy, K.F., Champion, D.C., Mole, D.R., Zibra, I., Gessner, K., Sapkota, J., De Paoli, M.C., Poujol, M., 2019. No evidence for high-pressure melting of Earth's crust in the Archean. Nat. Commun. 10, 5559. https://doi.org/10.1038/s41467-019-13547-x

Smithies, R.H., Lu, Y., Kirkland, C.L., Johnson, T.E., Mole, D.R., Champion, D.C., Martin, L., Jeon, H., Wingate, M.T.D., Johnson, S.P., 2021. Oxygen isotopes trace the origins of Earth's earliest continental crust. Nature 592, 70–75.

Stampfli, G.M., Borel, G.D., Marchant, R., Mosar, J., 2002. Western Alps geological constraints on western Tethyan reconstructions. J. Virtual Explor. 8, 77–106.

Stampfli, G.M., Mosar, J., Marquer, D., Marchant, R., Baudin, T., Borel, G., 1998. Subduction and obduction processes in the Swiss Alps. Tectonophysics 296, 159–204. https://doi.org/https://doi.org/10.1016/S0040-1951(98)00142-5

Steenfelt, A., Garde, A.A., Moyen, J.-F., 2005. Mantle wedge involvement in the petrogenesis of Archaean grey gneisses in West Greenland. Lithos 79 (1–2), 207–228.

Stern, R.A., Hanson, G.N., Shirey, S.B., 1989. Petrogenesis of mantle-derived, LILE-enriched Archean monzodiorites and trachyandesites (sanukitoids) in southwestern Superior Province. Can. J. Earth Sci. 26, 1688–1712.

Stern, R.A., Hanson, G.N., 1991. Archean high-Mg granodiorite: a derivative of light rare earth element-enriched monzodiorite of mantle origin. J. Petrol. 32, 201–238.

Streck, M.J., 2008. Mineral textures and zoning as evidence for open system processes. Rev. Mineral. Geochemistry 69, 595–622. https://doi.org/10.2138/rmg.2008.69.15

Sun, W., Zhao, L., Malusà, M.G., Guillot, S., Fu, L.Y., 2019. 3-D Pn tomography reveals continental subduction at the boundaries of the Adriatic microplate in the absence of a precursor oceanic slab. Earth Planet. Sci. Lett. 510, 131–141. https://doi.org/10.1016/j.epsl.2019.01.012

Syracuse, E.M., van Keken, P.E., Abers, G.A., Suetsugu, D., Bina, C., Inoue, T., Wiens, D., Jellinek, M., 2010. The global range of subduction zone thermal models. Phys. Earth Planet. Inter. 183, 73–90. https://doi.org/10.1016/j.pepi.2010.02.004

Tarney, J., Jones, C.E., 1994. Trace element geochemistry of orogenic igneous rocks and crustal growth models. J. - Geol. Soc. 151, 855–868. https://doi.org/10.1144/gsjgs.151.5.0855

Tepley III, F.J., Davidson, J.P., Tilling, R.I., Arth, J.G., 2000. Magma Mixing, Recharge and Eruption Histories Recorded in Plagioclase Phenocrysts from El Chichón Volcano, Mexico. J. Petrol. 41, 1397–1411. https://doi.org/10.1093/petrology/41.9.1397

Tiepolo, M., Tribuzio, R., 2005. Slab-melting during Alpine orogeny: Evidence from mafic cumulates of the Adamello batholith (Central Alps, Italy). Chem. Geol. 216, 271–288. https://doi.org/10.1016/j.chemgeo.2004.11.014

Tiepolo, M., Tribuzio, R., Ji, W.Q., Wu, F.Y., Lustrino, M., 2014. Alpine Tethys closure as revealed by amphibole-rich mafic and ultramafic rocks from the Adamello and the Bergell intrusions (Central Alps). J. Geol. Soc. London. 171, 793–799.

https://doi.org/10.1144/jgs2013-139

Tiepolo, M., Tribuzio, R., Langone, A., 2011. High-mg andesite petrogenesis by amphibole crystallization and ultramafic crust assimilation: Evidence from Adamello hornblendites (Central Alps, Italy). J. Petrol. 52, 1011–1045. https://doi.org/10.1093/petrology/egr016

Tiepolo, M., Tribuzio, R., Vannucci, R., 2002. The compositions of mantle-derived melts developed during the alpine continental collision. Contrib. to Mineral. Petrol. 144, 1–15. https://doi.org/10.1007/s00410-002-0387-0

Trener, G.B., 1912. Die sechsfache Eruptionsfolge des Adamello. Das postrhfitische Alter der Tonalizwillingsmasse. Vehr Geol Reichsanst 3, 98–112.

Turner, S., Costa, F., 2007. Measuring Timescales of Magmatic Evolution. Elements 3, 267–272. https://doi.org/10.2113/gselements.3.4.267

Ulmer, P., Callegari, E., Sonderegger, U.C., 1983. Genesis of the mafic and ultramafic rocks and their genetical relations to the tonalitic-trondhjemitic granitoids of the southern part of the Adamello Batholith (Northern Italy). Mem. Soc. Geol. It. 26, 171–222.

Veizer, J., Mackenzie, F.T., 2003. Evolution of sedimentary rocks.

Vermeesch, P., 2018. IsoplotR: A free and open toolbox for geochronology. Geosci. Front. 9, 1479–1493. https://doi.org/https://doi.org/10.1016/j.gsf.2018.04.001

Vervoort, J.D., Kemp, A.I.S., 2016. Clarifying the zircon Hf isotope record of crust-mantle evolution. Chem. Geol. 425, 65–75. https://doi.org/10.1016/j.chemgeo.2016.01.023

Vervoort, J.D., Plank, T., Prytulak, J., 2011. The Hf-Nd isotopic composition of marine sediments. Geochim. Cosmochim. Acta 75, 5903–5926. https://doi.org/10.1016/j.gca.2011.07.046

VILLA, I.M., 1983. 40Ar/39Ar chronology of the Adamello gabbros, southern Alps. Mem. della Soc. Geol. Ital. 26, 309–318.

Viola, G., Mancktelow, N.S., Seward, D., 2001. Late Oligocene-Neogene evolution of Europe-Adria collision: New structural and geochronological evidence from the Giudicarie fault system (Italian Eastern Alps). Tectonics 20, 999–1020.

Visonà, D., Caironi, V., Carraro, A., Dallai, L., Fioretti, A.M., Fanning, M., 2007. Zircon megacrysts from basalts of the Venetian Volcanic Province (NE Italy): U-Pb ages, oxygen isotopes and REE data. Lithos 94, 168–180. https://doi.org/10.1016/j.lithos.2006.06.007

Wiedenbeck, M., Hanchar, J.M., Peck, W.H., Sylvester, P., Valley, J., Whitehouse, M., Kronz, A., Morishita, Y., Nasdala, L., n.d. Further Characterisation of the 91500 Zircon Crystal 28, 9–39.

Wiederkehr, M., Sudo, M., Bousquet, R., Berger, A., Schmid, S.M., 2009. Alpine orogenic evolution from subduction to collisional thermal overprint: The 40Ar/39Ar age constraints from the Valaisan Ocean, central Alps. Tectonics 28.

Wilde, S.A., Valley, J.W., Peck, W.H., Graham, C.M., 2001. Evidence from detrital zircons for the existence of continental crust and oceans on the Earth 4.4 Gyr ago. Nature 409, 175–178.

Woodhead, J.D., Hergt, J.M., 2005. A preliminary appraisal of seven natural zircon reference materials for in situ Hf isotope determination. Geostand. Geoanalytical Res. 29, 183–195. https://doi.org/10.1111/j.1751-908x.2005.tb00891.x

Ye, H.M., Li, X.H., Li, Z.X., Zhang, C.L., 2008. Age and origin of high Ba-Sr appinite-granites at the northwestern margin of the Tibet Plateau: Implications for early Paleozoic tectonic evolution of the Western Kunlun orogenic belt. Gondwana Res. 13, 126–138. https://doi.org/10.1016/j.gr.2007.08.005

Yuan, C., Zhou, M.F., Sun, M., Zhao, Y., Wilde, S., Long, X., Yan, D., 2010. Triassic granitoids in the eastern Songpan Ganzi Fold Belt, SW China: Magmatic response to geodynamics of the deep lithosphere. Earth Planet. Sci. Lett. 290, 481–492. https://doi.org/10.1016/j.epsl.2010.01.005

Zaccaria, D., Vicentini, N., Perna, M.G., Rosatelli, G., Sharygin, V. V., Humphreys-Williams, E., Brownscombe, W., Stoppa, F., 2021. Lamprophyre as the source of zircon in the Veneto region, Italy. Minerals 11, 1–29. https://doi.org/10.3390/min11101081

Zanchetta, S., Garzanti, E., Doglioni, C., Zanchi, A., 2012. The Alps in the Cretaceous: a doubly vergent pre-collisional orogen. Terra Nov. 24, 351–356.

Zanetti, A., Mazzucchelli, M., Rivalenti, G., Vannucci, R., 1999. The Finero phlogopite-peridotite massif: An example of subduction-related metasomatism. Contrib. to Mineral. Petrol. 134, 107–122. https://doi.org/10.1007/s004100050472

Zattin, M., Bazzolo, F., Giorio, L., Martin, S., Tornielli, V., 1995. Intrusioni multiple nell'area del Corno Alto, Massiccio dell'Adamello. Atti Ticinesi di Sci. della Terra 3, 45–56.

Zen, E.A., Hammarstrom, J.M., 1984. Magmatic epidote and its petrologic significance. Geology 12, 515–518.

Zhao, L., Paul, A., Malusà, M.G., Xu, X., Zheng, T., Solarino, S., Guillot, S., Schwartz, S., Dumont, T., Salimbeni, S., Aubert, C., Pondrelli, S., Wang, Q., Zhu, R., 2016. Continuity of the Alpine slab unraveled by high-resolution P wave tomography. J. Geophys. Res. Solid Earth 121, 8720–8737. https://doi.org/10.1002/2016JB013310

Zheng, Y.F., 2012. Metamorphic chemical geodynamics in continental subduction zones. Chem. Geol. 328, 5–48. https://doi.org/10.1016/j.chemgeo.2012.02.005

Zheng, Y.F., Xia, Q.X., Chen, R.X., Gao, X.Y., 2011. Partial melting, fluid supercriticality and element mobility in ultrahigh-pressure metamorphic rocks during continental collision. Earth-Science Rev. 107, 342–374. https://doi.org/10.1016/j.earscirev.2011.04.004

Appendix A

Table A.1 Compilation of geographic coordinates (location GPS points WGS84) from all samples.

Sample	Rock type	Name	Stop	Latitude	Longitude
CA19-15	Equigranular Tonalite	ETN	7	46° 8'9.29"N	10°42'34.14"E
CA19-16	Porphyritic Tonalite	PTN	7	46° 8'9.29"N	10°42'34.14"E
CA19-21	Equigranular Tonalite	ETN	11	46° 8'52.31"N	10°44'28.05"E
CA19-24	Equigranular Tonalite	ETN	13	46° 9'12.00"N	10°44'39.26"E
CA19-9	Two mica granodiorite	TMG	4	46° 8'35.28"N	10°41'28.38"E
CA19-10	Two mica granodiorite	TMG	5	46° 8'21.78"N	10°41'38.78"E
CA19-12	Two mica granodiorite	TMG	5	46° 8'21.78"N	10°41'38.78"E
CA19-13	Two mica granodiorite	TMG	6	46° 8'40.48"N	10°41'59.77"E
CA19-17	Two mica granodiorite	TMG	8	46° 8'5.68"N	10°42'34.14"E
CA19-36	Two mica granodiorite	TMG	18	46° 8'9.39"N	10°42'57.17"E
CA19-37	Two mica granodiorite	TMG	18	46° 8'9.39"N	10°42'57.17"E
CA19-39	Two mica granodiorite	TMG	20	46° 8'14.05"N	10°43'21.73"E
CA19-41	Two mica granodiorite	TMG	21	46° 8'11.75"N	10°43'30.57"E
CA19-26	Ep-bearing granodiorite	EBG	13	46° 9'12.00"N	10°44'39.26"E
CA19-29	Ep-bearing granodiorite	EBG	16	46°6'15.11"N	10°43'04.48"E
CA19-30	Ep-bearing granodiorite	EBG	16	46°6'15.11"N	10°43'04.48"E
CA19-31	Ep-bearing granodiorite	EBG	16	46°6'15.11"N	10°43'04.48"E
CA19-3	Diorite	MDR	3	46° 9'8.87"N	10°41'20.27"E
CA19-8	Mt. Ospedale tonalite	OTN	2	46° 9'8.87"N	10°41'20.27"E

Table A.2 Representative major element analyses of the Corno Alto and Sostino rocks.
Major element compositions are expressed in RAW.

wt.%

Sample	Rock Type	SiO_2	TiO_2	Al_2O_3	Fe_2O_3	MnO	MgO	CaO	Na_2O	K_2O	Cr_2O_3	P_2O_5	L.O.I.
CA19-9	TMG	70.20	0.21	16.98	1.89	0.09	0.81	3.09	4.50	1.90	bdl	0.11	0.60
CA19-10	TMG	71.49	0.23	15.59	1.90	0.10	0.62	2.38	3.88	3.12	bdl	0.13	0.62
CA19-12	TMG	71.08	0.25	15.96	2.25	0.09	0.71	2.74	4.04	2.07	bdl	0.12	0.74
CA19-13	TMG	70.09	0.22	16.63	2.25	0.12	0.82	3.25	4.42	2.10	bdl	0.13	0.49
CA19-17	TMG	69.66	0.24	16.90	2.13	0.08	0.75	3.07	4.52	1.78	bdl	0.10	0.78
CA19-36	TMG	71.00	0.22	16.14	2.01	0.07	0.67	2.52	4.12	2.42	bdl	0.10	0.85
CA19-37	TMG	70.29	0.25	16.66	2.41	0.09	0.84	3.18	4.50	1.58	bdl	0.09	0.55
CA19-39	TMG	71.43	0.22	15.88	2.10	0.08	0.65	2.64	4.39	2.33	bdl	0.09	0.62
CA19-41	TMG	71.16	0.21	16.17	2.04	0.10	0.66	2.61	4.09	2.63	bdl	0.13	0.68
CA19-15	ETN	66.21	0.34	17.68	3.33	0.10	1.36	4.29	4.39	1.78	bdl	0.15	0.62
CA19-16	PTN	65.51	0.37	17.68	3.54	0.13	1.65	4.44	4.23	1.73	bdl	0.19	0.69
CA19-24	ETN	65.28	0.46	17.97	3.93	0.12	1.54	4.43	4.42	1.62	bdl	0.20	0.61
CA19-21	ETN	67.11	0.43	16.83	3.58	0.11	1.49	4.13	4.08	1.96	bdl	0.16	0.64
CA19-26	EBG	69.25	0.31	16.56	2.42	0.09	0.89	3.13	4.32	2.38	bdl	0.12	0.77
CA19-29	EBG	68.33	0.31	16.66	2.34	0.08	0.96	3.49	4.52	2.53	bdl	0.11	1.12
CA19-30	EBG	68.50	0.30	16.80	2.24	0.07	0.90	3.34	4.47	2.69	bdl	0.14	0.69
CA19-31	EBG	69.29	0.35	15.67	2.47	0.08	1.04	3.42	4.04	2.83	bdl	0.20	1.22
CA19-3	MDR	48.87	1.31	16.11	9.28	0.30	9.62	9.01	2.24	1.89	0.03	0.29	1.05
CA19-8	OTN	62.37	0.61	17.63	5.71	0.12	2.21	5.50	3.00	2.17	bdl	0.18	0.61

Table A.3a Representative trace element analyses of the Corno Alto and Sostino rocks.
Trace element compositions are expressed in ppm.

Sample	CA19-9	CA19-10	CA19-12	CA19-13	CA19-17	CA19-36	CA19-37	CA19-39	CA19-41
Rock Type	TMG	TMG	TMG	TMG	TMG	TMG	TMG	TMG	TMG
Sc	5.31	5.10	5.93	5.40	4.88	5.09	5.79	5.24	5.28
V	34.1	32.5	36.1	42.0	31.1	30.2	33.1	33.5	31.4
Cr	26.0	20.8	30.1	23.4	22.8	25.5	16.7	30.0	22.9
Co	3.20	2.54	2.59	3.27	2.34	2.34	2.47	2.53	2.80
Ni	6.80	5.45	5.05	36.35	5.60	5.05	5.45	6.60	5.85
Cu	5.94	3.61	18.00	5.84	9.10	4.02	4.28	10.50	7.76
Zn	35.4	39.6	40.1	40.4	37.9	27.9	37.1	37.5	45.1
Rb	55.5	97.3	66.0	65.9	52.1	72.0	50.3	62.3	84.2
Sr	470	405	476	461	532	459	551	455	452
Y	12.2	13.7	13.9	9.4	11.8	10.6	16.1	14.2	12.0
Zr	77.2	87.6	94.7	83.7	103	89.4	120	101	95.5
Nb	16.2	18.1	18.4	16.9	16.1	17.4	16.7	21.3	17.3
Mo	0.375	0.285	0.275	0.635	0.335	0.470	0.460	0.400	0.615
Cs	1.45	2.38	2.35	2.20	1.11	1.50	1.51	1.55	2.99
Ba	917	949	702	821	1098	983	796	1053	1016
La	32.5	35.1	46.4	36.8	44.5	38.4	49.8	39.9	40.5
Ce	55.1	60.8	80.4	62.2	77.4	67.9	86.3	69.4	70.8
Pr	4.97	5.51	7.41	5.54	7.16	6.28	7.96	6.54	6.49
Nd	16.0	18.5	25.6	19.1	24.8	20.7	28.0	22.2	21.7
Sm	2.34	3.09	3.72	2.92	3.65	3.10	3.91	3.48	3.43
Eu	0.665	0.766	0.895	0.700	0.960	0.785	1.04	0.886	0.830
Gd	1.87	2.25	2.78	2.07	2.52	2.41	3.14	2.57	2.41
Tb	0.245	0.324	0.392	0.253	0.359	0.335	0.413	0.351	0.330
Dy	1.87	2.40	2.47	1.55	2.09	1.85	2.99	2.43	2.11
Ho	0.368	0.472	0.498	0.316	0.379	0.339	0.533	0.450	0.425
Er	1.19	1.42	1.34	1.00	1.24	1.08	1.78	1.41	1.17
Tm	0.164	0.185	0.233	0.150	0.173	0.154	0.233	0.236	0.187
Yb	1.48	1.55	1.56	1.09	1.16	1.00	1.57	1.67	1.32
Lu	0.205	0.214	0.222	0.163	0.190	0.164	0.211	0.227	0.173
Hf	2.20	2.54	2.65	2.35	2.78	2.42	3.30	2.74	2.67
Ta	1.48	1.43	1.11	1.08	0.75	1.10	0.714	2.10	1.32
Pb	34.1	37.5	25.0	23.7	27.1	32.6	22.9	43.5	30.2
Th	13.0	14.1	18.9	12.3	16.5	14.4	19.3	16.7	15.3
U	4.77	4.64	3.63	1.64	2.36	2.52	2.53	3.43	2.55
La/Yb_N	15.0	15.4	20.2	23.0	26.2	26.2	21.6	16.3	20.8
Sr/Y	38.3	29.6	34.2	49.2	45.2	43.1	34.1	32.1	37.5

Table A.3b Representative trace element analyses of the Corno Alto and Sostino rocks.
Trace element compositions are expressed in ppm.

Sample	CA19-15	CA19-16	CA19-24	CA19-21	CA19-26	CA19-29	CA19-30	CA19-31	CA19-3	CA19-8
Rock type	ETN	PTN	ETN	ETN	EBG	EBG	EBG	EBG	MDR	OTN
Sc	6.83	9.17	6.50	7.05	5.11	4.97	4.70	5.18	40.79	13.18
V	68.6	70.0	78.7	75.6	51.9	55.0	53.0	56.4	269	102
Cr	14.6	21.6	25.6	15.8	33.1	25.9	23.1	27.3	225	16.8
Co	5.57	6.44	6.93	6.47	4.45	4.58	4.42	4.72	33.0	9.44
Ni	5.70	7.85	8.85	6.85	7.75	6.60	8.20	5.65	103	7.00
Cu	18.70	5.23	8.69	7.53	70.40	9.16	6.56	4.59	5.99	5.27
Zn	49.7	65.7	52.2	44.9	45.9	37.9	33.2	38.1	151	65.6
Rb	50.6	57.7	60.0	62.1	62.3	77.2	80.7	83.8	69.8	79.4
Sr	662	884	577	511	665	661	675	597	544	299
Y	10.5	12.6	10.6	10.5	10.0	9.80	9.69	10.3	18.7	17.7
Zr	120	111	159	126	120	109	113	116	94.8	138
Nb	17.7	20.5	17.0	15.4	25.0	19.6	19.7	21.4	16.7	12.7
Mo	0.265	0.315	0.410	0.250	0.505	0.370	0.605	0.390	0.34	0.48
Cs	1.63	1.59	1.43	1.45	1.10	2.15	2.28	2.44	3.66	3.10
Ba	897	879	826	682	1614	1069	1167	1336	626.8	485.9
La	45.6	117	58.6	50.0	46.6	33.7	35.5	33.3	34.5	41.7
Ce	77.2	173	94.2	80.8	78.8	57.8	60.6	56.7	66.0	79.2
Pr	7.28	14.5	8.39	7.40	7.28	5.46	5.51	5.50	7.36	8.15
Nd	24.9	46.1	28.5	25.3	25.4	19.2	20.0	19.9	31.3	31.3
Sm	3.87	5.53	4.12	3.73	3.90	2.85	3.10	3.41	6.05	5.44
Eu	0.986	1.30	0.973	0.947	0.900	0.814	0.834	0.743	1.66	1.16
Gd	2.60	3.40	2.63	2.61	2.37	1.98	2.02	2.34	4.86	4.00
Tb	0.310	0.411	0.370	0.333	0.305	0.296	0.275	0.291	0.632	0.531
Dy	1.95	2.45	2.00	1.97	1.98	1.73	1.76	1.75	3.90	3.36
Ho	0.360	0.455	0.395	0.380	0.333	0.302	0.376	0.329	0.715	0.638
Er	1.04	1.32	1.11	1.08	0.970	1.02	1.04	1.05	2.00	1.84
Tm	0.152	0.191	0.162	0.159	0.135	0.130	0.144	0.150	0.274	0.259
Yb	1.12	1.30	1.12	1.22	1.03	1.08	1.01	1.09	1.78	2.00
Lu	0.171	0.193	0.176	0.184	0.155	0.182	0.172	0.175	0.250	0.284
Hf	3.14	2.76	3.89	3.21	3.15	3.05	3.06	3.04	2.57	3.60
Ta	1.17	1.12	0.93	0.92	1.69	1.44	1.41	1.47	0.812	0.972
Pb	18.8	16.7	19.3	17.1	27.3	40.9	40.6	32.3	6.37	14.9
Th	17.8	42.6	21.5	21.5	22.6	16.1	16.6	16.3	14.5	17.3
U	5.53	4.86	2.70	3.18	8.36	9.25	9.74	9.25	3.78	1.84
La/Yb_N	27.8	61.2	35.7	27.8	30.7	21.3	24.0	20.7	13.2	14.2
Sr/Y	62.9	70.4	54.2	48.5	66.4	67.4	69.6	58.0	29.1	16.9

Table A.4 Whole-rock standards analysis

	BE-N		JB-1		BHVO-1		JG-1		HUSG-1		WITS-G	
	Average	viation (%)	Average	iation (%)	Average	iation (%)	Average	iation (%)	Average	iation (%)	Average	iation (%)
	n=30		n=35		n=35		n=33		n=39		n=33	
SiO_2	38.42	0.09	52.41	0.46	49.80	0.04	72.47	0.24	69.92	0.22	74.91	0.51
TiO_2	2.65	2.41	1.31	2.02	2.75	0.55	0.26	0.36	0.57	4.31	0.27	6.90
Al_2O_3	10.19	1.40	14.61	0.55	13.87	1.17	14.54	2.37	14.06	2.25	12.13	5.19
Fe_2O_3	12.97	0.99	8.94	0.33	12.43	0.54	2.09	2.32	3.71	1.71	3.40	5.15
MnO	0.20	1.67	0.16	1.29	0.17	0.69	0.06	2.18	0.05	18.72	0.05	3.75
MgO	13.26	0.85	7.92	2.40	7.31	1.18	0.66	10.52	1.02	1.86	0.02	80.94
CaO	14.08	0.38	9.32	0.29	11.44	0.43	2.16	1.06	1.55	1.57	1.49	1.53
Na_2O	3.15	0.89	2.84	1.91	2.27	1.68	3.37	0.59	2.71	5.49	2.74	7.79
K_2O	1.41	0.92	1.44	0.78	0.52	2.94	3.98	0.36	4.63	0.54	4.45	0.27
Cr_2O_3	0.05	-	0.06	10.03	0.04	-	0.01	6.38	-	-	-	-
P_2O_5	1.08	1.36	0.27	5.54	0.28	5.34	0.09	6.89	0.21	0.43	0.04	1.56
L.O.I.	-	-	-	-	0.52	-	-	-	0.90	23.28	0.07	12.50
Sum Of Conc.	97.46	0.60	99.29	0.56	101.39	0.31	99.69	0.34	99.33	0.69	99.55	0.42

PANalytical
Results quantitative - MajorBasic32+Zn
Major element analysis by XRF, Rh Tube, 3kWatt
BDL = Below Detection Limit
Note: LOI = weight loss or gain at 1000ºC.
LOI (loss on ignition) includes the total of volatiles content of the rock
(including the water combined to the lattice of silicate minerals)
and the gain on ignition related to the oxidation of the rock (mostly due to Fe).

Table A.5 Trace element standards

	Certified BHVO glass		Certified BCR glass		Certified BHVO powder		Certified BCR powder	
	Average Analysed	*% Dev. from ref.value*	Average Analysed	*% Dev. from ref.value*	Average Analysed	*% Dev. from ref.value*	Average Analysed	*% Dev. from ref.value*
	n=5		n=5		n=10		n=10	
Sc	30.6	7.40	32.2	2.41	31.8	1.20	33.5	0.14
V	326	5.95	426	0.34	315	0.36	413	1.19
Cr	277	5.31	14.2	16.4	281	2.37	22.0	38.9
Co	44.1	0.11	36.0	5.26	41.1	8.53	34.4	7.79
Ni	122	4.98	11.6	10.8	124	3.68	14.2	12.9
Cu	122	3.70	16.1	23.2	126	8.51	20.4	3.91
Zn	119	16.5	151	21.0	97.3	7.41	127.8	1.34
Rb	9.27	0.72	46.9	0.18	8.77	7.93	43.6	5.19
Sr	380	4.14	318	7.11	371	7.04	317	5.98
Y	21.5	17.2	29.6	15.5	22.9	12.9	31.1	13.8
Zr	155	8.93	171	7.09	157	9.90	170	8.79
Nb	16.4	10.2	11.2	10.4	16.8	9.35	11.4	8.33
Mo	4.05	6.68	255	5.64	1.43	35.2	238	5.22
Cs	0.11	3.21	1.12	3.34	0.21	103	1.04	10.6
Ba	126	3.80	688	0.72	130	3.41	667	2.43
La	14.0	7.66	22.8	7.55	14.7	4.64	23.8	4.94
Ce	35.0	6.80	49.1	7.85	36.4	4.41	50.3	5.34
Pr	4.70	12.1	5.91	11.8	4.88	9.99	6.13	10.2
Nd	22.8	6.78	26.7	7.65	24.1	2.63	28.0	0.90
Sm	5.70	6.49	6.12	7.17	6.07	1.48	6.44	1.60
Eu	1.89	8.87	1.78	9.43	1.96	4.39	1.88	5.69
Gd	5.54	10.1	5.91	11.9	5.86	6.79	6.25	8.30
Tb	0.79	14.2	0.87	14.8	0.83	12.2	0.92	14.5
Dy	4.83	8.59	5.82	9.58	5.12	2.94	6.20	3.50
Ho	0.87	11.2	1.14	10.6	0.93	5.93	1.20	8.85
Er	2.29	10.5	3.30	10.8	2.44	2.55	3.50	4.63
Tm	0.29	12.8	0.47	8.82	0.32	4.07	0.48	9.79
Yb	1.83	9.01	3.10	8.44	1.96	1.46	3.25	4.27
Lu	0.25	10.4	0.45	11.3	0.26	5.80	0.47	7.80
Hf	3.85	10.9	4.24	12.4	4.07	8.29	4.47	10.1
Ta	1.02	11.3	0.69	11.5	1.07	8.71	0.70	10.7
Pb	1.72	1.46	10.4	5.73	2.30	12.8	10.9	3.29
Th	1.12	8.06	5.40	8.49	1.19	3.19	5.65	3.09
U	0.41	1.14	1.59	5.74	0.41	1.29	1.60	5.00

Analytical conditions:

Laser:
Resonetics 193nm Excimer laser
Energy: 3J/cm2
Frequency: 8 Hz
Spot: 2 spots of 104µm per sample
Ablation gas: He @ 0.4L/min
Ablation time: 25sec background, 40sec ablation

ICP-MS:
Agilent 8800
Carrier gas: 0.8L/min Ar + 0.004L/min Nitrogen

Reference std values:
BHVO & BCR glass

Jochum, K. P., Nohl, U., Herwig, K., Lammel, E., Stoll, B. and Hofmann, A. W. (2005), GeoReM: A New Geochemical Database for Reference Materials and Isotopic Standards. Geostandards and Geoanalytical

Jochum, K. P., Weis, U., Schwager, B., Stoll, B., Wilson, S. A., Haug, G. H., Andreae, M. O. and Enzweiler, J. (2016), Reference Values Following ISO Guidelines for Frequently Requested Rock Reference Materials. Geostandards and Geoanalytical Research. doi: 10.1111/j.1751-908X.2015.00392.x

Table A.6a Major element compositions of TMG plagioclase crystals

Sample	Rock	grain	Position	Spot	SiO_2	TiO_2	Al_2O_3	FeO	CaO	Na_2O	K_2O	Total	**An**	Ab	Or
CA19-13	TMG	1	rim	C3-19	60.36	0.00	25.11	0.00	6.59	7.33	0.21	99.63	**32.78**	65.98	1.24
CA19-13	TMG	1	mantle	C3-20	59.97	0.07	25.11	0.03	6.81	7.30	0.25	99.55	**33.51**	65.00	1.49
CA19-13	TMG	1	mantle	C3-21	60.97	0.00	24.49	0.06	5.97	8.13	0.31	99.97	**28.36**	69.88	1.76
CA19-13	TMG	1	mantle	C3-22	59.51	0.03	25.25	0.03	6.67	7.46	0.27	99.29	**32.55**	65.88	1.56
CA19-13	TMG	1	mantle	C3-23	56.73	0.00	27.25	0.04	9.00	5.99	0.18	99.26	**44.88**	54.05	1.07
CA19-13	TMG	1	core	C3-24	46.58	0.00	34.19	0.08	17.09	1.72	0.03	99.76	**84.47**	15.38	0.15
CA19-13	TMG	1	core	C3-25	48.57	0.01	32.73	0.13	15.28	2.51	0.05	99.30	**76.85**	22.84	0.31
CA19-13	TMG	1	mantle	C3-26	56.34	0.00	27.68	0.03	9.32	5.77	0.17	99.32	**46.68**	52.30	1.02
CA19-13	TMG	1	mantle	C3-27	58.92	0.00	25.21	0.00	7.01	7.09	0.24	98.51	**34.84**	63.76	1.41
CA19-13	TMG	1	mantle	C3-28	60.42	0.00	24.32	0.05	5.83	7.91	0.30	98.90	**28.44**	69.83	1.73
CA19-13	TMG	1	mantle	C3-29	59.34	0.00	25.35	0.01	6.50	7.38	0.25	98.93	**32.25**	66.27	1.48
CA19-13	TMG	1	rim	C3-5	63.89	0.00	20.33	0.05	2.82	10.85	0.23	98.94	**12.41**	86.41	1.18
CA19-13	TMG	1	core	C3-30	49.51	0.01	32.03	0.15	15.00	2.85	0.07	99.64	**74.12**	25.48	0.40
CA19-13	TMG	1	core	C3-31	47.07	0.00	33.59	0.03	16.67	1.90	0.03	99.29	**82.74**	17.06	0.20
CA19-13	TMG	1	core	C3-32	45.67	0.00	34.79	0.10	17.65	1.36	0.01	99.64	**87.71**	12.23	0.06
CA19-13	TMG	1	core	C3-33	47.46	0.00	33.63	0.06	16.51	2.07	0.03	99.81	**81.36**	18.46	0.18
CA19-13	TMG	1	core	C3-34	46.94	0.00	34.14	0.07	16.84	1.66	0.01	99.75	**84.82**	15.13	0.05
CA19-13	TMG	2	rim	A5-19	64.83	0.00	21.39	0.05	2.92	9.72	0.16	99.07	**14.11**	84.98	0.92
CA19-13	TMG	2	mantle	A5-20	60.07	0.00	24.37	0.11	6.52	7.58	0.20	98.85	**31.85**	67.00	1.15
CA19-13	TMG	2	mantle	A5-21	57.35	0.06	25.80	0.08	8.40	6.59	0.09	98.39	**41.10**	58.35	0.55
CA19-13	TMG	2	core	A5-22	56.70	0.02	26.22	0.02	8.86	6.28	0.17	98.34	**43.38**	55.64	0.98
CA19-13	TMG	2	core	A5-23	55.84	0.03	27.33	0.06	10.16	5.83	0.13	99.43	**48.70**	50.57	0.72
CA19-13	TMG	3	rim	C1-1	63.54	0.00	22.19	0.09	4.41	9.37	0.13	99.72	**20.50**	78.80	0.70
CA19-13	TMG	3	mantle	C1-2	61.57	0.04	24.91	0.07	7.15	7.10	0.24	101.11	**35.25**	63.34	1.41
CA19-13	TMG	3	mantle	C1-3	57.12	0.00	26.02	0.09	9.04	6.22	0.17	98.72	**44.09**	54.90	1.01
CA19-13	TMG	3	core	C1-4	57.39	0.00	26.43	0.05	9.10	6.23	0.13	99.42	**44.33**	54.92	0.75
CA19-13	TMG	3	core	C1-5	56.90	0.05	26.74	0.06	9.28	6.12	0.13	99.33	**45.25**	54.00	0.75
CA19-13	TMG	3	mantle	C1-6	60.49	0.03	24.83	0.09	6.95	7.55	0.26	100.20	**33.22**	65.30	1.48
CA19-13	TMG	3	rim	C1-7	65.49	0.02	21.31	0.04	3.02	9.58	0.36	99.83	**14.53**	83.40	2.07
CA19-13	TMG	4	rim	C2-8	63.09	0.00	21.28	0.01	4.45	8.92	0.19	97.96	**21.38**	77.56	1.06
CA19-13	TMG	4	mantle	C2-9	62.39	0.04	21.45	0.06	4.88	8.79	0.16	97.78	**23.26**	75.82	0.92
CA19-13	TMG	4	mantle	C2-10	59.05	0.06	23.62	0.04	7.47	7.21	0.20	97.73	**36.00**	62.87	1.14
CA19-13	TMG	4	core	C2-11	57.62	0.00	24.19	0.10	8.38	6.58	0.19	97.06	**40.86**	58.06	1.08
CA19-13	TMG	4	core	C2-12	56.51	0.03	25.15	0.05	9.13	6.12	0.18	97.23	**44.72**	54.25	1.03
CA19-13	TMG	4	core	C2-13	59.40	0.00	24.13	0.00	7.43	7.31	0.09	98.38	**35.79**	63.72	0.49
CA19-13	TMG	4	mantle	C2-14	59.95	0.00	23.25	0.05	6.79	7.57	0.25	97.89	**32.67**	65.91	1.41
CA19-13	TMG	4	mantle	C2-15	60.59	0.00	23.20	0.11	6.52	7.62	0.25	98.29	**31.65**	66.93	1.43
CA19-13	TMG	4	mantle	C2-16	62.53	0.01	22.45	0.10	5.07	8.44	0.27	98.95	**24.53**	73.90	1.57
CA19-13	TMG	4	rim	C2-17	63.85	0.04	21.39	0.02	3.68	9.36	0.17	98.51	**17.68**	81.36	0.97
CA19-13	TMG	34	ep in plag	A-4	58.95	0.03	27.99	0.20	0.76	6.07	5.46	99.41	**4.19**	60.19	35.62
CA19-13	TMG	34	core	A-6	56.45	0.04	27.97	0.08	9.92	6.05	0.11	99.32	**47.23**	52.13	0.64
CA19-13	TMG	34	core	A-7	59.64	0.00	25.83	0.03	7.51	7.41	0.09	98.51	**35.72**	63.78	0.51
CA19-13	TMG	34	mantle	A-8	58.21	0.00	26.73	0.05	8.72	6.65	0.10	98.90	**41.78**	57.65	0.57
CA19-13	TMG	34	mantle	A-9	60.40	0.01	25.60	0.03	7.35	7.50	0.20	98.93	**34.73**	64.14	1.13
CA19-13	TMG	34	mantle	A-10	65.77	0.05	21.81	0.08	2.73	10.23	0.09	99.64	**12.79**	86.70	0.51
CA19-13	TMG	34	rim	A-11	64.87	0.00	22.63	0.03	3.76	9.85	0.12	99.29	**17.30**	82.03	0.66
CA19-13	TMG	35	rim	B-13	65.46	0.00	21.45	0.17	2.62	10.20	0.16	99.64	**12.32**	86.78	0.90
CA19-13	TMG	35	mantle	B-14	63.53	0.03	23.60	0.05	4.93	8.94	0.28	99.81	**22.99**	75.45	1.55
CA19-13	TMG	35	mantle	B-15	60.18	0.00	25.80	0.03	7.37	7.59	0.22	99.75	**34.49**	64.28	1.22
CA19-13	TMG	35	core	B-16	59.59	0.03	25.99	0.00	7.83	7.34	0.22	99.79	**36.63**	62.14	1.23
CA19-13	TMG	35	core	B-17	55.62	0.02	27.13	0.10	9.54	6.11	0.30	99.79	**45.53**	52.77	1.70
CA19-13	TMG	35	core	B-18	57.28	0.00	27.56	0.16	9.51	6.39	0.18	99.96	**44.67**	54.32	1.01
CA19-10	TMG	5	rim	A1-1	64.11	0.00	21.36	0.00	3.56	9.43	0.15	98.62	**17.11**	82.02	0.87
CA19-10	TMG	5	mantle	A1-2	55.29	0.00	26.91	0.05	10.35	5.70	0.11	98.44	**49.76**	49.59	0.65
CA19-10	TMG	5	core	A1-3	56.69	0.07	25.92	0.06	9.32	6.36	0.11	98.53	**44.48**	54.92	0.60
CA19-17	TMG	6	rim	A1-4	62.98	0.02	21.89	0.02	4.58	8.64	0.25	98.43	**22.33**	76.23	1.45
CA19-17	TMG	6	mantle	A1-5	61.59	0.00	22.92	0.01	5.57	8.20	0.19	98.49	**27.00**	71.91	1.09
CA19-17	TMG	6	core	A1-6	57.92	0.00	25.67	0.05	8.79	6.52	0.10	99.07	**42.44**	56.97	0.59
CA19-17	TMG	6	core	A1-7	58.43	0.02	24.97	0.01	8.35	6.73	0.18	98.69	**40.25**	58.70	1.05
CA19-17	TMG	6	rim	A1-8	63.00	0.00	23.28	0.00	5.34	8.19	0.11	99.92	**26.32**	73.04	0.64
CA19-17	TMG	6	-	A1-9	50.99	0.00	18.62	0.02	5.66	8.57	0.28	84.20	**26.32**	72.12	1.56
CA19-17	TMG	6	-	A1-10	61.92	0.01	22.46	0.04	4.93	8.43	0.14	97.96	**24.23**	74.98	0.79

Table A.6b Major element compositions of ETN plagioclase crystals

Sample	Rock	grain	Position	Spot	SiO_2	TiO_2	Al_2O_3	FeO	CaO	Na_2O	K_2O	Total	**An**	Ab	Or
CA19-15	ETN	7	rim	C2-23	59.79	0.00	23.72	0.08	7.26	7.49	0.17	98.55	**34.54**	64.48	0.97
CA19-15	ETN	7	mantle	C2-24	56.66	0.04	25.48	0.11	9.66	6.05	0.14	98.15	**46.49**	52.69	0.82
CA19-15	ETN	7	core	C2-25	54.23	0.00	27.11	0.10	11.73	4.74	0.06	98.01	**57.54**	42.08	0.38
CA19-15	ETN	7	core	C2-26	56.06	0.07	25.77	0.11	10.00	5.59	0.14	97.76	**49.31**	49.88	0.80
CA19-15	ETN	7	core	C2-27	51.84	0.02	28.19	0.16	13.20	3.89	0.10	97.41	**64.85**	34.58	0.56
CA19-15	ETN	7	core	C2-28	58.41	0.06	24.46	0.17	8.32	6.69	0.18	98.31	**40.31**	58.66	1.03
CA19-15	ETN	7	core	C2-29	58.82	0.01	23.93	0.11	7.96	6.82	0.16	97.86	**38.85**	60.24	0.90
CA19-15	ETN	7	core	C2-30	61.78	0.01	22.19	0.02	5.70	8.10	0.16	97.96	**27.74**	71.33	0.93
CA19-15	ETN	7	mantle	C2-31	56.57	0.00	25.21	0.20	8.24	6.39	0.59	97.30	**40.17**	56.38	3.45
CA19-15	ETN	7	mantle	C2-32	59.24	0.01	23.84	0.11	7.47	6.86	0.16	97.70	**37.22**	61.86	0.92
CA19-15	ETN	7	rim	C2-33	61.28	0.00	22.59	0.11	6.09	7.49	0.22	97.80	**30.60**	68.10	1.30
CA19-15	ETN	8	rim	C1-1	59.69	0.00	24.11	0.14	7.33	7.30	0.20	98.81	**35.28**	63.57	1.15
CA19-15	ETN	8	mantle	C1-2	59.73	0.00	24.22	0.13	7.48	7.09	0.16	98.84	**36.49**	62.59	0.92
CA19-15	ETN	8	maantle	C1-3	58.98	0.00	24.76	0.10	7.98	6.78	0.15	98.83	**39.07**	60.07	0.86
CA19-15	ETN	8	core	C1-4	56.28	0.00	26.35	0.10	9.62	5.83	0.15	98.39	**47.26**	51.83	0.91
CA19-15	ETN	8	core	C1-5	59.22	0.00	24.91	0.04	8.02	6.90	0.13	99.23	**38.81**	60.42	0.76
CA19-15	ETN	8	core	C1-6	55.46	0.03	27.08	0.09	10.36	5.54	0.12	98.73	**50.46**	48.83	0.71
CA19-15	ETN	8	core	C1-7	58.27	0.02	25.37	0.06	8.36	6.43	0.09	98.63	**41.58**	57.87	0.55
CA19-15	ETN	8	core	C1-8	57.22	0.00	26.33	0.30	9.12	6.15	0.18	99.30	**44.57**	54.39	1.04
CA19-15	ETN	8	mantle	C1-9	59.53	0.00	24.58	0.17	7.50	6.95	0.23	98.99	**36.85**	61.80	1.35
CA19-15	ETN	8	rim	C1-10	64.42	0.00	21.41	0.21	3.87	9.21	0.35	99.49	**18.47**	79.56	1.96
CA19-15	ETN	9	rim	A1-1	60.04	0.00	24.20	0.03	6.29	7.86	0.18	98.60	**30.35**	68.62	1.03
CA19-15	ETN	9	mantle	A1-2	58.21	0.02	25.32	0.15	7.88	6.81	0.22	98.63	**38.51**	60.22	1.27
CA19-15	ETN	9	core	A1-3	56.42	0.05	26.42	0.11	9.09	6.17	0.19	98.45	**44.37**	54.50	1.13
CA19-15	ETN	10	rim	A1-5	61.45	0.00	22.78	0.10	5.19	8.36	0.22	98.11	**25.21**	73.49	1.30
CA19-15	ETN	10	mantle	A1-6	54.14	0.01	27.97	0.14	11.15	5.13	0.10	98.65	**54.27**	45.18	0.56
CA19-15	ETN	10	core	A1-7	58.41	0.00	24.96	0.01	7.32	7.13	0.11	97.94	**35.97**	63.40	0.63
CA19-15	ETN	10	mantle	A1-8	57.81	0.00	25.36	0.08	8.15	6.78	0.13	98.32	**39.62**	59.64	0.73
CA19-15	ETN	10	rim	A1-9	58.92	0.01	24.10	0.15	6.96	7.09	0.20	97.44	**34.75**	64.06	1.18
CA19-15	ETN	11	rim	A2-17	57.65	0.07	21.06	0.17	5.15	7.97	0.16	92.27	**26.06**	72.98	0.96
CA19-15	ETN	11	mantle	A2-18	56.25	0.00	26.08	0.10	9.27	6.15	0.16	98.04	**45.03**	54.06	0.90
CA19-15	ETN	11	core	A2-19	57.71	0.00	25.22	0.13	8.08	6.86	0.19	98.23	**38.99**	59.90	1.12
CA19-15	ETN	11	mantle	A2-20	56.23	0.00	26.13	0.12	9.78	5.86	0.14	98.28	**47.58**	51.59	0.83
CA19-15	ETN	11	mantle	A2-21	58.77	0.00	24.31	0.06	7.44	7.32	0.13	98.05	**35.70**	63.56	0.73
CA19-15	ETN	11	rim	A2-22	59.80	0.00	23.71	0.13	6.45	7.72	0.19	98.01	**31.23**	67.65	1.12
CA19-15	ETN	12	rim	A3-26	59.68	0.02	23.90	0.16	6.57	7.70	0.23	98.28	**31.62**	67.07	1.31
CA19-15	ETN	12	mantle	A3-27	55.68	0.02	26.26	0.09	9.93	5.86	0.12	97.98	**48.02**	51.28	0.69
CA19-15	ETN	12	mantle	A3-28	55.85	0.02	26.22	0.10	9.65	6.00	0.19	98.04	**46.54**	52.37	1.09
CA19-15	ETN	12	core	A3-29	55.67	0.00	26.42	0.11	9.60	5.94	0.08	97.84	**46.95**	52.57	0.48
CA19-15	ETN	12	mantle	A3-30	53.67	0.02	27.53	0.20	11.12	4.90	0.15	97.62	**55.16**	43.98	0.86
CA19-15	ETN	12	rim	A3-31	58.04	0.02	25.18	0.13	7.76	6.89	0.22	98.24	**37.88**	60.86	1.25
CA19-21	ETN	36	rim	B-96	58.97	0.00	25.43	0.07	7.48	7.38	0.21	99.64	**35.48**	63.35	1.17
CA19-21	ETN	36	mantle	B-97	57.91	0.00	26.04	0.12	8.44	6.66	0.19	99.34	**40.74**	58.18	1.07
CA19-21	ETN	36	mantle	B-98	56.24	0.01	27.60	0.18	9.77	5.95	0.16	99.32	**47.15**	51.96	0.89
CA19-21	ETN	36	mantle	B-99	56.83	0.00	27.81	0.10	9.72	5.91	0.13	98.85	**47.25**	51.98	0.77
CA19-21	ETN	36	core	B-100	51.12	0.00	31.33	0.11	14.31	3.48	0.08	99.15	**69.14**	30.42	0.44
CA19-21	ETN	36	core	B-101	51.71	0.01	31.70	0.07	14.01	3.43	0.36	99.82	**67.84**	30.06	2.10
CA19-21	ETN	36	core	B-102	50.93	0.00	30.91	0.14	14.10	3.64	0.08	99.39	**67.84**	31.69	0.47
CA19-21	ETN	36	mantle	B-103	56.12	0.03	27.58	0.12	10.15	5.77	0.16	98.72	**48.84**	50.24	0.92
CA19-21	ETN	36	mantle	B-104	56.61	0.02	27.39	0.14	9.78	5.89	0.21	99.66	**47.27**	51.52	1.21
CA19-21	ETN	36	mantle	B-105	57.94	0.05	26.29	0.10	8.40	6.55	0.22	99.19	**40.96**	57.79	1.25
CA19-21	ETN	36	rim	B-106	59.19	0.00	25.59	0.16	7.49	7.31	0.24	99.23	**35.67**	62.99	1.34

Table A.6c Major element compositions of PTN plagioclase crystals

Sample	Rock	grain	Position	Spot	SiO_2	TiO_2	Al_2O_3	FeO	CaO	Na_2O	K_2O	Total	**An**	Ab	Or
CA19-16	PTN	13	rim	A1-1	60.60	0.05	28.12	0.08	8.75	5.90	0.16	103.67	**44.60**	54.41	0.99
CA19-16	PTN	13	mantle	A1-2	58.80	0.00	24.91	0.17	7.25	6.94	0.28	98.37	**35.99**	62.34	1.67
CA19-16	PTN	13	mantle	A1-3	58.28	0.00	25.46	0.15	7.75	6.70	0.24	98.60	**38.43**	60.12	1.44
CA19-16	PTN	13	mantle	A1-4	58.24	0.01	25.28	0.14	7.66	6.93	0.24	98.53	**37.39**	61.21	1.40
CA19-16	PTN	13	mantle	A1-5	59.45	0.03	25.01	0.08	7.15	7.20	0.22	99.16	**34.97**	63.73	1.30
CA19-16	PTN	13	core	A1-6	57.61	0.03	25.97	0.16	8.48	6.47	0.18	98.91	**41.56**	57.38	1.06
CA19-16	PTN	13	mantle	A1-7	59.67	0.01	24.55	0.07	6.83	7.56	0.20	98.96	**32.91**	65.93	1.16
CA19-16	PTN	13	mantle	A1-8	58.11	0.00	25.61	0.06	7.70	6.88	0.16	98.58	**37.86**	61.22	0.92
CA19-16	PTN	13	mantle	A1-9	58.53	0.02	25.17	0.08	7.33	7.26	0.18	98.59	**35.44**	63.51	1.05
CA19-16	PTN	13	rim	A1-10	56.46	0.03	26.71	0.15	8.88	6.19	0.14	98.56	**43.86**	55.32	0.82
CA19-16	PTN	13	matrix	A1-11	60.65	0.00	23.71	0.09	5.97	7.71	0.16	98.31	**29.68**	69.37	0.95
CA19-16	PTN	14	rim	A2-14	57.44	0.00	26.12	0.13	8.94	6.52	0.19	99.35	**42.65**	56.29	1.06
CA19-16	PTN	14	mantle	A2-15	58.72	0.00	24.95	0.11	7.59	7.02	0.21	98.61	**36.95**	61.84	1.21
CA19-16	PTN	14	mantle	A2-16	58.85	0.00	24.71	0.12	7.02	7.21	0.10	98.02	**34.78**	64.65	0.57
CA19-16	PTN	14	mantle	A2-17	58.77	0.02	25.14	0.06	7.74	6.83	0.23	98.84	**37.98**	60.65	1.37
CA19-16	PTN	14	core	A2-18	55.69	0.03	26.85	0.10	9.88	5.90	0.17	98.66	**47.61**	51.44	0.95
CA19-16	PTN	14	mantle	A2-19	57.81	0.03	25.93	0.15	8.41	6.61	0.19	99.15	**40.82**	58.06	1.11
CA19-16	PTN	14	mantle	A2-20	58.76	0.01	25.05	0.08	7.55	7.17	0.24	98.90	**36.27**	62.34	1.39
CA19-16	PTN	14	rim	A2-21	56.84	0.00	26.25	0.15	8.90	6.19	0.18	98.53	**43.80**	55.12	1.08
CA19-16	PTN	15	rim	A3-27	57.41	0.00	25.58	0.15	8.52	6.44	0.18	98.31	**41.79**	57.16	1.05
CA19-16	PTN	15	mantle	A3-28	58.73	0.01	24.29	0.11	7.26	7.45	0.24	98.10	**34.53**	64.13	1.34
CA19-16	PTN	15	mantle	A3-29	59.99	0.06	24.09	0.05	6.38	7.79	0.15	98.51	**30.88**	68.24	0.88
CA19-16	PTN	15	core	A3-30	58.05	0.00	25.13	0.13	8.05	6.53	0.29	98.22	**39.82**	58.45	1.73
CA19-16	PTN	15	core	A3-31	58.10	0.02	25.34	0.14	7.83	6.77	0.24	98.45	**38.45**	60.15	1.40
CA19-16	PTN	15	mantle	A3-32	58.73	0.01	24.93	0.04	7.41	7.17	0.12	98.42	**36.10**	63.21	0.69
CA19-16	PTN	15	rim	A3-33	59.22	0.01	24.86	0.06	7.07	7.13	0.19	98.56	**35.00**	63.87	1.12
CA19-16	PTN	16	core	A4-45	59.12	0.00	24.77	0.15	7.47	7.08	0.24	98.83	**36.32**	62.29	1.39
CA19-16	PTN	16	core	A4-46	54.86	0.01	27.35	0.13	10.62	5.21	0.18	98.41	**52.40**	46.52	1.08
CA19-16	PTN	16	mantle	A4-47	57.39	0.02	26.04	0.00	8.82	6.45	0.10	98.84	**42.79**	56.62	0.60
CA19-16	PTN	16	rim	A4-48	57.91	0.00	25.33	0.13	8.09	6.56	0.20	98.26	**40.05**	58.77	1.18
CA19-16	PTN	16	corona	A4-49	60.47	0.00	23.29	0.03	5.93	8.32	0.08	98.12	**28.14**	71.43	0.43
CA19-16	PTN	29	rim	A-55	61.95	0.00	23.41	0.14	4.94	8.78	0.19	99.66	**23.46**	75.46	1.08
CA19-16	PTN	29	mantle	A-56	60.66	0.00	25.00	0.07	6.55	7.69	0.17	99.27	**31.70**	67.34	0.96
CA19-16	PTN	29	mantle	A-57	55.85	0.01	27.86	0.12	10.27	5.68	0.15	99.83	**49.55**	49.59	0.85
CA19-16	PTN	29	core	A-58	46.74	0.00	33.64	0.26	17.19	1.73	0.04	99.56	**84.38**	15.37	0.25
CA19-16	PTN	29	core	A-59	46.57	0.02	34.07	0.37	17.68	1.57	0.05	99.31	**85.90**	13.80	0.29
CA19-16	PTN	29	core	A-60	47.00	0.00	33.71	0.10	17.07	2.06	0.06	99.99	**81.80**	17.86	0.33
CA19-16	PTN	29	core	A-61	47.65	0.00	33.00	0.27	16.55	2.25	0.06	99.72	**79.99**	19.68	0.33
CA19-16	PTN	29	core	A-62	47.84	0.02	33.23	0.23	16.83	2.09	0.06	99.11	**81.35**	18.28	0.37
CA19-16	PTN	29	core	A-63	47.12	0.00	33.33	0.31	16.96	1.95	0.11	99.66	**82.25**	17.11	0.64
CA19-16	PTN	29	mantle	A-64	50.95	0.08	30.22	0.24	13.59	3.92	0.12	99.94	**65.26**	34.06	0.67
CA19-16	PTN	29	mantle	A-65	56.48	0.06	27.34	0.14	9.89	6.00	0.19	99.56	**47.15**	51.76	1.08
CA19-16	PTN	29	mantle	A-66	61.39	0.00	24.36	0.05	5.91	8.21	0.10	99.88	**28.30**	71.14	0.56
CA19-16	PTN	29	rim	A-67	60.87	0.01	24.66	0.06	6.27	8.21	0.13	100.03	**29.45**	69.79	0.75
CA19-16	PTN	30	rim	A-69	60.91	0.03	24.28	0.07	6.04	8.37	0.11	99.55	**28.34**	71.06	0.60
CA19-16	PTN	30	mantle	A-70	60.61	0.00	24.48	0.07	6.27	7.75	0.14	98.78	**30.64**	68.54	0.81
CA19-16	PTN	30	mantle	A-71	59.15	0.00	25.67	0.06	7.78	7.33	0.11	100.03	**36.73**	62.62	0.65
CA19-16	PTN	30	core	A-72	50.47	0.03	31.19	0.07	14.40	3.59	0.08	99.32	**68.59**	30.94	0.46
CA19-16	PTN	30	core	A-73	57.85	0.07	26.38	0.06	8.42	6.88	0.10	99.46	**40.11**	59.31	0.58
CA19-16	PTN	30	core	A-74	51.89	0.00	29.14	0.19	12.58	4.29	0.12	99.88	**61.42**	37.90	0.68
CA19-16	PTN	30	core	A-75	51.74	0.02	30.43	0.21	13.24	3.96	0.15	98.72	**64.33**	34.82	0.86
CA19-16	PTN	30	core	A-76	50.54	0.00	30.96	0.26	13.85	3.64	0.10	99.07	**67.39**	32.05	0.56
CA19-16	PTN	30	core	A-77	51.13	0.02	31.08	0.14	14.10	3.76	0.09	98.87	**67.11**	32.38	0.51
CA19-16	PTN	30	mantle	A-78	56.35	0.04	27.52	0.07	9.56	6.09	0.14	100.18	**46.07**	53.10	0.83
CA19-16	PTN	30	mantle	A-79	57.40	0.02	26.81	0.05	9.03	6.58	0.16	99.93	**42.74**	56.35	0.91
CA19-16	PTN	30	rim	A-80	61.40	0.00	23.81	0.07	5.64	8.32	0.18	99.83	**26.97**	71.99	1.04
CA19-16	PTN	31	rim	C-46	59.69	0.01	24.85	0.06	6.58	7.93	0.16	99.74	**31.16**	67.95	0.90
CA19-16	PTN	31	mantle	C-45	56.38	0.01	27.31	0.08	9.60	5.93	0.10	99.76	**46.94**	52.47	0.60
CA19-16	PTN	31	core	C-42	47.58	0.03	32.84	0.18	16.55	2.25	0.06	99.64	**79.98**	19.68	0.34
CA19-16	PTN	31	core	C-43	44.74	0.02	26.47	0.04	21.78	0.21	1.98	99.68	**88.87**	1.51	9.62
CA19-16	PTN	31	core	C-44	57.10	0.00	26.94	0.11	9.36	6.32	0.12	99.19	**44.70**	54.62	0.68
CA19-16	PTN	31	core	C-48	45.22	0.01	29.88	0.16	15.82	0.65	0.05	99.50	**92.71**	6.94	0.35
CA19-16	PTN	31	core	C-49	46.19	0.04	33.14	0.18	16.64	1.93	0.30	99.59	**81.21**	17.04	1.75
CA19-16	PTN	31	core	C-50	56.67	0.00	27.68	0.12	9.92	5.94	0.14	100.36	**47.62**	51.60	0.79
CA19-16	PTN	31	mantle	C-51	53.67	0.00	29.17	0.17	11.85	4.94	0.11	99.72	**56.63**	42.72	0.65
CA19-16	PTN	31	mantle	C-52	57.12	0.00	27.27	0.15	9.33	6.05	0.18	101.11	**45.53**	53.43	1.04
CA19-16	PTN	31	mantle	C-53	60.28	0.00	24.92	0.10	6.72	7.31	0.15	98.72	**33.38**	65.71	0.90
CA19-16	PTN	31	rim	C-54	60.38	0.00	24.96	0.11	6.69	7.75	0.20	99.42	**31.93**	66.93	1.14
CA19-16	PTN	32	rim	E-85	61.09	0.02	24.49	0.01	6.28	8.01	0.14	99.33	**29.99**	69.23	0.78
CA19-16	PTN	32	mantle	E-86	57.17	0.00	26.81	0.10	9.14	6.59	0.14	100.20	**43.05**	56.17	0.78
CA19-16	PTN	32	core	E-87	53.41	0.00	29.17	0.11	12.10	4.84	0.09	99.83	**57.71**	41.77	0.52
CA19-16	PTN	32	core	E-88	50.94	0.02	30.90	0.16	13.93	3.85	0.08	97.96	**66.36**	33.19	0.45
CA19-16	PTN	32	mantle	E-89	56.76	0.00	26.88	0.10	8.10	6.37	0.73	97.78	**39.51**	56.23	4.26
CA19-16	PTN	32	rim	E-90	60.00	0.03	24.63	0.05	6.25	7.85	0.21	97.73	**30.19**	68.61	1.20
CA19-16	PTN	33	rim	E-83	60.42	0.00	25.02	0.04	6.81	7.84	0.11	98.38	**32.23**	67.15	0.61
CA19-16	PTN	33	core	E-81	50.96	0.00	31.00	0.07	14.09	3.82	0.07	97.06	**66.82**	32.78	0.40
CA19-16	PTN	33	mantle	E-82	57.26	0.02	26.98	0.11	9.36	6.27	0.18	97.23	**44.75**	54.25	1.00
CA19-16	PTN	33	rim	E-84	56.92	0.01	27.44	0.01	9.37	6.22	0.16	97.89	**45.02**	54.08	0.89

Table A.6d Major element compositions of EBG plagioclase crystals

Sample	Rock	grain	Position	Spot	SiO_2	TiO_2	Al_2O_3	FeO	CaO	Na_2O	K_2O	Total	**An**	Ab	Or
CA19-26	EBG	17a	rim	C1-23	63.39	0.00	22.54	0.17	4.02	8.83	0.21	99.19	**19.86**	78.94	1.21
CA19-26	EBG	17a	mantle	C1-24	62.15	0.03	23.14	0.11	4.91	8.59	0.27	99.23	**23.63**	74.82	1.55
CA19-26	EBG	17a	mantle	C1-25	56.94	0.00	26.72	0.20	9.25	6.08	0.18	99.38	**45.18**	53.74	1.08
CA19-26	EBG	17a	core	C1-26	56.57	0.07	26.94	0.16	9.44	6.00	0.20	99.38	**45.96**	52.87	1.17
CA19-26	EBG	17a	core	C1-27	56.00	0.04	27.32	0.16	10.03	5.48	0.18	99.27	**49.75**	49.18	1.07
CA19-26	EBG	17a	core	C1-28	55.95	0.05	27.23	0.22	9.73	5.56	0.18	98.97	**48.64**	50.30	1.06
CA19-26	EBG	17a	core	C1-29	56.45	0.03	27.53	0.17	9.92	5.63	0.19	99.95	**48.78**	50.10	1.11
CA19-26	EBG	17a	core	C1-30	55.36	0.00	27.74	0.17	10.43	5.28	0.15	99.21	**51.74**	47.39	0.87
CA19-26	EBG	17a	mantle	C1-31	62.19	0.00	23.89	0.14	5.55	8.02	0.35	100.23	**27.09**	70.85	2.06
CA19-26	EBG	17a	rim	C1-32	62.78	0.00	23.17	0.13	4.91	8.65	0.15	99.79	**23.68**	75.48	0.84
CA19-26	EBG	17b	rim	C1-33	62.77	0.00	23.36	0.07	5.20	8.57	0.12	100.09	**24.94**	74.39	0.67
CA19-26	EBG	17b	core	C1-34	56.12	0.00	27.45	0.27	10.18	5.46	0.19	99.76	**50.18**	48.70	1.13
CA19-26	EBG	17b	core	C1-35	55.80	0.02	27.80	0.11	10.33	5.48	0.09	99.67	**50.76**	48.73	0.51
CA19-26	EBG	17b	core	C1-36	55.73	0.00	27.67	0.08	10.20	5.39	0.14	99.24	**50.71**	48.49	0.80
CA19-26	EBG	17b	mantle	C1-37	60.35	0.00	24.73	0.16	6.75	7.42	0.16	99.61	**33.15**	65.94	0.91
CA19-26	EBG	17b	mantle	C1-38	62.25	0.01	23.27	0.07	5.31	8.36	0.16	99.51	**25.74**	73.33	0.92
CA19-26	EBG	17b	rim	C1-39	61.78	0.02	23.75	0.10	5.79	7.89	0.13	99.48	**28.63**	70.60	0.77
CA19-26	EBG	18a	rim	C2-40	62.21	0.00	23.90	0.12	5.72	7.72	0.15	99.88	**28.79**	70.30	0.91
CA19-26	EBG	18a	mantle	C2-41	62.32	0.01	23.41	0.09	5.37	8.24	0.21	99.71	**26.15**	72.61	1.24
CA19-26	EBG	18a	mantle	C2-42	62.36	0.01	23.68	0.18	5.53	8.02	0.25	100.02	**27.19**	71.35	1.46
CA19-26	EBG	18a	core	C2-43	59.88	0.03	23.21	0.10	5.92	7.51	0.23	96.97	**29.92**	68.69	1.39
CA19-26	EBG	18a	core	C2-44	57.66	0.05	26.28	0.19	8.73	6.33	0.24	99.54	**42.64**	55.95	1.41
CA19-26	EBG	18a	core	C2-45	57.90	0.01	26.69	0.24	8.92	6.10	0.28	100.17	**43.95**	54.38	1.67
CA19-26	EBG	18a	core	C2-46	59.98	0.00	25.07	0.14	7.26	7.16	0.27	99.90	**35.35**	63.09	1.55
CA19-26	EBG	18a	mantle	C2-47	62.44	0.00	23.20	0.17	5.40	8.05	0.23	99.52	**26.67**	71.96	1.37
CA19-26	EBG	18a	mantle	C2-48	62.59	0.04	22.89	0.17	5.28	8.41	0.18	99.60	**25.49**	73.48	1.03
CA19-26	EBG	18a	rim	C2-49	65.09	0.00	21.08	0.10	3.58	9.13	0.19	99.19	**17.62**	81.29	1.09
CA19-26	EBG	18b	rim	C2-50	63.16	0.00	22.89	0.17	4.94	8.68	0.18	100.07	**23.69**	75.31	1.01
CA19-26	EBG	18b	mantle	C2-51	62.13	0.06	24.11	0.12	5.87	7.68	0.21	100.21	**29.33**	69.44	1.23
CA19-26	EBG	18b	mantle	C2-52	60.47	0.01	23.92	0.21	6.72	7.45	0.17	99.04	**32.93**	66.06	1.01
CA19-26	EBG	18b	mantle	C2-53	60.24	0.02	24.69	0.13	7.08	7.20	0.26	99.68	**34.67**	63.79	1.54
CA19-26	EBG	18b	core	C2-54	61.06	0.00	24.44	0.12	6.74	7.53	0.27	100.21	**32.58**	65.86	1.56
CA19-26	EBG	18b	core	C2-55	61.48	0.00	24.36	0.17	6.18	7.74	0.27	100.20	**30.14**	68.30	1.56
CA19-26	EBG	18b	core	C2-56	62.38	0.03	23.51	0.06	5.45	8.18	0.21	99.82	**26.59**	72.22	1.19
CA19-26	EBG	18b	core	C2-57	61.36	0.00	24.43	0.14	6.23	7.91	0.14	100.21	**30.09**	69.13	0.78
CA19-26	EBG	18b	rim	C2-58	61.98	0.01	23.91	0.18	5.95	7.91	0.11	100.12	**29.18**	70.20	0.61
CA19-26	EBG	19	rim	C4-11	61.26	0.00	24.08	0.16	5.85	7.88	0.34	99.57	**28.52**	69.51	1.97
CA19-26	EBG	19	mantle	C4-12	60.98	0.00	24.19	0.15	6.20	7.67	0.20	99.41	**30.51**	68.31	1.18
CA19-26	EBG	19	mantle	C4-13	60.76	0.03	24.32	0.14	6.48	7.48	0.32	99.64	**31.77**	66.36	1.87
CA19-26	EBG	19	core	C4-14	60.73	0.00	24.02	0.15	6.45	7.71	0.21	99.34	**31.23**	67.56	1.21
CA19-26	EBG	19	core	C4-15	61.03	0.00	23.91	0.16	6.22	7.70	0.28	99.32	**30.36**	68.02	1.62
CA19-26	EBG	19	core	C4-16	60.97	0.00	23.66	0.09	5.93	8.07	0.13	98.85	**28.67**	70.60	0.73
CA19-26	EBG	19	core	C4-17	61.21	0.06	23.24	0.17	5.94	8.14	0.38	99.15	**28.13**	69.76	2.11
CA19-26	EBG	19	core	C4-18	62.95	0.00	22.92	0.13	5.11	8.29	0.42	99.82	**24.79**	72.77	2.44
CA19-26	EBG	19	mantle	C4-19	61.27	0.01	23.57	0.13	6.08	7.92	0.40	99.39	**29.11**	68.62	2.27
CA19-26	EBG	19	mantle	C4-20	61.15	0.01	23.21	0.08	6.06	7.89	0.30	98.72	**29.29**	69.00	1.72
CA19-26	EBG	19	rim	C4-21	63.12	0.00	22.77	0.10	4.74	8.70	0.21	99.66	**22.86**	75.92	1.23
CA19-26	EBG	20	rim	A2-13	62.35	0.04	22.93	0.17	4.42	8.59	0.26	98.76	**21.80**	76.66	1.54
CA19-26	EBG	20	core	A2-14	57.76	0.02	25.37	0.14	7.31	7.11	0.16	97.87	**35.90**	63.18	0.92
CA19-26	EBG	20	mantle	A2-15	59.61	0.05	24.38	0.17	6.50	7.54	0.37	98.63	**31.58**	66.28	2.14
CA19-26	EBG	20	rim	A2-16	60.29	0.03	23.68	0.13	5.33	8.31	0.11	97.92	**26.01**	73.38	0.62
CA19-29	EBG	21a	rim	A1-3	64.36	0.00	21.46	0.09	3.27	9.88	0.11	99.18	**15.37**	84.01	0.62
CA19-29	EBG	21a	mantle	A1-4	59.23	0.00	24.42	0.17	7.11	7.32	0.15	98.43	**34.63**	64.51	0.87
CA19-29	EBG	21a	core	A1-5	60.44	0.01	23.45	0.19	5.99	7.31	1.46	98.86	**28.58**	63.12	8.30
CA19-29	EBG	21b	core	A1-6	59.41	0.03	24.23	0.15	7.23	7.05	0.37	98.46	**35.40**	62.47	2.13
CA19-29	EBG	21b	core	A1-7	57.81	0.03	25.10	0.15	7.89	7.15	0.16	98.30	**37.55**	61.57	0.88
CA19-29	EBG	21b	mantle	A1-8	59.97	0.01	23.67	0.10	6.30	7.79	0.18	98.11	**30.57**	68.39	1.04
CA19-29	EBG	21b	rim	A1-9	62.84	0.03	22.32	0.08	4.69	8.73	0.14	98.86	**22.70**	76.46	0.83
CA19-29	EBG	22	rim	C1-3	60.04	0.03	24.59	0.18	6.64	7.84	0.12	99.46	**31.66**	67.64	0.70
CA19-29	EBG	22	mantle	C1-4	61.16	0.02	24.11	0.18	6.27	7.96	0.17	99.88	**30.04**	69.00	0.96
CA19-29	EBG	22	core	C1-5	60.20	0.04	24.28	0.19	6.59	7.24	0.16	98.72	**33.14**	65.88	0.98
CA19-29	EBG	22	mantle	C1-6	60.45	0.00	24.13	0.16	6.42	7.78	0.12	99.07	**31.10**	68.19	0.71
CA19-29	EBG	22	rim	C1-7	61.02	0.00	23.69	0.19	6.03	7.82	0.13	98.87	**29.66**	69.59	0.75
CA19-29	EBG	23a	rim	C3-16	65.25	0.00	21.41	0.17	3.15	9.52	0.12	99.64	**15.35**	83.95	0.69
CA19-29	EBG	23a	core	C3-17	61.62	0.02	23.96	0.11	5.66	7.95	0.30	99.68	**27.75**	70.52	1.73
CA19-29	EBG	23a	core	C3-18	63.89	0.03	22.15	0.10	3.45	9.25	0.31	99.19	**16.78**	81.42	1.80
CA19-29	EBG	23a	rim	C3-19	66.60	0.00	21.09	0.06	1.82	10.08	0.12	99.76	**9.01**	90.30	0.69
CA19-29	EBG	23b	rim	C3-20	64.42	0.00	21.72	0.13	3.73	9.56	0.12	99.74	**17.62**	81.72	0.66
CA19-29	EBG	23b	core	C3-21	63.44	0.06	22.48	0.13	4.40	8.81	0.15	99.50	**21.45**	77.71	0.85
CA19-29	EBG	23b	core	C3-22	63.68	0.00	22.18	0.09	4.31	9.16	0.16	99.59	**20.44**	78.63	0.93
CA19-29	EBG	23b	rim	C3-23	65.01	0.01	22.11	0.16	3.42	9.53	0.12	100.36	**16.43**	82.86	0.71

Table A.6e Major element compositions of MDR and OTN plagioclase crystals

Sample	Rock	grain	Position	Spot	SiO_2	TiO_2	Al_2O_3	FeO	CaO	Na_2O	K_2O	Total	**An**	Ab	Or
CA19-3	MDR	27a	rim	C1-8	54.38	0.01	28.87	0.07	11.39	4.90	0.03	99.66	**56.11**	43.68	0.20
CA19-3	MDR	27a	core	C1-9	55.31	0.00	28.01	0.00	10.35	5.47	0.06	99.27	**50.95**	48.72	0.33
CA19-3	MDR	27a	rim	C1-10	56.50	0.00	27.51	0.02	9.94	5.79	0.06	99.83	**48.52**	51.14	0.34
CA19-3	MDR	27b	rim	C1-11	57.80	0.06	26.29	0.13	8.85	6.29	0.07	99.56	**43.56**	56.02	0.41
CA19-3	MDR	27b	inter	C1-12	58.59	0.00	25.70	0.04	8.10	6.79	0.09	99.31	**39.52**	59.95	0.53
CA19-3	MDR	27b	core	C1-13	57.67	0.00	26.69	0.02	9.02	6.47	0.09	99.99	**43.30**	56.21	0.49
CA19-3	MDR	27b	rim	C1-14	55.72	0.00	28.07	0.07	10.25	5.47	0.06	99.72	**50.70**	48.96	0.33
CA19-3	MDR	28a	rim	C2-16	55.71	0.00	27.72	0.09	9.88	5.60	0.07	99.11	**49.15**	50.41	0.43
CA19-3	MDR	28a	inter	C2-17	54.97	0.02	28.68	0.02	10.97	4.93	0.06	99.66	**54.95**	44.69	0.36
CA19-3	MDR	28a	core	C2-18	54.67	0.06	28.89	0.00	11.20	5.06	0.03	99.94	**54.93**	44.90	0.17
CA19-3	MDR	28a	core	C2-19	55.89	0.02	28.14	0.00	10.07	5.36	0.06	99.56	**50.76**	48.89	0.34
CA19-3	MDR	28a	inter	C2-20	56.43	0.00	27.72	0.11	9.44	5.98	0.11	99.88	**46.30**	53.07	0.63
CA19-3	MDR	28a	rim	C2-21	57.98	0.00	26.93	0.07	8.64	6.28	0.08	100.03	**42.99**	56.55	0.46
CA19-3	MDR	28b	rim	C2-22	57.75	0.00	26.48	0.04	8.79	6.39	0.08	99.55	**42.97**	56.53	0.49
CA19-3	MDR	28b	core	C2-23	56.42	0.02	26.82	0.03	9.50	5.84	0.13	98.78	**46.98**	52.26	0.75
CA19-3	MDR	28b	core	C2-24	57.02	0.00	27.41	0.05	9.53	5.88	0.12	100.03	**46.91**	52.37	0.73
CA19-3	MDR	28b	rim	C2-25	57.43	0.00	26.62	0.04	9.09	5.98	0.14	99.32	**45.29**	53.91	0.80
CA19-8	OTN	50	rim	A1-2	57.29	0.00	26.42	0.17	8.92	6.74	0.09	99.66	**42.02**	57.45	0.53
CA19-8	OTN	50	rim	A1-3	52.81	0.00	28.72	0.16	12.03	4.60	0.16	98.49	**58.55**	40.51	0.94
CA19-8	OTN	50	core	A1-4	54.20	0.05	27.81	0.18	11.26	5.10	0.17	98.78	**54.41**	44.60	0.99
CA19-8	OTN	50	rim	A1-5	54.10	0.00	28.57	0.18	11.37	5.03	0.12	99.43	**55.15**	44.15	0.71
CA19-8	OTN	50	rim	A1-6	54.65	0.01	27.94	0.23	11.04	5.24	0.13	99.25	**53.39**	45.86	0.75
CA19-8	OTN	50	rim	A1-7	57.67	0.04	25.88	0.11	8.73	6.67	0.26	99.36	**41.37**	57.19	1.44
CA19-8	OTN	50	core	A1-8	53.86	0.06	28.46	0.17	11.88	4.77	0.16	99.36	**57.38**	41.69	0.92
CA19-8	OTN	50	core	A1-9	53.90	0.00	28.25	0.17	11.71	4.87	0.17	99.07	**56.51**	42.53	0.96
CA19-8	OTN	51	core	A1-10	56.13	0.00	26.81	0.16	10.27	5.80	0.19	99.37	**48.93**	50.01	1.06
CA19-8	OTN	51	rim	A2-14	57.57	0.01	26.00	0.10	9.06	6.32	0.16	99.22	**43.80**	55.29	0.90
CA19-8	OTN	51	core	A2-15	52.48	0.02	29.34	0.19	13.02	4.16	0.11	99.32	**62.97**	36.41	0.62
CA19-8	OTN	51	core	A2-16	54.67	0.02	28.04	0.16	11.13	5.29	0.20	99.54	**53.15**	45.71	1.14
CA19-8	OTN	51	core	A2-17	55.16	0.01	26.81	0.14	10.39	5.47	0.15	98.16	**50.77**	48.36	0.87
CA19-8	OTN	51	rim	A2-18	57.77	0.00	25.68	0.20	8.61	6.59	0.19	99.05	**41.47**	57.44	1.09
CA19-8	OTN	51	core	A2-19	55.15	0.01	27.17	0.17	10.87	5.33	0.21	98.97	**52.36**	46.46	1.18
CA19-8	OTN	51	core	A2-20	55.68	0.00	27.22	0.10	10.29	5.90	0.23	99.44	**48.45**	50.26	1.29
CA19-8	OTN	51	rim	A2-21	52.70	0.00	29.25	0.22	13.03	4.20	0.11	99.54	**62.76**	36.61	0.64
CA19-8	OTN	51	core	A2-22	56.80	0.02	26.19	0.13	9.61	5.90	0.17	98.82	**46.91**	52.12	0.97
CA19-8	OTN	51	rim	A2-23	49.03	0.00	30.76	0.20		2.98	0.06	97.92	**73.13**	26.50	0.37
CA19-8	OTN	51	rim	A2-24	57.53	0.00	25.70	0.08	8.46	6.65	0.13	98.58	**40.98**	58.29	0.73
CA19-8	OTN	52	rim	A3-29	56.51	0.00	26.22	0.25	9.65	6.12	0.18	98.97	**46.09**	52.89	1.03
CA19-8	OTN	52	rim	A3-30	54.37	0.03	27.43	0.13	11.27	5.15	0.18	98.58	**54.18**	44.80	1.02
CA19-8	OTN	52	core	A3-31	53.89	0.00	28.02	0.17	11.86	4.66	0.15	98.75	**57.93**	41.19	0.88
CA19-8	OTN	52	rim	A3-32	56.15	0.07	27.01	0.16	9.75	5.73	0.28	99.15	**47.68**	50.70	1.62
CA19-8	OTN	52	core	A3-33	57.80	0.00	25.79	0.13	8.63	6.56	0.23	99.16	**41.54**	57.13	1.33
CA19-8	OTN	52	core	A3-34	55.61	0.06	27.27	0.14	10.36	5.51	0.23	99.18	**50.29**	48.40	1.31
CA19-8	OTN	52	core	A3-35	56.22	0.00	26.43	0.13	9.56	6.05	0.09	98.53	**46.37**	53.10	0.52
CA19-8	OTN	52	rim	A3-36	54.06	0.00	27.87	0.18		5.07	0.16	98.64	**54.67**	44.39	0.94
CA19-8	OTN	52	rim	A3-37	57.03	0.00	26.22	0.06	9.24	6.30	0.19	99.05	**44.28**	54.64	1.08

Table A.7 Representative microprobe analyses of TMG biotite crystals

Chemical formulas were calculated on the basis of 11 cation charges. Fe# is $Fe^{2+}/(Fe^{2+}+Mg^{2+})$

Cr. N#	Sample	Rock	Si	Al iv	Al vi	Ti	Fe^{3+}	Fe^{2+}	Mn	Mg	Ca	Na	K	Fe#
A1-18	CA19-10	TMG	2.74	1.19	0.36	0.14	0.17	1.09	0.08	1.07	0.01	0.02	0.95	0.50
A2-20	CA19-10	TMG	2.75	1.18	0.36	0.14	0.15	1.10	0.08	1.08	0.00	0.02	0.97	0.51
A3-26	CA19-10	TMG	2.77	1.17	0.37	0.15	0.14	1.08	0.08	1.07	0.01	0.02	0.97	0.50
A1-1	CA19-17	TMG	2.73	1.18	0.38	0.15	0.10	1.14	0.05	1.11	0.00	0.01	0.97	0.51
A1-3	CA19-17	TMG	2.77	1.16	0.39	0.16	0.09	1.11	0.05	1.10	0.00	0.01	0.97	0.50
A1-11	CA19-17	TMG	2.73	1.21	0.37	0.14	0.13	1.14	0.06	1.07	0.01	0.01	0.96	0.52
A2-23	CA19-17	TMG	2.74	1.19	0.37	0.14	0.13	1.11	0.06	1.10	0.00	0.01	0.96	0.50
A2-24	CA19-17	TMG	2.75	1.19	0.39	0.13	0.13	1.10	0.06	1.07	0.01	0.02	0.95	0.51
A3-27	CA19-17	TMG	2.71	1.23	0.37	0.13	0.13	1.12	0.06	1.12	0.00	0.03	0.98	0.50
A3-29	CA19-17	TMG	2.74	1.18	0.39	0.11	0.12	1.07	0.05	1.14	0.00	0.02	0.95	0.48
A3-7	CA19-13	TMG	2.74	1.18	0.35	0.11	0.15	1.04	0.08	1.19	0.00	0.01	0.98	0.47
A1-10	CA19-13	TMG	2.77	1.20	0.42	0.11	0.12	1.05	0.07	1.11	0.00	0.01	0.97	0.49
A4-16	CA19-13	TMG	2.74	1.22	0.39	0.14	0.12	1.06	0.08	1.12	0.00	0.01	0.97	0.49
A5-26	CA19-13	TMG	2.77	1.19	0.37	0.15	0.12	1.05	0.08	1.15	0.00	0.01	0.98	0.48
A2-14	CA19-29	EBG	2.81	1.05	0.32	0.20	0.08	1.05	0.04	1.21	0.00	0.01	0.95	0.47
A6-2	CA19-26	EBG	2.82	1.10	0.38	0.17	0.11	1.07	0.05	1.07	0.01	0.01	0.94	0.50
A2-19	CA19-26	EBG	2.77	1.13	0.37	0.14	0.09	1.07	0.05	1.17	0.00	0.01	0.96	0.48
A5-32	CA19-26	EBG	2.79	1.09	0.35	0.16	0.11	1.07	0.05	1.15	0.00	0.01	0.95	0.48
C3-2	CA19-26	EBG	2.79	1.11	0.38	0.16	0.12	1.03	0.05	1.15	0.00	0.01	0.91	0.47
C3-3	CA19-26	EBG	2.79	1.11	0.38	0.16	0.13	1.01	0.05	1.16	0.00	0.01	0.91	0.46
C4-22	CA19-26	EBG	2.85	1.06	0.40	0.19	0.09	1.05	0.05	1.07	0.00	0.01	0.93	0.49
C1-9	CA19-29	EBG	2.85	1.02	0.34	0.21	0.11	1.02	0.04	1.16	0.00	0.02	0.92	0.47
C1-10	CA19-29	EBG	2.85	1.01	0.33	0.20	0.10	0.99	0.04	1.20	0.00	0.02	0.93	0.45
A1-13	CA19-15	ETN	2.82	1.03	0.31	0.13	0.15	0.93	0.05	1.30	0.01	0.02	0.93	0.42
A1-14	CA19-15	ETN	2.81	1.03	0.36	0.12	0.10	0.99	0.04	1.26	0.00	0.01	0.95	0.44
A2-23	CA19-15	ETN	2.79	1.08	0.34	0.12	0.11	0.98	0.05	1.29	0.00	0.01	0.96	0.43
A3-25	CA19-15	ETN	2.81	1.04	0.30	0.16	0.12	0.93	0.05	1.36	0.00	0.02	0.95	0.41
A3-34	CA19-15	ETN	2.79	1.09	0.32	0.16	0.12	0.99	0.05	1.27	0.00	0.02	0.95	0.44
A1-12	CA19-16	PTN	2.81	1.08	0.28	0.15	0.11	0.82	0.03	1.51	0.00	0.01	0.94	0.35
A1-13	CA19-16	PTN	2.83	1.07	0.29	0.15	0.12	0.77	0.03	1.54	0.00	0.02	0.93	0.33
A2-22	CA19-16	PTN	2.80	1.06	0.31	0.14	0.13	0.95	0.05	1.32	0.00	0.01	0.94	0.42
A7-24	CA19-16	PTN	2.82	1.04	0.32	0.14	0.16	0.91	0.05	1.32	0.00	0.02	0.91	0.41
A3-25	CA19-16	PTN	2.82	1.06	0.31	0.13	0.08	0.82	0.02	1.52	0.00	0.01	0.94	0.35
A3-26	CA19-16	PTN	2.83	1.06	0.32	0.15	0.13	0.85	0.05	1.39	0.00	0.01	0.93	0.38
A4-50	CA19-16	PTN	2.80	1.08	0.33	0.15	0.12	1.00	0.05	1.23	0.01	0.01	0.95	0.45
A6-59	CA19-16	PTN	2.79	1.09	0.31	0.14	0.13	0.95	0.05	1.34	0.00	0.01	0.95	0.42
D108	CA19-21	ETN	2.81	1.09	0.37	0.14	0.11	1.02	0.05	0.05	0.01	0.03	0.95	0.96

Table A.8 Representative microprobe analyses of white micas from the Corno Alto and Sostino rocks.
Chemical formulas were calculated on the basis of 11 cation charges.

An. N#	A1-8	A4-17	13-A5-24	A1-17	A2-19	A3-25	A1-2	A1-12	A1-2	A2-22	A2-25	A3-26	A3-28
Sample	CA19-13	CA19-13	CA19-13	CA19-10	CA19-10	CA19-10	CA19-17	CA19-17	CA19-17	CA19-17	CA19-17	CA19-17	CA19-17
Rock	TMG	TMG	TMG	TMG	TMG	TMG	TMG	TMG	TMG	TMG	TMG	TMG	TMG
Si	3.14	3.14	3.15	3.13	3.11	3.11	3.18	3.11	3.18	3.15	3.08	3.09	3.10
Al iv	0.81	0.81	0.82	0.84	0.85	0.86	0.78	0.85	0.78	0.79	0.89	0.88	0.90
Al vi	1.71	1.71	1.69	1.70	1.74	1.74	1.66	1.77	1.66	1.70	1.77	1.77	1.74
Ti	0.04	0.04	0.03	0.03	0.04	0.03	0.04	0.03	0.04	0.07	0.03	0.03	0.04
Fe	0.26	0.26	0.28	0.26	0.23	0.23	0.27	0.22	0.27	0.25	0.22	0.22	0.22
Mn	0.00	0.00	0.00	0.01	0.00	0.00	0.00	0.00	0.00	0.00	0.00	0.00	0.00
Mg	0.10	0.09	0.10	0.10	0.07	0.08	0.14	0.09	0.14	0.11	0.07	0.07	0.07
Ca	0.00	0.01	0.00	0.00	0.00	0.00	0.00	0.00	0.00	0.00	0.00	0.00	0.00
Na	0.05	0.05	0.04	0.05	0.05	0.08	0.04	0.06	0.04	0.03	0.07	0.05	0.05
K	0.91	0.90	0.95	0.95	0.96	0.92	0.94	0.88	0.94	0.93	0.92	0.91	0.92
Mg + Fe	0.35	0.35	0.38	0.36	0.31	0.31	0.40	0.30	0.40	0.36	0.29	0.29	0.28
mgli	0.10	0.09	0.10	0.10	0.07	0.08	0.14	0.09	0.14	0.11	0.07	0.07	0.07
feal	-1.41	-1.41	-1.37	-1.41	-1.47	-1.49	-1.36	-1.52	-1.36	-1.38	-1.51	-1.52	-1.48
Al_{tot}	2.53	2.53	2.50	2.54	2.59	2.61	2.44	2.62	2.44	2.48	2.65	2.66	2.64
Sum (Mg+Ti+Na)	0.18	0.18	0.18	0.18	0.15	0.19	0.21	0.18	0.21	0.21	0.17	0.15	0.16
Mg %	51.83	49.94	57.06	54.96	47.97	41.37	63.54	47.17	63.54	52.27	42.80	45.63	41.87
Ti %	22.66	24.13	18.58	14.85	22.93	14.96	17.20	18.79	17.20	31.34	16.87	18.92	22.91
Na %	25.51	25.94	24.35	30.18	29.10	43.67	19.26	34.05	19.26	16.38	40.33	35.45	35.23
Sum (Fe+Na+Mg)	0.40	0.40	0.42	0.41	0.35	0.39	0.44	0.36	0.44	0.39	0.36	0.34	0.34
Fe %	64.53	64.77	65.62	63.47	66.29	59.00	60.17	59.29	60.17	63.59	60.70	64.63	64.59
Na %	11.70	12.04	10.28	12.95	12.73	21.06	9.26	17.07	9.26	8.69	19.06	15.47	16.18
Mg %	23.77	23.19	24.10	23.58	20.98	19.95	30.57	23.64	30.57	27.72	20.23	19.91	19.23

Table A.9 Representative microprobe analyses of amphibole from the Corno Alto and Sostino rocks.
Formula based on 24 (OH, F, Cl, O)

An. N#	A1-12	A1-13	A2-25	A4-41	A4-42	A1-7	A1-8	A2-14	A2-15	A2-19	A3-22
Sample	CA19-8	CA19-8	CA19-8	CA19-8	CA19-8	CA19-3	CA19-3	CA19-3	CA19-3	CA19-3	CA19-3
Rock	OTN	OTN	OTN	OTN	OTN	MDR	MDR	MDR	MDR	MDR	MDR
SiO_2	44.19	45.49	44.14	44.06	44.08	45.84	44.05	46.88	45.59	46.19	43.47
TiO_2	0.74	0.99	0.85	0.84	0.76	0.75	0.94	0.65	0.71	0.73	1.21
Al_2O_3	9.10	8.79	9.60	9.30	9.34	8.89	10.54	8.61	9.66	9.13	11.07
FeO	18.85	17.55	19.25	19.23	19.11	14.53	15.46	14.57	14.72	14.71	15.79
MnO	0.76	0.94	0.81	0.88	0.94	0.47	0.42	0.41	0.43	0.38	0.47
MgO	9.90	10.70	9.66	10.00	9.83	13.17	11.80	12.99	12.64	12.88	11.56
CaO	12.01	11.82	11.83	11.90	11.87	11.72	11.84	11.80	11.87	11.98	11.72
Na_2O	1.02	1.14	1.02	1.09	1.19	0.95	1.08	0.93	1.03	0.88	1.17
K_2O	0.90	0.61	0.98	0.82	1.02	0.35	0.52	0.34	0.41	0.37	0.66
Total	97.46	98.03	98.16	98.12	98.16	96.67	96.65	97.18	97.06	97.25	97.12
Si	6.72	6.81	6.68	6.67	6.68	6.83	6.62	6.93	6.77	6.84	6.52
Ti	0.08	0.11	0.10	0.10	0.09	0.08	0.11	0.07	0.08	0.08	0.14
Al	1.63	1.55	1.71	1.66	1.67	1.56	1.87	1.50	1.69	1.59	1.96
Cr	0.00	0.00	0.00	0.00	0.00	0.00	0.00	0.00	0.00	0.00	0.00
Fe^{2+}	2.40	2.20	2.44	2.44	2.42	1.81	1.94	1.80	1.83	1.82	1.98
Fe^{3+}	0.00	0.00	0.00	0.00	0.00	0.00	0.00	0.00	0.00	0.00	0.00
Mn	0.10	0.12	0.10	0.11	0.12	0.06	0.05	0.05	0.05	0.05	0.06
Ni	0.00	0.00	0.00	0.00	0.00	0.00	0.00	0.00	0.00	0.00	0.00
Mg	2.24	2.39	2.18	2.26	2.22	2.92	2.64	2.86	2.80	2.84	2.58
Ca	1.96	1.90	1.92	1.93	1.93	1.87	1.91	1.87	1.89	1.90	1.88
Na	0.30	0.33	0.30	0.32	0.35	0.28	0.31	0.27	0.30	0.25	0.34
K	0.17	0.12	0.19	0.16	0.20	0.07	0.10	0.06	0.08	0.07	0.13
cations	15.61	15.52	15.61	15.64	15.67	15.48	15.55	15.41	15.49	15.44	15.60
$(Mg+Fe^{2+})$	0.48	0.52	0.47	0.48	0.48	0.62	0.58	0.61	0.60	0.61	0.57
(Na+K)A	0.47	0.45	0.49	0.48	0.55	0.34	0.41	0.33	0.37	0.32	0.47

Table A.10 Representative microprobe analyses of epidotes from the Corno Alto and Sostino rocks. <dl - below detection limits. Formula: 8 cations and 12.5 oxygens, Fe3+=3-Alvi_Ti-Cr

An. N#	D109	A-94	A-95	C3-34	C3-35	C-47	E-91	C3-1	C4-10	C-36	A-22	A-25	E-F-37	E-124	E-120	A-2
Sample	CA19-21	CA19-21	CA19-21	CA19-15	CA19-15	CA19-16	CA19-16	CA19-26	CA19-26	CA19-29	CA19-29	CA19-29	CA19-29	CA19-31	CA19-31	CA19-13
Rock	ETN	ETN	ETN	ETN	ETN	PTN	PTN	EBG	EBG	EBG	EBG	EBG	EBG	EBG	EBG	TMG
position	interstitial magmatic	incl. in plg magmatic	incl. in plg magmatic	interstitial magmatic	interstitial magmatic	incl. in plg magmatic	ısion in plg magmatic	interstitial magmatic	interstitial magmatic	interstitial magmatic	interstitial magnatic	interstitial magmatic	incl. in plg magmatic	interstitial magmatic	incl. in plg magmatic	incl. in plg magmatic
SiO_2	37.51	36.54	37.87	38.55	38.34	36.53	37.65	37.86	37.93	38.17	38.30	38.03	38.67	38.39	38.12	37.98
TiO_2	0.11	0.11	0.14	0.19	0.06	0.13	0.07	0.15	0.22	0.10	0.25	0.12	0.07	0.05	0.07	0.25
Al_2O_3	22.60	21.13	22.92	21.93	23.30	22.35	23.66	22.90	22.56	22.86	23.12	23.04	25.53	23.76	24.74	23.71
FeO	12.79	12.69	12.66	13.53	11.68	12.27	11.85	13.13	13.50	13.41	12.77	12.50	9.67	12.06	11.01	12.51
MnO	0.44	0.63	0.45	0.50	0.62	0.82	0.49	0.53	0.44	0.34	0.55	0.57	1.53	0.53	0.37	2.61
MgO	0.01	0.15	0.04	0.04	0.07	0.08	0.04	0.01	0.03	0.00	0.04	0.01	0.09	0.00	0.01	0.07
CaO	23.57	21.40	23.56	22.69	22.80	22.81	23.20	22.61	22.61	23.68	23.59	23.57	22.66	23.58	23.72	21.83
Na_2O	0.00	0.05	0.04	0.00	0.00	0.10	0.00	0.01	0.00	0.00	0.00	0.00	0.00	0.03	0.00	0.00
K_2O	0.00	0.04	0.02	0.00	0.00	0.09	0.02	0.01	0.01	0.00	0.00	0.00	0.01	0.01	0.01	0.01
Cr_2O_3	0.00	0.00	0.00	0.00	0.02	0.05	0.00	0.03	0.08	0.08	0.26	0.09	0.00	0.00	0.00	0.00
Total	97.04	92.73	97.70	97.43	96.90	95.19	96.99	97.24	97.38	98.65	98.88	97.92	98.23	98.40	98.04	98.97
Si	2.98	3.05	2.99	3.06	3.05	2.96	2.99	3.01	3.01	2.99	2.99	3.00	3.01	3.00	2.98	2.97
Al^{iv}	0.02	0.00	0.01	0.00	0.00	0.04	0.01	0.00	0.00	0.01	0.01	0.00	0.00	0.00	0.02	0.03
Al^{vi}	2.10	2.08	2.12	2.05	2.18	2.09	2.20	2.14	2.11	2.10	2.12	2.14	2.35	2.19	2.26	2.16
Ti	0.01	0.01	0.01	0.01	0.00	0.01	0.00	0.01	0.01	0.01	0.01	0.01	0.00	0.00	0.00	0.01
Cr	0.00	0.00	0.00	0.00	0.00	0.00	0.00	0.00	0.01	0.01	0.02	0.01	0.00	0.00	0.00	0.00
Fe^{3+}	0.85	0.88	0.84	0.90	0.78	0.83	0.79	0.84	0.87	0.88	0.83	0.82	0.63	0.79	0.72	0.82
Fe^{2+}	0.00	0.00	0.00	0.00	0.00	0.00	0.00	0.03	0.03	0.00	0.00	0.00	0.00	0.00	0.00	0.00
Mg	0.00	0.02	0.01	0.00	0.01	0.01	0.01	0.00	0.00	0.00	0.01	0.00	0.01	0.00	0.00	0.01
Ni	0.00	0.00	0.00	0.00	0.00	0.00	0.00	0.00	0.00	0.00	0.00	0.00	0.00	0.00	0.00	0.00
Mn	0.03	0.04	0.03	0.03	0.04	0.06	0.03	0.04	0.03	0.02	0.04	0.04	0.10	0.03	0.02	0.17
Ca	2.01	1.91	1.99	1.93	1.94	1.98	1.97	1.92	1.92	1.99	1.97	1.99	1.89	1.98	1.99	1.83
Na	0.00	0.01	0.01	0.00	0.00	0.02	0.00	0.00	0.00	0.00	0.00	0.00	0.00	0.00	0.00	0.00
K	0.00	0.00	0.00	0.00	0.00	0.01	0.00	0.00	0.00	0.00	0.00	0.00	0.00	0.00	0.00	0.00
Ps	**28.74**	**29.81**	**28.18**	**30.33**	**26.19**	**28.34**	**26.30**	**28.15**	**28.96**	**29.38**	**27.95**	**27.71**	**21.15**	**26.45**	**24.11**	**27.37**

Table A.11a U-Pb age determinations by LA-ICP-MS
*= old dates; **= discordant dates

serie LA	Age [Ma]	± 2σ abs	$^{207}Pb/^{235}U$	± 1σ abs	$^{206}Pb/^{238}U$	± 1σ abs	$^{207}Pb/^{206}Pb$	± 1σ abs	rho	Conc.%
TMG CA10-10										
CA1910.2core	38.6	1.5	0.0388	0.0035	0.0060	0.0001	0.0468	0.0044	0.2205	100.3
CA1910.2rim	39.5	2.2	0.0412	0.0053	0.0061	0.0002	0.0485	0.0064	0.2138	103.5
CA1910.5rim	39.3	1.2	0.0391	0.0022	0.0061	0.0001	0.0464	0.0027	0.2584	99.2
CA1910.6core	38.1	1.3	0.0393	0.0029	0.0059	0.0001	0.0481	0.0036	0.2320	102.9
CA1910.6rim	39.3	1	0.0395	0.0017	0.0061	0.0001	0.0468	0.1461	0.3000	100.0
CA1910.11core	39.3	1.4	0.0421	0.0032	0.0061	0.0001	0.0499	0.0038	0.2402	106.6
CA1910.20core	38.8	1.2	0.0387	0.0022	0.0060	0.0001	0.0465	0.0028	0.2604	99.5
CA1910.20rim	38.4	1.2	0.0397	0.0024	0.0060	0.0001	0.0481	0.0031	0.2459	102.6
CA1910.22core	38.2	1.7	0.0383	0.0039	0.0059	0.0001	0.0467	0.0049	0.2153	99.7
CA1910.25core	40.7	1.4	0.0413	0.0038	0.0063	0.0001	0.0474	0.0044	0.1895	101.0
CA1910.25rim	40.9	1.2	0.0412	0.0020	0.0064	0.0001	0.0470	0.0024	0.2886	100.5
CA1910.33rim	39.1	1	0.0391	0.0021	0.0061	0.0001	0.0465	0.0026	0.2421	99.5
CA1910.35core	38	1.2	0.0371	0.0029	0.0059	0.0001	0.0454	0.0036	0.1973	97.1
CA1910.35rim	39.7	1.2	0.0396	0.0024	0.0062	0.0001	0.0466	0.0029	0.2409	99.5
CA1910.38core	38.7	1	0.0418	0.0017	0.0060	0.0001	0.0502	0.0022	0.3299	107.2
CA1910.38rim	38.8	1	0.0417	0.0019	0.0060	0.0001	0.0500	0.0024	0.2920	106.7
CA1910.45core	39.9	1.8	0.0391	0.0044	0.0062	0.0001	0.0457	0.0052	0.2019	97.7
CA1910.45rim	39.7	1.2	0.0406	0.0022	0.0062	0.0001	0.0476	0.0027	0.2649	101.8
CA1910.12rim	44.12	0.9	0.0465	0.0009	0.0069	0.0001	0.0491	0.0011	0.5264	104.5
CA1910.17rim	42	1	0.0437	0.0016	0.0065	0.0001	0.0485	0.0019	0.3348	103.6
CA1910.21rim	43.3	0.9	0.0436	0.0013	0.0067	0.0001	0.0469	0.0015	0.3510	100.0
CA1910.4rim	44.8	1	0.0448	0.0015	0.0070	0.0001	0.0466	0.0016	0.3521	99.3
CA1910.16rim	43.6	1.2	0.0454	0.0019	0.0068	0.0001	0.0484	0.0021	0.3233	103.4
CA1910.46rim	42.5	1.2	0.0453	0.0021	0.0066	0.0001	0.0496	0.0024	0.3006	105.9
CA1910.16core*	514.9	9.7	0.6813	0.0110	0.0828	0.0008	0.0596	0.0012	0.6110	102.8
CA1910.7core*	449.4	8.5	0.5609	0.0079	0.0721	0.0007	0.0564	0.0010	0.7067	100.8
CA1910.7rim*	454.4	9	0.5841	0.0106	0.0728	0.0008	0.0582	0.0013	0.5696	103.1
CA1910.12core*	661	13	0.9216	0.0165	0.1080	0.0011	0.0619	0.0013	0.5780	100.3
CA1910.24core*	879	30	1.3396	0.1031	0.1463	0.0027	0.0664	0.0053	0.2407	98.1
CA1910.4core*	980	20	1.6617	0.0393	0.1636	0.0019	0.0736	0.0020	0.4785	101.8
CA1910.24rim**	45.1	1.2	0.0419	0.0020	0.0070	0.0001	0.0432	0.0021	0.2740	92.5
CA1910.22rim**	39.4	1.3	0.0446	0.0030	0.0061	0.0001	0.0527	0.0036	0.2447	112.4
CA1910.31rim**	38.7	1.3	0.0428	0.0026	0.0060	0.0001	0.0515	0.0032	0.2744	109.8
CA1910.33core**	39.9	1.7	0.0496	0.0042	0.0062	0.0001	0.0578	0.0050	0.2488	123.0
CA1910.17core**	discordant		0.8892	0.0108	0.0972	0.0010	0.0663	0.0011	0.8016	108.0
CA1910.46core**	discordant		1.1316	0.0202	0.1193	0.0012	0.0688	0.0015	0.5832	105.8
CA1910.5core**	discordant		4.0711	0.0531	0.1683	0.0017	0.1754	0.0031	0.7888	164.4
CA1910.21core**	discordant		0.5071	0.0104	0.0595	0.0006	0.0617	0.0015	0.5072	111.7
CA1910.31core**	discordant		0.0570	0.0040	0.0060	0.0001	0.0689	0.0051	0.2846	146.2
TMG CA10-13										
CA19-13_10core	43.43	1.66	0.0439	0.0032	0.0068	0.0001	0.0471	0.0035	0.2639	99.5
CA19-13_16rim	44.14	1.54	0.0445	0.0028	0.0069	0.0001	0.0469	0.0030	0.2825	99.8
CA19-13_17core	42.82	1.54	0.0431	0.0030	0.0067	0.0001	0.0468	0.0033	0.2575	100.0
CA19-13_32rim	41.83	1.8	0.0425	0.0040	0.0065	0.0001	0.0474	0.0045	0.2299	99.1
CA19-13_36core	42.3	2	0.0427	0.0058	0.0066	0.0002	0.0471	0.0064	0.1805	99.5
CA19-13_36rim	43.88	1.42	0.0442	0.0023	0.0068	0.0001	0.0469	0.0024	0.3120	100.0
CA19-13_59core	44.71	1.54	0.0450	0.0024	0.0070	0.0001	0.0469	0.0026	0.3180	100.0
CA19-13_59rim	43.69	1.8	0.0439	0.0038	0.0068	0.0001	0.0468	0.0042	0.2352	100.2
CA19-13_10rim	43.05	1.16	0.0438	0.0014	0.0067	0.0001	0.0474	0.0015	0.4321	98.9
CA19-13_4core	45.54	1.92	0.0460	0.0040	0.0071	0.0002	0.0471	0.0042	0.2432	99.8
CA19-13_6rim	44.84	1.42	0.0451	0.0024	0.0070	0.0001	0.0468	0.0025	0.2996	100.0
CA19-13_4rim	46.82	1.54	0.0474	0.0025	0.0073	0.0001	0.0471	0.0026	0.3084	99.6
CA19-13_5core**	discordant		0.0747	0.0048	0.0067	0.0001	0.0811	0.0053	0.3063	58.7
CA19-13_5rim**	43.37	0.77	0.0451	0.0029	0.0068	0.0001	0.0485	0.0032	0.2766	96.9

Table A.11b U-Pb age determinations by LA-ICP-MS; *= old dates; **= discordant dates

serie LA TMG CA19-37	Age [Ma]	± 2σ abs	$^{207}Pb/^{235}U$	± 1σ abs	$^{206}Pb/^{238}U$	± 1σ abs	$^{207}Pb/^{206}Pb$	± 1σ abs	rho	Conc.%
CA19-37_1rim	41.2	1.4	0.0411	0.0034	0.0064	0.0001	0.2105	0.0465	0.0038	99.3
CA19-37_2rim	41.8	1.2	0.0436	0.0011	0.0065	0.0001	0.5629	0.0486	0.0012	103.6
CA19-37_9core	40.5	1.8	0.0404	0.0041	0.0063	0.0001	0.2196	0.0466	0.0048	99.3
CA19-37_13rim	41.8	1.4	0.0432	0.0022	0.0065	0.0001	0.3329	0.0481	0.0025	102.6
CA19-37_13core	42.1	1.4	0.0437	0.0026	0.0066	0.0001	0.2772	0.0482	0.0030	102.8
CA19-37_14rim	42	1.7	0.0418	0.0025	0.0065	0.0001	0.3346	0.0463	0.0028	98.6
CA19-37_15rim	42.1	1.9	0.0432	0.0031	0.0066	0.0002	0.3188	0.0480	0.0035	101.9
CA19-37_16rim	41.5	1.8	0.0414	0.0028	0.0065	0.0001	0.3168	0.0465	0.0032	99.3
CA19-37_17rim	41.1	1.4	0.0423	0.0022	0.0064	0.0001	0.3383	0.0479	0.0025	102.4
CA19-37_17core	41.3	1.5	0.0414	0.0024	0.0064	0.0001	0.3196	0.0468	0.0028	100.0
CA19-37_19core	42.9	2	0.0427	0.0043	0.0067	0.0002	0.2377	0.0464	0.0047	99.1
CA19-37_6core	43.7	1.8	0.0434	0.0037	0.0068	0.0001	0.2410	0.0464	0.0040	98.9
CA19-37_9rim	44.2	1.4	0.0441	0.0018	0.0069	0.0001	0.3896	0.0465	0.0019	99.1
CA19-37_6rim	44.6	1.5	0.0450	0.0028	0.0070	0.0001	0.2777	0.0470	0.0030	100.2
CA19-37_3rim	44.9	1.3	0.0452	0.0016	0.0070	0.0001	0.4172	0.0469	0.0016	100.0
CA19-37_5core*	637	17	0.9366	0.0271	0.1034	0.0014	0.0657	0.0019	0.4754	122.2
CA19-37_7core*	471	12	0.5954	0.0158	0.0757	0.0010	0.0570	0.0015	0.5117	105.8
CA19-37_16core*	769	28	1.1591	0.0675	0.1266	0.0024	0.0664	0.0039	0.3313	101.7
CA19-37_18core*	2461	71	10.9545	0.5838	0.4599	0.0087	0.1728	0.0093	0.3562	103.3
CA19-37_22core*	710	43	0.9549	0.1010	0.1167	0.0037	0.0594	0.0064	0.3014	95.7
CA19-37_25core*	479	32	0.6498	0.0758	0.0771	0.0027	0.0612	0.0072	0.3002	106.2
CA19-37_15core**	discordant		1.9965	0.2199	0.1379	0.0047	0.1054	0.0120	0.3081	133.8
CA19-37_5rim**	discordant		0.0852	0.0026	0.0106	0.0002	0.0583	0.0018	0.4657	122.2
CA19-37_7rim**	discordant		0.2973	0.0076	0.0373	0.0005	0.0577	0.0015	0.5259	111.8
CA19-37_14core**	discordant		0.7920	0.0272	0.0840	0.0013	0.0684	0.0024	0.4362	113.9

Table A.11c U-Pb age determinations by LA-ICP-MS; *= old dates; **= discordant dates

serie LA TMG CA19-41	Age [Ma]	± 2σ abs	$^{207}Pb/^{235}U$	± 1σ abs	$^{206}Pb/^{238}U$	± 1σ abs	$^{207}Pb/^{206}Pb$	± 1σ abs	rho	Conc.%
CA19-41_1core	44.2	1.9	0.0411	0.0046	0.0069	0.0002	0.0433	0.0049	0.1953	92.3
CA19-41_1rim	45.2	1.7	0.0468	0.0033	0.0070	0.0001	0.0483	0.0034	0.2643	102.7
CA19-41_2core	44	1.2	0.0455	0.0012	0.0069	0.0001	0.0482	0.0012	0.5067	102.7
CA19-41_3rim	43.8	1.2	0.0423	0.0010	0.0068	0.0001	0.0449	0.0011	0.5466	95.9
CA19-41_5rim	43.1	1.2	0.0463	0.0013	0.0067	0.0001	0.0501	0.0014	0.4856	106.7
CA19-41_6rim	44.8	1.2	0.0451	0.0010	0.0070	0.0001	0.0469	0.0010	0.5998	100.0
CA19-41_7rim	43.2	1.2	0.0432	0.0012	0.0067	0.0001	0.0466	0.0013	0.4658	99.3
CA19-41_7core	43.6	1.5	0.0460	0.0026	0.0068	0.0001	0.0492	0.0029	0.3082	104.8
CA19-41_9rim	45.4	1.5	0.0465	0.0022	0.0071	0.0001	0.0477	0.0023	0.3571	101.5
CA19-41_10rim	43.2	1.2	0.0434	0.0012	0.0067	0.0001	0.0468	0.0012	0.5046	99.8
CA19-41_10core	44.5	1.3	0.0485	0.0015	0.0069	0.0001	0.0507	0.0016	0.4573	108.1
CA19-41_18core	44.2	1.7	0.0501	0.0029	0.0069	0.0001	0.0527	0.0031	0.3235	112.0
CA19-41_19rim	43.5	1.3	0.0438	0.0017	0.0068	0.0001	0.0469	0.0019	0.3803	100.0
CA19-41_21rim	43.3	1.4	0.0440	0.0017	0.0067	0.0001	0.0473	0.0019	0.4219	100.9
CA19-41_22rim	43.2	1.8	0.0467	0.0029	0.0067	0.0001	0.0506	0.0033	0.3337	107.2
CA19-41_28rim	42.3	1.9	0.0417	0.0041	0.0066	0.0002	0.0460	0.0046	0.2328	98.1
CA19-41_30rim	43.8	2.3	0.0432	0.0041	0.0068	0.0002	0.0460	0.0045	0.2764	97.9
CA19-41_31core	42.6	2	0.0451	0.0038	0.0066	0.0002	0.0494	0.0043	0.2842	105.2
CA19-41_40core	42.5	2	0.0434	0.0033	0.0066	0.0002	0.0475	0.0037	0.3215	101.4
CA19-41_44core	42.6	2	0.0439	0.0032	0.0066	0.0002	0.0480	0.0036	0.3307	102.3
CA19-41_45rim	42.6	2.2	0.0427	0.0035	0.0066	0.0002	0.0467	0.0039	0.3172	99.5
CA19-41_13rim	42.1	1.2	0.0438	0.0014	0.0066	0.0001	0.0485	0.0016	0.4205	103.3
CA19-41_17rim	41.8	1.2	0.0432	0.0014	0.0065	0.0001	0.0481	0.0015	0.4422	102.6
CA19-41_19rim	42.3	1.5	0.0425	0.0022	0.0066	0.0001	0.0468	0.0025	0.3565	99.5
CA19-41_26core	41.2	1.4	0.0428	0.0019	0.0064	0.0001	0.0485	0.0022	0.3848	103.4
CA19-41_28core	40	2.1	0.0409	0.0044	0.0062	0.0002	0.0478	0.0052	0.2411	101.8
CA19-41_30core	40.8	2.2	0.0418	0.0049	0.0064	0.0002	0.0478	0.0057	0.2277	101.7
CA19-41_41core	40.4	2.3	0.0412	0.0039	0.0063	0.0002	0.0476	0.0048	0.3003	101.5
CA19-41_31rim	40.4	2.1	0.0402	0.0034	0.0063	0.0002	0.0465	0.0042	0.3021	99.0
CA19-41_9core*	783	19	1.1820	0.0262	0.1287	0.0017	0.0666	0.0014	0.6068	101.5
CA19-41_14core*	586	17	0.7867	0.0289	0.0951	0.0015	0.0601	0.0022	0.4233	100.7
CA19-41_15core*	656	20	0.9122	0.0353	0.1071	0.0017	0.0619	0.0025	0.4172	100.4
CA19-41_22core*	1068	30	1.9133	0.0727	0.1797	0.0028	0.0772	0.0030	0.4157	101.9
CA19-41_23core*	591	19	0.8032	0.0375	0.0960	0.0016	0.0607	0.0029	0.3637	101.3
CA19-41_27core*	558	21	0.7325	0.0427	0.0904	0.0018	0.0589	0.0036	0.3394	100.0
CA19-41_29rim*	516	18	0.7165	0.0352	0.0832	0.0015	0.0625	0.0032	0.3647	106.4
CA19-41_29core*	1019	35	1.7967	0.0939	0.1708	0.0032	0.0763	0.0041	0.3564	102.7
CA19-41_32core*	452	31	0.6436	0.0758	0.0727	0.0025	0.0645	0.0082	0.2968	111.6
CA19-41_35core*	1716	83	5.0078	0.4584	0.3026	0.0086	0.1204	0.0118	0.3087	106.8
CA19-41_42core*	151.1	7.7	0.1896	0.0157	0.0238	0.0006	0.0580	0.0050	0.3112	116.5
CA19-41_45core*	463	22	0.6153	0.0491	0.0744	0.0019	0.0600	0.0050	0.3132	105.3
CA19-41_17core*	737	20	1.1180	0.0346	0.1207	0.0018	0.0672	0.0021	0.4718	103.7
CA19-41_27rim*	226.6	8	0.2930	0.0141	0.0358	0.0006	0.0594	0.0030	0.3702	115.0
CA19-41_35rim**	discordant		0.0894	0.0092	0.0091	0.0003	0.0713	0.0078	0.2986	148.3
CA19-41_36core**	42.8	5	0.0564	0.0125	0.0067	0.0004	0.0614	0.0144	0.2637	129.8
CA19-41_12rim**	discordant		0.1925	0.0047	0.0239	0.0003	0.0586	0.0014	0.5618	117.6
CA19-41_12core**	discordant		4.6135	0.1354	0.2849	0.0042	0.1175	0.0035	0.5047	108.4
CA19-41_21core**	discordant		0.1095	0.0061	0.0103	0.0002	0.0771	0.0045	0.3489	159.1
CA19-41_39rim**	42.7	2.3	0.0481	0.0043	0.0067	0.0002	0.0526	0.0049	0.3044	111.7
CA19-41_32rim**	39.3	1.8	0.0433	0.0030	0.0061	0.0001	0.0514	0.0038	0.3258	109.4
CA19-41_36rim**	41.8	2.8	0.0565	0.0072	0.0065	0.0002	0.0629	0.0084	0.2630	133.2
CA19-41_26rim**	41.6	1.5	0.0442	0.0022	0.0065	0.0001	0.0496	0.0026	0.3661	105.5
CA19-41_42rim**	40.3	1.9	0.0433	0.0034	0.0063	0.0002	0.0500	0.0040	0.3075	106.7
CA19-41_18rim **	47.3	3.2	0.0407	0.0077	0.0074	0.0003	0.0403	0.0078	0.1789	85.4

Table A.11d U-Pb age determinations by LA-ICP-MS; *= old dates; **= discordant dates

serie LA PTN CA19-16	Age [Ma]	± 2σ abs	$^{207}Pb/^{235}U$	± 1σ abs	$^{206}Pb/^{238}U$	± 1σ abs	$^{207}Pb/^{206}Pb$	± 1σ abs	rho	Conc.%
CA19-16_1rimb	42.1	1.2	0.0434	0.0013	0.0066	0.0001	0.0481	0.0015	0.4452	102.6
CA19-16_6rim	41.8	1.2	0.0414	0.0009	0.0065	0.0001	0.0462	0.0010	0.6374	98.6
CA19-16_8core	42.2	1.5	0.0435	0.0029	0.0066	0.0001	0.0481	0.0032	0.2770	102.6
CA19-16_9rim	42.1	1.2	0.0420	0.0016	0.0066	0.0001	0.0465	0.0017	0.3674	99.3
CA19-16_9core	41.9	1.2	0.0420	0.0009	0.0065	0.0001	0.0467	0.0010	0.6296	99.5
CA19-16_13rim	42.5	1.5	0.0439	0.0028	0.0066	0.0001	0.0481	0.0031	0.2890	102.6
CA19-16_14rim	42.6	1.2	0.0426	0.0012	0.0066	0.0001	0.0466	0.0013	0.4816	99.3
CA19-16_15core	42.4	1.2	0.0420	0.0013	0.0066	0.0001	0.0462	0.0014	0.4309	98.6
CA19-16_17rima	42.2	1.2	0.0423	0.0009	0.0066	0.0001	0.0467	0.0010	0.6167	99.8
CA19-16_17rimb	42.6	1.2	0.0423	0.0010	0.0066	0.0001	0.0462	0.0010	0.5965	98.6
CA19-16_23rim	42.6	1.2	0.0416	0.0009	0.0065	0.0001	0.0466	0.0009	0.6573	99.5
CA19-16_26core	42.9	1.4	0.0424	0.0021	0.0067	0.0001	0.0462	0.0023	0.3376	98.1
CA19-16_29rim	42.3	1.2	0.0421	0.0012	0.0066	0.0001	0.0464	0.0013	0.4754	99.1
CA19-16_34core	42.5	1.4	0.0425	0.0021	0.0066	0.0001	0.0467	0.0023	0.3350	99.3
CA19-16_37rim	41.9	1.2	0.0429	0.0012	0.0065	0.0001	0.0477	0.0013	0.4893	101.7
CA19-16_37core	42.7	1.2	0.0423	0.0009	0.0067	0.0001	0.0462	0.0010	0.6159	98.6
CA19-16_39rim	42.1	1.2	0.0422	0.0012	0.0066	0.0001	0.0467	0.0013	0.4995	99.8
CA19-16_44rim	43	1.2	0.0432	0.0010	0.0067	0.0001	0.0468	0.0010	0.5980	99.5
CA19-16_44core	41.6	1.3	0.0426	0.0015	0.0065	0.0001	0.0478	0.0017	0.4306	101.9
CA19-16_59rim	41.4	1.3	0.0411	0.0015	0.0065	0.0001	0.0462	0.0017	0.4303	98.6
CA19-16_59core	42.8	1.3	0.0430	0.0023	0.0067	0.0001	0.0468	0.0025	0.2856	99.8
CA19-16_47rim	41.4	1	0.0411	0.0008	0.0065	0.0001	0.0461	0.0009	0.6278	98.6
CA19-16_47core	42.7	1.2	0.0425	0.0012	0.0067	0.0001	0.0464	0.0013	0.4921	99.1
CA19-16_48core	41.6	1.2	0.0417	0.0015	0.0065	0.0001	0.0467	0.0017	0.3864	99.8
CA19-16_50core	42.3	1.4	0.0419	0.0022	0.0066	0.0001	0.0462	0.0025	0.3171	98.6
CA19-16_51rim	42.5	1.3	0.0419	0.0019	0.0066	0.0001	0.0460	0.0021	0.3302	98.1
CA19-16_52rim	42.5	1.2	0.0426	0.0010	0.0066	0.0001	0.0467	0.0011	0.5687	99.8
CA19-16_55core	42.3	1.3	0.0425	0.0017	0.0066	0.0001	0.0469	0.0019	0.3818	100.0
CA19-16_56rim	42.4	1.2	0.0426	0.0010	0.0066	0.0001	0.0468	0.0010	0.5983	99.8
CA19-16_57core	42.1	1.3	0.0417	0.0018	0.0066	0.0001	0.0461	0.0019	0.3633	98.3
CA19-16_53rim	41.5	1.3	0.0431	0.0015	0.0065	0.0001	0.0485	0.0017	0.4334	103.4
CA19-16_49rim	41.1	1	0.0411	0.0008	0.0064	0.0001	0.0466	0.0008	0.6764	99.8
CA19-16_34rim	41.2	1	0.0408	0.0009	0.0064	0.0001	0.0462	0.0009	0.5924	98.5
CA19-16_27rim	41.5	1.2	0.0411	0.0011	0.0065	0.0001	0.0461	0.0012	0.5155	98.6
CA19-16_30rim	40.5	1	0.0406	0.0009	0.0063	0.0001	0.0466	0.0010	0.5842	99.5
CA19-16_35rim	40.4	1.2	0.0404	0.0011	0.0063	0.0001	0.0467	0.0012	0.5262	99.8
CA19-16_55rim	40.6	1.2	0.0406	0.0013	0.0063	0.0001	0.0466	0.0014	0.4584	99.5
CA19-16_40core	43.2	1.3	0.0438	0.0015	0.0067	0.0001	0.0472	0.0016	0.4394	100.5
CA19-16_13core	43.4	1.5	0.0434	0.0029	0.0068	0.0001	0.0466	0.0031	0.2707	99.3
CA19-16_27core	43.3	1.4	0.0435	0.0026	0.0067	0.0001	0.0469	0.0028	0.2744	100.0
CA19-16_52core	43.6	1.7	0.0430	0.0039	0.0068	0.0001	0.0460	0.0042	0.2144	98.2
CA19-16_21rim	43.9	1.2	0.0454	0.0011	0.0068	0.0001	0.0482	0.0011	0.5491	102.7
CA19-16_39core	43.8	1.7	0.0453	0.0030	0.0068	0.0001	0.0483	0.0033	0.2873	102.7
CA19-16_46core	43.8	1.4	0.0441	0.0022	0.0068	0.0001	0.0470	0.0023	0.3310	100.2
CA19-16_6core	44.3	1.4	0.0453	0.0024	0.0069	0.0001	0.0476	0.0025	0.3019	101.4
CA19-16_25rim	44.6	1.3	0.0441	0.0014	0.0070	0.0001	0.0461	0.0015	0.4473	98.2
CA19-16_23core	45.6	1.3	0.0458	0.0014	0.0071	0.0001	0.0468	0.0014	0.4575	99.8
CA19-16_30core	44.4	1.3	0.0446	0.0014	0.0069	0.0001	0.0468	0.0015	0.4516	99.8
CA19-16_49core	44.4	1.2	0.0450	0.0012	0.0069	0.0001	0.0472	0.0012	0.4882	100.7
CA19-16_53core	44.8	1.3	0.0447	0.0015	0.0070	0.0001	0.0465	0.0015	0.4388	99.1
CA19-16_35core	45.2	1.3	0.0470	0.0014	0.0070	0.0001	0.0485	0.0014	0.4876	103.3
CA19-16_3core	44.1	1.5	0.0479	0.0028	0.0069	0.0001	0.0507	0.0030	0.3030	107.5
CA19-16_24core*	568	14	0.7534	0.0136	0.0919	0.0012	0.0595	0.0010	0.7244	100.6
CA19-16_29core*	574	17	0.7370	0.0341	0.0932	0.0015	0.0574	0.0027	0.3433	97.6
CA19-16_31core*	186.6	4.7	0.2018	0.0030	0.0294	0.0004	0.0499	0.0006	0.8762	100.0
CA19-16_51core*	867	19	1.3451	0.0226	0.1443	0.0019	0.0676	0.0010	0.7703	99.6
CA19-16_58core*	521	12	0.6719	0.0100	0.0837	0.0011	0.0582	0.0008	0.8594	100.7
CA19-16_21core**	42	1.5	0.0377	0.0030	0.0065	0.0001	0.0418	0.0034	0.2284	89.5
CA19-16_25core**	discordant		-0.0120	0.0047	0.0022	0.0002	-0.0405	0.0160	-0.1781	-88.5
CA19-16_58rim**	40.5	1.4	0.0428	0.0026	0.0063	0.0001	0.0494	0.0030	0.2932	105.2
CA19-16_40rim**	41	1.2	0.0397	0.0013	0.0064	0.0001	0.0452	0.0015	0.4271	96.3
CA19-16_46rim**	41.7	1.2	0.0404	0.0010	0.0065	0.0001	0.0450	0.0010	0.5764	96.2
CA19-16_14core**	42.5	1.4	0.0409	0.0025	0.0066	0.0001	0.0449	0.0028	0.2676	95.8
CA19-16_15rim**	40	1.2	0.0422	0.0014	0.0062	0.0001	0.0492	0.0017	0.4265	104.7

Table A.11e U-Pb age determinations by LA-ICP-MS
*= old dates; **= discordant dates

serie LA ETN CA19-21	Age [Ma]	± 2σ abs	$^{207}Pb/^{235}U$	± 1σ abs	$^{206}Pb/^{238}U$	± 1σ abs	$^{207}Pb/^{206}Pb$	± 1σ abs	rho	Conc.%
CA19-21-1rim	46.1	1.3	0.0466	0.0020	0.0072	0.0001	0.0471	0.0020	0.3233	100.2
CA19-21-25rim	45.2	1.22	0.0461	0.0012	0.0070	0.0001	0.0477	0.0012	0.5617	101.6
CA19-21-26rim	44.4	1.12	0.0447	0.0013	0.0069	0.0001	0.0469	0.0013	0.4547	100.0
CA19-21-31core	43.4	1.28	0.0449	0.0020	0.0068	0.0001	0.0483	0.0021	0.3338	102.8
CA19-21-31rim	45.1	1.4	0.0449	0.0018	0.0070	0.0001	0.0464	0.0019	0.3817	98.7
CA19-21-40core	46	1.78	0.0472	0.0038	0.0072	0.0001	0.0479	0.0039	0.2437	102.0
CA19-21-41core	45.3	1.4	0.0454	0.0018	0.0071	0.0001	0.0468	0.0018	0.4004	99.6
CA19-21-41rim	44.5	1.24	0.0453	0.0014	0.0069	0.0001	0.0476	0.0015	0.4647	101.4
CA19-21-43core	43.4	1.78	0.0438	0.0038	0.0068	0.0001	0.0471	0.0041	0.2408	100.5
CA19-21-43rim	43.6	1.38	0.0441	0.0018	0.0068	0.0001	0.0472	0.0020	0.3886	100.7
CA19-21-44core	45	1.8	0.0455	0.0030	0.0070	0.0001	0.0471	0.0031	0.3036	100.0
CA19-21-44rim	45.2	1.52	0.0477	0.0023	0.0070	0.0001	0.0493	0.0024	0.3527	104.6
CA19-21-45core	46.3	2.2	0.0471	0.0041	0.0072	0.0002	0.0474	0.0041	0.2732	100.9
CA19-21-45rim	45.3	1.78	0.0464	0.0027	0.0070	0.0001	0.0478	0.0028	0.3467	101.8
CA19-21-49core	44	1.66	0.0443	0.0026	0.0069	0.0001	0.0469	0.0028	0.3281	100.0
CA19-21-49rim	44.2	1.66	0.0452	0.0025	0.0069	0.0001	0.0478	0.0027	0.3447	101.6
CA19-21-51core2	45.9	2.2	0.0460	0.0038	0.0072	0.0002	0.0467	0.0039	0.2917	99.6
CA19-21-51rim1	43	1.66	0.0438	0.0027	0.0067	0.0001	0.0474	0.0030	0.3156	100.9
CA19-21-52rim	43.8	1.9	0.0444	0.0031	0.0068	0.0002	0.0473	0.0033	0.3196	100.9
CA19-21-54rim	45	2	0.0444	0.0033	0.0070	0.0002	0.0463	0.0034	0.3138	98.4
CA19-21-55rim	45.4	1.9	0.0466	0.0033	0.0071	0.0002	0.0479	0.0035	0.2980	101.8
CA19-21-56core	44.4	2.8	0.0446	0.0051	0.0069	0.0002	0.0469	0.0055	0.2781	99.8
CA19-21-56rim	44.9	2.4	0.0462	0.0040	0.0070	0.0002	0.0479	0.0042	0.2986	102.0
CA19-21-26core*	433	11.2	0.5535	0.0146	0.0690	0.0010	0.0582	0.0015	0.5335	104.0
CA19-21-6core**	45.5	1.92	0.0532	0.0059	0.0071	0.0002	0.0545	0.0061	0.1926	115.6
CA19-21-51rim2**	47.5	2.2	0.0477	0.0035	0.0074	0.0002	0.0468	0.0035	0.3114	99.6
CA19-21-52core**	45.6	3.2	0.0474	0.0060	0.0071	0.0003	0.0485	0.0063	0.2779	103.1
CA19-21-54core**	44.7	3.2	0.0455	0.0061	0.0070	0.0003	0.0475	0.0065	0.2668	100.9
CA19-21-51core1**	45	1.8	0.0432	0.0029	0.0070	0.0001	0.0447	0.0030	0.3018	95.3
CA19-21-55core**	42.6	2.2	0.0448	0.0041	0.0066	0.0002	0.0490	0.0046	0.2792	104.2
CA19-21-42rim**	43.4	1.28	0.0462	0.0019	0.0067	0.0001	0.0498	0.0021	0.3535	106.0
CA19-21-40rim**	44.4	1.26	0.0471	0.0017	0.0069	0.0001	0.0497	0.0017	0.4151	105.9
CA19-21-33rim**	44.7	1.38	0.0470	0.0020	0.0069	0.0001	0.0493	0.0021	0.3789	104.9
CA19-21-33core**	42.9	1.54	0.0489	0.0031	0.0067	0.0001	0.0530	0.0034	0.2836	112.6
CA19-21-58rim**	43	2	0.0459	0.0035	0.0068	0.0002	0.0493	0.0038	0.3115	105.1
CA19-21-1core**	43.7	1.3	0.0478	0.0039	0.0068	0.0001	0.0510	0.0042	0.2361	108.5
CA19-21-25core**	43.7	1.28	0.0423	0.0021	0.0068	0.0001	0.0450	0.0022	0.3026	95.9
CA19-21-42core**	43.3	1.54	0.0459	0.0030	0.0067	0.0001	0.0498	0.0033	0.2744	106.0

Table A.11f U-Pb age determinations by LA-ICP-MS
*= old dates; **= discordant dates

serie LA EBG CA19-26	Age [Ma]	± 2σ abs	$^{207}Pb/^{235}U$	± 1σ abs	$^{206}Pb/^{238}U$	± 1σ abs	$^{207}Pb/^{206}Pb$	± 1σ abs	rho	Conc.%
CA19-26_1rim	44.6	1.5	0.0447	0.0025	0.0070	0.0001	0.0467	0.0026	0.3102	99.3
CA19-26_2rim	44.4	1.2	0.0445	0.0010	0.0069	0.0001	0.0467	0.0011	0.5572	99.5
CA19-26_2core	44.6	1.4	0.0453	0.0022	0.0070	0.0001	0.0473	0.0023	0.3288	100.9
CA19-26_3rim	43.9	1.3	0.0437	0.0015	0.0068	0.0001	0.0463	0.0016	0.4172	98.9
CA19-26_4core	44.7	1.3	0.0448	0.0013	0.0070	0.0001	0.0467	0.0013	0.5146	99.6
CA19-26_4rim	44.1	1.3	0.0450	0.0015	0.0069	0.0001	0.0476	0.0015	0.4465	101.4
CA19-26_5core	45.2	1.4	0.0452	0.0022	0.0070	0.0001	0.0466	0.0022	0.3269	99.3
CA19-26_6rim	43.1	1.3	0.0430	0.0016	0.0067	0.0001	0.0465	0.0017	0.4051	99.1
CA19-26_8rim	42.7	1.3	0.0428	0.0016	0.0067	0.0001	0.0467	0.0017	0.4051	99.8
CA19-26_8core	45	0.5	0.0452	0.0020	0.0070	0.0001	0.0468	0.0020	0.3948	99.8
CA19-26_9rim	44.6	1.4	0.0448	0.0019	0.0070	0.0001	0.0468	0.0020	0.3754	99.6
CA19-26_9core	44.1	1.3	0.0443	0.0016	0.0069	0.0001	0.0468	0.0016	0.4134	99.8
CA19-26_10rim	43.6	1.7	0.0433	0.0024	0.0068	0.0001	0.0463	0.0025	0.3498	98.4
CA19-26_10core	43.2	1.4	0.0433	0.0020	0.0067	0.0001	0.0467	0.0021	0.3629	99.3
CA19-26_11rim	44.5	1.8	0.0448	0.0026	0.0069	0.0001	0.0468	0.0027	0.3533	100.0
CA19-26_12rim	44.4	1.7	0.0447	0.0024	0.0069	0.0001	0.0469	0.0026	0.3486	100.0
CA19-26_14core	44.6	1.9	0.0445	0.0042	0.0069	0.0002	0.0466	0.0044	0.2291	99.1
CA19-26_15rim	43.6	1.7	0.0438	0.0026	0.0068	0.0001	0.0468	0.0028	0.3289	99.8
CA19-26_16rim	43.6	2	0.0437	0.0032	0.0068	0.0002	0.0467	0.0034	0.3218	99.5
CA19-26_19rim	44.1	1.7	0.0443	0.0025	0.0069	0.0001	0.0469	0.0026	0.3412	99.8
CA19-26_20rim	45.2	2.3	0.0454	0.0038	0.0070	0.0002	0.0468	0.0040	0.3036	99.8
CA19-26_45rim	43.1	1.7	0.0433	0.0025	0.0067	0.0001	0.0469	0.0028	0.3318	100.0
CA19-26_47rim	43.3	2.4	0.0436	0.0041	0.0068	0.0002	0.0469	0.0046	0.2966	100.2
CA19-26_50rim	44.5	2.6	0.0446	0.0043	0.0069	0.0002	0.0467	0.0046	0.3021	99.6
CA19-26_50core	43	1.9	0.0432	0.0031	0.0067	0.0002	0.0468	0.0034	0.3142	99.8
CA19-26_51rim	43.2	2	0.0432	0.0032	0.0067	0.0002	0.0466	0.0035	0.3235	99.5
CA19-26_56rim	45	2.4	0.0452	0.0045	0.0070	0.0002	0.0468	0.0048	0.2735	99.8
CA19-26_56core	45	2.4	0.0447	0.0047	0.0070	0.0002	0.0464	0.0050	0.2578	98.7
CA19-26_3core*	680	17	0.9618	0.0213	0.1112	0.0015	0.0628	0.0013	0.6045	100.7
CA19-26_12core*	556	18	0.7453	0.0336	0.0900	0.0015	0.0601	0.0027	0.3702	101.8
CA19-26_16core*	666	23	0.9326	0.0446	0.1089	0.0020	0.0622	0.0030	0.3745	100.4
CA19-26_44core*	1849	60	5.3924	0.2964	0.3305	0.0064	0.1184	0.0066	0.3546	102.3
CA19-26_47core*	568	23	0.7589	0.0485	0.0920	0.0019	0.0598	0.0039	0.3301	101.1
CA19-26_51core*	333	18	0.4134	0.0382	0.0530	0.0015	0.0566	0.0054	0.3046	105.5
CA19-26_55rim*	868	37	1.4702	0.1020	0.1438	0.0033	0.0741	0.0053	0.3278	106.0
CA19-26_55core*	927	40	1.5336	0.1118	0.1546	0.0036	0.0720	0.0054	0.3232	101.9
CA19-26_21rima*	1917	59	6.4142	0.3297	0.3414	0.0064	0.1363	0.0071	0.3653	107.4
CA19-26_21rimb*	2174	64	7.6070	0.3950	0.4001	0.0075	0.1380	0.0073	0.3625	100.8
CA19-26_7rim**	discordant		0.0633	0.0029	0.0079	0.0001	0.0579	0.0027	0.3591	122.4
CA19-26_7core**	48.1	1.8	0.0544	0.0030	0.0075	0.0001	0.0528	0.0030	0.3376	111.9
CA19-26_19core**	46.4	1.7	0.0498	0.0026	0.0072	0.0001	0.0501	0.0027	0.3436	106.5

Table A.11g U-Pb age determinations by LA-ICP-MS
*= old dates; **= discordant dates

serie LA EBG CA19-26	Age [Ma]	± 2σ abs	$^{207}Pb/^{235}U$	± 1σ abs	$^{206}Pb/^{238}U$	± 1σ abs	$^{207}Pb/^{206}Pb$	± 1σ abs	rho	Conc.%
CA1930.3core	44.58	1.8	0.0449	0.0027	0.0069	0.0001	0.0471	0.0028	0.3380	100.0
CA1930.3rim	45.67	1.66	0.0459	0.0022	0.0071	0.0001	0.0469	0.0022	0.3828	99.1
CA1930.4core	43.94	1.42	0.0451	0.0016	0.0068	0.0001	0.0478	0.0017	0.4472	100.5
CA1930.4rim	43.3	1.42	0.0436	0.0015	0.0067	0.0001	0.0470	0.0016	0.4649	100.0
CA1930.6core	43.05	1.42	0.0432	0.0016	0.0067	0.0001	0.0468	0.0017	0.4518	99.6
CA1930.6rim	45.67	1.34	0.0471	0.0017	0.0071	0.0001	0.0480	0.0017	0.4813	98.0
CA1930.11rim	43.88	1.8	0.0478	0.0016	0.0070	0.0001	0.0499	0.0017	0.4615	100.9
CA1930.17core	43.75	1.66	0.0440	0.0025	0.0068	0.0001	0.0469	0.0027	0.3402	99.7
CA1930.17rim	43.62	1.54	0.0443	0.0019	0.0068	0.0001	0.0473	0.0021	0.4037	100.3
CA1930.18rim	45.03	1.54	0.0453	0.0016	0.0070	0.0001	0.0469	0.0016	0.4904	98.6
CA1930.20core	44.39	1.8	0.0449	0.0026	0.0069	0.0001	0.0471	0.0027	0.3513	100.8
CA1930.20rim	44.83	1.66	0.0455	0.0023	0.0069	0.0001	0.0480	0.0024	0.3735	101.3
CA1930.30core	44.65	1.8	0.0445	0.0027	0.0070	0.0001	0.0465	0.0028	0.3347	98.2
CA1930.30rim	44.2	1.54	0.0440	0.0019	0.0069	0.0001	0.0465	0.0020	0.4107	98.4
CA1930.31core	44.14	1.8	0.0447	0.0026	0.0069	0.0001	0.0472	0.0028	0.3515	99.8
CA1930.31rim	44.7	2.2	0.0448	0.0032	0.0070	0.0002	0.0466	0.0035	0.3386	100.2
CA1930.32core	43.6	2.4	0.0447	0.0039	0.0068	0.0002	0.0478	0.0044	0.3006	100.9
CA1930.35core	45.6	2	0.0454	0.0031	0.0071	0.0002	0.0463	0.0032	0.3307	98.1
CA1930.35rim	45.16	1.8	0.0462	0.0025	0.0070	0.0001	0.0477	0.0026	0.3727	99.8
CA1930.36core	44.5	2.2	0.0461	0.0035	0.0069	0.0002	0.0483	0.0037	0.3257	100.4
CA1930.41core	44.2	1.92	0.0446	0.0028	0.0069	0.0002	0.0470	0.0030	0.3496	101.7
CA1930.52core	44.6	2.4	0.0448	0.0037	0.0069	0.0002	0.0468	0.0039	0.3175	100.5
CA1930.18core**	43.69	1.42	0.0438	0.0018	0.0068	0.0001	0.0467	0.0019	0.4025	97.5
CA1930.41rim**	44.58	1.92	0.0448	0.0027	0.0069	0.0002	0.0468	0.0028	0.3656	96.5
CA1930.43rim**	44.9	2.6	0.0446	0.0043	0.0070	0.0002	0.0462	0.0071	0.3113	97.2
CA1930.48core**	45.9	3.2	0.0473	0.0068	0.0072	0.0003	0.0480	0.0071	0.2426	97.3
CA1930.56rim**	44.6	2.4	0.0460	0.0041	0.0070	0.0002	0.0480	0.0043	0.3082	96.3

Table A.11h U-Pb age determinations by LA-ICP-MS
*= old dates; **= discordant dates

serie LA	Age [Ma]	± 2σ abs	$^{207}Pb/^{235}U$	± 1σ abs	$^{206}Pb/^{238}U$	± 1σ abs	$^{207}Pb/^{206}Pb$	± 1σ abs	rho	Conc.%
MDR CA19-3										
CA19-3_14rim	40.6	1.3	0.0409	0.0019	0.0063	0.0001	0.3356	0.0469	0.0022	100.2
CA19-3_14core	40.4	1.3	0.0409	0.0020	0.0063	0.0001	0.3184	0.0471	0.0024	100.7
CA19-3_15rim	39.6	1.2	0.0411	0.0014	0.0062	0.0001	0.4253	0.0483	0.0017	103.0
CA19-3_18core	39.8	1.2	0.0394	0.0014	0.0062	0.0001	0.4208	0.0461	0.0016	98.7
CA19-3_20rim	39.8	1.3	0.0412	0.0019	0.0062	0.0001	0.3536	0.0482	0.0022	102.8
CA19-3_20core	39.3	1.3	0.0406	0.0016	0.0061	0.0001	0.4150	0.0482	0.0019	102.8
CA19-3_31rim	38.4	1.5	0.0401	0.0025	0.0060	0.0001	0.3258	0.0486	0.0030	103.6
CA19-3_32rim	38.2	1.4	0.0396	0.0022	0.0060	0.0001	0.3330	0.0483	0.0027	103.4
CA19-3_45rima	39.1	1.5	0.0404	0.0024	0.0061	0.0001	0.3394	0.0482	0.0029	102.8
CA19-3_45rimc	39.5	2.7	0.0406	0.0049	0.0061	0.0002	0.2845	0.0480	0.0059	102.5
CA19-3_45rimd	39.7	1.7	0.0409	0.0026	0.0062	0.0001	0.3288	0.0480	0.0031	102.5
CA19-3_49rim	39.7	1.9	0.0401	0.0032	0.0062	0.0002	0.3052	0.0471	0.0038	100.5
CA19-3_52core	40.9	2.9	0.0406	0.0053	0.0064	0.0002	0.2772	0.0462	0.0062	98.8
CA19-3_54rim	40.7	1.8	0.0405	0.0030	0.0063	0.0001	0.3037	0.0464	0.0035	99.0
CA19-3_35core	40.5	2.2	0.0403	0.0038	0.0063	0.0002	0.2856	0.0464	0.0045	99.0
CA19-3_4core*	44.8	1.4	0.0456	0.0016	0.0070	0.0001	0.4496	0.0475	0.0017	101.1
CA19-3_54core**	discordant		0.1040	0.0145	0.0062	0.0003	0.2895	0.1219	0.0176	252.5
OTN CA19-8										
CA19-8-2core	35	1.5	0.0344	0.0044	0.0055	0.0001	0.0456	0.0058	0.1728	97.7
CA19-8-2rim	36.8	1.7	0.0338	0.0046	0.0057	0.0001	0.0429	0.0059	0.1672	91.8
CA19-8-3core	39	1.5	0.0412	0.0037	0.0061	0.0001	0.0491	0.0045	0.2187	104.9
CA19-8-3rim	34.5	1.8	0.0353	0.0052	0.0054	0.0001	0.0477	0.0071	0.1765	102.3
CA19-8-4core	36	2.2	0.0366	0.0061	0.0056	0.0002	0.0474	0.0080	0.1821	101.4
CA19-8-4rim	36.8	1.9	0.0373	0.0044	0.0057	0.0002	0.0472	0.0056	0.2212	100.8
CA19-8-5rim	37.5	1.7	0.0365	0.0048	0.0057	0.0001	0.0467	0.0061	0.1753	99.7
CA19-8-6core	34.5	2.3	0.0326	0.0045	0.0054	0.0002	0.0440	0.0062	0.2412	94.5
CA19-8-9core	39.3	3.1	0.0360	0.0083	0.0061	0.0002	0.0427	0.0100	0.1693	91.3
CA19-8-9rim	40.2	2.2	0.0447	0.0052	0.0063	0.0002	0.0519	0.0061	0.2329	110.4
CA19-8-10core	36.8	2.7	0.0394	0.0061	0.0057	0.0002	0.0500	0.0078	0.2369	106.8
CA19-8-10rim	37.3	2.8	0.0391	0.0074	0.0058	0.0002	0.0488	0.0093	0.2007	104.0
CA19-8-20core	37.6	3.6	0.0388	0.0100	0.0059	0.0003	0.0481	0.0125	0.1853	102.7
CA19-8-20rim	37	2.3	0.0421	0.0059	0.0058	0.0002	0.0530	0.0075	0.2227	113.0
CA19-8-18rim	37.1	2.1	0.0462	0.0060	0.0058	0.0002	0.0580	0.0076	0.2269	123.4
CA19-8-13core	36.1	3.6	0.0395	0.0083	0.0056	0.0003	0.0509	0.0108	0.2361	108.9
CA19-8-13rim	36.8	2.8	0.0370	0.0061	0.0057	0.0002	0.0469	0.0078	0.2349	100.0
CA19-8-14core	38.2	3.3	0.0402	0.0071	0.0059	0.0003	0.0491	0.0088	0.2468	104.7
CA19-8-14rim	37.1	2.5	0.0469	0.0059	0.0058	0.0002	0.0589	0.0075	0.2481	125.3
CA19-8-35rim	36.2	2.6	0.0400	0.0056	0.0056	0.0002	0.0516	0.0074	0.2530	109.9
CA19-8-18core*	736	36	1.2317	0.1040	0.1207	0.0031	0.0742	0.0063	0.3053	111.0
CA19-8-35core*	941	54	1.5788	0.1686	0.1570	0.0049	0.0731	0.0079	0.2893	102.3

Table 12a Trace element analysis of the Corno Alto and Sostino zircons (continue in the next table)

LA-ICP-MS

	sample	CA19-41	CA19-41	CA19-41	CA19-16	CA19-13	CA19-16	CA19-16	CA19-16	CA19-16	CA19-16	CA1910	CA19-41	CA19-41	CA19-41	CA19-41
		1core	7core	36rim	50core	32rim	52rim	6rim	17rim	50rim	1rim	12rim	7rim	17rim	26rim	6rim
	Rock	TMG	TMG	TMG	TMG	TMG	PTN	PTN	PTN	PTN	PTN	TMG	TMG	TMG	TMG	TMG
	domain	b-type	b-type	b-type	b-type	a-type	a-type	a-type	a-type	a-type	a-type	a-type	a-type	a-type	a-type	a-type
P	**(ppm)**	123	189	128	206	n.m.	194	245	247	374	148	n.m.	639	793	1090	203
Li	**(ppm)**	b.d.l.	0.590	b.d.l.	b.d.l.	n.m.	1.24	1.34	1.72	1.39	b.d.l.	*b.d.l.*	1.83	1.49	5.24	b.d.l.
Be	**(ppm)**	n.m.	n.m.	n.m.	n.m.	n.m.	n.m.	n.m.	n.m.	n.m.	n.m.	0.270	n.m.	n.m.	n.m.	n.m.
Cd	**(ppm)**	n.m.	n.m.	n.m.	n.m.	38.5	n.m.	n.m.	n.m.	n.m.	n.m.	20.1	n.m.	n.m.	n.m.	n.m.
Sc	**(ppm)**	212	173	200	224	588	380	371	357	402	342	546	668	995	789	422
Sr	**(ppm)**	0.154	0.505	0.208	0.298	0.152	0.333	0.363	0.806	0.553	0.214	0.48	0.644	0.823	1.016	0.404
Y	**(ppm)**	1188	3319	1483	2053	1890	1455	1522	1663	1943	919	3197	2827	4035	4469	1816
Nb	**(ppm)**	1.66	10.6	3.17	8.13	6.69	25.7	26.4	27.1	34.2	9.53	31.2	24.5	32.8	31.3	18.8
Ba	**(ppm)**	0.015	0.013	0.034	b.d.l.	b.d.l.	b.d.l.	0.015	1.69	0.02	0.027	b.d.l.	0.103	0.062	b.d.l.	0.064
La	**(ppm)**	0.07	0.07	0.02	0.02	0.013	0.008	0.007	0.080	0.004	0.004	0.000	0.019	0.008	0.229	0.013
Ce	**(ppm)**	22.6	119.4	45.8	68.1	13.9	22.4	21.7	24.5	18.6	24.3	10.6	22.8	28.3	15.9	47.1
Pr	**(ppm)**	0.599	0.824	0.221	0.323	0.081	0.026	0.014	0.071	0.021	0.042	0.033	0.042	0.046	0.133	0.065
Nd	**(ppm)**	8.70	12.6	5.38	6.11	1.44	0.634	0.518	0.920	0.306	1.03	0.680	1.06	1.11	1.53	1.43
Sm	**(ppm)**	13.8	19.4	10.4	12.7	2.62	2.87	2.14	2.79	1.57	2.77	3.07	3.16	4.76	4.40	3.80
Eu	**(ppm)**	6.01	9.11	5.55	6.18	1.29	0.97	0.865	1.08	0.843	0.98	1.30	1.40	1.96	1.87	1.49
Gd	**(ppm)**	45.0	91.2	51.4	62.1	20.1	19.7	16.7	21.8	18.6	13.6	29.5	31.6	46.7	39.7	25.9
Tb	**(ppm)**	10.9	26.3	14.3	16.7	7.39	8.31	7.54	8.28	9.11	5.05	13.2	13.6	21.4	21.3	9.44
Dy	**(ppm)**	123	338	170	202	127	126	120	138	150	73.1	245	235	363	369	144
Ho	**(ppm)**	35.9	121.9	46.3	68.0	54.1	47.4	50.2	55.7	64.6	27.8	95.4	94.7	145	151	58.2
Er	**(ppm)**	154	514	192	286	294	229	256	257	340	151	719	498	740	785	296
Tm	**(ppm)**	37.7	123.2	42.5	67.2	76.3	66.1	69.2	70.0	88.9	41.1	128	139	194	218	75.4
Yb	**(ppm)**	394	1209	393	717	834	707	789	730	997	458	1129	1371	1890	2205	841
Lu	**(ppm)**	63.4	197	57.0	112	174	115	125	123	162	80.4	221	209	318	345	149
Hf	**(ppm)**	5574	5538	5711	4332	10670	8588	8305	9107	10252	7033	7264	8594	8919	11437	7373
Ta	**(ppm)**	0.569	2.18	0.823	1.92	3.21	10.2	11.8	13.6	17.8	3.39	11.1	9.68	10.0	13.5	5.36
W	**(ppm)**	0.136	0.457	0.195	0.305	0.101	0.225	0.283	0.290	0.306	0.104	0.670	0.513	0.911	1.64	0.286
Pb	**(ppm)**	0.945	3.22	1.56	2.32	0.420	2.47	2.07	3.25	1.29	1.16	1.67	1.50	2.08	2.28	2.68
Th	**(ppm)**	235	807	405	537	164	594	441	705	342	269	210	362	466	563	582
U	**(ppm)**	153	504	236	670	757	2966	2909	4093	3363	1042	2491	2081	2438	4724	1331

Table 12b Trace element analysis of the Corno Alto and Sostino zircons

LA-ICP-MS

	sample	CA19-41	CA19-21	CA19-21	CA19-21	CA19-21	CA1930	CA1930	CA1930	CA1930	CA1930	CA1930
		44rim	41rim	49rim	56rim	49core	4rim	41core	41rim	31rim	31core	52core
	Rock	TMG	ETN	ETN	ETN	ETN	EBG	EBG	EBG	EBG	EBG	EBG
	domain	a-type	a-type	a-type	a-type	a-type	a-type	a-type	a-type	a-type	a-type	a-type
P	**(ppm)**	317	n.m.	n.m.	n.m.	n.m.	n.m.	n.m.	n.m.	n.m.	n.m.	n.m.
Li	**(ppm)**	0.79	*b.d.l.*	*b.d.l.*	*b.d.l.*	*b.d.l.*	*b.d.l.*	*b.d.l.*	*b.d.l.*	*b.d.l.*	*b.d.l.*	*b.d.l.*
Be	**(ppm)**	n.m.	*b.d.l.*	*b.d.l.*	*b.d.l.*	*b.d.l.*	*b.d.l.*	*b.d.l.*	*b.d.l.*	*b.d.l.*	*b.d.l.*	0.590
Cd	**(ppm)**	n.m.	18.4	20.4	19.0	21.9	34.3	41.2	45.5	38.7	40.5	33.2
Sc	**(ppm)**	429	474	437	338	291	214	185	210	199	213	192
Sr	**(ppm)**	0.509	0.804	0.651	0.313	0.300	0.055	b.d.l.	0.128	0.076	0.152	0.367
Y	**(ppm)**	2711	3666	2584	1762	1070	1033	860	1259	1155	708	1350
Nb	**(ppm)**	41.0	86.1	39.9	30.8	7.27	13.2	5.82	13.1	11.9	5.59	17.4
Ba	**(ppm)**	0.1	b.d.l.	0.320	b.d.l.	0.123	0.230	b.d.l.	b.d.l.	0.16	b.d.l.	2.18
La	**(ppm)**	0.034	0.004	0.013	0.018	0.023	0.000	0.016	0.000	0.000	0.000	0.221
Ce	**(ppm)**	51.7	115	45.4	46.4	20.9	12.0	14.3	25.5	16.7	12.4	26.6
Pr	**(ppm)**	0.055	0.131	0.049	0.045	0.064	0.020	0.010	0.052	0.019	0.000	0.128
Nd	**(ppm)**	1.43	2.54	0.9	0.900	0.800	0.330	0.380	0.650	0.310	0.230	1.04
Sm	**(ppm)**	5.36	9.80	2.99	3.12	1.95	1.40	1.80	2.02	1.72	0.79	2.18
Eu	**(ppm)**	1.83	3.25	1.34	1.19	0.868	0.830	0.850	1.27	0.870	0.460	1.51
Gd	**(ppm)**	41.8	67.5	27.7	24.1	16.0	8.89	10.1	14.2	10.7	7.03	18.8
Tb	**(ppm)**	16.7	27.0	12.6	10.3	5.66	3.61	3.80	5.47	4.35	2.93	7.07
Dy	**(ppm)**	237	385	197	164	82.3	67.1	55.9	83.8	66.0	48.5	100
Ho	**(ppm)**	97.8	143	87.0	66.6	35.5	28.9	23.8	34.4	30.0	22.3	40.7
Er	**(ppm)**	468	635	453	335	191	158	132	200	175	124	216
Tm	**(ppm)**	113	152	122	80.4	50.9	46.0	37.5	55.3	51.4	33.2	56.3
Yb	**(ppm)**	1138	1554	1285	880	556	573	455	617	611	414	622
Lu	**(ppm)**	194	218	179	118	89.4	108	92.9	120	125	87.0	119
Hf	**(ppm)**	9628	6721	7494	6681	6791	8505	7712	8075	7907	8467	7094
Ta	**(ppm)**	12.2	18.5	12.3	9.82	2.73	3.64	1.58	3.36	2.50	1.44	3.36
W	**(ppm)**	0.435	0.646	0.483	0.259	0.194	0.139	0.067	0.310	b.d.l.	0.200	0.187
Pb	**(ppm)**	8.62	14.9	3.69	4.43	1.27	0.900	1.26	2.15	1.93	1.26	3.38
Th	**(ppm)**	1971	3275	884	969	315	164	258	394	354	241	536
U	**(ppm)**	3786	5553	2978	2853	1030	2419	2421	3158	3338	2380	3740

Table 13a In situ Hf isotopes of the Corno alto zircons

Sample	Domain	Age (Ma)	2σ	$^{176}Lu/^{177}Hf$	2σ	$^{76}Hf/^{177}H$	2σ	εHf$_t$	2σ	$^{176}Hf/^{177}Hf_{(t)}$	2σ
TMG											
CA19-41											
CA19-41.1CORE	B-Type	44.2	1.9	0.00216	0.00001	0.28309	0.00004	11.5	1.4	0.28308	0.00004
CA19-41.3RIM	A-Type	43.8	1.2	0.00607	0.00010	0.28287	0.00004	3.9	1.4	0.28287	0.00004
CA19-41.5RIM	A-Type	43.1	1.2	0.00319	0.00004	0.28267	0.00004	-3.2	1.5	0.28267	0.00004
CA19-41.6RIM	A-Type	44.8	1.2	0.00357	0.00002	0.28298	0.00003	7.8	1.1	0.28298	0.00003
CA19-41.7CORE	B-Type	43.6	1.5	0.00662	0.00013	0.28316	0.00005	14.1	1.9	0.28316	0.00005
CA19-41.10RIM	A-Type	43.2	1.2	0.00281	0.00005	0.28275	0.00003	-0.5	1.1	0.28274	0.00003
CA19-41.21RIM	A-Type	43.3	1.4	0.00311	0.00011	0.28284	0.00004	2.8	1.4	0.28284	0.00004
CA19-41.40CORE	B-Type	42.5	2	0.00591	0.00050	0.28305	0.00004	10.3	1.6	0.28305	0.00004
CA19-41.44RIM	A-Type	42.6	2	0.00260	0.00002	0.28290	0.00003	5.1	1.1	0.28290	0.00003
CA19-41.17RIM	A-Type	41.8	1.2	0.00425	0.00021	0.28285	0.00003	3.2	1.0	0.28285	0.00003
CA19-41.19RIM	A-Type	42.3	1.5	0.00478	0.00010	0.28281	0.00004	1.6	1.4	0.28280	0.00004
CA19-41.26RIM	A-Type	41.2	1.4	0.00548	0.00007	0.28284	0.00004	2.6	1.3	0.28283	0.00004
CA19-41.31CORE	A-Type	42.6	2	0.00299	0.00006	0.28292	0.00004	5.7	1.6	0.28292	0.00004
CA19-41.36CORE**	B-Type	42.8	5	0.00230	0.00010	0.28306	0.00004	10.5	1.4	0.28306	0.00004
CA19-41.22CORE*	C-type	1068	30	0.00071	0.00002	0.28211	0.00003	-0.6	1.1	0.28209	0.00003
CA19-41.23CORE*	C-type	591	19	0.00070	0.00004	0.28225	0.00003	-5.9	1.0	0.28225	0.00003
CA19-41.42CORE*	C-type	151	8	0.00290	0.00004	0.28270	0.00004	0.2	1.4	0.28269	0.00004
CA19-13											
CA19-13.32RIM	A-Type	41.8	1.8	0.00256	0.00004	0.28290	0.00002	4.9	1.0	0.28290	0.00002
CA19-13.32CORE	A-Type	41.8	1.8	0.00149	0.00014	0.28297	0.00003	7.4	1.2	0.28297	0.00003
CA19-13.5CORE	A-Type	discordant		0.00168	0.00005	0.28294	0.00003	6.3	1.1	0.28294	0.00003
CA19-13.5RIM	A-Type	43.4	0.77	0.00191	0.00006	0.28295	0.00003	6.7	1.1	0.28295	0.00003
PTN											
CA19-16											
CA19-16_1RIM	A-Type	42.1	1.2	0.00175	0.00005	0.28293	0.00003	6.2	1.1	0.28293	0.00003
CA19-16_6RIM	A-Type	41.8	1.2	0.00230	0.00001	0.28298	0.00003	7.8	1.2	0.28298	0.00003
CA19-16_9RIM	A-Type	42.1	1.2	0.00313	0.00002	0.28298	0.00003	7.7	1.2	0.28298	0.00003
CA19-16.17RIM	A-Type	42.6	1.2	0.00229	0.00001	0.28297	0.00003	7.6	1.0	0.28297	0.00003
CA19-16.17RIM(2)	A-Type	42.2	1.2	0.00292	0.00005	0.28294	0.00003	6.4	1.1	0.28294	0.00003
CA19-16_15RIM	A-Type	42.4	1.2	0.00274	0.00003	0.28295	0.00005	6.8	1.8	0.28295	0.00005
CA19-16.34CORE	A-Type	42.5	1.4	0.00245	0.00002	0.28291	0.00003	5.2	1.2	0.28291	0.00003
CA19-16_37RIM	A-Type	41.9	1.2	0.00290	0.00003	0.28296	0.00003	7.0	1.1	0.28296	0.00003
CA19-16_39RIM	A-Type	42.1	1.2	0.00143	0.00004	0.28292	0.00003	5.7	1.1	0.28292	0.00003
CA19-16_44RIM	A-Type	43.0	1.2	0.00323	0.00002	0.28295	0.00004	6.5	1.5	0.28294	0.00004
CA19-16_44CORE	A-Type	41.6	1.3	0.00246	0.00008	0.28293	0.00003	6.0	1.1	0.28293	0.00003
CA19-16_48CORE	A-Type	41.6	1.2	0.00258	0.00007	0.28290	0.00002	4.9	1.0	0.28290	0.00002
CA19-16_50CORE	B-Type	42.3	1.4	0.00465	0.00002	0.28314	0.00005	13.3	1.7	0.28314	0.00005
CA19-16_51RIM	A-Type	42.5	1.3	0.00139	0.00011	0.28289	0.00003	4.6	1.1	0.28289	0.00003
CA19-16_52RIM	A-Type	42.5	1.2	0.00265	0.00007	0.28290	0.00003	4.9	1.0	0.28290	0.00003
CA19-16_56RIM	A-Type	42.4	1.2	0.00239	0.00004	0.28291	0.00004	5.4	1.4	0.28291	0.00004
CA19-16_53RIM	A-Type	41.5	1.3	0.00245	0.00003	0.28293	0.00003	5.9	1.0	0.28293	0.00003
CA19-16_49RIM	A-Type	41.1	1	0.00248	0.00002	0.28293	0.00003	6.0	1.0	0.28293	0.00003
CA19-16.27RIM	A-Type	41.5	1.2	0.00150	0.00004	0.28294	0.00002	6.3	0.9	0.28294	0.00002
CA19-16.30RIM	A-Type	40.5	1	0.00258	0.00001	0.28297	0.00003	7.3	1.2	0.28297	0.00003
CA19-16.35RIM	A-Type	40.4	1.2	0.00239	0.00001	0.28294	0.00003	6.4	1.0	0.28294	0.00003
CA19-16.26RIM	A-Type	42.9	1.4	0.00396	0.00011	0.28302	0.00005	9.0	1.7	0.28301	0.00005
CA19-16_50RIM	A-Type	42.3	1.4	0.00246	0.00014	0.28297	0.00003	7.5	1.0	0.28297	0.00003
CA19-16_6CORE	A-Type	44.3	1.4	0.00104	0.00003	0.28294	0.00003	6.3	1.1	0.28293	0.00003
CA19-16.21RIM	A-Type	43.9	1.2	0.00272	0.00008	0.28295	0.00003	6.8	1.1	0.28295	0.00003
CA19-16.31CORE*	C-Type	187	5	0.00051	0.00000	0.28261	0.00002	-2.1	0.7	0.28261	0.00002
CA19-16.31CORE(2)*	C-Type	187	5	0.00033	0.00001	0.28262	0.00002	-1.7	0.8	0.28262	0.00002
CA19-16_58CORE*	C-Type	521	12	0.00094	0.00001	0.28181	0.00003	-23.3	1.1	0.28180	0.00003

Table 13b In situ Hf isotopes of the Corno alto zircons

Sample	Domain	Age (Ma)	2σ	$^{176}Lu/^{177}Hf$	2σ	$^{76}Hf/^{177}H$	2σ	εHf$_t$	2σ	$^{176}Hf/^{177}Hf_{(t)}$	2σ
ETN											
CA19-21											
CA19-21.1CORE	A-Type	43.7	1.3	0.00160	0.00014	0.28288	0.00004	4.4	1.5	0.28288	0.00004
CA19-21.25CORE	A-Type	43.7	1.28	0.00266	0.00007	0.28290	0.00003	4.8	1.2	0.28289	0.00003
CA19-21.31RIM	A-Type	45.1	1.4	0.00269	0.00005	0.28292	0.00004	5.7	1.5	0.28292	0.00004
CA19-21.40CORE1	A-Type	46.0	1.78	0.00240	0.00018	0.28295	0.00004	6.9	1.4	0.28295	0.00004
CA19-21.40CORE2	A-Type	46.0	1.78	0.00336	0.00007	0.28293	0.00004	6.1	1.6	0.28293	0.00004
CA19-21.41CORE	A-Type	45.3	1.4	0.00274	0.00010	0.28295	0.00004	6.7	1.4	0.28295	0.00004
CA19-21.41RIM	A-Type	44.5	1.24	0.00409	0.00021	0.28294	0.00005	6.5	1.8	0.28294	0.00005
CA19-21.44CORE	A-Type	45.0	1.8	0.00173	0.00013	0.28294	0.00005	6.4	1.8	0.28294	0.00005
CA19-21.44RIM	A-Type	45.2	1.52	0.00435	0.00017	0.28291	0.00004	5.1	1.5	0.28290	0.00004
CA19-21.45CORE	A-Type	46.3	2.2	0.00256	0.00023	0.28293	0.00005	6.0	1.7	0.28293	0.00005
CA19-21.49CORE	A-Type	44.0	1.66	0.00256	0.00007	0.28289	0.00004	4.8	1.4	0.28289	0.00004
CA19-21.51CORE	A-Type	45.9	2.2	0.00229	0.00011	0.28296	0.00004	7.1	1.4	0.28296	0.00004
CA19-21.51RIM	A-Type	43.0	1.66	0.00385	0.00013	0.28287	0.00004	4.0	1.6	0.28287	0.00004
CA19-21.52RIM	A-Type	43.8	1.9	0.00313	0.00018	0.28283	0.00005	2.5	1.7	0.28283	0.00005
CA19-21.54RIM	A-Type	45.0	2	0.00305	0.00008	0.28289	0.00004	4.6	1.4	0.28289	0.00004
CA19-21.55RIM	A-Type	45.4	1.9	0.00249	0.00008	0.28293	0.00005	6.2	1.7	0.28293	0.00005
CA19-21.55CORE**	A-Type	42.6	2.2	0.00289	0.00022	0.28295	0.00004	6.8	1.5	0.28295	0.00004
CA19-21.54CORE**	A-Type	44.7	3.2	0.00217	0.00020	0.28289	0.00004	4.6	1.5	0.28289	0.00004
CA19-21.52CORE**	A-Type	45.6	3.2	0.00233	0.00024	0.28290	0.00004	5.0	1.6	0.28290	0.00004
CA19-21.42RIM**	A-Type	43.4	1.28	0.00307	0.00008	0.28294	0.00004	6.5	1.3	0.28294	0.00004
CA19-21.33CORE**	A-Type	42.9	1.54	0.00237	0.00020	0.28291	0.00004	5.3	1.6	0.28291	0.00004
CA19-21.25CORE**	A-Type	43.7	1.28	0.00266	0.00007	0.28290	0.00003	4.8	1.2	0.28289	0.00003
EBG											
CA19-26											
CA19-26.1RIM	A-Type	44.6	1.5	0.00239	0.00014	0.28295	0.00003	6.6	1.1	0.28294	0.00003
CA19-26.2RIM	A-Type	44.4	1.2	0.00212	0.00006	0.28293	0.00003	6.2	1.2	0.28293	0.00003
CA19-26.3RIM	A-Type	43.9	1.3	0.00160	0.00003	0.28284	0.00003	3.0	1.1	0.28284	0.00003
CA19-26.4RIM	A-Type	44.1	1.3	0.00237	0.00009	0.28302	0.00004	9.1	1.5	0.28301	0.00004
CA19-26.5CORE	A-Type	45.2	1.4	0.00195	0.00010	0.28299	0.00003	8.1	1.2	0.28299	0.00003
CA19-26.6RIM	A-Type	43.1	1.3	0.00181	0.00005	0.28291	0.00003	5.4	1.1	0.28291	0.00003
CA19-26.8RIM	A-Type	42.7	1.3	0.00147	0.00006	0.28294	0.00003	6.3	1.1	0.28294	0.00003
CA19-26.9RIM	A-Type	44.6	1.4	0.00218	0.00004	0.28289	0.00003	4.7	1.3	0.28289	0.00003
CA19-26.10RIM	A-Type	43.6	1.7	0.00187	0.00005	0.28294	0.00003	6.3	1.3	0.28294	0.00003
CA19-26.11RIM	A-Type	44.5	1.8	0.00223	0.00005	0.28296	0.00004	7.0	1.4	0.28296	0.00004
CA19-26.12RIM	A-Type	44.4	1.7	0.00184	0.00008	0.28276	0.00005	0.0	1.7	0.28276	0.00005
CA19-26.14CORE	A-Type	44.6	1.9	0.00161	0.00001	0.28300	0.00004	8.5	1.4	0.28300	0.00004
CA19-26.15RIM	A-Type	43.6	1.7	0.00205	0.00009	0.28290	0.00003	5.0	1.1	0.28290	0.00003
CA19-26.19RIM1	A-Type	44.1	1.7	0.00201	0.00005	0.28295	0.00005	6.9	1.7	0.28295	0.00005
CA19-26.19RIM2	A-Type	44.1	1.7	0.00175	0.00014	0.28293	0.00004	5.9	1.4	0.28292	0.00004
CA19-26.20RIM	A-Type	45.2	2.3	0.00202	0.00003	0.28292	0.00003	5.6	1.3	0.28292	0.00003
CA19-26.45RIM	A-Type	43.1	1.7	0.00215	0.00002	0.28289	0.00004	4.8	1.4	0.28289	0.00004
CA19-26.47RIM	A-Type	43.3	2.4	0.00117	0.00004	0.28269	0.00003	-2.5	1.3	0.28269	0.00003
CA19-26.50RIM	A-Type	44.5	2.6	0.00203	0.00003	0.28291	0.00004	5.2	1.4	0.28290	0.00004
CA19-26.51RIM	A-Type	43.2	2	0.00120	0.00002	0.28289	0.00003	4.8	1.3	0.28289	0.00003
CA19-26.14CORE	A-Type	44.6	1.9	0.00161	0.00001	0.28300	0.00004	8.5	1.4	0.28300	0.00004
CA19-26.50RIM	A-Type	44.5	2.6	0.00203	0.00003	0.28291	0.00004	5.2	1.4	0.28290	0.00004
CA19-26.12CORE*	C-Type	556	18	0.00056	0.00001	0.28216	0.00003	-9.9	1.1	0.28216	0.00003
CA19-26.21CORE*	C-Type	2174	64	0.00138	0.00006	0.28147	0.00003	-5.1	1.3	0.28142	0.00003
CA19-26.47CORE*	C-Type	568	23	0.00108	0.00001	0.28231	0.00004	-4.6	1.3	0.28230	0.00004
CA19-26.51CORE*	C-Type	333	18	0.00108	0.00004	0.28223	0.00004	-12.6	1.5	0.28222	0.00004
CA19-26.55CORE*	C-Type	927	40	0.00049	0.00001	0.28179	0.00003	-14.7	1.3	0.28178	0.00003
CA19-26.15CORE**	A-Type	43.6	1.7	0.00173	0.00005	0.28289	0.00004	4.7	1.4	0.28289	0.00004

Table 13c In situ Hf isotopes of the Corno alto zircons

Sample	Domain	Age (Ma)	2σ	$^{176}Lu/^{177}Hf$	2σ	$^{76}Hf/^{177}H$	2σ	εHf_t	2σ	$^{176}Hf/^{177}Hf_{(t)}$	2σ
EBG											
CA19-30											
CA19-30-3CORE	A-Type	44.6	1.8	0.00141	0.00005	0.28291	0.00002	5.3	0.8	0.28291	0.00002
CA19-30-3rim	A-Type	45.7	1.66	0.00212	0.00002	0.28292	0.00003	5.9	1.1	0.28292	0.00003
CA19-30-4core	A-Type	43.9	1.42	0.00212	0.00002	0.28292	0.00003	5.9	1.1	0.28292	0.00003
CA19-30-4rim	A-Type	43.3	1.42	0.00217	0.00003	0.28291	0.00003	5.5	1.2	0.28291	0.00003
CA19-30-6core	A-Type	43.1	1.42	0.00158	0.00007	0.28298	0.00003	7.8	1.0	0.28298	0.00003
CA19-30-6rim	A-Type	45.7	1.34	0.00171	0.00011	0.28291	0.00002	5.5	0.8	0.28291	0.00002
CA19-30-11rim	A-Type	43.9	1.8	0.00261	0.00004	0.28297	0.00003	7.6	1.3	0.28297	0.00003
CA19-30-17core	A-Type	43.8	1.66	0.00257	0.00019	0.28290	0.00003	4.9	1.1	0.28290	0.00003
CA19-30-17rim	A-Type	43.6	1.54	0.00156	0.00001	0.28290	0.00002	4.9	0.9	0.28290	0.00002
CA19-30-18rim	A-Type	45.0	1.54	0.00251	0.00004	0.28291	0.00003	5.3	1.1	0.28291	0.00003
CA19-30-20core	A-Type	44.4	1.8	0.00129	0.00006	0.28293	0.00003	5.9	1.0	0.28292	0.00003
CA19-30-20rim	A-Type	44.8	1.66	0.00167	0.00009	0.28292	0.00002	5.8	0.9	0.28292	0.00002
CA19-30-30core	A-Type	44.7	1.8	0.00185	0.00006	0.28291	0.00002	5.3	0.8	0.28291	0.00002
CA19-30-30rim	A-Type	44.2	1.54	0.00206	0.00009	0.28293	0.00003	6.2	1.1	0.28293	0.00003
CA19-30-31core	A-Type	44.1	1.8	0.00158	0.00005	0.28291	0.00003	5.3	1.0	0.28291	0.00003
CA19-30-31rim	A-Type	44.7	2.2	0.00169	0.00009	0.28289	0.00002	4.8	0.8	0.28289	0.00002
CA19-30-32core	A-Type	43.6	2.4	0.00149	0.00005	0.28293	0.00002	6.1	0.8	0.28293	0.00002
CA19-30-35core	A-Type	45.6	2	0.00185	0.00004	0.28293	0.00002	6.2	1.0	0.28293	0.00002
CA19-30-35rim	A-Type	45.2	1.8	0.00227	0.00003	0.28290	0.00002	5.0	0.9	0.28290	0.00002
CA19-30-52rim	A-Type	44.6	2.4	0.00187	0.00006	0.28293	0.00003	6.1	1.1	0.28293	0.00003
CA19-30-48core**	A-Type	45.9	3.2	0.00158	0.00008	0.28283	0.00003	2.4	1.0	0.28282	0.00003
CA19-30-43core**	A-Type	44.9	2.6	0.00217	0.00008	0.28296	0.00003	7.2	1.3	0.28296	0.00003
CA19-30-18core**	A-Type	43.7	1.42	0.00183	0.00006	0.28292	0.00002	5.7	0.9	0.28292	0.00002
MDR											
CA19-3											
CA19-3.4CORE	b-type	44.8	1.4	0.00145	0.00004	0.28310	0.00004	12.0	1.5	0.28310	0.00004
CA19-3.14CORE		40.4	1.3	0.00042	0.00002	0.28293	0.00005	5.9	1.9	0.28293	0.00005
CA19-3.14RIM		40.4	1.3	0.00150	0.00010	0.28296	0.00006	7.0	2.0	0.28296	0.00006
CA19-3.18RIM		39.8	1.2	0.00117	0.00005	0.28294	0.00003	6.3	1.1	0.28294	0.00003
CA19-3.20CORE		39.3	1.3	0.00087	0.00016	0.28274	0.00016	-0.7	5.8	0.28274	0.00016
CA19-3.31		38.4	1.5	0.00068	0.00003	0.28291	0.00006	5.5	2.0	0.28291	0.00006
CA19-3.32CORE		38.2	1.4	0.00094	0.00004	0.28289	0.00005	4.7	1.8	0.28289	0.00005
CA19-3.45CORE1		39.1	1.5	0.00061	0.00003	0.28294	0.00004	6.5	1.4	0.28294	0.00004
CA19-3.45CORE2		39.7	1.7	0.00129	0.00017	0.28294	0.00003	6.4	1.2	0.28294	0.00003
CA19-3.32RIM		38.2	1.4	0.00092	0.00004	0.28293	0.00004	5.9	1.4	0.28293	0.00004
CA19-3.44		discordant		0.00090	0.00004	0.28295	0.00005	6.6	1.9	0.28295	0.00005
CA19-3.54CORE		discordant		0.00253	0.00004	0.28298	0.00005	7.6	1.7	0.28297	0.00005
CA19-3.54RIM		40.7	1.8	0.00115	0.00004	0.28294	0.00004	6.2	1.4	0.28294	0.00004
OTN											
CA19-8											
CA19-8_2	A-Type	35	1.5	0.00133	0.00010	0.28264	0.00003	-4.4	1.0	0.28264	0.00003
CA19-8_2core	A-Type	36.8	1.7	0.00123	0.00010	0.28264	0.00002	-4.4	0.9	0.28264	0.00002
CA19-8_3core	A-Type	39	1.5	0.00116	0.00005	0.28261	0.00003	-5.5	1.0	0.28261	0.00003
CA19-8_3core	A-Type	39	1.5	0.00132	0.00005	0.28264	0.00003	-4.2	1.1	0.28264	0.00003
CA19-8_3rim	A-Type	34.5	1.8	0.00132	0.00004	0.28267	0.00002	-3.2	0.8	0.28267	0.00002
CA19-8_5rim	A-Type	37.5	1.7	0.00072	0.00001	0.28265	0.00002	-4.1	0.8	0.28265	0.00002
CA19-8_5core	A-Type	37.5	1.7	0.00249	0.00047	0.28265	0.00003	-4.1	1.3	0.28265	0.00003
CA19-8_6rim	A-Type	34.5	2.3	0.00104	0.00003	0.28262	0.00002	-5.0	0.9	0.28262	0.00002
CA19-8_9rim	A-Type	40.2	2.2	0.00103	0.00002	0.28263	0.00002	-4.6	0.8	0.28263	0.00002
CA19-8_9core	A-Type	39.3	3.1	0.00088	0.00005	0.28267	0.00003	-3.4	1.1	0.28267	0.00003
CA19-8_10core	A-Type	36.8	2.7	0.00088	0.00005	0.28267	0.00003	-3.4	1.1	0.28266	0.00003
CA19-8_10rim	A-Type	37.3	2.8	0.00101	0.00002	0.28265	0.00002	-3.8	0.9	0.28265	0.00002
CA19-8_13rim	A-Type	36.8	2.8	0.00096	0.00004	0.28261	0.00003	-5.3	1.0	0.28261	0.00003
CA19-8_18rim	A-Type	37.1	2.1	0.00089	0.00001	0.28249	0.00003	-9.6	1.1	0.28249	0.00003
CA19-8_18rim2	A-Type	37.1	2.1	0.00078	0.00002	0.28263	0.00002	-4.7	0.9	0.28263	0.00002
CA19-8_20rim1	A-Type	37	2.3	0.00157	0.00008	0.28266	0.00002	-3.6	0.9	0.28266	0.00002
CA19-8_20rim2	A-Type	37	2.3	0.00106	0.00002	0.28267	0.00002	-3.3	1.0	0.28267	0.00002
CA19-8_28rim	A-Type	discordant		0.00155	0.00010	0.28259	0.00002	-6.1	0.9	0.28259	0.00002

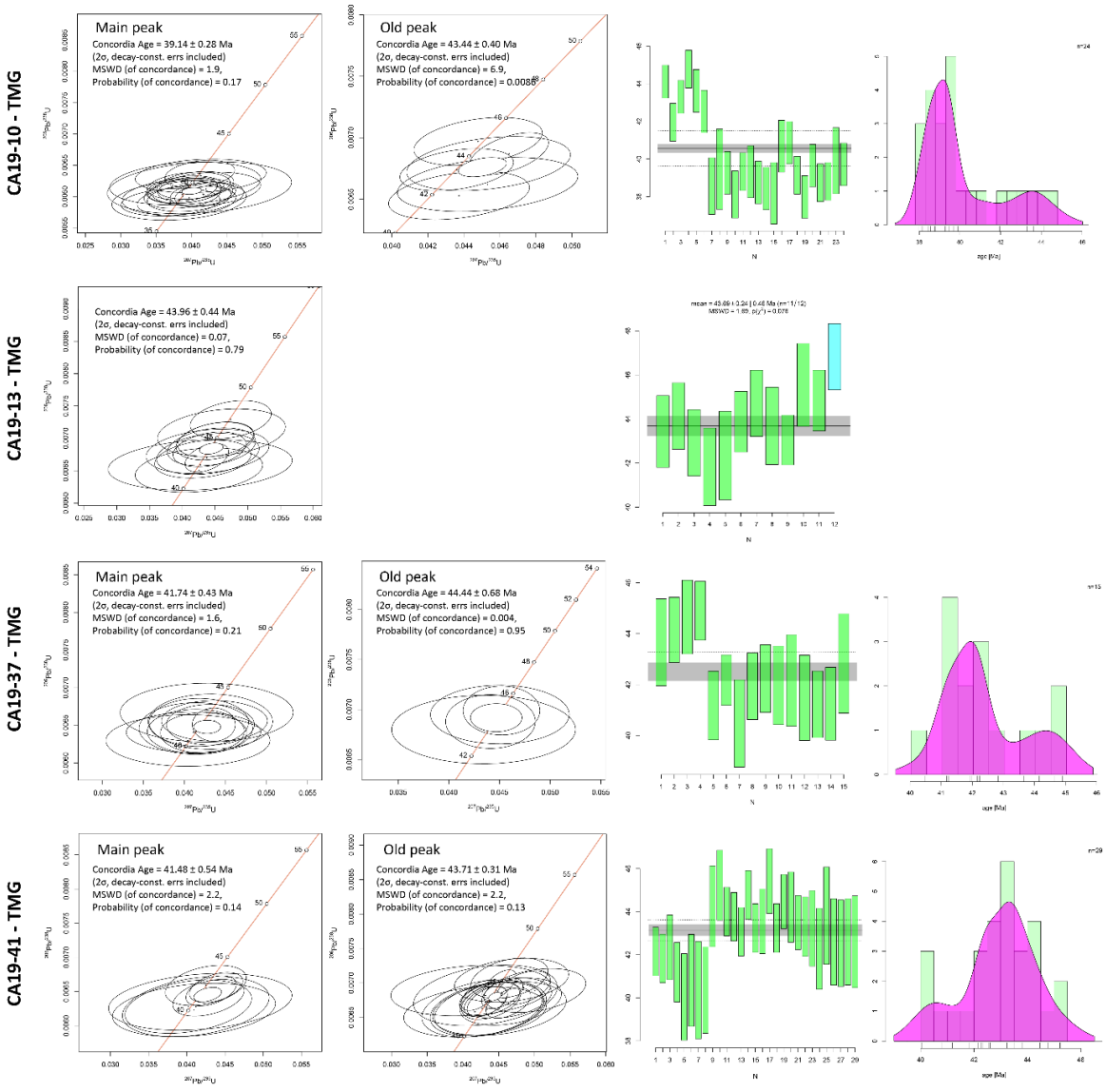

Figure A.1 Zircon U-Pb dating results of samples from TMG rocks.

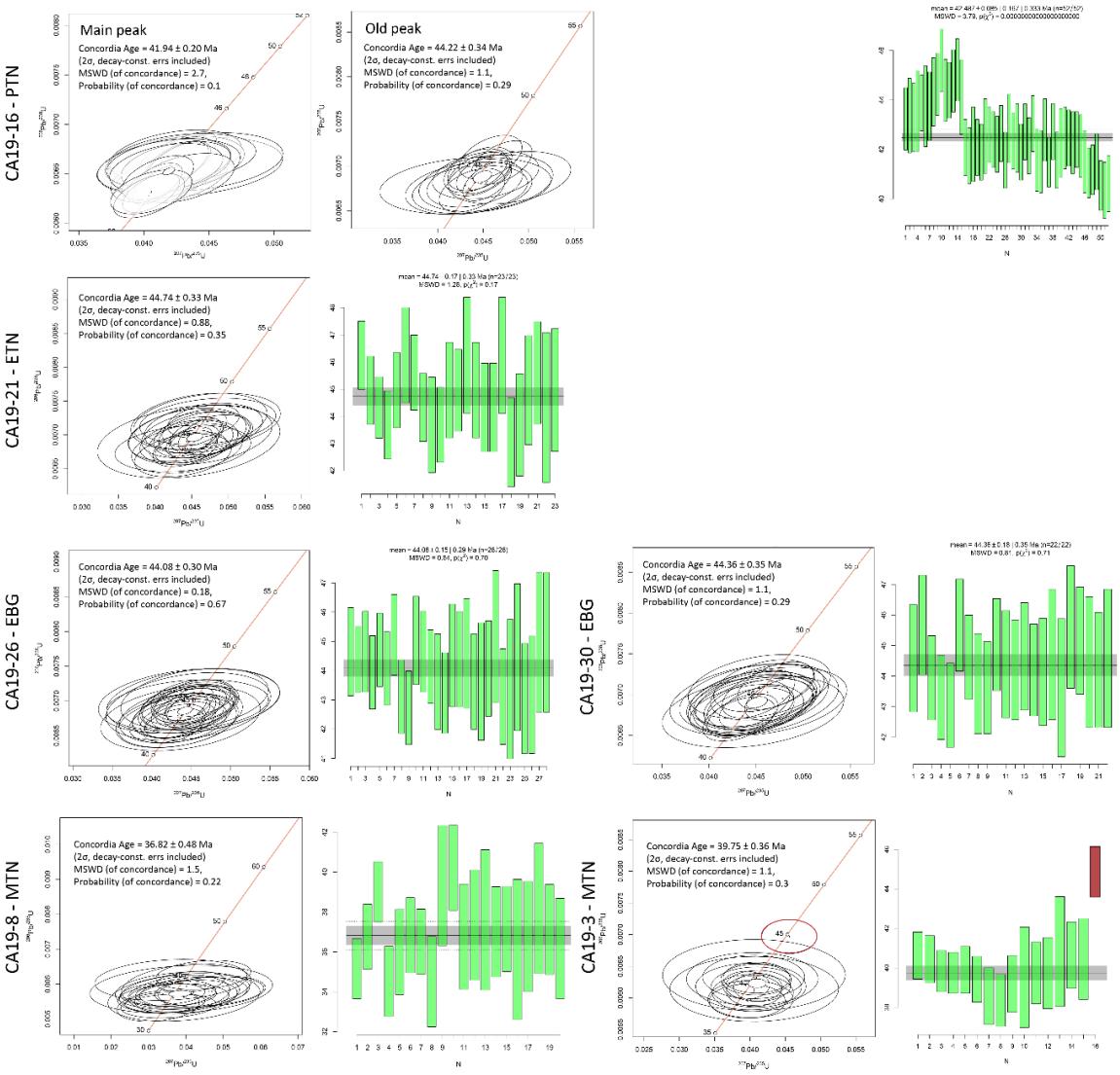

Figure A.2 Zircon U-Pb dating results of samples from PTN, ETN, OTN, and MDR rocks.


Sample CA19-10 (error 2s)
CA19-10.2
*38.6 ± 1.5 Ma
**39.5 ± 2.2 Ma
CA19-10.4
*(980 ± 20 Ma)
**44.8 ± 1 Ma
CA19-10.5
*discordant
**39.3 ± 1.2 Ma
CA19-10.6
*38.1 ± 1.3 Ma
**39.3 ± 1.0 Ma
CA19-10.7
*(449 ± 8.5 Ma)
**(454 ± 9 Ma)
CA19-10.11
*39.3 ± 1.4 Ma
CA19-10.12
*(661 ± 13 Ma)
**44.1 ± 0.9 Ma
CA19-10.16
*(514 ± 9 Ma)
**(43.6 ± 1.2 Ma)
CA19-10.17
*discordant
CA19-10.20
*38.8 ± 1.2 Ma
**38.4 ± 1.2 Ma
CA19-10.21
*discordant
**43.3 ± 0.9 Ma
CA19-10.22
*38.2 ± 1.7 Ma
**(39.4 ± 1.3 Ma)
CA19-10.24
*(879 ± 30 Ma)
**(45.1 ± 1.2 Ma)
CA19-10.25
*40.7 ± 1.4 Ma
**40.9 ± 1.2 Ma
CA19-10.31
*discordant
**(38.7 ± 1.3 Ma)
CA19-10.33
*(39.9 ± 1.7 Ma)
**39.1 ± 1 Ma
CA19-10.35
*38 ± 1.2 Ma
**39.7 ± 1.2 Ma
CA19-10.38
*38.7 ± 1 Ma
**38.8 ± 1 Ma
CA19-10.45
*39.9 ± 1.8 Ma
**39.7 ± 1.2 Ma
CA19-10.46
*discordant
**42.5 ± 1.2 Ma
U-Pb age (Ma)
trace el. spot
50 µm

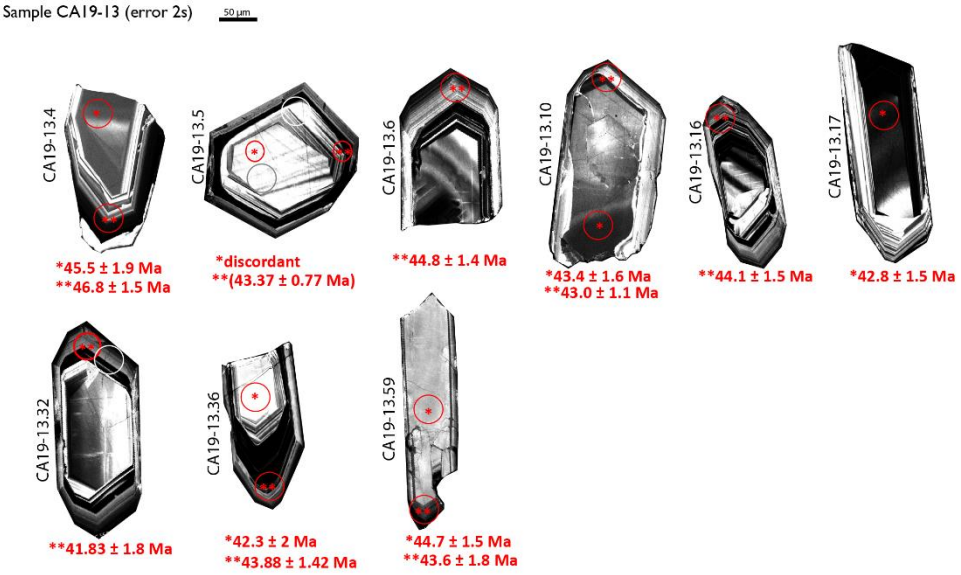
Sample CA19-13 (error 2s)
50 µm
CA19-13.4
*45.5 ± 1.9 Ma
**46.8 ± 1.5 Ma
CA19-13.5
*discordant
**(43.37 ± 0.77 Ma)
CA19-13.6
**44.8 ± 1.4 Ma
CA19-13.10
*43.4 ± 1.6 Ma
**43.0 ± 1.1 Ma
CA19-13.16
**44.1 ± 1.5 Ma
CA19-13.17
*42.8 ± 1.5 Ma
CA19-13.32
**41.83 ± 1.8 Ma
CA19-13.36
*42.3 ± 2 Ma
**43.88 ± 1.42 Ma
CA19-13.59
*44.7 ± 1.5 Ma
**43.6 ± 1.8 Ma


Sample CA19-41 (error 2s)
50 μm
CA19-41.1
*44.2 ± 1.9 Ma
**45.2 ± 1.7 Ma
*εHft +11.5± 1.4
CA19-41.2
*44 ± 1.2 Ma
CA19-41.3
**43.8 ± 1.2 Ma
**εHft +3.9± 1.4
CA19-41.5
**43.1 ± 1.2 Ma
**εHft -3.2 ± 1.5
CA19-41.6
**44.8 ± 1.2 Ma
**εHft +7.8± 1.1
CA19-41.7
**43.2 ± 1.2 Ma
*43.6 ± 1.5 Ma
*εHft +14.4± 1.9
CA19-41.9
*(783 ± 19 Ma)
**45.4 ± 1.5 Ma
CA19-41.10
*44.5 ± 1.3 Ma
**43.2 ± 1.2 Ma
**εHft -0.5± 1.1
CA19-41.13
*discordant
**42.1 ± 1.2 Ma
CA19-41.14
*(586 ± 17 Ma)
CA19-41.15
*(656 ± 20 Ma)
CA19-41.17
**41.8 ± 1.2 Ma
**εHft +3.2 ± 1.0
CA19-41.18
*44.2 ± 1.7 Ma
**(47.3 ± 3.2 Ma)
CA19-41.19
**εHft +1.6 ± 1.9
*(47.3 ± 3.2 Ma)
**42.3 ± 1.5 Ma
CA19-41.21
**εHft +2.8 ± 1.4
*discordant
**43.3 ± 1.4 Ma
CA19-41.22
**εHft -0.6 ± 1.1
*(1068 ± 30 Ma)
**43.2 ± 1.8 Ma
CA19-41.23
*(591 ± 19 Ma)
**εHft -5.9 ± 1.0
CA19-41.26
(41 ± 1.5 Ma)
**εHft +2.6 ± 1.3
CA19-41.29
*(1019 ± 35 Ma)
**(516 ± 18 Ma)
CA19-41.30
**40.8 ± 2.2 Ma
CA19-41.31
*εHft +5.7 ± 1.6
*42.6 ± 2 Ma
**40.4 ± 2.1 Ma
CA19-41.32
*(452 ± 31 Ma)
**(39.3 ± 1.8 Ma)
CA19-41.36
*(42.8 ± 5 Ma)
*(41.8 ± 2.8 Ma)
*(εHft +10.5 ± 1.4)
CA19-41.27
*(558 ± 21 Ma)
**(226.6 ± 8 Ma)
CA19-41.28
*40 ± 2.1 Ma
**42.3 ± 1.9 Ma
CA19-41.39
**discordant
CA19-41.40
*εHft +10.3 ± 1.6
CA19-41.41
*40.4 ± 2.3 Ma
CA19-41.42
*εHft +0.2 ± 1.4
*151.1 ± 7.7 Ma
**(40.3 ± 1.9 Ma)
CA19-41.44
**εHft +5.1 ± 1.1
**42.6 ± 2 Ma
CA19-41.45
*(463 ± 22 Ma)
**42.6 ± 2.2 Ma
U-Pb age (Ma)
trace el. spot
Hf isotopes

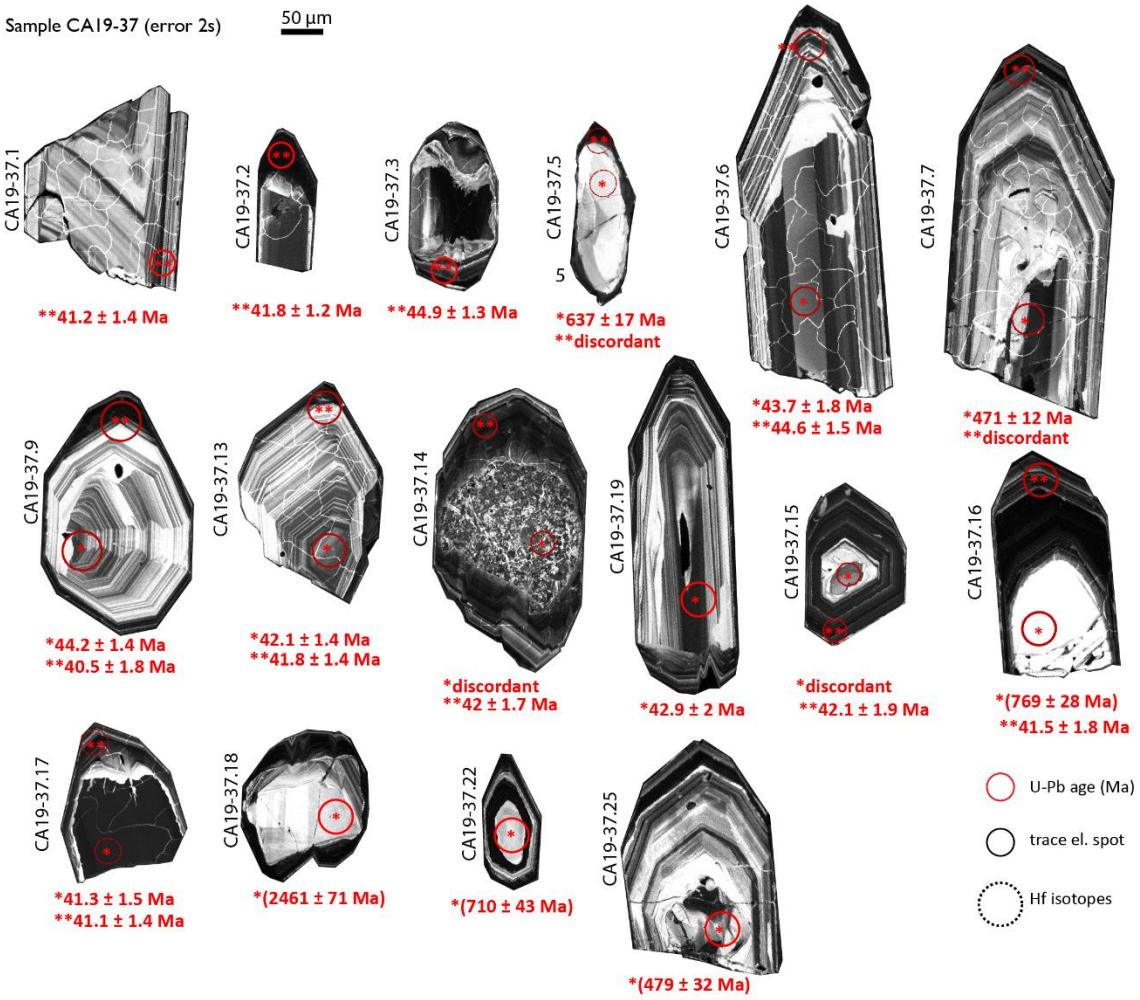
Sample CA19-37 (error 2s)
50 µm
CA19-37.1
**41.2 ± 1.4 Ma
CA19-37.2
**41.8 ± 1.2 Ma
CA19-37.3
**44.9 ± 1.3 Ma
CA19-37.5
5
*637 ± 17 Ma
**discordant
CA19-37.6
*43.7 ± 1.8 Ma
**44.6 ± 1.5 Ma
CA19-37.7
*471 ± 12 Ma
**discordant
CA19-37.9
*44.2 ± 1.4 Ma
**40.5 ± 1.8 Ma
CA19-37.13
*42.1 ± 1.4 Ma
**41.8 ± 1.4 Ma
CA19-37.14
*discordant
**42 ± 1.7 Ma
CA19-37.19
*42.9 ± 2 Ma
CA19-37.15
*discordant
**42.1 ± 1.9 Ma
CA19-37.16
*(769 ± 28 Ma)
**41.5 ± 1.8 Ma
CA19-37.17
*41.3 ± 1.5 Ma
**41.1 ± 1.4 Ma
CA19-37.18
*(2461 ± 71 Ma)
CA19-37.22
*(710 ± 43 Ma)
CA19-37.25
*(479 ± 32 Ma)
U-Pb age (Ma)
trace el. spot
Hf isotopes


Sample CA19-16 (error 2s)
50 µm
CA19-16_1
**42.1 ± 1.2 Ma
**εHf$_t$ +6.2 ± 1.1
CA19-16_3
*44.1 ± 1.5 Ma
CA19-16_15
*42.4 ± 1.2 Ma
**(40 ± 1.2 Ma)
**εHf$_t$ +6.8 ± 1.8
CA19-16_6
44.3 ± 1.4 Ma
*44.3 ± 1.4 Ma
**41.8 ± 1.2 Ma
*εHf$_t$ +6.3 ± 1.1
**εHf$_t$ +7.8 ± 1.2
CA19-16_8
*42.2 ± 1.5 Ma
CA19-16_9
*41.9 ± 1.2 Ma
**42.1 ± 1.2 Ma
**εHf$_t$ +7.7 ± 1.2
CA19-16_13
*43.4 ± 1.5 Ma
**42.5 ± 1.5 Ma
CA19-16_14
*(42.5 ± 1.4 Ma)
**42.6 ± 1.2 Ma
CA19-16_17
*42.6 ± 1.2 Ma
**41.2 ± 1.2 Ma
*εHf$_t$ +7.6 ± 1.0
CA19-16_25
*discordant
**44.6 ± 1.3 Ma
CA19-16_26
*42.9 ± 1.4 Ma
**εHf$_t$ +9.0 ± 1.7
CA19-16_27
*43.3 ± 1.4 Ma
**41.5 ± 1.2 Ma
**εHf$_t$ +6.3 ± 0.9
CA19-16_29
*(574 ± 17 Ma)
**42.3 ± 1.2 Ma
CA19-16_30
*44.4 ± 1.3 Ma
**40.5 ± 1 Ma
**εHf$_t$ +7.3 ± 1.2
CA19-16_24
*(568 ± 14 Ma)
CA19-16_21
*(42 ± 1.5 Ma)
**43.9 ± 1.2 Ma
**εHf$_t$ +6.8 ± 1.1
CA19-16_23
*43.4 ± 1.5 Ma
**42.6 ± 1.2 Ma
CA19-16_31
(186.6 ± 4.7 Ma)
*εHf$_t$ -2.1 ± 0.7
**εHf$_t$ -1.7 ± 0.8
CA19-16_34
*42.5 ± 1.4 Ma
**41.2 ± 1 Ma
*εHf$_t$ +5.2 ± 1.2
CA19-16_35
*45.2 ± 1.3 Ma
**40.4 ± 1.2 Ma
**εHf$_t$ +6.4 ± 1.0
CA19-16_37
**41.9 ± 1.2 Ma
*42.7 ± 1.2 Ma
**εHf$_t$ +7.0 ± 1.1
CA19-16_39
*43.8 ± 1.7 Ma
**42.1 ± 1.2 Ma
**εHf$_t$ +5.7 ± 1.1
CA19-16_40
*43.2 ± 1.3 Ma
**(41 ± 1.2 Ma)
CA19-16_44
*41.6 ± 1.3 Ma
**43 ± 1.2 Ma
*εHf$_t$ +6.0 ± 1.1
**εHf$_t$ +6.5 ± 1.5
CA19-16_46
*43.8 ± 1.4 Ma
**(41.7 ± 1.2 Ma)
CA19-16_47
*42.7 ± 1.2 Ma
**41.4 ± 1 Ma
CA19-16_48
*41.6 ± 1.2 Ma
*εHf$_t$ +4.9 ± 1.0
CA19-16_49
*44.4 ± 1.2 Ma
**41.1 ± 1 Ma
**εHf$_t$ +6.0 ± 1.0
CA19-16_50
*42.3 ± 1.4 Ma
*εHf$_t$ +13.3 ± 1.7
**εHf$_t$ +7.5 ± 1.0
CA19-16_51
*867 ± 19 Ma
**42.5 ± 1.3 Ma
**εHf$_t$ +4.6 ± 1.1
CA19-16_52
*43.6 ± 1.7 Ma
**42.5 ± 1.2 Ma
**εHf$_t$ +4.9 ± 1.1
CA19-16_53
*44.8 ± 1.3 Ma
**41.5 ± 1.3 Ma
**εHf$_t$ +5.9 ± 1.0
CA19-16_55
*42.3 ± 1.3 Ma
**40.6 ± 1.2 Ma
CA19-16_58
*(521 ± 12 Ma)
**(40.5 ± 1.4 Ma)
CA19-16_56
**42.4 ± 1.2 Ma
CA19-16_57
*42.1 ± 1.3 Ma
59
CA19-16_59
*42.8 ± 1.3 Ma
**41.4 ± 1.3 Ma
U-Pb age (Ma)
trace el. spot
Hf isotopes


Sample CA19-21 (error 2s)
CA19-21.1
eHf: +4.4
*(43.7 ± 1.3 Ma)
**46.1 ± 1.3 Ma
*εHf$_t$ +4.4 ± 1.5
CA19-21.6
*(45.5 ± 1.92 Ma)
CA19-21.25
*(43.7 ± 1.3 Ma)
**45.2 ± 1.2 Ma
*εHf$_t$ +4.8 ± 1.2
CA19-21.26
*433 ± 11.2 Ma
**44.4 ± 1.12 Ma
CA19-21.31
*43.4 ± 1.2 Ma
**45.1 ± 1.4 Ma
*εHf$_t$ +5.7 ± 1.5
CA19-21.33
*(42.9 ± 1.54 Ma)
**(44.7 ± 1.38 Ma)
*εHf$_t$ +5.3 ± 1.6
CA19-21.40
*46 ± 1.78 Ma
**(44.4 ± 1.26 Ma)
*εHf$_t$ +6.9 ± 1.4
**εHf$_t$ +6.1 ± 1.6
CA19-21.41
*45.3 ± 1.4 Ma
**44.5 ± 1.24 Ma
*εHf$_t$ +6.7 ± 1.4
**εHf$_t$ +6.5 ± 1.8
CA19-21.42
*(43.3 ± 1.54 Ma)
**(43.4 ± 1.28 Ma)
**(εHf$_t$ +6.5 ± 1.3)
CA19-21.43
*43.4 ± 1.78 Ma
**43.6 ± 1.38 Ma
CA19-21.44
*45 ± 1.8 Ma
**45.2 ± 1.52 Ma
*εHf$_t$ +6.4 ± 1.8
**εHf$_t$ +5.1 ± 1.5
CA19-21.45
*46.3 ± 2.2 Ma
**45.3 ± 1.78 Ma
*εHf$_t$ +6.0 ± 1.7
CA19-21.49
*44 ± 1.66 Ma
**44.2 ± 1.66 Ma
*εHf$_t$ +4.8 ± 1.4
CA19-21.51
*^{1}45.9 ± 2.2 Ma
**^{1}43 ± 1.6 Ma
*^{2}(45 ± 1.8 Ma)
**^{2}43.8 ± 1.9 Ma
*εHf$_t$ +7.1 ± 1.4
**εHf$_t$ +4.0 ± 1.6
CA19-21.52
εHf: +2.5
εHf: +5.0
*(45.6 ± 3.2 Ma)
**43.8 ± 1.9 Ma
*(εHf$_t$ +5.0 ± 1.6)
**εHf$_t$ +2.5 ± 1.7
CA19-21.54
*(44.7 ± 3.2 Ma)
**45.0 ± 2.0 Ma
*(εHf$_t$ +4.6 ± 1.5)
**εHf$_t$ +4.6 ± 1.4
CA19-21.55
55
εHf: +6.2
*(42.6 ± 2.2 Ma)
**45.4 ± 1.9 Ma
*(εHf$_t$ +6.8 ± 1.5)
**εHf$_t$ +6.2 ± 1.7
CA19-21.56
*44.4 ± 2.8 Ma
**44.9 ± 2.4 Ma
CA19-21_58
**(43 ± 1.2 Ma)
U-Pb age (Ma)
trace el. spot
Hf isotopes

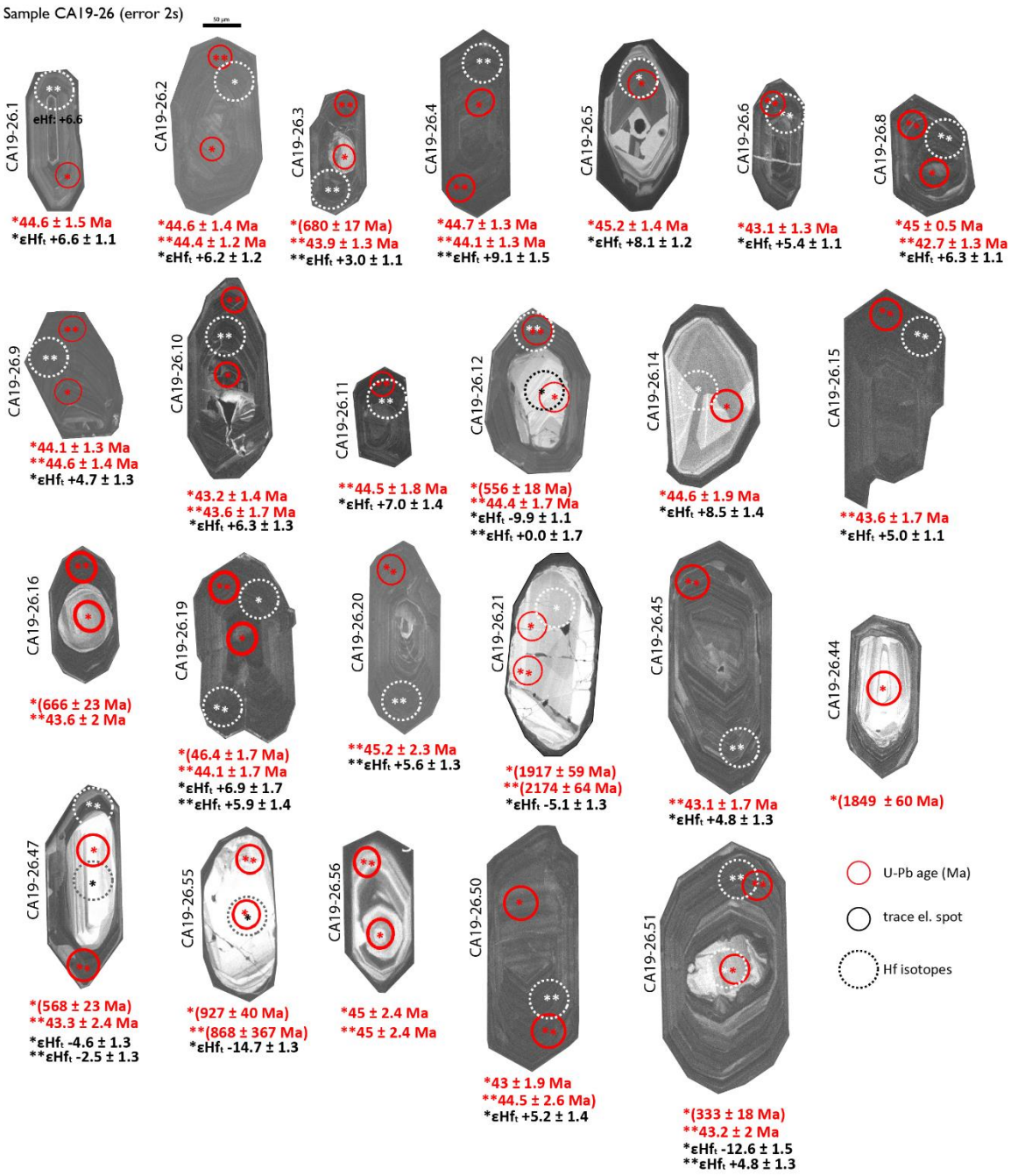
Sample CA19-26 (error 2s)
50 µm
CA19-26.1
eHf: +6.6
*44.6 ± 1.5 Ma
*εHf$_t$ +6.6 ± 1.1
CA19-26.2
*44.6 ± 1.4 Ma
**44.4 ± 1.2 Ma
*εHf$_t$ +6.2 ± 1.2
CA19-26.3
*(680 ± 17 Ma)
**43.9 ± 1.3 Ma
**εHf$_t$ +3.0 ± 1.1
CA19-26.4
*44.7 ± 1.3 Ma
**44.1 ± 1.3 Ma
**εHf$_t$ +9.1 ± 1.5
CA19-26.5
*45.2 ± 1.4 Ma
*εHf$_t$ +8.1 ± 1.2
CA19-26.6
*43.1 ± 1.3 Ma
*εHf$_t$ +5.4 ± 1.1
CA19-26.8
*45 ± 0.5 Ma
**42.7 ± 1.3 Ma
*εHf$_t$ +6.3 ± 1.1
CA19-26.9
*44.1 ± 1.3 Ma
**44.6 ± 1.4 Ma
*εHf$_t$ +4.7 ± 1.3
CA19-26.10
*43.2 ± 1.4 Ma
**43.6 ± 1.7 Ma
*εHf$_t$ +6.3 ± 1.3
CA19-26.11
**44.5 ± 1.8 Ma
*εHf$_t$ +7.0 ± 1.4
CA19-26.12
*(556 ± 18 Ma)
**44.4 ± 1.7 Ma
*εHf$_t$ -9.9 ± 1.1
**εHf$_t$ +0.0 ± 1.7
CA19-26.14
*44.6 ± 1.9 Ma
*εHf$_t$ +8.5 ± 1.4
CA19-26.15
**43.6 ± 1.7 Ma
*εHf$_t$ +5.0 ± 1.1
CA19-26.16
*(666 ± 23 Ma)
**43.6 ± 2 Ma
CA19-26.19
*(46.4 ± 1.7 Ma)
**44.1 ± 1.7 Ma
*εHf$_t$ +6.9 ± 1.7
**εHf$_t$ +5.9 ± 1.4
CA19-26.20
**45.2 ± 2.3 Ma
**εHf$_t$ +5.6 ± 1.3
CA19-26.21
*(1917 ± 59 Ma)
**(2174 ± 64 Ma)
*εHf$_t$ -5.1 ± 1.3
CA19-26.45
**43.1 ± 1.7 Ma
*εHf$_t$ +4.8 ± 1.3
CA19-26.44
*(1849 ± 60 Ma)
CA19-26.47
*(568 ± 23 Ma)
**43.3 ± 2.4 Ma
*εHf$_t$ -4.6 ± 1.3
**εHf$_t$ -2.5 ± 1.3
CA19-26.55
*(927 ± 40 Ma)
**(868 ± 367 Ma)
*εHf$_t$ -14.7 ± 1.3
CA19-26.56
*45 ± 2.4 Ma
**45 ± 2.4 Ma
CA19-26.50
*43 ± 1.9 Ma
**44.5 ± 2.6 Ma)
*εHf$_t$ +5.2 ± 1.4
CA19-26.51
*(333 ± 18 Ma)
**43.2 ± 2 Ma
*εHf$_t$ -12.6 ± 1.5
**εHf$_t$ +4.8 ± 1.3
U-Pb age (Ma)
trace el. spot
Hf isotopes

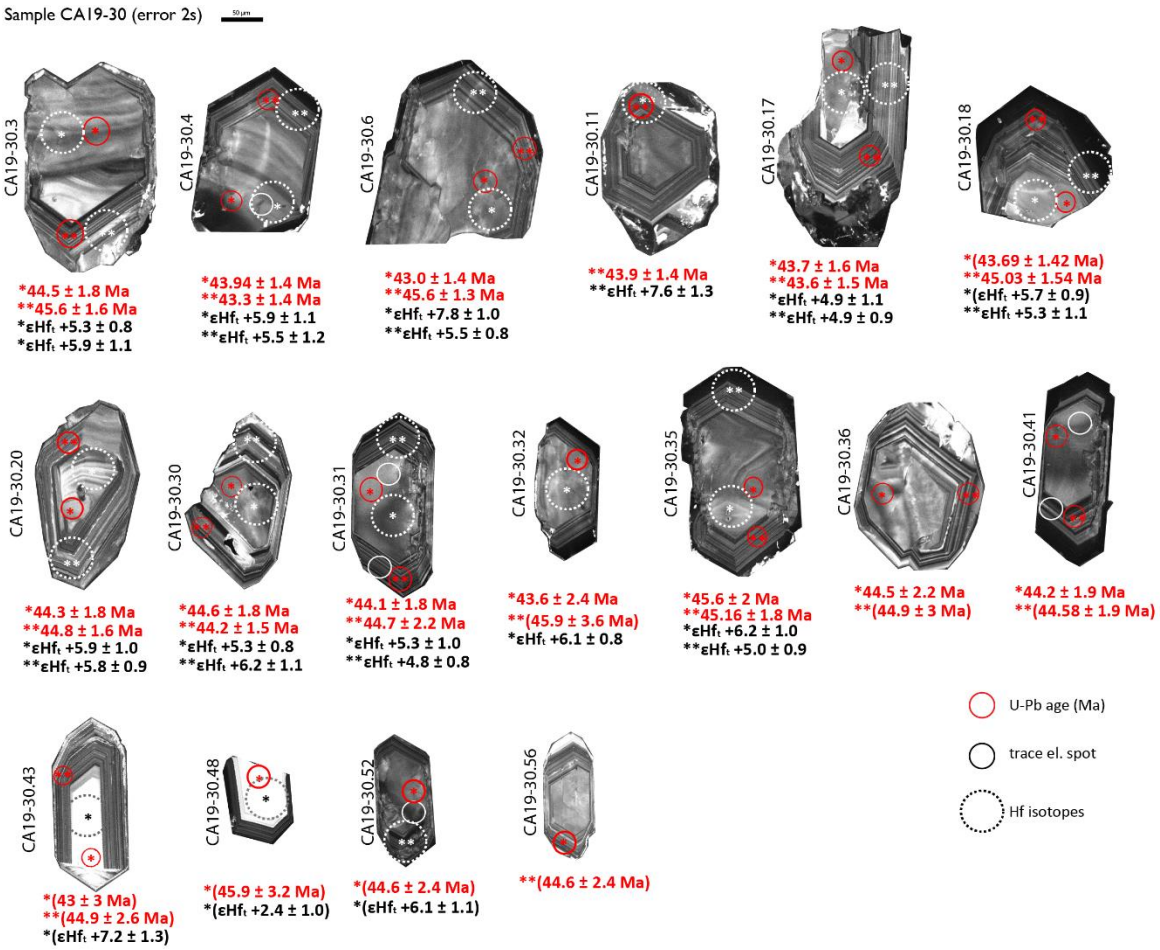
Sample CA19-30 (error 2s)
50 µm
CA19-30.3
*44.5 ± 1.8 Ma
**45.6 ± 1.6 Ma
*εHf$_t$ +5.3 ± 0.8
*εHf$_t$ +5.9 ± 1.1
CA19-30.4
*43.94 ± 1.4 Ma
**43.3 ± 1.4 Ma
*εHf$_t$ +5.9 ± 1.1
**εHf$_t$ +5.5 ± 1.2
CA19-30.6
*43.0 ± 1.4 Ma
**45.6 ± 1.3 Ma
*εHf$_t$ +7.8 ± 1.0
**εHf$_t$ +5.5 ± 0.8
CA19-30.11
**43.9 ± 1.4 Ma
**εHf$_t$ +7.6 ± 1.3
CA19-30.17
*43.7 ± 1.6 Ma
**43.6 ± 1.5 Ma
*εHf$_t$ +4.9 ± 1.1
**εHf$_t$ +4.9 ± 0.9
CA19-30.18
*(43.69 ± 1.42 Ma)
**45.03 ± 1.54 Ma
*(εHf$_t$ +5.7 ± 0.9)
**εHf$_t$ +5.3 ± 1.1
CA19-30.20
*44.3 ± 1.8 Ma
**44.8 ± 1.6 Ma
*εHf$_t$ +5.9 ± 1.0
**εHf$_t$ +5.8 ± 0.9
CA19-30.30
*44.6 ± 1.8 Ma
**44.2 ± 1.5 Ma
*εHf$_t$ +5.3 ± 0.8
**εHf$_t$ +6.2 ± 1.1
CA19-30.31
*44.1 ± 1.8 Ma
**44.7 ± 2.2 Ma
*εHf$_t$ +5.3 ± 1.0
**εHf$_t$ +4.8 ± 0.8
CA19-30.32
*43.6 ± 2.4 Ma
**(45.9 ± 3.6 Ma)
*εHf$_t$ +6.1 ± 0.8
CA19-30.35
*45.6 ± 2 Ma
**45.16 ± 1.8 Ma
*εHf$_t$ +6.2 ± 1.0
**εHf$_t$ +5.0 ± 0.9
CA19-30.36
*44.5 ± 2.2 Ma
**(44.9 ± 3 Ma)
CA19-30.41
*44.2 ± 1.9 Ma
**(44.58 ± 1.9 Ma)
U-Pb age (Ma)
trace el. spot
Hf isotopes
CA19-30.43
*(43 ± 3 Ma)
**(44.9 ± 2.6 Ma)
*(εHf$_t$ +7.2 ± 1.3)
CA19-30.48
*(45.9 ± 3.2 Ma)
*(εHf$_t$ +2.4 ± 1.0)
CA19-30.52
*(44.6 ± 2.4 Ma)
*(εHf$_t$ +6.1 ± 1.1)
CA19-30.56
**(44.6 ± 2.4 Ma)

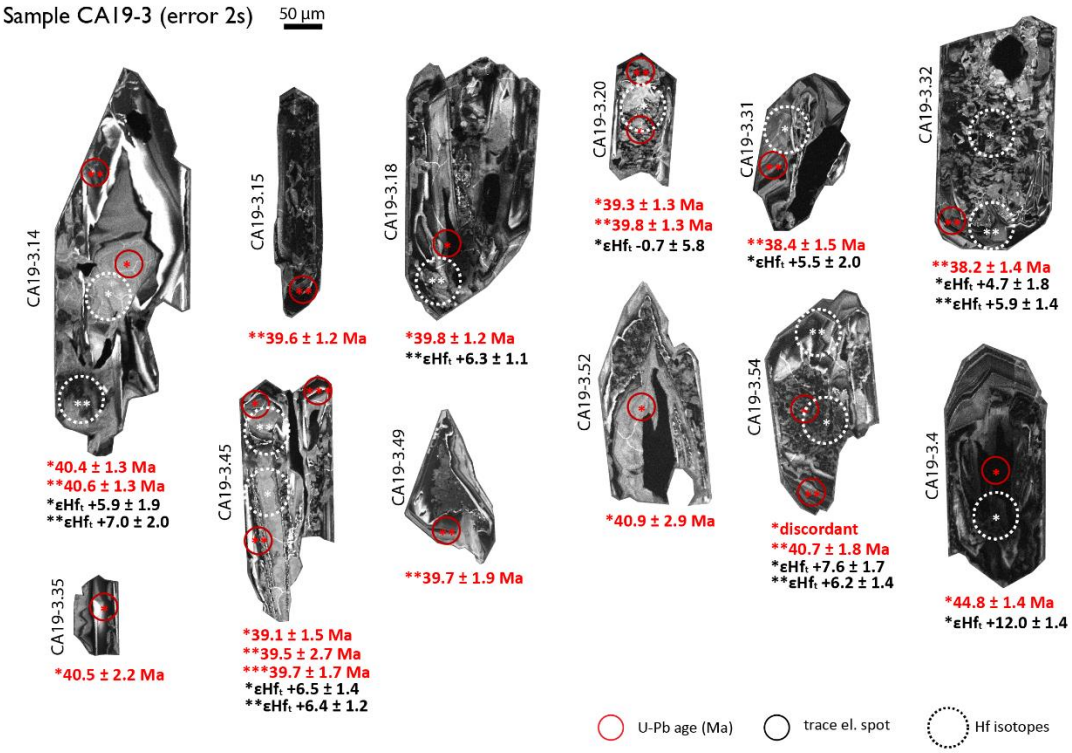
Sample CA19-3 (error 2s)
50 µm
CA19-3.14
*40.4 ± 1.3 Ma
**40.6 ± 1.3 Ma
*εHf$_t$ +5.9 ± 1.9
**εHf$_t$ +7.0 ± 2.0
CA19-3.35
*40.5 ± 2.2 Ma
CA19-3.15
**39.6 ± 1.2 Ma
CA19-3.45
*39.1 ± 1.5 Ma
**39.5 ± 2.7 Ma
***39.7 ± 1.7 Ma
*εHf$_t$ +6.5 ± 1.4
**εHf$_t$ +6.4 ± 1.2
CA19-3.18
*39.8 ± 1.2 Ma
**εHf$_t$ +6.3 ± 1.1
CA19-3.49
**39.7 ± 1.9 Ma
CA19-3.20
*39.3 ± 1.3 Ma
**39.8 ± 1.3 Ma
*εHf$_t$ -0.7 ± 5.8
CA19-3.52
*40.9 ± 2.9 Ma
CA19-3.31
**38.4 ± 1.5 Ma
*εHf$_t$ +5.5 ± 2.0
CA19-3.54
*discordant
**40.7 ± 1.8 Ma
*εHf$_t$ +7.6 ± 1.7
**εHf$_t$ +6.2 ± 1.4
CA19-3.32
**38.2 ± 1.4 Ma
*εHf$_t$ +4.7 ± 1.8
**εHf$_t$ +5.9 ± 1.4
CA19-3.4
*44.8 ± 1.4 Ma
*εHf$_t$ +12.0 ± 1.4
U-Pb age (Ma)
trace el. spot
Hf isotopes

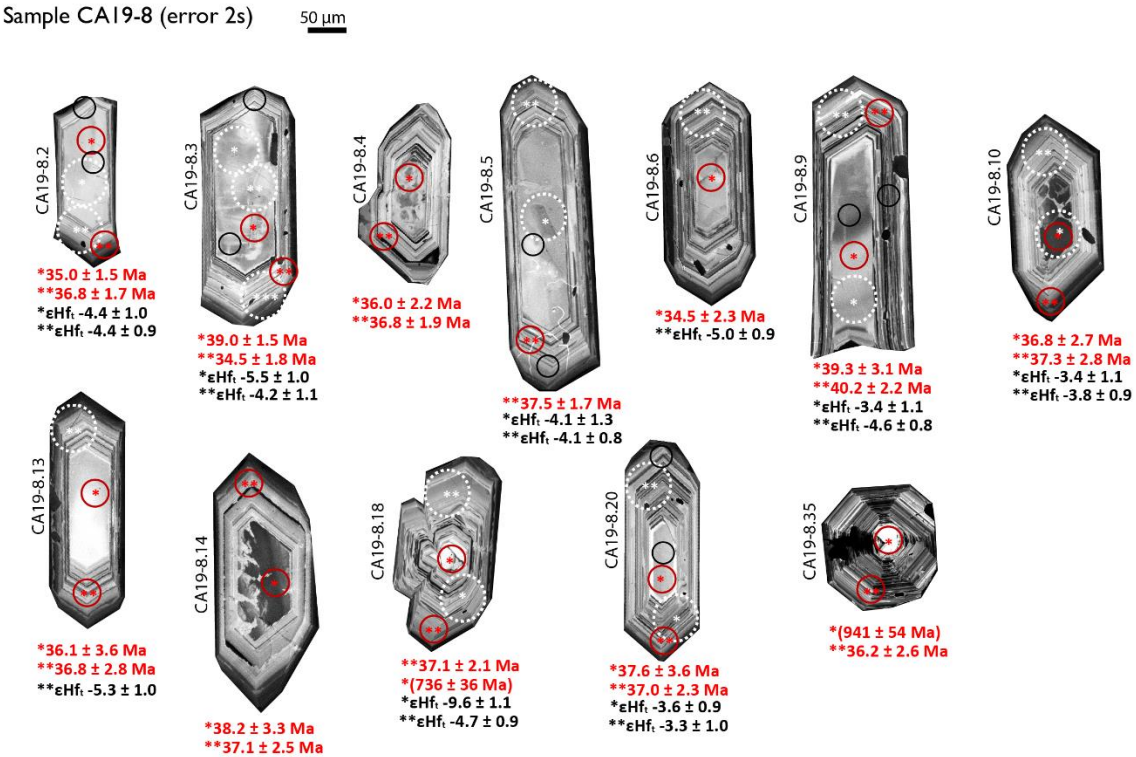
Sample CA19-8 (error 2s)
50 µm
CA19-8.2
*35.0 ± 1.5 Ma
**36.8 ± 1.7 Ma
*εHf$_t$ -4.4 ± 1.0
**εHf$_t$ -4.4 ± 0.9
CA19-8.3
*39.0 ± 1.5 Ma
**34.5 ± 1.8 Ma
*εHf$_t$ -5.5 ± 1.0
**εHf$_t$ -4.2 ± 1.1
CA19-8.4
*36.0 ± 2.2 Ma
**36.8 ± 1.9 Ma
CA19-8.5
**37.5 ± 1.7 Ma
*εHf$_t$ -4.1 ± 1.3
**εHf$_t$ -4.1 ± 0.8
CA19-8.6
*34.5 ± 2.3 Ma
**εHf$_t$ -5.0 ± 0.9
CA19-8.9
*39.3 ± 3.1 Ma
**40.2 ± 2.2 Ma
*εHf$_t$ -3.4 ± 1.1
**εHf$_t$ -4.6 ± 0.8
CA19-8.10
*36.8 ± 2.7 Ma
**37.3 ± 2.8 Ma
*εHf$_t$ -3.4 ± 1.1
**εHf$_t$ -3.8 ± 0.9
CA19-8.13
*36.1 ± 3.6 Ma
**36.8 ± 2.8 Ma
**εHf$_t$ -5.3 ± 1.0
CA19-8.14
*38.2 ± 3.3 Ma
**37.1 ± 2.5 Ma
CA19-8.18
**37.1 ± 2.1 Ma
*(736 ± 36 Ma)
*εHf$_t$ -9.6 ± 1.1
**εHf$_t$ -4.7 ± 0.9
CA19-8.20
*37.6 ± 3.6 Ma
**37.0 ± 2.3 Ma
*εHf$_t$ -3.6 ± 0.9
**εHf$_t$ -3.3 ± 1.0
CA19-8.35
*(941 ± 54 Ma)
**36.2 ± 2.6 Ma

Hf isotopes methods

On the same zircon domains of U-Pb dating, in-situ Hf isotope analyses were performed using a 193nm Excimer Laser Ablation System (Analyte Excite by Teledyne Cetac Technologies) connected with a Thermo Fisher Scientific MC-ICP-MS Neptune XT at the Department of Earth Sciences "A. Desio" University of Milan. Each initial $^{176}Hf/^{177}Hf$ ratio and initial εHf was calculated according to the corresponding U/Pb date.

The diameter was 50 μm, the repetition rate at 6 Hz and the energy density was set at 3.5 J/cm^2. He gas flow rate in the sample cell was set at 0.51 l/min, and at 0.2 l/min in the cup. Ar was used as sample gas (1.1 l/min), cool gas (12.7 l/min) and auxiliary gas (1.1 l/min), with a little addition (2.5 ml/min) of N_2 gas downstream to the ablation cell.

The detailed description of the data reduction scheme is given by Fisher et al. (2014). The applied correction is calculated with a peak stripping procedure.

The cup configuration is given in table *SX.1*. The Neptune instrument is equipped with 9 faraday cups (H4 is not used) connected with 1011 Ω resistors current amplifiers. Every analysis is composed of 35 s of background signal, 60 s of ablation signal, and 50 s of wash out. The integration time is ~1.05 s, giving 50-57 measured isotopic ratios during ablation.

	L4	L3	L2	L1	C	H1	H2	H3
Analytes	^{171}Yb	^{173}Yb	^{174}Yb, ^{174}Hf	^{175}Lu	^{176}Hf	^{177}Hf	^{178}Hf	^{179}Hf
Monoatomic interferents					^{176}Yb ^{176}Lu			
Polyatomic interferents	$^{155}Gd^{16}O$	$^{157}Gd^{16}O$	$^{158}Gd^{16}O$	$^{159}Tb^{16}O$	$^{160}Gd^{16}O$	$^{161}Dy^{16}O$	$^{162}Dy^{16}O$ $^{162}Er^{16}O$	$^{163}Dy^{16}O$

Figure A.3 Cup configuration and interferences

The $^{173}Yb/^{171}Yb$ ratio of the individual spots was used to calculate the fractionation coefficient (βYb) for each integrated cycle of ~1.05 s allowing time dependent mass bias changes to be corrected, and then to calculate the contribution of ^{176}Yb on ^{176}Hf. For data reduction we used the natural isotopic ratio $^{176}Yb/^{173}Yb$ of 0.793813 and $^{173}Yb/^{171}Yb$ of 1.130171 published by Segal et al. (2003).

The ^{176}Lu interference correction is of minor importance. The mass fractionation behaviour for Lu is assumed to be equal to that of Yb (Fisher et al., 2011; Woodhead et al., 2004) and use βYb and the reference value of $^{176}Lu/^{175}Lu$ published in Vervoort et al. (2004) to calculate the interference correction. The correction for mass fractionation between Hf isotopes is applied using the calculated fractionation coefficient (βHf) obtained by dividing the measured $^{179}Hf/^{177}Hf$ ratio, two stable and interference free Hf isotopes, by the reference natural value from Patchett and Tatsumoto (1980). As for βYb, it is calculated for each integrated cycle.

For data reduction, the calculation of initial $^{176}Hf/^{177}Hf$ and εHf is obtained using decay constant of ^{176}Lu of Söderlund et al., (2004) and the $^{176}Hf/^{177}Hf$ and $^{176}Lu/^{177}Hf$ of CHUR proposed in Bouvier et al. (2008). Propagation of uncertainties in the calculated initial values is accomplished using the Excel spreadsheet published by Ickert (2013).

Together with unknown samples were analysed two common zircon reference materials, Plešovice and Temora-2, as quality control.

During data acquisition of the first run, analyses of Temora-2 yielded a mean $^{176}Hf/^{177}Hf$ ratio of 0.282675 ± 0.000034 (2s; n=6) whereas the same value for Plesovice was 0.282496 ± 0.000041 (2s; n=8). During the second run, the analyses yielded a Tem-2 mean $^{176}Hf/^{177}Hf$ ratio of 0.282674 ± 0.000044 (2s; n=7) and a ratio for Ples of 0.282476 ± 0.000037 (2s; n=7). During the third analytical session, TEM-2 analyses gave a mean $^{176}Hf/^{177}Hf$ ratio of 0.282678 ± 0.000043 (2s; n=14) while those on Ples returned a mean ratio of 0.282496 ± 0.000027 (2s; n= 14). In the fourth run, the TEM-2 mean $^{176}Hf/^{177}Hf$ ratio was 0.282666 ± 0.000053 (2s; n=16); for Ples it was 0.282475 ± 0.000047 (2s; n= 16). Along two months of analysis in the laboratory, the obtained $^{176}Hf/^{177}Hf$ value of Temora-2 is 0.282675 ± 0.000047 (2s; n=58) . The obtained $^{176}Hf/^{177}Hf$ value of PLesovice is 0.282486 ± 0.000044 (2s; n=60). Analyses on Temora-2 result within error with the reported value of 0.282686 ± 0.000008 by Woodhead and Hergt (2005). Analyses conducted on Plesovice are within error with the reported value of 0.282482 ± 0.000012 by Slama et al., (2008).

Appendix B

Table B.1 Trace element compositions of TMG plagioclase crystals measured by LA-ICP-MS

Sample	n#	pos.	Spot	Be	Sc	Ti	Mn	Zn	Rb	Sr	Ba	La	Ce	Pr	Nd	Sm	Eu	Gd	Pb	Eu/Eu*	La/Sm
TMG																					
CA19-13	**1**	rim	1	2.30	7.34	19.3	104	1.29	1.97	929	289	5.67	9.55	0.564	1.48	0.209	0.682	0.098	41.4	8.78	16.9
CA19-13	**1**	mantle	2	2.48	10.1	23.4	96.0	2.98	0.41	1124	478	5.91	9.45	0.636	1.64	0.181	0.944	0.129	54.6	12.3	20.4
CA19-13	**1**	mantle	3	2.21	8.57	19.4	72.5	1.56	0.36	1098	412	5.42	8.21	0.583	1.52	0.188	0.983	0.130	43.7	12.6	18.0
CA19-13	**1**	mantle	4	0.790	6.87	25.1	84.7	1.27	0.08	1276	173	9.23	15.1	1.10	2.81	0.260	0.851	0.129	14.9	9.75	22.2
CA19-13	**1**	mantle	5	0.620	7.29	39.5	118	1.66	0.08	1531	154	16.7	25.1	1.80	4.52	0.312	0.875	0.158	9.52	9.12	33.4
CA19-13	**1**	core	6	1.50	6.26	46.8	376	21.7	23.2	1436	128	13.1	26.1	1.93	5.57	0.459	0.859	0.218	15.2	7.45	17.8
CA19-13	**1**	core	7	0.670	6.39	21.5	215	2.34	20.2	2513	155	10.0	18.3	1.41	3.93	0.216	0.619	0.161	11.2	7.30	29.0
CA19-13	**1**	core	8	5.82	6.75	28.2	250	29.8	17.1	1392	95.0	12.9	21.6	1.84	5.01	0.513	0.862	0.299	14.4	6.87	15.7
CA19-13	**1**	core	9	0.920	7.67	33.2	220	2.86	0.84	1646	95.0	14.4	23.2	1.74	4.82	0.322	0.796	0.230	9.17	7.75	27.8
CA19-13	**1**	mantle	10	0.870	7.46	37.2	136	1.12	0.06	1529	145	16.7	25.6	1.76	4.84	0.329	0.902	0.170	13.0	9.13	31.6
CA19-13	**1**	mantle	11	1.47	8.11	24.3	92.3	1.32	0.12	1347	261	7.62	12.2	0.926	2.19	0.232	1.013	0.140	27.9	11.9	20.5
CA19-13	**1**	mantle	12	2.09	8.22	22.5	81.5	1.55	0.78	931	449	5.22	9.43	0.610	1.60	0.212	0.859	0.101	46.3	11.0	15.4
CA19-13	**1**	mantle	13	2.81	8.11	19.4	85.2	0.860	0.11	965	279	5.42	8.44	0.612	1.47	0.186	0.910	0.108	49.9	12.0	18.2
CA19-13	**3**	rim	1	2.47	8.06	14.8	33.8	0.760	0.406	635	590	2.12	3.66	0.290	0.772	0.089	0.759	0.111	55.9	12.5	14.9
CA19-13	**3**	mantle	2	2.32	6.98	26.5	90.4	2.23	0.242	1065	181	8.22	12.2	0.937	2.32	0.242	1.03	0.112	19.8	12.4	21.2
CA19-13	**3**	mantle	3	1.67	6.78	40.9	188	7.60	63.4	1291	211	12.5	17.0	1.195	2.80	0.242	0.789	0.0840	16.6	9.77	32.2
CA19-13	**3**	core	4	2.69	7.56	36.9	82.1	1.68	33.7	1192	135	7.06	9.99	0.667	1.84	0.225	0.592	0.0810	31.4	7.57	19.6
CA19-13	**3**	core	5	1.87	6.44	39.1	134	1.96	0.292	1186	131	11.1	22.8	2.17	6.76	0.890	0.757	0.504	19.0	4.60	7.76
CA19-13	**3**	mantle	6	1.14	4.87	24.2	85.9	0.990	0.211	940	108	9.39	13.3	0.894	2.19	0.159	0.534	0.0790	16.1	7.82	36.9
CA19-13	**3**	rim	7	1.04	2.98	10.9	42.8	0.649	0.111	429	78.4	3.03	4.82	0.352	1.00	0.086	0.450	0.0570	9.88	8.58	22.0
CA19-13	**4**	rim	1																		
CA19-13	**4**	mantle	2	2.03	6.42	17.5	48.0	0.800	0.254	746	237	3.63	5.93	0.493	1.25	0.176	0.850	0.0890	36.4	11.8	12.9
CA19-13	**4**	mantle	3	2.11	7.04	26.9	95.5	1.19	0.118	1105	170	9.94	14.1	0.997	2.55	0.260	1.04	0.113	28.6	12.1	23.9
CA19-13	**4**	core	4	2.40	7.53	26.8	81.3	1.65	0.101	1225	177	11.4	15.5	1.11	2.81	0.193	0.897	0.104	25.4	11.8	36.7
CA19-13	**4**	core	5	2.05	7.31	30.5	108	1.29	0.0920	1304	151	14.1	18.8	1.29	3.02	0.235	0.850	0.104	23.2	10.4	37.4
CA19-13	**4**	core	6	2.66	7.86	29.1	62.2	1.23	0.221	1084	211	8.28	12.6	0.933	2.43	0.261	1.06	0.136	31.2	12.1	19.8
CA19-13	**4**	mantle	7	2.19	7.41	26.6	65.7	1.40	0.165	1016	225	7.02	10.7	0.839	2.31	0.192	1.17	0.125	26.7	14.9	22.8
CA19-13	**4**	mantle	8	2.65	7.57	23.2	52.4	1.14	0.146	944	212	5.88	9.51	0.742	1.96	0.182	1.11	0.0900	34.6	15.1	20.2
CA19-13	**4**	mantle	9	1.99	6.29	18.5	48.0	0.86	0.219	779	233	3.82	6.64	0.521	1.37	0.200	0.902	0.0770	27.9	12.2	11.9
CA19-13	**4**	rim	10	2.30	8.25	13.8	8.95	0.59	0.245	462	410	1.87	2.85	0.212	0.507	0.111	0.429	0.0640	47.2	7.36	10.5

Table B.2 Trace element compositions of ETN and PTN plagioclase crystals measured by LA-ICP-MS

Sample	n#	pos.	Spot	Be	Sc	Ti	Mn	Zn	Rb	Sr	Ba	La	Ce	Pr	Nd	Sm	Eu	Gd	Pb	Eu/Eu*	La/Sm
ETN																					
CA19-15	**7**	rim	1	8.01	9.25	11.6	10.9	4.53	0.142	1111	260	0.995	1.60	0.145	0.562	0.0910	0.884	0.067	47.2	16.1	6.83
CA19-15	**7**	mantle	2	1.43	5.99	35.5	30.1	4.06	<0.032	1132	110	8.49	11.5	0.787	2.10	0.147	0.550	0.0900	20.4	8.13	36.1
CA19-15	**7**	core	3	2.83	8.55	27.7	26.3	5.84	0.883	1330	195	8.49	11.9	0.900	2.15	0.226	0.782	0.118	25.4	9.54	23.5
CA19-15	**7**	core	4	2.31	7.41	23.6	19.5	4.66	0.0700	1168	180	6.59	9.19	0.683	1.82	0.164	0.799	0.0770	31.6	11.6	25.1
CA19-15	**7**	rim	5	4.47	7.61	17.1	9.91	4.23	0.736	964	206	2.27	3.34	0.267	0.751	0.0760	0.789	0.0960	37.8	14.0	18.7
CA19-15	**8**	mantle	1	2.68	7.75	26.2	21.1	3.90	0.182	1244	205	7.92	10.6	0.774	1.91	0.174	0.890	0.0870	23.3	12.4	28.4
CA19-15	**8**	core	2	2.36	8.00	29.9	26.6	4.69	0.154	1246	154	11.1	14.0	0.989	2.38	0.173	0.814	0.0820	27.1	11.5	40.2
CA19-15	**8**	core	3	2.00	6.94	18.8	16.4	4.61	5.93	991	123	6.43	8.25	0.518	1.23	0.0640	0.424	0.0700	23.1	8.50	62.7
CA19-15	**8**	core	4	2.22	8.64	37.0	25.3	5.99	2.97	1299	175	8.54	12.3	0.856	1.95	0.141	0.814	0.130	33.0	11.4	37.8
CA19-15	**8**	mantle	5	8.50	13.1	23.6	11.5	6.02	0.259	1435	294	2.92	4.27	0.337	0.879	0.116	0.967	0.0200	60.4	18.3	15.7
PTN																					
CA19-16	**29**	rim	1	4.45	7.87	12.6	7.90	3.31	0.0780	1025	208	3.44	3.95	0.253	0.683	0.068	0.633	0.0600	30.7	12.9	31.6
CA19-16	**29**	mantle	2	3.91	11.2	46.9	35.7	7.27	0.738	2181	274	12.5	16.3	1.05	2.33	0.149	0.924	0.136	53.1	12.6	52.3
CA19-16	**29**	core	3	1.52	9.42	49.9	116	12.9	21.4	2570	178	19.3	29.0	1.93	4.64	0.340	0.878	0.212	26.9	8.50	35.4
CA19-16	**29**	mantle	4	3.41	10.8	66.8	59.1	8.57	4.03	2995	298	24.1	34.0	2.21	5.08	0.322	1.30	0.187	30.7	13.1	46.8
CA19-16	**29**	mantle	5	4.66	11.4	26.6	26.8	6.56	0.641	2147	364	8.91	12.4	0.838	1.90	0.136	1.18	0.179	47.7	15.5	40.9
CA19-16	**29**	rim	6	6.17	8.80	10.2	10.9	3.75	0.370	1312	211	3.71	4.29	0.247	0.629	0.0770	0.295	0.0530	35.9	5.91	30.1
CA19-16	**30**	mantle	1	2.40	11.6	26.4	10.4	8.72	<0.13	1518	329	9.60	11.2	0.680	2.02	0.160	0.720	bdl	62.5	-	37.5
CA19-16	**30**	mantle	2	3.12	5.8	29.5	20.4	3.30	1.02	1281	110	12.1	13.2	0.817	1.99	0.168	0.520	0.0880	30.3	7.35	45.0
CA19-16	**30**	core	3	1.25	8.11	97.5	43.3	5.64	4.10	3329	202	34.7	41.7	2.42	5.62	0.377	0.759	0.222	27.6	7.04	57.5
CA19-16	**30**	core	4	1.36	8.05	106	82.9	5.30	0.712	4218	261	37.5	46.9	2.81	6.30	0.421	0.807	0.229	8.29	7.17	55.6
CA19-16	**30**	mantle	5	4.91	13.6	50.3	35.0	8.60	2.60	3273	357	21.4	29.4	1.75	4.22	0.327	1.47	0.180	63.2	14.8	40.9

Table B.3 Trace element compositions of PTN plagioclase crystals measured by LA-ICP-MS

Sample	n#	pos.	Spot	Be	Sc	Ti	Mn	Zn	Rb	Sr	Ba	La	Ce	Pr	Nd	Sm	Eu	Gd	Pb	Eu/Eu*	La/Sm
PTN																					
CA19-16	**31**	rim	1	2.37	6.46	21.9	16.2	3.92	<0.056	1359	177	9.38	12.3	0.707	1.63	0.123	0.625	0.0410	27.2	10.9	47.6
CA19-16	**31**	core	2	3.01	8.30	23.3	22.1	5.79	4.31	1903	219	9.34	11.8	0.732	1.70	0.104	0.677	0.0860	25.1	11.3	56.1
CA19-16	**31**	core	3	3.28	10.2	25.3	23.5	10.8	7.28	1847	270	8.05	13.0	0.842	1.70	0.059	0.910	<0.027	36.4	-	85.2
CA19-16	**31**	core	4	2.38	9.15	30.7	29.8	6.62	30.2	2096	239	11.2	14.7	0.886	1.90	0.103	0.778	0.0990	28.0	12.6	68.1
CA19-16	**31**	core	5	4.92	10.5	28.1	19.6	7.12	2.04	2137	316	7.54	10.5	0.633	1.41	0.174	0.865	0.0860	35.2	12.1	27.1
CA19-16	**31**	core	6	3.29	9.20	26.9	23.2	7.32	10.1	2018	249	9.62	13.1	0.735	1.58	0.123	0.806	0.103	30.7	12.3	48.8
CA19-16	**31**	core	7	3.20	9.15	25.1	21.7	6.33	1.63	1909	248	9.94	12.7	0.749	1.77	0.097	0.687	0.0750	33.6	12.0	64.0
CA19-16	**31**	core	8	4.94	11.9	23.6	18.7	8.71	4.23	2201	407	4.82	6.48	0.423	0.999	0.074	0.903	0.0780	40.0	17.0	40.7
CA19-16	**31**	core	9	3.74	10.6	23.5	17.5	6.57	1.66	2140	293	8.53	10.9	0.604	1.44	0.124	0.790	0.0720	42.0	12.8	43.0
CA19-16	**31**	core	10	2.58	8.13	46.2	35.4	5.61	0.380	2242	227	20.1	26.4	1.541	3.24	0.142	0.846	0.101	26.0	12.4	88.4
CA19-16	**31**	core	11	2.92	8.36	36.1	27.6	5.22	0.212	2206	240	15.9	20.7	1.26	2.53	0.143	0.845	0.0820	31.4	12.8	69.2
CA19-16	**31**	core	12	6.85	10.3	16.8	16.9	4.90	1.75	1578	243	1.54	2.64	0.170	0.540	0.122	0.429	0.0590	39.6	7.20	7.88
CA19-16	**31**	rim	13	5.40	9.26	15.4	13.9	4.73	0.363	1382	390	1.42	2.21	0.180	0.562	0.063	0.854	0.0670	45.2	17.4	14.0
CA19-16	**13**	rim	1	3.34	3.10	29.0	24.2	4.01	0.0980	1855	199	11.4	14.1	0.959	2.49	0.216	0.980	0.218	31.9	10.9	33.1
CA19-16	**13**	mantle	2	2.87	2.96	25.2	20.5	3.85	<0.101	1473	230	6.76	8.33	0.610	1.52	0.136	0.766	0.159	27.1	10.4	31.0
CA19-16	**13**	mantle	3	3.66	3.40	18.8	23.0	4.32	0.237	1209	260	4.97	6.26	0.478	1.33	0.177	0.940	0.165	27.7	11.7	17.5
CA19-16	**13**	mantle	4	3.15	3.45	20.9	28.4	3.58	0.177	1106	229	5.34	6.82	0.497	1.56	0.108	0.880	0.149	26.1	12.9	30.9
CA19-16	**13**	mantle	5	3.36	3.44	20.4	26.4	3.72	0.523	985	251	5.47	7.18	0.492	1.50	0.237	0.839	0.189	25.7	9.33	14.4
CA19-16	**13**	mantle	6	4.18	3.93	21.7	24.6	3.95	<0.124	1006	238	5.10	6.95	0.535	1.52	0.164	1.00	0.142	26.2	13.2	19.4
CA19-16	**13**	mantle	7	3.59	3.29	21.6	29.1	3.72	0.164	976	208	4.99	6.28	0.484	1.40	0.176	0.906	0.135	22.9	11.8	17.7
CA19-16	**13**	mantle	8	3.71	3.22	19.4	74.2	4.21	0.210	997	224	4.10	6.42	0.454	1.31	0.191	0.946	0.186	25.4	11.3	13.4
CA19-16	**13**	mantle	9	3.84	3.85	18.8	17.6	4.48	8.68	1113	851	5.27	6.57	0.526	1.53	0.125	0.729	0.416	31.9	7.56	26.3
CA19-16	**13**	mantle	10	3.27	3.07	23.3	18.8	3.26	0.305	1005	188	5.23	6.55	0.482	1.35	0.153	0.805	0.158	21.1	10.58	21.3
CA19-16	**13**	mantle	11	3.34	3.38	25.2	42.0	4.09	0.174	973	178	4.57	6.36	0.455	1.28	0.164	0.705	0.142	21.5	9.28	17.4
CA19-16	**13**	mantle	12	3.08	3.17	24.5	13.4	3.89	<0.099	1065	160	7.05	8.53	0.617	1.68	0.142	0.636	0.139	22.3	8.77	31.0
CA19-16	**13**	mantle	13	3.51	2.82	21.1	9.31	2.81	0.110	1075	143	5.95	6.89	0.483	1.10	0.074	0.327	0.112	25.7	5.63	50.2
CA19-16	**13**	core	14	3.27	3.08	24.1	16.5	3.62	<0.104	1128	168	6.30	7.86	0.621	1.70	0.150	0.744	0.097	25.9	10.8	26.2
CA19-16	**13**	core	15	5.54	3.60	22.7	10.5	3.57	0.308	1361	209	5.33	6.54	0.516	1.27	0.127	0.485	0.159	35.1	6.69	26.2
CA19-16	**13**	core	16	3.26	3.40	27.9	20.4	3.88	0.125	1168	203	7.07	9.13	0.682	1.95	0.166	0.868	0.179	29.1	10.8	26.6
CA19-16	**13**	mantle	17	4.23	3.10	12.1	22.6	2.79	<0.083	1229	172	4.77	5.86	0.422	1.26	0.155	0.338	0.102	33.7	4.81	19.2
CA19-16	**13**	mantle	18	4.30	2.84	17.1	10.3	3.75	<0.092	945	174	4.67	5.60	0.422	1.23	0.259	0.539	0.098	29.2	6.39	11.3
CA19-16	**13**	mantle	19	3.11	2.81	16.1	16.6	3.72	0.183	861	185	4.38	5.58	0.462	1.35	0.208	0.735	0.130	21.4	9.10	13.1
CA19-16	**13**	mantle	20	3.06	2.82	23.4	18.7	3.14	0.213	1001	250	8.75	11.4	0.815	2.28	0.186	1.02	0.162	23.7	12.6	29.4
CA19-16	**13**	mantle	21	2.73	2.97	25.4	37.7	3.54	0.256	1016	174	7.73	9.80	0.694	1.92	0.138	0.751	0.184	20.0	9.79	35.0
CA19-16	**13**	mantle	22	3.67	3.31	21.5	38.8	3.59	0.321	1227	307	5.40	6.84	0.529	1.42	0.131	0.966	0.198	27.3	12.5	25.7
CA19-16	**13**	rim	23	4.81	4.50	23.7	46.4	4.35	0.420	1538	342	7.69	9.45	0.678	1.92	0.166	1.10	0.184	34.7	13.7	28.9

Table B.4 Trace element compositions of PTN and EBG plagioclase crystals measured by LA-ICP-MS

Sample	n#	pos.	Spot	Be	Sc	Ti	Mn	Zn	Rb	Sr	Ba	La	Ce	Pr	Nd	Sm	Eu	Gd	Pb	Eu/Eu*	La/Sm
PTN																					
CA19-16	**14**	mantle	1	3.83	3.45	24.7	19.4	4.44	0.752	1677	293	6.44	7.75	0.610	1.66	0.105	0.944	0.198	28.5	12.8	38.3
CA19-16	**14**	mantle	2	2.68	2.78	21.0	16.4	3.78	<0.098	1007	201	5.78	7.28	0.522	1.52	0.133	0.839	0.154	25.2	11.5	27.1
CA19-16	**14**	mantle	3	0.920	2.47	32.4	30.6	3.29	0.104	1013	101	16.2	21.4	1.53	3.88	0.293	0.691	0.151	17.5	7.42	34.5
CA19-16	**14**	core	4	2.53	2.22	18.0	24.7	4.25	6.80	910	140	6.32	7.70	0.536	1.48	0.176	0.547	0.076	16.7	7.75	22.4
CA19-16	**14**	core	5	2.78	2.97	40.7	30.4	5.02	2.86	1361	156	11.6	15.1	1.10	2.71	0.220	0.742	0.190	18.9	8.44	33.0
CA19-16	**14**	core	6	2.77	3.08	31.6	33.8	4.5	<0.102	1302	139	11.5	14.5	1.05	2.49	0.189	0.769	0.142	17.7	9.68	37.9
CA19-16	**14**	core	7	3.58	4.04	19.8	20.6	7.84	0.148	1456	260	7.94	9.03	0.647	1.67	0.096	0.684	0.141	27.5	10.43	51.6
CA19-16	**14**	mantle	8	1.27	2.21	26.1	26.4	3.88	<0.063	930	86	6.38	9.68	0.667	1.63	0.199	0.508	0.049	11.6	7.15	20.0
CA19-16	**14**	mantle	9	2.80	3.24	28.1	27.1	4.35	0.190	1102	188	7.36	9.54	0.665	1.98	0.175	0.860	0.176	21.5	10.6	26.3
CA19-16	**14**	mantle	10	3.37	3.39	20.2	17.9	3.59	0.152	991	213	4.34	5.61	0.472	1.32	0.177	0.915	0.191	24.8	11.1	15.3
CA19-16	**14**	mantle	11	3.15	3.06	23.2	27.8	3.89	0.175	968	205	5.73	7.20	0.533	1.62	0.216	0.935	0.193	21.8	10.7	16.6
CA19-16	**14**	rim	12	3.15	3.23	32.0	24.9	3.72	0.122	1200	226	9.69	12.1	0.856	2.18	0.172	0.958	0.170	27.8	12.0	35.2
EBG																					
CA19-26	**20**	rim		3.59	3.13	18.0	6.44	2.93	<0.119	808	249	1.00	1.35	0.100	0.288	0.0900	0.601	0.189	48.6	8.55	6.95
CA19-26	**20**	mantle		3.37	3.50	18.8	12.4	4.03	0.377	932	362	1.27	1.57	0.133	0.367	0.0630	0.600	0.215	38.1	8.68	12.6
CA19-26	**20**	mantle		3.39	4.07	22.8	23.5	4.90	0.440	1256	443	1.31	1.73	0.135	0.393	0.0310	0.532	0.270	33.0	7.55	26.3
CA19-26	**20**	mantle		2.67	4.15	24.0	25.9	5.26	0.465	1367	559	1.62	2.06	0.139	0.370	0.0320	0.437	0.306	28.6	5.86	31.5
CA19-26	**20**	core		3.02	4.11	32.9	23.5	5.5	0.502	1686	603	3.05	3.54	0.245	0.693	0.0550	0.640	0.353	32.8	7.76	34.6
CA19-26	**20**	core		3.26	4.07	29.6	17.8	5.03	0.539	1582	626	2.48	3.10	0.203	0.531	<0.035	0.559	0.424	33.0	-	-
CA19-26	**20**	core		2.48	4.05	35.8	14.6	6.43	0.328	2184	602	3.72	4.37	0.322	0.722	<0.035	0.549	0.279	33.4	-	-
CA19-26	**20**	core		2.48	4.05	35.8	14.6	6.43	0.328	2184	602	3.72	4.37	0.322	0.722	<0.035	0.549	0.279	33.4	-	-
CA19-26	**20**	mantle		3.62	4.10	24.1	29.3	5.91	0.600	1618	640	2.15	2.54	0.168	0.480	0.0610	0.464	0.343	41.6	5.64	22.0
CA19-26	**20**	mantle		2.47	3.14	26.8	18.0	3.35	0.336	1359	465	2.83	3.46	0.246	0.757	0.0410	0.582	0.268	32.8	8.11	43.1
CA19-26	**20**	mantle		3.07	3.29	22.5	21.7	4.25	0.643	1335	490	1.26	1.68	0.149	0.420	0.0870	0.530	0.221	31.2	7.22	9.05
CA19-26	**20**	rim		9.07	5.97	23.2	10.8	5.49	0.340	1070	152	1.42	2.15	0.189	0.624	0.0250	0.783	0.185	70.2	13.3	35.5

Table B.5 Trace element compositions of EBG and BLU plagioclase crystals measured by LA-ICP-MS. n.m.= not measured.

Sample	n#	pos.	Spot	Be	Sc	Ti	Mn	Zn	Rb	Sr	Ba	La	Ce	Pr	Nd	Sm	Eu	Gd	Pb	Eu/Eu*	La/Sm
EBG																					
CA19-26	**17a**	rim	1	4.04	6.43	14.8	6.59	3.25	0.555	472	102	0.701	1.11	0.0959	0.287	0.0830	0.569	0.0440	45.5	11.4	5.27
CA19-26	**17a**	mantle	2	3.00	6.37	20.0	8.97	3.81	0.123	1044	315	1.61	2.21	0.167	0.433	0.0660	0.686	0.0610	47.7	14.0	15.2
CA19-26	**17a**	mantle	3	1.90	6.73	52.9	58.4	6.65	0.344	2163	386	14.3	19.7	1.37	3.55	0.230	1.08	0.0970	19.8	13.4	38.9
CA19-26	**17a**	core	4	1.42	6.71	58.2	52.4	8.35	0.698	2125	297	13.5	19.0	1.33	3.47	0.315	0.848	0.166	14.5	8.75	26.8
CA19-26	**17a**	core	5	1.64	6.35	53.4	47.3	7.50	0.127	2031	234	13.2	19.5	1.39	3.57	0.309	0.822	0.0960	11.5	9.11	26.6
CA19-26	**17a**	core	6	1.50	6.19	56.9	43.4	7.83	0.189	1977	227	13.0	18.3	1.31	3.21	0.220	0.822	0.0890	11.2	10.5	37.0
CA19-26	**17a**	core	7	1.54	6.73	61.2	38.9	6.77	0.303	2372	324	14.7	20.1	1.36	3.30	0.238	0.921	0.100	14.0	11.3	38.5
CA19-26	**17a**	core	8	2.05	7.63	59.4	56.9	9.33	1.16	2296	409	15.9	22.7	1.57	4.08	0.361	1.17	0.239	25.6	10.9	27.5
CA19-26	**17a**	rim	9	4.77	7.88	19.7	7.04	5.05	0.238	917	285	1.18	1.92	0.150	0.469	0.082	0.751	0.0600	62.2	14.4	8.98
CA19-26	**18**	rim	1	4.33	8.63	20.1	12.2	4.81	0.0940	812	236	1.08	1.68	0.142	0.447	0.0520	0.714	0.0430	62.6	16.8	12.9
CA19-26	**18**	mantle	2	2.95	7.07	19.6	19.6	4.84	0.342	1350	622	1.92	2.52	0.193	0.458	0.0840	0.844	0.0860	42.9	15.0	14.3
CA19-26	**18**	core	3	2.40	6.71	25.9	18.5	4.70	0.270	1586	646	6.13	7.30	0.467	1.10	0.0940	0.885	0.0620	35.2	16.2	40.7
CA19-26	**18**	core	4	1.72	6.91	71.9	54.8	8.33	0.865	2441	529	19.7	24.0	1.61	3.93	0.443	1.03	0.282	23.8	8.71	27.8
CA19-26	**18**	core	5	1.52	6.79	70.5	51.1	12.1	0.621	2379	535	18.5	24.9	1.56	3.66	0.236	1.02	0.107	19.0	12.4	48.9
CA19-26	**18**	core	6	1.92	6.73	45.1	37.6	5.72	0.507	1979	620	12.8	15.5	0.984	2.37	0.253	0.946	0.124	24.3	11.0	31.6
CA19-26	**18**	mantle	7	2.96	7.05	19.6	24.0	5.61	0.597	1339	745	3.16	4.40	0.273	0.657	0.0540	0.800	0.00710	33.4	22.5	36.5
CA19-26	**18**	mantle	8	3.25	8.03	19.5	9.31	4.68	1.22	1297	464	1.92	2.92	0.252	0.746	0.139	0.792	0.133	51.2	11.1	8.63
CA19-26	**18**	rim	9	3.98	6.23	14.6	5.95	3.53	0.191	459	126	0.711	1.20	0.103	0.368	0.0560	0.458	0.0560	43.9	10.0	7.93
BLU																					
Blu08/02	**41**	rim	1	<0.40	12.2	409	203	n.m.	11.7	2522.7	104	4.30	7.24	0.724	2.51	0.250	0.792	0.226	3.12	8.37	10.7
Blu08/02	**41**	core	2	0.770	12.8	183	132	n.m.	1.19	2767.1	126	5.57	6.25	0.514	1.36	0.188	0.803	0.140	4.60	10.2	18.5
Blu08/02	**42**	rim	1	<0.45	12.1	322	150	n.m.	<0.188	2072.8	70.9	2.90	4.71	0.503	1.47	0.217	0.574	<0.108	2.65	-	8.35
Blu08/02	**42**	core	2	0.410	11.8	249	148	n.m.	<0.180	2608.5	78.7	3.72	6.01	0.580	2.11	0.348	0.744	0.148	2.58	7.51	6.68
Blu08/02	**43**	core	1	0.290	11.0	353	255	n.m.	1.85	2712.4	70.1	3.39	5.75	0.513	1.70	0.331	0.821	0.189	2.09	8.17	6.40
Blu08/02	**43**	rim	2	<0.62	12.4	358	528	n.m.	<0.214	2629.5	66.3	3.52	5.68	0.534	1.79	0.136	0.753	0.159	2.03	10.2	16.2
Blu08/02	**44**	rim	1	0.290	11.5	213	239	n.m.	0.57	2634.4	72.0	3.86	5.36	0.438	1.11	0.069	0.775	0.092	3.10	14.3	34.9
Blu08/02	**44**	core	2	0.550	9.82	161	338	n.m.	<0.197	2658.9	62.8	3.74	5.06	0.372	0.98	0.132	0.728	0.155	3.02	10.0	17.7

Table B.6. Trace element composition of reference materials for plagioclase analysis

	Run1 BCR2g					Run2 BCR2g					Run3 BCR2g				
	Mean	**SD**	**RSD%**	**REF**	**Acc%**	**Mean**	**SD**	**RSD%**	**REF**	**Acc%**	**Mean**	**SD**	**RSD%**	**REF**	**Acc%**
ppm	n=3					n=3					n=3				
Be	2.16	0.0907	4.19	2.3	-6%	2.195	0.120	5.48	2.3	-5%	1.98	0	0	2.3	-16%
Mn	1517	16.2	1.07	1550	-2%	1523	25.7	1.69	1550	-2%	1551	25.0	1.61	1550	0%
Zn	140	3.20	2.29	125	10%	140	1.56	1.12	125	11%	151	0.410	0.272	125	17%
Rb	47.5	1.06	2.23	47	1%	47.0	0.0495	0.105	47	0%	50.7	0.262	0.516	47	7%
Sr	322	3.82	1.19	342	-6%	323	6.54	2.03	342	-6%	327	0.912	0.279	342	-4%
Ba	648	11.8	1.82	683	-5%	645	0.233	0.0362	683	-6%	659	3.87	0.588	683	-4%
La	23.8	0.0635	0.267	24.7	-4%	23.64	0.0566	0.239	24.7	-4%	23.6	0.0141	0.0599	24.7	-5%
Ce	50.3	0.423	0.842	53.3	-6%	50.1	0.629	1.26	53.3	-6%	51.5	0.438	0.852	53.3	-4%
Pr	6.28	0.0306	0.486	6.7	-7%	6.26	0.120	1.92	6.7	-7%	6.28	0.0919	1.46	6.7	-7%
Nd	27.2	0.290	1.07	28.9	-6%	27.0	0.120	0.446	28.9	-7%	26.7	0.0212	0.0796	28.9	-8%
Sm	6.22	0.0751	1.21	6.59	-6%	6.15	0.290	4.72	6.59	-7%	6.07	0.0636	1.049	6.59	-9%
Eu	1.85	0.0192	1.04	1.97	-7%	1.91	0.0212	1.11	1.97	-3%	1.85	0.0778	4.22	1.97	-7%
Gd	6.27	0.0723	1.15	6.71	-7%	6.44	0.0283	0.439	6.71	-4%	6.18	0.0919	1.49	6.71	-9%
Pb	10.4	0.486	4.67	11	-6%	10.1	0.0495	0.488	11	-9%	10.8	0.134	1.24	11	-2%

Table B7a. Results for in situ Sr isotope measurements of plagioclase feldspars

Crystal	spot	n	$^{87}Sr/^{86}Sr_{corr}$	$^{87}Sr/^{86}Sr$ 2se	Sr (V)	$^{84}Sr/^{86}Sr_{corr}$	$^{84}Sr/^{86}Sr$ 2se	$^{85}Rb/^{88}Sr$	^{84}Sr (V)	^{85}Rb (V)	^{86}Sr (V)	^{87}Sr (V)	^{88}Sr (V)
TMG													
CA19-13	1	83	0.705705	0.000171	2.58322	0.066190	0.000088	0.000251	0.016004	0.000516	0.248686	0.177781	2.14075
CA19-13	2	82	0.706122	0.000156	2.17051	0.066502	0.000093	0.000335	0.013513	0.000579	0.208971	0.149456	1.79857
CA19-13	3	80	0.706177	0.000146	2.41574	0.065924	0.000090	0.000466	0.014910	0.000895	0.232580	0.166361	2.00189
CA19-13	4	82	0.706048	0.000158	3.51181	0.064957	0.000082	0.000138	0.021357	0.000385	0.338148	0.241824	2.91048
CA19-13	5	82	0.704985	0.000120	4.07423	0.064770	0.000068	0.000067	0.024701	0.000216	0.392292	0.280147	3.37709
CA19-13	6	81	0.705158	0.000112	3.99129	0.066885	0.000068	0.012662	0.025006	0.040208	0.384398	0.274494	3.30739
CA19-13	7	80	0.704900	0.000106	4.32177	0.066262	0.000064	0.000152	0.026808	0.000522	0.416091	0.297097	3.58178
CA19-13	8	82	0.704978	0.000119	4.94812	0.066568	0.000060	0.000036	0.030843	0.000141	0.476448	0.340182	4.10064
CA19-13	9	81	0.704695	0.000120	3.96791	0.066934	0.000068	0.000111	0.024887	0.000351	0.382180	0.272740	3.28810
CA19-13	10	82	0.704778	0.000123	3.97664	0.065388	0.000080	0.000074	0.024354	0.000234	0.382973	0.273371	3.29594
CA19-13	11	83	0.706044	0.000124	3.31834	0.065786	0.000074	0.000185	0.020445	0.000488	0.319550	0.228484	2.74986
CA19-13	12	82	0.706075	0.000162	2.36024	0.066911	0.000110	0.000339	0.014789	0.000636	0.227256	0.162515	1.95568

Table B7b. Results for in situ Sr isotope measurements of plagioclase feldspars

Crystal	spot	n	$^{87}Sr/^{86}Sr_{corr}$	$^{87}Sr/^{86}Sr$ 2se	Sr (V)	$^{84}Sr/^{86}Sr_{corr}$	$^{84}Sr/^{86}Sr$ 2se	$^{85}Rb/^{88}Sr$	^{84}Sr (V)	^{85}Rb (V)	^{86}Sr (V)	^{87}Sr (V)	^{88}Sr (V)
EBG													
CA19-26-20	1	81	0.705899	0.000112	2.825561	0.059892	0.000047	0.000518	0.015845	0.001164	0.272128	0.194828	2.342760
CA19-26-20	2	84	0.705951	0.000153	2.999636	0.059849	0.000049	0.000914	0.016826	0.002183	0.289027	0.206903	2.486879
CA19-26-20	3	84	0.706015	0.000161	2.702664	0.059866	0.000059	0.000811	0.015156	0.001745	0.260337	0.186411	2.240759
CA19-26-20	4	83	0.705970	0.000136	2.373931	0.059908	0.000065	0.000327	0.013315	0.000617	0.228614	0.163703	1.968299
CA19-26-20	5	82	0.706003	0.000119	3.599431	0.059635	0.000040	0.000544	0.020098	0.001557	0.346658	0.248234	2.984440
CA19-26-20	6	80	0.705837	0.000126	3.179600	0.059657	0.000044	0.000422	0.017759	0.001067	0.306217	0.219236	2.636387
CA19-26-20	7	82	0.705819	0.000099	3.506290	0.059595	0.000045	0.000568	0.019571	0.001585	0.337739	0.241773	2.907206
CA19-26-20	8	83	0.705751	0.000114	3.845857	0.059554	0.000042	0.000357	0.021442	0.001093	0.370387	0.265142	3.188885
CA19-26-20	9	84	0.705714	0.000124	3.693725	0.059550	0.000042	0.000409	0.020602	0.001202	0.355806	0.254665	3.062653
CA19-26-20	10	80	0.705670	0.000120	3.724737	0.059564	0.000042	0.000515	0.020776	0.001525	0.358772	0.256774	3.088416
CA19-26-20	11	83	0.705538	0.000129	3.682245	0.059555	0.000040	0.000299	0.020533	0.000875	0.354652	0.253793	3.053268
CA19-26-20	12	83	0.705422	0.000106	4.081333	0.059391	0.000033	0.000352	0.022683	0.001141	0.392988	0.281227	3.384434
CA19-26-20	13	83	0.705534	0.000119	4.436093	0.059373	0.000041	0.000276	0.024642	0.000973	0.427104	0.305691	3.678655
CA19-26-20	14	83	0.705461	0.000115	4.285302	0.059401	0.000038	0.000338	0.023781	0.001149	0.412313	0.295191	3.554018
CA19-26-20	15	83	0.705260	0.000134	4.424818	0.059377	0.000032	0.000197	0.024568	0.000692	0.425923	0.304805	3.669522
CA19-26-20	16	81	0.705227	0.000108	5.090933	0.059200	0.000035	0.000292	0.028188	0.001182	0.490088	0.350671	4.221986
CA19-26-20	17	81	0.705337	0.000120	4.188114	0.059368	0.000034	0.000364	0.023262	0.001213	0.403224	0.288570	3.473059
CA19-26-20	18	84	0.705870	0.000139	3.827533	0.059464	0.000042	0.000382	0.021290	0.001161	0.368469	0.263882	3.173891
CA19-26-20	19	81	0.705904	0.000142	3.500288	0.059510	0.000043	0.000875	0.019490	0.002434	0.336999	0.241350	2.902450
CA19-26-20	20	82	0.705870	0.000130	3.801275	0.059447	0.000040	0.000890	0.021143	0.002689	0.365977	0.262098	3.152057
CA19-26-20	21	83	0.705868	0.000157	2.937216	0.059587	0.000048	0.001181	0.016375	0.002756	0.282781	0.202505	2.435555
PTN													
CA19-16-14	1	83	0.706562	0.000132	3.920186	0.059424	0.000044	0.000375	0.021777	0.001167	0.377276	0.270471	3.250661
CA19-16-14	2	80	0.706147	0.000119	3.193238	0.059834	0.000045	0.000263	0.017851	0.000667	0.307226	0.220158	2.648003
CA19-16-14	3	80	0.706008	0.000144	2.561754	0.059954	0.000058	0.000170	0.014356	0.000347	0.246515	0.176602	2.124282
CA19-16-14	4	83	0.705852	0.000113	2.879296	0.060025	0.000050	0.003153	0.016154	0.007211	0.277079	0.198472	2.387591
CA19-16-14	5	81	0.705506	0.000116	3.285509	0.059713	0.000048	0.000528	0.018337	0.001379	0.316183	0.226362	2.724626
CA19-16-14	6	79	0.705533	0.000109	3.260960	0.059848	0.000045	0.001370	0.018238	0.003548	0.313803	0.224697	2.704222
CA19-16-14	7	84	0.705549	0.000132	3.092304	0.059782	0.000044	0.000482	0.017283	0.001185	0.297619	0.213073	2.564329
CA19-16-14	8	84	0.705595	0.000128	3.011690	0.059876	0.000040	0.000686	0.016855	0.001641	0.289823	0.207521	2.497490
CA19-16-14	9	84	0.706154	0.000110	2.531822	0.059907	0.000058	0.000699	0.014181	0.001407	0.243682	0.174592	2.099367
CA19-16-14	10	83	0.706327	0.000142	2.356922	0.059991	0.000056	0.000269	0.013222	0.000504	0.226846	0.162571	1.954282
CA19-16-14	11	79	0.705952	0.000127	2.365198	0.060009	0.000053	0.000330	0.013276	0.000620	0.227676	0.163060	1.961187
CA19-16-14	12	81	0.706096	0.000127	2.687631	0.060011	0.000057	0.000165	0.015080	0.000353	0.258667	0.185320	2.228564

Table B7c. Results for in situ Sr isotope measurements of plagioclase feldspars

Crystal	spot	n	$^{87}Sr/^{86}Sr_{corr}$	$^{87}Sr/^{86}Sr$ 2se	Sr (V)	$^{84}Sr/^{86}Sr_{corr}$	$^{84}Sr/^{86}Sr$ 2se	$^{85}Rb/^{88}Sr$	^{84}Sr (V)	^{85}Rb (V)	^{86}Sr (V)	^{87}Sr (V)	^{88}Sr (V)
BLU													
BLU-41	1	85	0.70379	0.000100	1.94655	0.05886	0.000068	0.000366	0.01076	0.00057	0.18774	0.13391	1.61414
BLU-41	2	85	0.70389	0.000087	2.06733	0.05856	0.000061	0.000068	0.01136	0.00011	0.19937	0.14224	1.71436
BLU-42	1	86	0.70398	0.000098	1.96922	0.05857	0.000067	0.000046	0.01083	0.00007	0.18990	0.13550	1.63300
BLU-42	2	86	0.70395	0.000089	2.11418	0.05848	0.000059	0.000056	0.01160	0.00010	0.20387	0.14547	1.75324
BLU-43	1	87	0.70386	0.000082	2.22929	0.05832	0.000066	0.000057	0.01220	0.00010	0.21497	0.15338	1.84873
BLU-43	2	83	0.70396	0.000079	2.16884	0.05843	0.000062	0.000031	0.01190	0.00005	0.20917	0.14925	1.79853
BLU-44	1	86	0.70383	0.000098	2.10343	0.05841	0.000066	0.000106	0.01153	0.00018	0.20285	0.14472	1.74433
BLU-44	2	87	0.70391	0.000088	2.22090	0.05840	0.000068	0.000040	0.01217	0.00007	0.21417	0.15280	1.84176
PTN													
CA19-16-30	1	85	0.70647	0.000064	3.94663	0.05708	0.000042	0.001674	0.02116	0.00527	0.38065	0.27253	3.27230
CA19-16-30	2	86	0.70643	0.000061	5.95672	0.05705	0.000032	0.002604	0.03186	0.01235	0.57411	0.41119	4.93956
CA19-16-30	3	88	0.70626	0.000049	15.79759	0.05692	0.000022	0.000078	0.08431	0.00098	1.52257	1.09024	13.10047
CA19-16-30	4	88	0.70656	0.000059	5.55797	0.05705	0.000029	0.000746	0.02975	0.00330	0.53580	0.38376	4.60866
CA19-16-29	2	87	0.70617	0.000057	8.50174	0.05712	0.000027	0.014210	0.04558	0.09627	0.81984	0.58678	7.04954
CA19-16-29	3	84	0.70640	0.000057	7.18295	0.05700	0.000031	0.000235	0.03843	0.00135	0.69262	0.49591	5.95599
CA19-16-29	1	86	0.70649	0.000071	3.70742	0.05709	0.000043	0.000178	0.01987	0.00053	0.35756	0.25601	3.07398
CA19-16-31	1	85	0.70649	0.000067	4.48385	0.05711	0.000035	0.000887	0.02405	0.00317	0.43247	0.30964	3.71769
CA19-16-31	2	86	0.70650	0.000056	5.73251	0.05703	0.000033	0.000314	0.03071	0.00144	0.55295	0.39587	4.75298
CA19-16-31	3	86	0.70658	0.000059	5.80113	0.05707	0.000033	0.014111	0.03109	0.06524	0.55945	0.40063	4.80997
CA19-16-31	4	84	0.70652	0.000059	4.89330	0.05709	0.000034	0.000249	0.02626	0.00097	0.47215	0.33797	4.05692
CA19-16-31	5	86	0.70641	0.000056	6.38886	0.05705	0.000035	0.000229	0.03421	0.00117	0.61607	0.44109	5.29749

Table B8. Plagioclase standard

	Calibrating standard				Quality control				
	$^{87}Sr/^{86}Sr_{measured}$	2se	Sr (V)		$^{87}Sr/^{86}Sr_{measured}$	2se	Sr (V)	$^{87}Sr/^{86}Sr_{corrected}$	2se
SO5/1	0.70390	0.00011	1.47	**SOX11**	0.70412	0.00011	1.50	0.70399	0.00011
	0.70395	0.00011	1.58		0.70424	0.00009	1.67	0.70411	0.00010
	0.70383	0.00013	1.63		0.70412	0.00011	1.71	0.70398	0.00011
	0.70393	0.00011	1.72		0.70424	0.00011	1.73	0.70410	0.00012
	0.70388	0.00010	1.69		0.70430	0.00009	1.78	0.70417	0.00009
	0.70376	0.00009	1.73		0.70414	0.00010	1.71	0.70400	0.00011
	0.70379	0.00010	1.74		0.70408	0.00008	1.74	0.70394	0.00008
	0.70381	0.00008	1.76		0.70427	0.00010	1.69	0.70413	0.00011
	0.70379	0.00009	1.74		0.70420	0.00011	1.64	0.70407	0.00011
	0.70390	0.00010	1.76		0.70416	0.00009	1.68	0.70402	0.00010
	0.70396	0.00010	1.75		0.70418	0.00009	1.69	0.70404	0.00010
	0.70387	0.00012	1.73		0.70434	0.00011	1.67	0.70421	0.00012
Mean	0.70386				0.70420			0.70406	
2sd	0.00013				0.00016			0.00016	
Reference value	0.70375				0.70406			0.70406	
d-bias	0.00011				0.00014				